

8-31-2015

# An Investigation into Transitions in Clay Mineral Chemistry on Mars

Seth Gainey

University of Nevada, Las Vegas, Seth.R.Gainey@gmail.com

Follow this and additional works at: <https://digitalscholarship.unlv.edu/thesesdissertations>



Part of the [Geochemistry Commons](#), [Geology Commons](#), and the [Mineral Physics Commons](#)

---

## Repository Citation

Gainey, Seth, "An Investigation into Transitions in Clay Mineral Chemistry on Mars" (2015). *UNLV Theses, Dissertations, Professional Papers, and Capstones*. 2475.

<https://digitalscholarship.unlv.edu/thesesdissertations/2475>

This Dissertation is protected by copyright and/or related rights. It has been brought to you by Digital Scholarship@UNLV with permission from the rights-holder(s). You are free to use this Dissertation in any way that is permitted by the copyright and related rights legislation that applies to your use. For other uses you need to obtain permission from the rights-holder(s) directly, unless additional rights are indicated by a Creative Commons license in the record and/or on the work itself.

This Dissertation has been accepted for inclusion in UNLV Theses, Dissertations, Professional Papers, and Capstones by an authorized administrator of Digital Scholarship@UNLV. For more information, please contact [digitalscholarship@unlv.edu](mailto:digitalscholarship@unlv.edu).

AN INVESTIGATION INTO TRANSITIONS IN CLAY MINERAL CHEMISTRY ON  
MARS

By

Seth R. Gainey

Bachelor of Science in Geology

St. Cloud State University

2009

Master of Science in Geology

University of Oklahoma

2011

A dissertation submitted in partial fulfillment  
of the requirements for the

Doctor of Philosophy – Geoscience

Department of Geoscience

College of Sciences

The Graduate College

University of Nevada, Las Vegas

August 2015

Copyright by Seth R. Gainey, 2015

All Rights Reserved



## **Dissertation Approval**

The Graduate College  
The University of Nevada, Las Vegas

May 1, 2015

This dissertation prepared by

Seth Gainey

entitled

An Investigation into Transitions in Clay Mineral Chemistry on Mars

is approved in partial fulfillment of the requirements for the degree of

Doctor of Philosophy – Geosciences  
Department of Geosciences

Elisabeth M. Hausrath, Ph.D.  
*Examination Committee Chair*

Kathryn Hausbeck Korgan, Ph.D.  
*Graduate College Interim Dean*

Joel Hurowitz, Ph.D.  
*Examination Committee Member*

Oliver Tschauner, Ph.D.  
*Examination Committee Member*

Arya Udry, Ph.D.  
*Examination Committee Member*

Paul Forster, Ph.D.  
*Graduate College Faculty Representative*

## ABSTRACT

# AN INVESTIGATION INTO TRANSITIONS IN CLAY MINERAL CHEMISTRY ON MARS

by

Seth R. Gainey

Dr. Elisabeth Hausrath, Examination Committee Chair

Assistant Professor of Geoscience

University of Nevada, Las Vegas

This dissertation is comprised of three studies investigating clay mineralogy on, or near the martian surface, with an introductory chapter, introducing and linking the three studies. Chapter two is on the subject of clay mineral synthesis, including Fe/Mg clay minerals which have been detected at multiple locations across the southern highlands. These Fe/Mg clay minerals have been previously interpreted as forming in anoxic/reducing environments, conducive to the preservation of organic matter. The results of this study suggest that the previous interpretation of Fe/Mg-rich clay as requiring anoxic/reducing conditions may not be accurate, as the minor presence of Mg (below what is found in many naturally occurring nontronites) allowed for the rapid precipitation of Fe-rich clay minerals under oxidized conditions. These results would prompt a reinterpretation of clay-bearing environments on the martian surface and may explain the relative dearth of detectable organic carbon on Mars.

Chapter three is on the subject of nontronite dissolution kinetics and its implications for Mars. Nontronite is a Fe-rich smectite and has been identified on the

martian surface with orbital Visible Near InfraRed (VNIR) spectrometers. The results of this study suggest nontronite is stable relative to the primary minerals in basalt under acidic and oxidizing conditions and once formed may remain on the martian surface for significant durations. Nontronite dissolution is more rapid than other clay minerals, such as kaolinite and montmorillonite (under acidic and oxidizing conditions). These results suggest the dissolution of mixed clay units may produce stratigraphy (e.g. Al-rich clay minerals overlying Fe/Mg-rich phyllosilicates) similar to that observed in the Mawrth Vallis region and other localities on the martian surface and may therefore imply surficial weathering.

In chapter four, reactive transport modeling was applied to investigate potential weathering profiles detected at, or near the martian surface. These results suggest that when Fe/Mg rich clay minerals are exposed to pedogenic conditions they alter to montmorillonite and kaolinite (i.e. the Al-rich overlying layer). The models included four scenarios where the parent materials consisted of: nontronite; nontronite and montmorillonite; nontronite and saponite and pure saponite. In all scenarios and in all cases (i.e. regardless of temperature, pH and flow rate) the weathering of the parent material resulted in the precipitation of an Al-rich layer. Similar stratigraphy has been observed in the Mawrth Vallis region and other localities on the martian surface. These results would suggest that the observed transitions in clay mineral chemistry are the result of weathering, implying the surface of Mars may have been exposed to long-term liquid water at its surface.

## ACKNOWLEDGEMENTS

I would like to first thank my father, for ultimately influencing my path in geoscience. It was my father that inspired me to pursue this tremendous undertaking and I wish he would have seen me finish. With that said, the list of support and thanks are extensive, and I truly apologize if I have missed anyone.

I would like to thank my family for their continued support through this process. I definitely had some ups and downs during this undertaking and if it was not for their support I would have never been able to reach this point. I would also like to thank Susan Nguyen who was extremely supportive of me and always willing to listen. She is a true inspiration to not only me, but many in her field.

I do not have enough thanks for Dr. Elisabeth Hausrath my committee chair. She was always willing to help me through this process. I lost count of how many hours I sat in her office, where she helped me with my research, writing and what to expect in the future. I do not believe a student could ask for a better advisor.

I would like to give my thanks to Dr. Joel Hurowitz, who was my mentor for two summers at the Jet Propulsion Laboratory. It was that first summer at JPL where I got kicked into gear on my research. I had a lot of fun and learned a lot that summer, and when I got to UNLV it felt like I hit the deck running.

I would like to thank Dr. Oliver Tschauner for all of his help on these manuscripts. Dr. Tschauner was the man that got me interested in X-Ray diffraction. It was in his class where we ran my first sample with powder diffraction. Now, I don't even know how many samples are in that folder or how many hours I logged on that machine.

My committee has been a tremendous help during this process. Paul Forster, you were always more than willing to help me and always positive when we met. Scott Nowicki, provided me with skills I probably would not have learned otherwise, and helped me expand my knowledge beyond Mars. Arya Udry, you have always been willing to meet and put the extra time aside to read my materials and better my research.

I would like to thank my office mates. Chris Adcock, who I probably argued with more than anybody I have ever met, but none the less was a tremendous help in my progression. Chris was one year ahead of me and I essentially followed in his path. Valerie Tu, who is probably one of the hardest working people I have ever met, kept a smile on my face and motivated. Michael Steiner, who at first almost never spoke became a friend to whom I probably talk to the most. Fritz Freudenberger, Courtney Bartlett, Brandon Guttery and all of my other office mates over the years, I thank you!

Lastly, I need to thank all the sources of funding that made this research possible. This material is based upon the work supported by the National Aeronautics and Space Administration under Grant No. NNX10AN23H issued through the NASA Training Grant: National Space Grant College and Fellowship Program (Space Grant) and the Mars Fundamental Research Program Grant No. NNX12AH96G. I would also thank the University of Nevada, Las Vegas's Graduate and Professional Student Association, Nevada Space Grant, the Jet Propulsion Laboratory and Argonne National Laboratory.

On to the science...



TABLE OF CONTENTS

ABSTRACT.....iii

ACKNOWLEDGMENTS.....v

LIST OF TABLES.....xiii

LIST OF FIGURES.....xv

CHAPTER ONE INTRODUCTION AND OVERVIEW.....1

CHAPTER TWO CLAY MINERALS DETECTED ON MARS CAN FORM IN  
ENVIRONMENTS THAT MAY DESTROY ORGANIC  
BIOSIGNITURES.....7

Abstract.....7

Introduction.....8

Methods.....11

Results and Discussion.....11

Conclusions.....14

Acknowledgments.....14

Tables.....16

Figures.....17

CHAPTER THREE NONTRONITE DISSOLUTION RATES AND IMPLICATIONS  
FOR MARS.....19

Abstract.....	19
Introduction.....	20
Mawrth Vallis.....	22
Methods.....	25
<u>Material</u> .....	25
<u>Reactor design</u> .....	26
<u>Analytical methods</u> .....	28
<u>Visible and infrared spectroscopy</u> .....	28
<u>Surface area measurement</u> .....	29
<u>Thermodynamic modeling</u> .....	29
Results.....	29
<u>Solution pH</u> .....	29
<u>Concentration versus time</u> .....	30
<u>Thermodynamic modeling</u> .....	31
<u>SEM/EDS and Vis-NIR of Altered material</u> .....	32
<u>Calculating nontronite dissolution rates</u> .....	33
Discussion.....	35
<u>Solution chemistry</u> .....	35

<u>Dissolution rates normalized to surface area and mass</u> .....	36
<u>Dissolution rates and calculation of rate law</u> .....	38
<u>Implications for Mars</u> .....	40
Conclusions.....	44
Acknowledgments.....	45
Figures.....	46
CHAPTER FOUR WEATHERING PROFILES AT MAWRTH VALLIS YIELD	
INSIGHT INTO THE AQUEOUS HISTORY AND POTENTIAL HABITABILITY OF	
MARS.....	56
Abstract.....	56
Introduction.....	58
Background.....	60
Methods.....	62
<u>Reactive transport modeling</u> .....	63
<u>Model inputs</u> .....	64
<u>Mineral dissolution kinetics</u> .....	70
<u>Solubilities</u> .....	71
<u>Temperature and solution flow</u> .....	73
Results and Discussion.....	75

<u>Mineralogy</u> .....	76
<u>Advance distance</u> .....	76
<u>Shape of the alteration front</u> .....	77
<u>Comparison to observations from Mars</u> .....	79
Conclusions.....	82
Acknowledgments.....	83
Tables.....	85
Figures.....	86
APPENDIX A: SUPPLEMENTARY INFORMATION FOR CHAPTER	
TWO.....	
Supplementary Experimental Methods.....	90
<u>Experimental Procedure – Synthesis</u> .....	90
<u>Experimental Procedure – Low Temperature Synthesis</u> .....	91
<u>Experimental Procedure – Rock Alteration</u> .....	92
<u>Analytical Techniques</u> .....	94
<i>X – Ray Diffraction</i> .....	95
<i>Observations of Clay Minerals on Mars to Precipitates Formed in this study</i> .....	96
<i>Synchrotron <math>\mu</math>-X-ray Diffraction</i> .....	96

<i>Synchrotron Mossbauer Spectroscopy</i> .....	97
<i>Visible Near Infrared Spectroscopy</i> .....	98
<i>Observations of Clay Minerals on Mars to Precipitates Formed in this Study</i> .....	99
<i>Scanning Electron Microscopy and Energy Dispersive Spectroscopy</i> ...	100
<i>Micro-Probe</i> .....	100
Supplementary Results Alteration Experiments.....	101
Supplementary Results Synthesis Experiments.....	101
<u>Experiment-1(100-Fe Control - Subsequently Oxidized)</u> .....	101
<u>Experiment-2 (100-Fe<sup>3+</sup>)</u> .....	102
<u>Experiment-3 (100-Mg, High SiO<sub>2</sub>)</u> .....	103
<u>Experiment-4 (15-Mg 85-Fe<sup>3+</sup>)</u> .....	104
<u>Experiment-5 (50-Mg 50-Fe<sup>3+</sup>)</u> .....	105
<u>Experiment-6 (10-Mg 90-Fe<sup>3+</sup>)</u> .....	105
<u>Experiment-7 (5-Mg 95-Fe<sup>3+</sup>)</u> .....	106
<u>Experiment-8 (100 Al Low SiO<sub>2</sub>)</u> .....	107
<u>Experiment-9 (100 Al Low SiO<sub>2</sub>)</u> .....	107
<u>Experiment-10 (100 Al Low SiO<sub>2</sub>)</u> .....	108
<u>Experiment-11 (100 Al Low SiO<sub>2</sub>)</u> .....	108

<u>Experiment-12 (100 Al Low SiO<sub>2</sub>)</u> .....	109
Supplementary Discussion.....	110
Supplementary Tables.....	119
Supplementary Figures.....	127
APPENDIX B: SUPPLEMENTARY INFORMATION FOR CHATER	
THREE.....	193
<u>Supplementary Tables</u> .....	193
<u>Supplementary Figures</u> .....	200
APPENDIX C: SUPPLMENTARY INFORMATION FOR CHAPTER	
FOUR.....	202
<u>Supplementary Tables</u> .....	202
<u>Supplementary Figures</u> .....	204
REFERENCES.....	212
CURRICULUM VITAE.....	252

## LIST OF TABLES

Table 1. Chemistry used in selected synthesis experiments.....	16
Table 2. Input parameters for reactive transport modeling.....	85
Table S1. Concentration of reagent grade chemicals that were incorporated into solution to produce the synthesized products at 150° C.....	113
Table S2. Concentration of reagent grade chemicals that were incorporated into solution to produce the synthesized products at 100° C.....	116
Table S3: Mössbauer parameters for synthesized materials, precipitated at 150° C, as well as natural nontronites for comparison.....	119
Table S4. Oxide weight percent of USGS standards used in this study.....	120
Table S5. Results of alteration experiments of andesite under alkaline conditions.....	121
Table S6. Results of alteration experiments of basalt under alkaline conditions.....	122
Table S7. Results of alteration experiments of diabase under alkaline conditions.....	123
Table S8. Results of alteration experiments of granodiorite under alkaline conditions..	124
Table S9: Compositions of synthesized material determined through microprobe analysis.....	125
Table S10: Compositions of naturally occurring nontronites, all of which contain at least minor concentrations of Mg.....	126
Table S11. Flow rate, pH elemental Concentration of pH 0.9 experiments at 26° C.....	193

Table S12. Flow rate, pH elemental concentration of pH 1.7 experiments at 26° C.....	195
Table S13. Flow rate, pH elemental concentration of pH 3.0 experiments at 26° C.....	197
Table S14: Steady state nontronite dissolution rates at 26 °C calculated from Si, Fe and Ca release rates assumed to be from the tetrahedral, octahedral and interlayer sites....	199
Table S15: Observed and calculated solubilities based on chemical analysis on naturally occurring nontronites.....	202
Table 16: Observed and calculated solubility based on chemical analysis on naturally occurring montmorillonites.....	203



## LIST OF FIGURES

Figure 1. X-Ray diffractograms of the precipitated Fe/Mg-rich clay minerals.....	17
Figure 2: Visible Near Infrared (VNIR) reflectance spectra (offset for clarity) of Fe/Mg bearing clay minerals. ....	18
Figure 3: Stratigraphic columns of Mawrth Vallis and Gale Crater.....	46
Figure 4. Elemental concentrations, pH and flow rate of out-put solutions from nontronite dissolution experiments with initial pH 0.9.....	47
Figure 5. Elemental concentrations, pH and flow rate of out-put solutions from nontronite dissolution experiments with initial pH 1.7.....	48
Figure 6. Elemental concentrations, pH and flow rate of out-put solutions from nontronite dissolution experiments with initial pH 3.0.....	49
Figure 7: SEM images and EDS spectra of Reacted and unreacted Nontronite.....	50
Figure 8: Visible-near infrared and Fourier Transform Infrared spectra of unreacted and reacted nontronite.....	51
Figure 9: Continuum removed spectra.....	52
Figure 10: Molar ratios of Fe and Al normalized to Si. ....	53
Figure 11: Dissolution rate law for nontronite.....	54
Figure 12: Dissolution rate law of nontronite compared to the rate laws of the primary minerals in basalt and other clay minerals.....	55

Figure 13: Stratigraphic columns of Mawrth Vallis, Gale Crater, East Nili Fossae and Valles Marineris.....	86
Figure 14: Comparison of dissolution rate laws for kaolinite, montmorillonite, nontronite and saponite.....	87
Figure 15: Modeled weathering profiles of the four scenarios.....	88
Figure 16: Model results of weathered nontronite + montmorillonite at pH = 5 showing the two reaction fronts within the system.....	89
Figure S1: Diffraction pattern taken of the reagent grade Al-sulfate, to characterize its hydration state. ....	127
Figure S2: Diffraction pattern of the reagent grade Fe <sup>3+</sup> -sulfate, to characterize its hydration state.....	128
Figure S3: Diffraction pattern taken of the Mg-sulfate, to characterize its hydration state. ....	129
Figure S4: Diffraction pattern taken of the reference powder AVG-1 (andesite).....	130
Figure S5: Diffraction pattern of the reference powder BIR-1a (basalt).....	131
Figure S6: Diffraction pattern of the reference powder DNC-1a (diabase/dolerite).....	132
Figure S7: Diffraction pattern of the reference powder GSP-2 (granodiorite).....	133
Figure S8: Synchrotron Mössbauer data of NAu-1 and NAu-1 with 10µm stainless steel foil. ....	134
Figure S9. Mössbauer spectra of nontronite NAu-1.....	135

Figure S10. Synchrotron Mössbauer data of N Au-1 with stainless steel foil.....	136
Figure S11: Synchrotron Mössbauer data of <i>Experiment-4 (15-Mg 85-Fe<sup>3+</sup>)</i> with stainless steel foil. ....	137
Figure S12: Synchrotron Mössbauer data of <i>Experiment-5 (50-Mg 50-Fe<sup>3+</sup>)</i> with stainless steel foil.....	138
Figure S13: Synchrotron Mössbauer data of <i>Experiment-1(100-Fe Control - Subsequently Oxidized)</i> with stainless steel foil.....	139
Figure S14: Visible Near Infrared (VNIR) spectra of the synthesized clay minerals precipitated at 150° C.....	140
Figure S15: Visible Near Infrared (VNIR) spectra of the synthesized clay minerals precipitated at 100° C.....	141
Figure S16: SEM image of altered Icelandic basalt (BIR-1a).....	142
Figure S17: SEM image of altered dolerite (DNC-1a).....	143
Figure S18: SEM image of altered mafic rock and the accompanying EDS-spectra.....	144
Figure S19: SEM image of altered mafic rock and the accompanying EDS-spectra.....	145
Figure S20: Photograph of the synthetic nontronite control - <i>Experiment-1(100-Fe Control - Subsequently Oxidized)</i> precipitated at 150° C .....	146
Figure S21: Photograph of the synthetic nontronite control - <i>Experiment-1(100-Fe Control - Subsequently Oxidized)</i> precipitated at 100° C.....	147

Figure S22: X-Ray diffraction pattern of <i>Experiment-1(100-Fe Control - Subsequently Oxidized)</i> , precipitated at 150° C.....	148
Figure S23: X-Ray diffraction pattern of <i>Experiment-1(100-Fe Control - Subsequently Oxidized)</i> precipitated at 100° C.....	149
Figure S24: Synchrotron $\mu$ -XRD (0.86 Å wavelength) pattern for <i>Experiment-1(100-Fe Control - Subsequently Oxidized)</i> precipitated at 150° C. ....	150
Figure S25: Photograph of Experiment-2 (100-Fe <sup>3+</sup> ) precipitated at 150° C.....	151
Figure S26: Photograph of the Experiment-2 (100-Fe <sup>3+</sup> ) precipitated at 100° C.....	152
Figure S27: X-Ray diffraction pattern of <i>Experiment-2 (100-Fe<sup>3+</sup>)</i> precipitated at 150° C .....	153
Figure S28: X-Ray diffraction pattern of <i>Experiment-2 (100-Fe<sup>3+</sup>)</i> precipitated at 100° C .....	154
Figure S29: Photograph of Experiment-3 (100-Mg, High SiO <sub>2</sub> ) precipitated at 150° C. .....	155
Figure S30: Photograph of the Experiment-3 (100-Mg, High SiO <sub>2</sub> ) precipitated at 100° C. .....	156
Figure S31: X-Ray diffraction pattern of <i>Experiment-3 (100-Mg, High SiO<sub>2</sub>)</i> precipitated at 150° C. ....	157
Figure S32: X-Ray diffraction pattern of <i>Experiment-3 (100-Mg, SiO<sub>2</sub>)</i> precipitated at 100° C.....	158

Figure S33: Photograph of the Experiment-4 (15-Mg 85-Fe <sup>3+</sup> ) precipitated at 150° C.	159
Figure S34: Photograph of the Experiment-4 (15-Mg 85-Fe <sup>3+</sup> ) precipitate at 100° C.	160
Figure S35: X-Ray diffraction pattern of <i>Experiment-4 (15-Mg 85-Fe<sup>3+</sup>)</i> precipitated at 150° C.....	161
Figure S36: X-Ray diffraction pattern of <i>Experiment-4 (15-Mg 85-Fe<sup>3+</sup>)</i> precipitated at 100° C.....	162
Figure S37: Synchrotron $\mu$ -XRD (0.86 Å wavelength) pattern for <i>Experiment-4 (15-Mg 85-Fe<sup>3+</sup>)</i> precipitated at 150° C.....	163
Figure S38: Photograph of the Experiment-5 (50-Mg 50-Fe <sup>3+</sup> ) precipitated at 150° C.	164
Figure S39: Photograph of the Experiment-5 (50-Mg 50-Fe <sup>3+</sup> ) precipitated at 100° C.....	165
Figure S40: X-Ray diffraction pattern of <i>Experiment-5 (50-Mg 50-Fe<sup>3+</sup>)</i> precipitated at 150° C.....	166
Figure S41: X-Ray diffraction pattern of <i>Experiment-5 (50-Mg 50-Fe<sup>3+</sup>)</i> precipitated at 100° C.....	167
Figure S42: Synchrotron $\mu$ -XRD (0.86 Å wavelength) pattern for <i>Experiment-5 (50-Mg 50-Fe<sup>3+</sup>)</i> precipitated at 150° C.....	168
Figure S43: Photograph of the <i>Experiment-6 (10-Mg 90-Fe<sup>3+</sup>)</i> precipitate at 150° C...	169
Figure S44: X-Ray diffraction pattern of <i>Experiment-6 (10-Mg 90-Fe<sup>3+</sup>)</i> precipitated at 150° C.....	170

Figure S45: Photograph of the <i>Experiment-7 (5-Mg 95-Fe<sup>3+</sup>)</i> precipitated at 150° C.....	171
Figure S46: X-Ray diffraction pattern of <i>Experiment-7 (5-Mg 95-Fe<sup>3+</sup>)</i> precipitated at 150° C.....	172
Figure S47: Photograph of the <i>Experiment-8 (100-Al, Low SiO<sub>2</sub>)</i> precipitated at 150° C.....	173
Figure S48: Photograph of the <i>Experiment-8 (100-Al, Low SiO<sub>2</sub>)</i> precipitated at 100° C.....	174
Figure S49: X-Ray diffraction pattern of <i>Experiment-8 (100-Al, Low SiO<sub>2</sub>)</i> precipitated at 150° C.....	175
Figure S50: X-Ray diffraction pattern of <i>Experiment-8 (100-Al, Low SiO<sub>2</sub>)</i> precipitated at 100° C.....	176
Figure S51: Photograph of the <i>Experiment-9 (100-Mg, Low SiO<sub>2</sub>)</i> precipitated at 150° C.....	177
Figure S52: Photograph of the <i>Experiment-9 (100-Mg, Low SiO<sub>2</sub>)</i> precipitated at 100° C.....	178
Figure S53: X-Ray diffraction pattern of <i>Experiment-9 (100-Mg, Low SiO<sub>2</sub>)</i> precipitated at 150° C.....	179
Figure S54: X-Ray diffraction pattern of <i>Experiment-9 (100-Mg, Low SiO<sub>2</sub>)</i> precipitated at 100° C.....	180
Figure S55: Photograph of the <i>Experiment-10 (100-Al, High SiO<sub>2</sub>)</i> precipitated at 150° C.....	181

Figure S56: Photograph of the Experiment-10 (100-Al, High SiO <sub>2</sub> ) precipitated at 100° C.....	182
Figure S57: X-Ray diffraction pattern of <i>Experiment-10 (100-Al, High SiO<sub>2</sub>)</i> precipitated at 150°.....	183
Figure S58: X-Ray diffraction pattern of <i>Experiment-10 (100-Al, High SiO<sub>2</sub>)</i> precipitated at 100° C.....	184
Figure S59: Photograph of the Experiment-11 (44-Al 14-Mg 42-Fe <sup>3+</sup> ) precipitated at 150° C.....	185
Figure S60: Photograph of the Experiment-11 (44-Al 14-Mg 42-Fe <sup>3+</sup> ) precipitated at 100° C.....	186
Figure S61: X-Ray diffraction pattern of <i>Experiment-11 (44-Al 14-Mg 42-Fe<sup>3+</sup>)</i> precipitated at 150° C.....	187
Figure S62: X-Ray diffraction pattern of <i>Experiment-11 (44-Al 14-Mg 42-Fe<sup>3+</sup>)</i> precipitated at 100° C.....	188
Figure S63: Photograph of the Experiment-12 (50-Al 50-Mg) precipitated at 150° C....	189
Figure S64: Photograph of the Experiment-12 (50-Al 50-Mg) precipitated at 100° C....	190
Figure S65: X-Ray diffraction pattern of Experiment-12 (50-Al 50-Mg) precipitated at 150° C.....	191
Figure S66: X-Ray diffraction pattern of <i>Experiment-12 (50-Al 50-Mg)</i> precipitated at 100° C.....	192

Figure S67. Raman spectra of nontronite standard NAu-1 .....	200
Figure S68. XRD pattern of the 45–150 $\mu\text{m}$ size fraction of NAu-1.....	201
Figure S69. Comparison of dissolution rates and rate laws for montmorillonite.....	204
Figure S70. Comparison of dissolution rates and rate laws for kaolinite.....	205
Figure S71: Dissolution rates and the determined rate law for saponite.....	206
Figure S72: Dissolution rates and the determined rate law for nontronite.....	207
Figure S73: Modeling result for scenario 1.....	208
Figure S74: Modeling result for scenario 2.....	209
Figure S75: Modeling result for scenario 3.....	210
Figure S76: Modeling result for scenario 4.....	211



## CHAPTER ONE

### INTRODUCTION AND OVERVIEW

Liquid-water is the quintessential ingredient for the development and sustenance of life on Earth (Davis and McKay, 1996) and would likely be essential in the development of life on Mars. Although liquid-water is no longer present at the Martian surface, the occurrence of aqueous minerals (e.g. requiring liquid water to precipitate) suggests that liquid-water has been present at or near the Martian surface. Therefore, the search for habitable environments will be closely related to the investigation of aqueous minerals on Mars. Currently, several aqueous minerals have been detected at the Martian surface using remote sensing data, which include; Fe-(oxyhydr)oxides (Christensen et al., 2001), hydrated silica (Milliken et al., 2008; Weitz et al., 2008; Weitz et al., 2010), phyllosilicates (Bibring et al., 2005b; Bishop et al., 2008b; Wray et al., 2008; Wray et al., 2009; Bishop et al., 2010; Milliken et al., 2010a; Noe Dobrea et al., 2010b), carbonates (Bandfield et al., 2003; Ehlmann et al., 2008b), hydrated sulfates (Langevin et al., 2005) and zeolites (Ruff, 2004; Ehlmann et al., 2009a). Of the previously stated aqueous minerals, phyllosilicates suggest past environments in which the activity and pH of water may have been the most suitable for the development of life (Poulet et al., 2005b; Ehlmann et al., 2009a; Milliken et al., 2009; Murchie et al., 2009a; Milliken et al., 2010a; Bristow and Milliken, 2011; Bishop et al., 2013).

Visible Near InfraRed (VNIR) and InfraRed (IR) reflectance data obtained from the; Thermal Emission Spectrometer (TES), Observatoire pour la Mineralogie, l'Eau, les Glaces, et l'Activité (OMEGA) and the Compact Reconnaissance Imaging Spectrometer for Mars (CRISM) have revealed phyllosilicate bearing materials on the martian surface

and represents the strongest mineralogical evidence for sustained aqueous activity on Mars (Poulet et al., 2005b; Bibring et al., 2006; Mustard et al., 2008b; Michalski et al., 2010a). However, the mineralogy of these phyllosilicates is heterogeneously distributed both spatially and stratigraphically across the martian surface. Of these locations, Mawrth Vallis represents one of the largest exposures of phyllosilicates on Mars (McKeown et al., 2009) and contains a characteristic stratigraphy of Al-rich clay minerals (spectrally similar to kaolinite and montmorillonite) mixed with hydrated silica, which is underlain by an Fe-rich clay (spectrally similar to nontronite and/or Mg-nontronite) (Michalski and Noe Dobrea, 2007; Bishop et al., 2008b; Wray et al., 2008; Bishop et al., 2010; Michalski et al., 2010c; Noe Dobrea et al., 2010b; Michalski et al., 2013). This stratigraphy has also been observed in Noachis Terra (Wray et al., 2009), Nili Fossae (Ehlmann et al., 2009b), Vallis Marineris (Murchie et al., 2009a; Le Deit et al., 2010) and the Eridiana Basin (Noe Dobrea et al., 2010a). Gale Crater, the landing site of the Mars Science Laboratory's *Curiosity* rover, also contains what is believed to be the clay mineral nontronite which grades into either intercalated beds or a mixed unit of nontronite and sulfate(s) (Milliken et al., 2010a). Therefore, transitions in clay mineral chemistry are potential indicators of the past aqueous and diagenetic/pedogenic history of Mars.

The observed transitions in clay mineral chemistry can preserve the kinetic and thermodynamic conditions under which these minerals precipitated. Dissolution kinetics may help explain the stratigraphy observed in the Mawrth Vallis region, as previous work has shown the solubility of clay minerals is dependent on the octahedral cation, with decreasing solubility (e.g.  $Mg > Fe > Al$ ) (Tardy and Fritz, 1981). Clay minerals may also be valuable when assessing the redox of the environment of which they formed (Harder,

1976; Harder, 1978a). Previously, Harder (1976; 1978a), suggested Fe-bearing phyllosilicate precipitation is favored by the presence of  $\text{Fe}^{2+}$  (e.g. reducing conditions) for the precipitation of both dioctahedral and trioctahedral clay minerals. Reactive transport modeling can also allow a greater understanding of the formation mechanisms of clay mineral transitions on or at the martian surface. It is the purpose of this research to address and further constrain the requirements for clay mineral precipitation, the dissolution kinetics of nontronite (a widespread clay mineral detected on the martian surface) and use reactive transport modeling to replicate observed clay mineral transitions, further elucidating to the duration of aqueous alteration occurring at or near the martian surface. These answers will be valuable when assessing environments suitable for the preservation of organic matter and past habitability. The following three chapters document investigations focusing on the precipitation of clay minerals detected on the martian surface, dissolution kinetics of nontronite and reactive transport modeling of clay mineral transition occurring at or near the martian surface to further constrain the duration of aqueous alteration the occurring in the Mawrth Vallis region and other location with similar transition in clay mineral chemistry.

Chapter two addresses nontronite dissolution kinetics and its implications for Mars. Nontronite is an Fe-rich smectite and has been identified on the martian surface with orbital Visible Near InfraRed (VNIR) spectrometers. These results suggest nontronite is a relatively stable phase compared to the primary minerals in basalt (under acidic and oxidizing conditions), and one formed would remain at the martian surface for prolonged times (in reference to primary minerals in basalt). However, nontronite dissolution is more rapid than other clay minerals detected on the martian surface (e.g.

kaolinite and montmorillonite), and therefore the dissolution of mixed units may produce the observed stratigraphy and amorphous Si, similar to that observed in the Mawrth Vallis region and other localities on the martian surface. This chapter has been previously published as; Gainey S.R., Hausrath, E.M., Hurowitz, J.A., Milliken R.E. (2014) Nontronite Dissolution Rates and Implications for Mars. *Geochimica et Cosmochimica Acta*, 126, 192-211.

Chapter three addresses clay mineral precipitation, including Fe/Mg clay minerals. Fe/Mg rich clay minerals have been detected in multiple locations across the southern highlands on Mars. The results of this study suggest that the previous interpretation of Fe/Mg-rich clay minerals requiring anoxic and/or reducing conditions may not be accurate, as the minor presence of Mg allowed for the rapid precipitation of ferric Fe-rich clay minerals, which was subsequently confirmed with Synchrotron Mossbauer Spectroscopy. These results may address the relative dearth of organic matter detected on the martian surface, which would be less likely to be preserved under oxidized conditions. Oxidizing conditions may also suggest less habitable environments and may therefore hinder the development and preservation of life.

In chapter four, the results of reactive transport modeling suggest that when Fe/Mg rich phyllosilicates are exposed to Mars-relevant pedogenic conditions an Al-rich capping unit (composed of montmorillonite and kaolinite) will form under all conditions and all scenarios examined in this investigation. Deposits consisting of nontronite, nontronite and montmorillonite, saponite and nontronite and pure saponite, when exposed to pedogenic conditions will produce similar stratigraphy to that observed in the Mawrth Vallis region, which is in agreement with the results of chapter 2. Therefore, although

the presence of clay minerals are indicative of aqueous alteration, the Al-rich unit overlying the Fe-Mg-rich unit may be suggestive of further alteration of the Fe/Mg-rich clay minerals. Increasing the flow rate and acidity of the reacting fluids resulted in more gradual transitions between the Fe-Mg-rich parent material and the Al-rich capping unit and increased thickness of the Al-rich unit. The transition between the Al-rich capping unit and the parent mineral beneath it may therefore preserve properties of past fluid-flow and aqueous conditions. Within the Al-rich capping unit, kaolinite occurred under conditions of greater aqueous alteration, due to either higher flow rates or more acidic conditions. The results of this study suggest that locations which have experienced the most aqueous alteration (e.g. due to weathering) would be characterized by a thick Al-rich capping unit composed of kaolinite and/or Fe-oxyhydr(oxide)s (a potential sign of oxidative weathering, supporting chapter 1), overlying predominately Fe<sup>3+</sup>-rich smectites (e.g. nontronite). Marwth Vallis, which is composed mostly of nontronite, with areas rich in kaolinite, may therefore represent one of the locations that was exposed to the longest duration of warm weathering and/or the highest water-rock ratios. The results suggest the surface of Mars was exposed to long-term near-neutral liquid water at its surface.

The goal of this dissertation was to interpret the implications of clay mineral transitions on Mars, including interpreting paleoredox conditions, as well as past kinetic and thermodynamic conditions. As of now, it is believed that clay minerals form in environments most suitable for habitability and the preservation of organic matter. The precipitation experiments indicate that while clay minerals suggestive of the past presence of liquid water, the specific clay minerals and the transitions in clay mineralogy may indicate formation under oxidizing condition that may be less suitable for

habitability and the preservation of organic matter. Mineral dissolution experiments indicate that nontronite dissolves more rapidly than montmorillonite or kaolinite, indicating that dissolution of a mixed deposit would result in a sequence observed at Mawrth Vallis. Quantitative analysis using the reactive transport model CrunchFlow indicates that the observed transition in clay mineralogy may have occurred from the weathering of Fe/Mg rich phyllosilicates. This Al-rich clay unit formed regardless of the parent mineralogy, including both nontronite, nontronite and montmorillonite, nontronite and saponite and pure saponite. These transitions in clay mineral chemistry therefore record important characteristics of the paleoenvironment.

## CHAPTER TWO

### CLAY MINERALS DETECTED ON MARS CAN FORM IN ENVIRONMENTS THAT MAY DESTROY ORGANIC MATTER

Seth R. Gainey<sup>1</sup>, Elisabeth M. Hausrath<sup>1</sup>, Christopher T. Adcock<sup>1</sup>, Oliver Tschauner<sup>1</sup>,  
Joel A. Hurowitz<sup>2</sup>, Bethany L. Ehlmann<sup>3,4</sup>, Yuming Xiao<sup>5</sup>, Courtney L. Bartlett<sup>1</sup>

<sup>1</sup>Department of Geoscience, University of Nevada, Las Vegas, 4505 S. Maryland Pkwy.,  
Las Vegas, Nevada 89154, USA

<sup>2</sup>Department of Geosciences, State University of New York, Stony Brook, New York  
11794-2100, USA

<sup>3</sup>Division of Geological and Planetary Sciences, California Institute of Technology,  
Pasadena, California 91125, USA

<sup>4</sup>Jet Propulsion Laboratory, California Institute of Technology, Pasadena, California  
91109, USA

<sup>5</sup>Argonne National Laboratory, Argonne, Illinois 60439, USA

#### ABSTRACT

The search for organic matter on Mars remains puzzling and inconclusive, as little organic material has been unambiguously detected despite a constant influx of organic compounds from meteorites. The paucity of organic molecules within clay-containing environments (Ming et al., 2014; Freissinet et al., 2015) is particularly surprising. Organic matter can adsorb onto clay mineral surfaces and interlayers and thus be preserved. Clay minerals, widespread on Mars, have therefore been targeted for martian exploration (Poulet et al., 2005b; Ehlmann et al., 2009b; Milliken et al., 2009; Michalski et al., 2010a; Bristow and Milliken, 2011; Bishop et al., 2013). In addition, Fe-rich smectites such as nontronite have been interpreted as requiring aqueous ferrous Fe early in their formation (Harder, 1976; Decarreau et al., 2008), and therefore have been used as indicators of past anoxic and/or reducing conditions on Mars (Milliken et al., 2009; Michalski et al., 2010b; Bristow and Milliken, 2011; Ehlmann et al., 2011; Bishop et al., 2013) which may represent environments that were more habitable than the oxidized

environments common on Mars today and would be more likely to preserve organic molecules. In contrast, we here present data from clay mineral synthesis experiments demonstrating the rapid formation of Fe-rich clay minerals from aqueous ferric Fe in the presence of Mg. Our results suggest that the requirement of anoxic/reducing conditions for Fe-rich clay mineral formation is not valid and, in fact, such minerals can form in an oxidized environment in the presence of small concentrations of a divalent cation (e.g. Mg). Formation of Fe-rich clay minerals in oxidized environments may therefore help explain the dearth of detected organic molecules.

## INTRODUCTION

In the search for possible past or present life on Mars, remnant organic matter is a crucial target. If Mars ever possessed life, or currently does, organic compounds should have been, or should still be present. Meteoritic inputs have also deposited significant quantities of organic carbon on Mars and continue to do so (Flynn, 1996; Benner et al., 2000; Botta and Bada, 2002). Despite these meteoritic inputs, detectable organic carbon remains elusive (Biemann et al., 1977; Leshin et al., 2013; Ming et al., 2014; Freissinet et al., 2015). Measurements by *Viking 1* and *Viking 2* conducted in 1976 were unable to positively detect organic molecules (Biemann et al., 1977), although these results have been challenged (Navarro-González et al., 2006). More recent analyses of Fe/Mg-rich smectites (Vaniman et al., 2014) by the Mars Science Laboratory's (MSL) Sample Analysis at Mars (SAM) suite of instruments at Yellowknife Bay have also suggested very limited organic carbon in the near surface (Ming et al., 2014; Vaniman et al., 2014; Freissinet et al., 2015). Chlorohydrocarbons (chlorinated organic compounds potentially resulting from organic matter interacting with perchlorates in martian soils) were detected



during SAM analyses; however, MTBSTFA (a derivatization agent present within SAM) contamination has complicated these results (Leshin et al., 2013; Ming et al., 2014). Relatively high concentrations of chlorohydrocarbons detected in the Cumberland sample from the Sheepbed member compared to the Rocknest aeolian deposit and Confidence Hills of Gale Crater does suggest the presence of organic carbon in the Cumberland mudstone (Leshin et al., 2013; Ming et al., 2014; Freissinet et al., 2015). However, measured concentrations continue to be significantly below those expected from organic matter deposited by meteorites (Flynn, 1996; Benner et al., 2000; Botta and Bada, 2002; Ming et al., 2014).

The lack of detected organic compounds on Mars, including those deposited by meteorites (Flynn, 1996; Benner et al., 2000; Botta and Bada, 2002; Ming et al., 2014), may be a consequence of their degradation throughout martian history. The martian surface is bombarded by ionizing radiation which can destroy organic compounds (Pavlov et al., 2002; Hassler et al., 2014), although persistence of organic compounds within carbonaceous chondrites provides evidence of their long-term survival in ionizing environments (Hassler et al., 2014). Due to the effects of ionizing radiation, the preservation of organic matter is likely enhanced at depth, where it is shielded from such radiation (Pavlov et al., 2002; Hassler et al., 2014). Previously buried samples that have been recently exposed, such as those at Yellowknife Bay, can be analyzed for organic matter. Organic compounds should therefore be detectable unless they have been destroyed by other processes occurring within martian soils, such as degradation by free radicals and oxidizers (e.g. H<sub>2</sub>O<sub>2</sub> and perchlorates) that may form in water-containing martian environments (Pavlov et al., 2002; Hassler et al., 2014).

The search for signs of life on Mars has targeted locations containing Fe/Mg-rich clay minerals (Poulet et al., 2005b; Michalski et al., 2010b; Ehlmann et al., 2011; Bishop et al., 2013), which can both preserve organic matter adsorbed onto the mineral surfaces and interlayers, and may also indicate initially anoxic and/or reducing formation conditions (Harder, 1976; Mizutani et al., 1991; Decarreau et al., 2008) beneficial for the development of life and the preservation of organic matter. Previous work by Harder (1976), Decarreau et al. (2008) and Mizutani et al. (1991) has shown that the precipitation of Fe-bearing clay minerals such as nontronite, the dioctahedral Fe<sup>3+</sup>-rich smectite endmember, occur under initially anoxic and/or reducing conditions. This is due to the requirement for a divalent cation such as Fe<sup>2+</sup> to stabilize the octahedral layers, a necessity for the early bi-dimensional growth of these clay minerals. Previous attempts to synthesize clay minerals from ferric Fe alone have formed amorphous (Harder, 1976) and/or very poorly crystalline products (Baker and Strawn, 2014), and been deemed prohibitively slow (Baker and Strawn, 2014). Thus, Fe/Mg smectites have been used as a signature of initially anoxic and/or reducing environments (Milliken et al., 2009; Michalski et al., 2010b; Ehlmann et al., 2011; Bishop et al., 2013; Treiman et al., 2014) in the interpretation of both orbital (Milliken et al., 2009; Michalski et al., 2010b; Bristow and Milliken, 2011; Ehlmann et al., 2011; Bishop et al., 2013) and CheMin (on board MSL) results (Treiman et al., 2014). In order to test this use of Fe/Mg smectites as an oxidation state indicator, we performed precipitation experiments of Fe-rich clay minerals and showed that they can rapidly precipitate under oxidized conditions in the presence of at least minor amounts of Mg. This shows that the requirement for anoxic/reducing conditions is not valid, prompting a re-evaluation of the past oxidation

state of clay mineral-forming environments on Mars with important implication for the preservation of organic matter including potential biosignatures.

## METHODS

Our clay mineral synthesis experiments were designed to be relevant to environmental conditions on Mars, containing a range of chemical compositions under oxidized conditions (Table 1). Initially acidic ferric sulfate and silica-containing solutions were made basic by the addition of NaOH and then incubated for 24 hours at room temperature and 48 hours at 150° C. This process is likely analogous to the interaction of acidic, ferric sulfate-containing solutions, such as those proposed on Mars (Tosca et al., 2004a), with silicate-containing minerals, resulting in an increased solution pH. To test the effect of temperature, identical synthesis experiments were conducted at 100° C for 60 days. In addition, a synthetic nontronite control was synthesized using standard methods from Fe<sup>2+</sup>-containing solutions (Mizutani et al., 1991), to reference against the experimental products. Synthesized materials were analyzed with Synchrotron Micro X-Ray Diffraction ( $\mu$ XRD), Synchrotron Mössbauer Spectroscopy (SMS), powder X-Ray Diffraction (XRD), Visible Near Infrared (VNIR) Spectroscopy, Infrared Spectroscopy (IR), Scanning Electron Microscopy (SEM) with Energy Dispersive Spectroscopy (EDS) and Electron MicroProbe (EMP) analysis by Wavelength Dispersive Spectroscopy (WDS) (see Supplementary Online Materials (SOM)).

## RESULTS AND DISCUSSION

We rapidly synthesized Fe-rich clay minerals including nontronite (Mizutani et al., 1991; Decarreau et al., 2008) under oxidized conditions from solutions containing

solely Fe<sup>3+</sup> with minor additions of Mg (e.g. at least 5%). The Eh of the system remained > 0.856 V (see SOM), significantly above that required for Fe reduction, and the Fe within the precipitates was confirmed to be ferric by SMS (SOM). The clay mineral is therefore dioctahedral when Mg is a minor component. Syntheses from pure Fe<sup>3+</sup> solutions with no Mg resulted in relatively amorphous precipitates (Figure 1) with VNIR and IR spectra distinctly different from Fe/Mg clay minerals (Figure 2), in agreement with prior findings<sup>8,24</sup>, whereas syntheses containing Fe<sup>3+</sup> with Mg concentrations of 5% or greater resulted in the precipitation of Fe/Mg clay minerals.

Magnesium concentrations of ~ 5% or greater are widely found in naturally occurring nontronites (SOM). Our precipitated Fe/Mg clay minerals, when compared by VNIR and IR at orbital instrument spectral resolution to synthetic, natural terrestrial, and martian Fe/Mg smectites (Clark et al., 2007b) were indistinguishable (Figure 2). Increasing concentrations of Mg (from 0 to 100 percent) show a band shift from the 2Fe-OH band (2.285 μm) towards the 3Mg-OH bending and stretching vibrations at 2.315 μm (Grauby et al., 1994; Bishop et al., 2002; Ehlmann et al., 2009b). A systematic shift is also evident in the structural OH overtone located at ~1.410 μm and the fundamental OH-stretch between 2.760 to 2.800 μm (Grauby et al., 1994; Bishop et al., 2002) (see SOM). In combination, these absorption features can be used to interpret the ratio of Fe and Mg in clay minerals observed on Mars (Figure 2). Powder XRD analysis of synthesized Fe/Mg materials indicates broad 001 peaks, which are characteristic of the large interlayer spacing of smectites (Figure 1), particularly given the lack of other well-defined peaks (mica) or a peak at a 7 Å spacing (1:1 clay minerals) (Vaniman et al., 2014). XRD results indicate varying degrees of crystallinity, with the material containing

a Fe:Mg ratio of 1:1 having the highest degree of crystallinity (Figure 1). Upon glycolation, synthesized products containing  $\text{Fe}^{3+}$  and  $\text{Fe}^{3+}$  with Mg showed increasing expansion as the ratio approached 1:1, with the 1:1 ratio material expanding to 17 Å, indicative of a Fe/Mg-rich smectite. The synthetic nontronite control synthesized using standard methods from  $\text{Fe}^{2+}$ -containing solutions also showed some degree of expansion after glycolation, with the basal plane expanding from approximately 13 to 14 Å (see SOM). Incorporation of iron into the precipitates was confirmed by SEM/EDS and EMP analysis as well as the Synchrotron Mössbauer spectra (see SOM). This study therefore indicates that Fe-rich clay minerals such as nontronite can form under oxidized conditions prompting an important re-evaluation of past martian environments and the potential for preservation of organic matter including biosignatures.

The results of this study further indicate that some poorly/nano crystalline materials may produce VNIR spectra similar to well-crystalline clay minerals with comparable chemical compositions (Figures 1 and 2). X-ray amorphous or poorly/nano crystalline phases have been proposed to be a significant component of the samples analyzed by MSL at Gale Crater (Bish et al., 2013). Work by Milliken et al. (2014) has indicated that the poorly crystalline material hisingerite has VNIR spectral properties similar to nontronite. If poorly/nano crystalline materials representing “proto-clays” are widespread on Mars, this may have important implications for interpreting the prevalence and longevity of martian water-rock interactions.

Despite previous experiments indicating that nontronite-like precipitation from aqueous  $\text{Fe}^{3+}$  solutions under oxidized conditions is amorphous or extremely poorly crystalline and prohibitively slow (Decarreau et al., 2008; Baker and Strawn, 2014), our

experiments rapidly formed Fe<sup>3+</sup>-bearing clay minerals under oxidized conditions in the presence of the divalent cation Mg. Since Fe-rich smectites containing Mg are widespread on Mars (Poulet et al., 2005b; Michalski et al., 2010a; Ehlmann et al., 2011; Bishop et al., 2013), they could have formed, like our synthesized minerals, from aqueous Fe<sup>3+</sup> in the presence of Mg under oxidized conditions. The requirement for anoxic/reducing conditions is not necessary and therefore, these results prompt an important re-evaluation of clay mineral-forming environments on Mars.

## CONCLUSIONS

Seeking possible signs of life, including organic biosignatures, is a crucial part of the Mars Exploration Program. Here we show that Fe/Mg-rich clay minerals such as nontronite, instead of indicating an initially anoxic and/or reducing environment, may instead form rapidly under oxidized conditions not conducive to the preservation of organic matter. These results may therefore help explain the unexpectedly low concentrations of organic compounds on Mars in smectite clay-bearing environments explored to date. Additional indicators of environments conducive to the formation and preservation of organic matter are needed in the continued search for locations that may preserve evidence of a past biosphere on Mars.

## ACKNOWLEDGEMENTS

This material is based upon work supported by the National Aeronautics and Space Administration under Grant No. NNX10AN23H issued through the NASA Training Grant: National Space Grant College and Fellowship Program (Space Grant) and the Mars Fundamental Research Program Grant No. NNX12AH96G. We

acknowledge the Advanced Photon Source at Argonne National Lab, Sector 16 ID-D. We also thank the University of Nevada, Las Vegas's Graduate and Professional Student Association. The authors would like to thank Michael Steiner, Valerie Tu, Renee Schofield and Angela Garcia for contributions and help in the development of this manuscript. We also thank Minghua Ren for aid in Microprobe analysis and George Rossman, Cedric Pilorget, Jennifer Buz and Lulu Pan for aid in the collection of spectra.

## TABLES

**Table 1. Chemistry used in selected synthesis experiments.**

	Exp. 1 (100-Fe Control) <sup>A</sup>	Exp. 2 (100-Fe <sup>2+</sup> )	Exp. 7 (5-Mg 95-Fe <sup>2+</sup> )	Exp. 4 (15-Mg 85-Fe <sup>3+</sup> )	Exp. 5 (50-Mg 50-Fe <sup>3+</sup> )	Exp. 3 (100-Mg)
Chemical Name	Amount Cation (mol)	Amount Cation (mol)	Amount Cation (mol)	Amount Cation (mol)	Amount Cation (mol)	Amount Cation (mol)
Sodium Metasilicate - Pentahydrate	0.0204	0.0204	0.0204	0.0205	0.0204	0.0205
Iron (II) Sulfate - Heptahydrate	0.0142	-	-	-	-	-
Sodium Dithionite	0.0241	-	-	-	-	-
Iron (III) Sulfate - Rhomboclase & Ferricopiapite	-	0.0138 <sup>C</sup>	0.0146 <sup>C</sup>	0.0118 <sup>C</sup>	0.0069 <sup>C</sup>	-
Magnesium Sulfate - Epsomite	-	-	0.0007	0.0022	0.0071	0.0142
<b>Fe:Mg ratio</b>	1:0	1:0	19:1	17:3	1:1	0:1
Solution Name	Amount (mL)	Amount (mL)	Amount (mL)	Amount (mL)	Amount (mL)	Amount (mL)
Sodium Hydroxide (5 M)	19.80	19.80	19.80	19.80	19.80	19.80
H <sub>2</sub> O	417.52	419.96	417.11	416.41	417.11	417.87
Sulfuric Acid (0.5 M)	41.00	42.00	40.00	42.00	42.00	42.00
<b>Ending pH</b>	12.49	12.69	12.64	12.76	12.74	12.88

All experiments were aged for one day at room temperature and then heated for an additional two days at 150° C.

<sup>A</sup>For all experimental conditions see SOM.

<sup>B</sup>100-Fe bearing control condition, which was synthesized from initially ferrous Fe-containing solutions (sodium dithionite was added to maintain reducing conditions for the ferrous Fe) and then oxidized using published methods (Mizutani et al., 1991).

<sup>C</sup>Fe(III) molar concentrations were determined by Atomic Adsorption (AA) spectroscopy.



## FIGURES

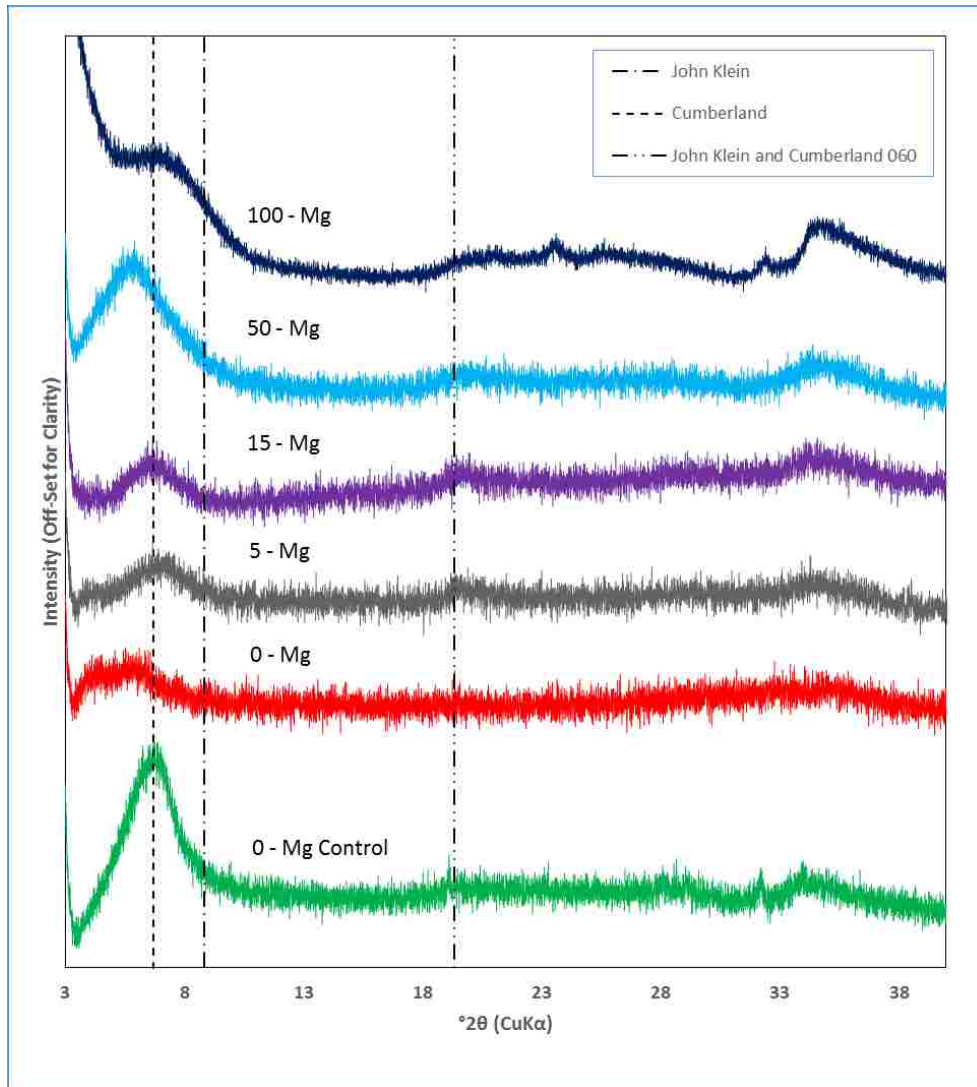


**Figure 1: X-Ray diffractograms of the precipitated Fe/Mg-rich clay minerals.** Samples were analyzed as oriented samples on Si-mounts. Note that the 001 diffraction of the 0 - Mg nontronite control is very crystalline, whereas the pure ferric synthesized material (0-Mg) is largely amorphous or nano-crystalline, which is also shown in the 100° C experiments (see SOM) and is in agreement with the previous studies of Harder (1976), Decarreau et al. (2008) and Baker and Strawn (2014). Increasing Mg concentrations in the Fe<sup>3+</sup> solutions resulted in increased crystallinity of the synthesized products. These results indicate that Fe-rich clay minerals can be precipitated under oxidized conditions, as long as Mg is present in at least small concentrations in the initial starting solution. The pure Mg precipitate had a much broader basal reflection, suggesting less coherent stacking along the c-axis. Vertical dashed lines represent the basal (shifting of the basal peak is likely the result of the charge imbalance of the clay minerals, where a higher charge may result in a smaller unit cell along the c-axis) and 020 reflections of the clay minerals identified in the John Klein and Cumberland samples (Vaniman et al., 2014).

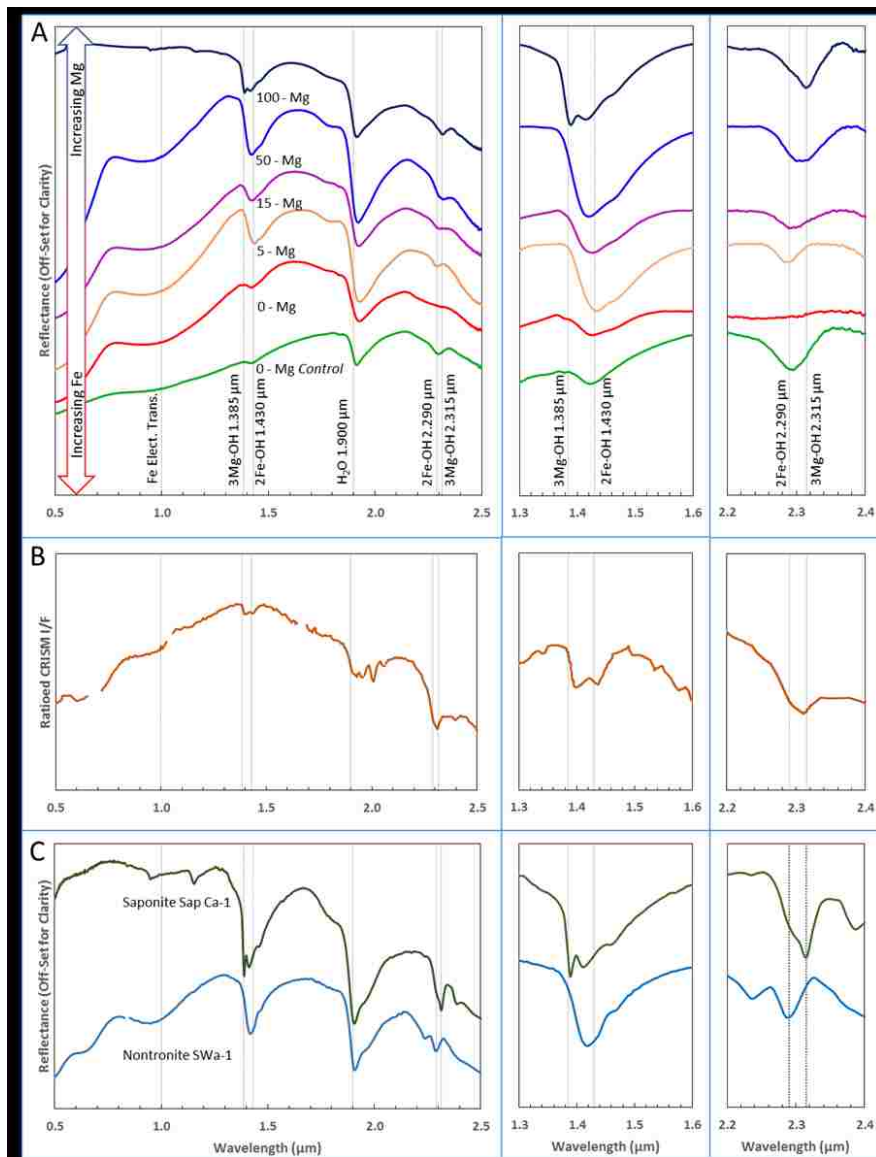


**Figure 2: Visible Near Infrared (VNIR) reflectance spectra (offset for clarity) of Fe/Mg bearing clay minerals.** (A) VNIR spectra of Fe/Mg rich clay minerals produced in this study, with Mg concentrations indicated on the figure in percent cation (0 - Mg control (green) indicates the synthetic nontronite control formed from aqueous ferrous solutions based on previous work by Mizutani et al. (1991) and Decarreau et al. (2008). 0-Mg (red) indicates 100 percent Fe<sup>3+</sup> under oxidized conditions). The absorption band for each synthesized material between 1.3-1.6 μm and 2.2-2.4 μm is enlarged for clarity and has had the continuum removed. Samples with increasing concentrations of Mg (from 0 to 100 percent) show shifts in the position of hydroxyl-related absorptions as octahedral Fe (2Fe-OH bands at 1.43 μm and 2.285 μm) is replaced by Mg (3Mg-OH bands at 1.385 μm and 2.315 μm) (Grauby et al., 1994; Bishop et al., 2002; Ehlmann et al., 2009b). (B) VNIR CRISM spectra of Fe/Mg-rich smectite from the Nili Fossae region, Mars from Ehlmann et al. (Ehlmann et al., 2009b) and (C) VNIR spectra of saponite (Mg-rich smectite) and nontronite (Fe<sup>3+</sup>-rich smectite) from the United States Geological Survey spectral library (Clark et al., 2007b) have similar absorption positions and shapes to the clay minerals precipitated in this study.

## CHAPTER THREE

### NONTRONITE DISSOLUTION RATES AND IMPLICATIONS FOR MARS

This chapter was originally published in *Geochimica et Cosmochimica Acta* in October 2013.

Citation: Gainey S.R., Hausrath, E.M., Hurowitz, J.A., Milliken R.E. (2014) Nontronite Dissolution Rates and Implications for Mars. *Geochimica et Cosmochimica Acta*, 126, 192-211.

#### ABSTRACT

The Fe-rich smectite nontronite  $M^{+}_{1.05}[\text{Si}_{6.98}\text{Al}_{1.02}][\text{Al}_{0.29}\text{Fe}_{3.68}\text{Mg}_{0.04}]\text{O}_{20}(\text{OH})_4$  has been detected using orbital data at multiple locations in ancient terrains on Mars, including Mawrth Vallis, Nilli Fossae, north of the Syrtis Major volcanic plateau, Terra Meridiani, and the landing site of the Mars Science Laboratory (MSL), Gale Crater. Given the antiquity of these sites (>3.0Ga), it is likely that nontronite has been exposed to the martian environment for long periods of time and therefore provides an integrated record of processes in near surface environments including pedogenesis and diagenesis. In particular, nontronite detected at Mawrth Vallis, is overlain by montmorillonite and kaolinite, and it has been previously suggested that this mineralogical sequence may be the result of surface weathering. In order to better understand clay mineral weathering on Mars, we measured dissolution rates of nontronite in column reactors at solution pH values of 0.9, 1.7, and 3.0, and two flow rates (0.16 ml/hr and 0.32 ml/hr). Solution chemistry indicates stoichiometric dissolution at pH = 0.9 and non-stoichiometric dissolution at pH = 1.7 and 3.0. Mineral dissolution rates based on elemental release rates at pH = 1.7 and 3.0 of Ca, Si and Fe follow the order interlayer > tetrahedral > octahedral sites, respectively. The behavior of all experiments suggest far from equilibrium conditions, with the exception of the experiment performed at pH 3.0 and

flow rate 0.16 ml/h. A pH-dependent dissolution rate law was calculated through Si release from experiments that showed no dependence on saturation (far from equilibrium conditions) under both flow rates and is  $r = 10^{-12.06 (\pm 0.123)} \cdot 10^{-0.297 (\pm 0.058) \cdot \text{pH}}$  where  $r$  has the units mol mineral m<sup>-2</sup>s<sup>-1</sup>. When compared to dissolution rates from the literature, our results indicate that nontronite dissolution is significantly slower than dissolution of the primary phases present in basalt under acidic conditions, suggesting that once nontronite forms it could remain stable at or near the surface of Mars for extended periods of time. Nontronite dissolution rates are faster than dissolution rates of montmorillonite (Rozalén et al., 2008b) and kaolinite (Huertas et al., 1999a), suggesting that chemical weathering of a mixed clay deposit would enrich the proportions of montmorillonite and kaolinite through the preferential dissolution of nontronite. VIS-NIR analyses of our reacted products and thermodynamic modeling of our experimental conditions both indicate the precipitation of amorphous silica within columns, and amorphous silica has also been observed in association with phyllosilicates on the martian surface (Mustard et al., 2008b; Ehlmann et al., 2009a; Murchie et al., 2009a). Therefore, chemical weathering of strata containing mixtures of montmorillonite, nontronite and kaolinite provides a potential formation mechanism for the mineralogic stratigraphy observed at Mawrth Vallis and other locations on Mars.

## INTRODUCTION

Spectral observations from the Compact Reconnaissance Imaging Spectrometer for Mars (CRISM) and the Observatoire pour la Mineralogie, L'Eau, les Glaces et l'Activite (OMEGA) spectrometer on board the Mars Reconnaissance and Mars Express orbiters, respectively, have detected spectral signatures indicative of clay minerals at

numerous locations across the martian surface (Bibring et al., 2005a; Poulet et al., 2005b; Bibring et al., 2006; Loizeau et al., 2007b; Michalski and Noe Dobrea, 2007; Bishop et al., 2008b; Ehlmann et al., 2008a; Mustard et al., 2008b; Murchie et al., 2009b; Wray et al., 2009; Ehlmann et al., 2011). These phyllosilicate detections occur throughout the ancient martian crust, including the Mawrth Vallis region, Nilli Fossae region, north of the Syrtis Major volcanic plateau, and the landing site of the Mars Science Laboratory (MSL), Gale Crater, as well as others (Bibring et al., 2005a; Bibring et al., 2006; Clark et al., 2007a; Michalski and Noe Dobrea, 2007; Ehlmann et al., 2008a; Mustard et al., 2008b; Murchie et al., 2009b; Wray et al., 2009; Milliken et al., 2010a). Clay minerals generally form from the hydrolysis of silicate minerals through hydrothermal alteration, metamorphism and/or weathering and some have speculated that the presence of clay minerals indicate long term water-rock interactions on Mars (Ehlmann et al., 2011). Liquid water is one of the essential requirements for life as we know it; constraining the duration and amount of water on Mars will enable the scientific community to make more accurate predictions regarding the paleo-environmental conditions and past habitability of Mars. Clay minerals may also act as a catalyst in the formation of organic chemical compounds, with clay minerals therefore having a direct impact on possible habitability of Mars (Ferris, 2005).

Stratigraphic relationships and age estimates from crater counting suggest that clay minerals detected from orbit on Mars are ancient (Bibring et al., 2006; Mustard et al., 2008b; Murchie et al., 2009a; Ehlmann et al., 2011) and are therefore likely to have been altered by diagenetic and pedogenic processes subsequent to their formation. Exposed stratigraphic units in the Mawrth Vallis region indicate a transition from an Fe-

and Mg-rich clay with a spectral signature consistent with nontronite to an Al-rich smectite, potentially montmorillonite mixed with kaolinite and silica (Loizeau et al., 2007b; Bishop et al., 2008b; Wray et al., 2009; Michalski et al., 2010c; Noe Dobrea et al., 2010b). The landing site of the Mars Science Laboratory *Curiosity* rover, Gale Crater, also contains deposits of clay minerals that include a thick (tens of meters) deposit of Fe-rich smectite, possibly nontronite (Figure 3) (Milliken et al., 2010a; Thomson et al., 2011). At Gale, the clay minerals are overlain by mixed beds of clay and sulfate minerals and/or sulfate cemented nontronite, which grade upward into sulfate-rich deposits (Milliken et al., 2010a). The mineralogical variation within the stratigraphy at these locations and others could indicate changes in depositional environments, diagenetic processes, as well as global changes in martian climate (Milliken et al., 2010a). However, few studies have examined nontronite dissolution kinetics and clay-to-clay alterations under Mars-relevant conditions, which could provide a better understanding of the processes that affected the minerals observed at the martian surface.

Here we report the results of experiments designed to determine the proton-promoted dissolution rates of nontronite and identify secondary precipitates formed during nontronite dissolution. These experimental results allow us to constrain the stability of nontronite at the martian surface and address whether pedogenic alteration can produce the spectral and mineralogical heterogeneity observed in the Mawrth Vallis region and other localities on Mars.

## MAWRTH VALLIS

The Mawrth Vallis region contains extensive deposits of phyllosilicate-bearing rock (Loizeau et al., 2007b; Loizeau et al., 2010b; Michalski et al., 2010c). Mawrth

Vallis is a valley that transects the region and is believed to have formed through fluvial processes. The rocks in which the clays reside pre-date the incision of the valley, placing their deposition in the early-middle Noachian (3.8-4.1 Gya) (Michalski and Noe Dobrea, 2007; Bishop et al., 2008b; Michalski et al., 2010c). However, whether the clays are detrital or authigenic is not known, thus the age of the clays is poorly constrained. The stratigraphy is generally characterized by a Fe- and Mg-rich nontronite-bearing unit overlain by an Al-rich montmorillonite-bearing unit (Figure 3) (Loizeau et al., 2007b; Bishop et al., 2008b; Wray et al., 2009; Michalski et al., 2010c). Several hypotheses exist addressing the origin and chemical composition of the Mawrth Vallis stratigraphy, including formation under volcanic, sedimentary and pedogenic conditions (Wray et al., 2009; Loizeau et al., 2010b; Michalski et al., 2010c; Noe Dobrea et al., 2010b; Gaudin et al., 2011).

The stratigraphy of the Mawrth Vallis region could have a volcanic origin (Bishop et al., 2008b; Michalski et al., 2010c), in which the Fe- and Mg-rich phyllosilicates were derived from a basaltic ash precursor (Bishop et al., 2008b; Michalski et al., 2010c). The mafic material could have been subsequently altered after deposition into surface waters and/or by diagenetic processes (Michalski et al., 2010c). The Al-rich clay could be the result of further alteration of the Fe- and Mg-rich phyllosilicates, or the subsequent deposition of more felsic ash or rock above the basaltic precursor followed by hydrolysis or diagenetic alteration (Bishop et al., 2008b; Michalski et al., 2010c). The volcanic origin hypothesis attempts to explain the stratigraphy as resulting from numerous volcanic eruptions, with the compositional boundary between the Fe- and Mg-

phyllosilicates to the Al-rich phyllosilicates caused by a shift in deposition of mafic to felsic materials (Michalski et al., 2010c).

The observed stratigraphy and chemical transition could also be explained by a sedimentary origin (Michalski et al., 2010c). Under this scenario, the sediment comprising the Mawrth Vallis region could either be eolian, fluvial, or impact ejecta. The Fe- and Mg- to Al-rich transition could be the result of a paleo-environment boundary between a saturated and unsaturated zone, producing a paleo-oxidation front (Michalski et al., 2010c). Previous work on nontronite synthesis under near-neutral pH and low temperature conditions indicates that anoxic conditions are required to form the Fe bearing octahedral sites required for nontronite precipitation (Harder, 1976; Harder, 1978a). This formation mechanism attempts to explain the Mawrth Vallis stratigraphy as the result of a redox front in which anoxic waters deeper within the sediments allowed for the precipitation of nontronite, whereas oxidized fluids would only allow for the precipitation of montmorillonite and Fe-oxides near the surface.

Finally, the Fe-Mg to Al-rich phyllosilicate transition could have a pedogenic origin (Loizeau et al., 2007b; Loizeau et al., 2010b; Michalski et al., 2010c; Gaudin et al., 2011). Under this scenario, the Fe- and Mg- rich material could have been deposited through any of the previously described conditions and subsequently altered through hydrolysis or diagenesis. The transition between the Fe/Mg and Al phyllosilicates would have been the result of weathering at or near the surface, where alteration and differences in mineral dissolution rates of a heterogeneous deposit could lead to the observed change in the chemical composition of the stratigraphy. This is supported by recent work by Gaudin et al. (2011), where the *in-situ* weathering of saprolite produced Fe and Mg-rich



phyllosilicates overlain by Al-bearing phyllosilicates. These observations also agree with highly weathered soil profiles, as Fe and Mg-rich triple layer clays weather to Al-rich kaolinite and oxides (Brady and Weil, 1999). These weathering profiles are similar to those observed in the Mawrth Vallis region. A purely depositional model such as those proposed above would support mineralogical boundaries that follow bedding, whereas chemical weathering could produce mineralogical boundaries between the Fe/Mg and Al rich phyllosilicates that cut across bedding surfaces. However, the morphology of these transitions are difficult to determine with current orbital observations.

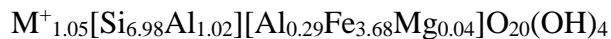
Although nontronite has been detected at multiple location on the martian surface, little work has been conducted on the dissolution of this Fe-rich smectite (Bickmore et al., 2001). Therefore, the effect of chemical weathering on a mixture of clay minerals containing nontronite is difficult to quantify. To help interpret the aqueous history of the Mawrth Vallis region and Gale Crater, this work measures the mineral dissolution rates and leached mineral characteristics of nontronite (NAu-1). These data will help shed light on the evolution of clay mineral deposits at Mawrth Vallis, Gale Crater, and elsewhere on Mars, and help constrain the duration of the presence of liquid water on or near the martian surface.

## METHODS

### Material

Nontronite (NAu-1) was purchased from the Clay Mineral Society, and was determined to have the following chemical formula (where  $M^+$  is generally a metallic

cation residing within the interlayer of the clay mineral, this may also include water) (Keeling et al., 2000):



Previous work using X-Ray Diffraction and infrared spectroscopy indicate N Au-1 is nontronite with trace amounts of kaolinite, quartz, biotite and goethite, which together total approximately 10 percent of the standard - for further details see Keeling et al., (2000), Frost et al. (2002) & Jaisi et al., (2005).

Raman spectra of unoriented, powdered unaltered nontronite (size fraction <45  $\mu\text{m}$ ) were taken using a Horiba Jobin Yvon LabRam HR confocal Raman microscope with a spectral resolution of  $0.3\text{ cm}^{-1}$ , spot size of  $\sim 5\text{ }\mu\text{m}$  using a 50x working distance microscope objective, and a 532 nm (green) wavelength laser. Raman spectra were compared with reference spectra available (R070286) from the RRUFF database to confirm mineralogy (<http://rruff.info>) (Figure S67).

Powder X-Ray Diffraction (XRD) data was collected on the unaltered N Au-1 powder size fraction 45-150  $\mu\text{m}$  (Figure S68) using a PANalytical X'Pert Pro X-Ray Diffraction Spectrometer at 40 kV and 20 mA using  $\text{CuK}\alpha$  radiation. Data was collected from  $5.0021$  to  $74.9981^{\circ}2\theta$  using a step size of  $0.0040^{\circ}2\theta$  and a count time of 21.9550 s per step. Samples were analyzed as random (back packed) mounts, in stainless steel holders. Patterns were taken under air dried conditions. The results indicate nontronite with only minor kaolinite, quartz, biotite and goethite, consistent with previous analyses of the bulk material which indicate that it is 90% nontronite by Keeling et al., (2000).

### Reactor Design

Three experiments were run in flow-through reactors using input solutions with pH values of 0.9, 1.7 and 3.0. Reactors were modeled after Taylor et al. (2000a; 2000b) and were constructed from 5.6 cm of Teflon tubing with an inner diameter of 0.5 cm; reactors were acid-washed prior to use. Nontronite (NAu-1) previously characterized as described above was powdered, dry sieved to 325-100 mesh (45-150  $\mu\text{m}$ ), and then 0.7 – 0.8 g was loaded into each open column. Columns had a total volume of  $1.1 \times 10^{-6} \text{ m}^3$ , and, therefore, assuming a density of nontronite of  $2200 \text{ kg/m}^3$ , columns had a pore volume of approximately 67 – 69 percent before expansion due to hydration. After the sample was loaded, the solution was pumped up through the columns from the bottom until they were filled, to ensure no bubbles were present, after which the outlet tubing was attached. No bubbles were observed in the columns or the tubing at any point during the experiment. Input solutions were prepared from 18.2 M $\Omega$  water and trace element grade HCl to pH values of 0.9, 1.7 and 3.0, and were in equilibrium with atmospheric O<sub>2</sub>. Hydrochloric acid was used because, although sulfates are common on Mars, indicating that sulfuric acid may be important e.g. (Squyres et al., 2004; Tosca et al., 2004b; Gendrin et al., 2005; Chevrier and Altheide, 2008), chlorides have also recently been detected on the surface of Mars (Osterloo et al., 2010) and we wished to measure mineral dissolution rates avoiding precipitation of secondary products such as sulfates. Three sterile 60 ml syringes were each filled with pH solution and loaded into an Orion Sage Syringe pump, model 362. Flow rates were set to 0.16 ml per hour for the first 837 hours, and 0.32 ml/hr for the remaining 410 hours. Each solution flowed through acid-washed 0.062 cm I.D. Teflon tubing, approximately 10 cm of which was submerged in the 26 °C water bath to ensure constant temperature conditions before the solution

entered the columns. The solutions flowed from the 0.062 cm Teflon tubing through a 0.45  $\mu\text{m}$  filter into the bottom of the columns to maximize saturation and minimize preferential flow paths. From the top of the columns effluent solution flowed through another 0.45  $\mu\text{m}$  filter, through 0.062 cm diameter Teflon tubing, and into 3 sterile syringes in which the solution samples were collected. Each filled output syringe was replaced with an empty sterile syringe every 24-48 hours and the output solution chemistry was analyzed. After every 12 days (0.16 ml/hour flow rate) or 6 days (0.32 ml/hour flow rate), input syringes were nearly empty and required replacement. Replacement occurred by exchanging the empty syringes with full ones, which incurred a stopped flow of no more than 3-5 minutes. Careful measures were taken to prevent introduction of bubbles into the tubing during syringe exchange.

#### Analytical Methods

The collected effluent was measured to determine flow rates, output pH, and elemental chemistry including Al, Ca, Fe, Mg, Na, S, Si and Ti concentrations. Flow rates were determined by weighing the effluent discharged since the last sampling period and dividing the weight by that time period (24-48 hours). An aliquot of the effluent solution was measured for pH using a Fisher Scientific Accumet Excel XL 15 pH meter standardized with 4, 7, and 10 pH standards. Solutions were diluted and acidified with high-purity 10 % v/v  $\text{HNO}_3$  for elemental analysis. Concentrations of Al, Ca, Fe, Mg, Na, S, and Si in output effluent were determined with a Thermo iCAP 6300 radial view Inductively Coupled Plasma-Optical Emission Spectrometer with 10 % nitric acid matrix-matched standards for elemental analysis.

#### Visible and Infrared Spectroscopy

Reflectance spectra of reacted and unreacted samples were measured using an ASD FieldSpec3 for the visible-near infrared range (0.35-2.5  $\mu\text{m}$ ), where a quartz tungsten halogen lamp was used as the light source and a Spectralon panel was used as a white reference standard. A Thermo Nicolet 6700 Fourier Transform Infrared Spectrometer (FTIR) was used to measure reflectance for the near and mid-infrared range (1.5-25  $\mu\text{m}$ ), with an infrared source and diffuse gold as a reflectance standard.

### Surface Area Measurement

Surface area was calculated using multi-point (10) adsorption data (Micromeritics ASAP 2020 Gas Sorption Analyzer) from the linear portion of the  $\text{N}_2$  adsorption isotherms between the relative pressures of 0.055 and 0.249 using the Brunauer-Emmett-Teller (BET) isotherm (Brunauer et al., 1938). Surface area was measured of both reacted and unreacted powders.

### Thermodynamic Modeling

PHREEQC version 3 was used to model the saturation of out-put solutions (Parkhurst, 1995; Parkhurst and Appelo, 1999). Thermodynamic data was obtained from the PHREEQC database, and the phases modeled include amorphous silica, chlorite,  $\text{Fe}(\text{OH})_3$ , goethite, gibbsite, hematite, kaolinite, and sepiolite.

## RESULTS

### Solution pH

The pH of the output solutions displayed two characteristic behaviors with time, either remaining relatively stable (pH = 0.9) or decreasing from an initial high pH to a

steady value (initial pH = 1.7 and pH = 3.0 flow rate = 0.32 ml/hr) (Figures 4 – 6, Tables S11-S13). The pH values of the output solutions did not change significantly from the input pH values for 5 of the 6 experiments, suggesting that acidic solutions were corrosive with respect to nontronite throughout the entire column. The output pH displayed two characteristic behaviors with the change in flow rate, either showing minimal change (initial pH = 0.9 and pH = 1.7) or decreasing with the increase in flow rate (initial pH = 3.0) (Figures 4 – 6, Supplementary Tables S11-S13). Steady state pH values varied minimally with time for initial pH = 0.9 and 1.7 for both flow rates, with slightly greater variation for the 0.32 ml/hr initial pH = 3.0 condition (Figures 4 - 6, Tables S11-S13).

#### Concentration versus time

Experiments with initial pH = 1.7 and 3.0 showed rapid release of Si during the initial 200 hours (Si data were not collected for the first 200 hours of the pH = 0.9, flow rate 0.16 ml/h experiment) (Figures 5 and 6). Silicon concentrations decreased in output solutions with the increase in flow rate for initial pH conditions = 0.9 and 1.7, but showed no significant change for initial pH = 3.0. Steady state Si concentrations varied minimally with time (Figures 4 - 6). Steady-state conditions were achieved earlier under more acidic conditions, which is similar to the results of Golubev et al., (2005). This may have resulted from the faster kinetics under higher acid concentrations.

Fe and Al release during dissolution in these experiments display very different behaviors. At initial pH = 0.9 conditions, Fe initially increases to steady state, whereas Al decreases from initially high values to steady state (Figure 4, Table S11). In contrast, at initial pH = 1.7, Fe decreases from high initial values to steady state, and Al increases

from low initial values to steady state. In both cases, steady state concentrations of Fe and Al are generally lower at higher flow rates. Fe and Al concentrations are below detection at all points for the initial pH = 3.0 condition, likely due to the elevated steady-state pH values attained in this experiment.

Ca and Mg are both likely released from interlayer sites in the nontronite structure (Velde, 1995; Keeling et al., 2000) and they display very similar behaviors. Mg can be a significant component of the octahedral layer, but it has previously been shown to be a minor (comprising ~1 percent of the octahedral cations) component of the octahedral layer in NAu-1 (Keeling et al., 2000). For initial pH conditions = 0.9 and 1.7, Ca and Mg rapidly decrease to concentrations that are below detection (Tables S11, S12), similar to the rapid Ca and Mg loss observed in work by Metz et al.(2005b) and Rozalen et al. (2008b), who suggested that this behavior is the result of exchange reactions (replacement by protons) within the interlayer of the smectite. The rapid complete loss of Ca and Mg also suggests interaction of corrosive solutions throughout the reactor, rather than preferential dissolution toward the top of the columns. For initial pH conditions = 3.0, Ca and Mg concentrations increase from initial low concentrations to steady state values (Figure 6, Supplementary Table S13).

Steady state concentrations of K, Na, S and Ti were generally below detection; some initial values were measurable but decreased within the first few sample periods, perhaps in part reflecting early dissolution of trace Ca-sulfate and ilmenite observed during SEM examination of the samples.

### Thermodynamic Modeling

Thermodynamic modeling using PHREEQC suggest that the output solutions are oversaturated with respect to amorphous silica at pH = 0.9 under both flow rates and under saturated with respect to amorphous silica under all other pH and flow conditions. All solutions were undersaturated with respect to the other phases tested (chlorite, Fe(OH)<sub>3</sub>, goethite, gibbsite, hematite, kaolinite, and sepiolite).

#### SEM/EDS and Vis-NIR of Altered Material

SEM images of reacted nontronite showed no unambiguous indication of morphological alteration (Figure 7). No Si, Al and Fe depletion was detected relative to the starting material and no precipitates were observed. Kaolinite was not observed in the SEM/EDS analysis of either reacted or unreacted material, which may be due to the previously documented low concentrations (4%) of kaolinite in the original bulk material. Nontronite reacted with pH 0.9 and 1.7 solutions was depleted in Ca relative to the unaltered samples as measured by EDS (Figure 7), which is consistent with solution chemistry measured by ICP-OES (Figures 4, 5 and Tables S11, S12). Ca was detected in the altered material reacted with pH = 3.0 solutions (Figure 7), which is also consistent with solution chemistry measured by ICP-OES where Ca continued to be released into solution throughout the experiments (Figure 6, Table S13).

The Vis-NIR spectra features at 2.21 and 2.17  $\mu\text{m}$  suggest that kaolinite is present within the altered and unaltered samples. Reacted samples also indicate evidence of a weak and somewhat broader feature from  $\sim 2.15 - 2.33 \mu\text{m}$  in the pH 0.9 and pH 1.7 samples (Figure 8 and 9). This feature is consistent with the presence of Si-OH, and could indicate formation of amorphous silica (opaline silica). The superposition of the kaolinite bands on this broader feature could make the kaolinite bands appear 'weaker' in



these reacted samples without any change in the concentration of kaolinite due to dissolution. These results suggest that 1) amorphous hydrated silica has formed in the samples and 2) there is little or no evidence for dissolution of kaolinite.

Calculation Nontronite Dissolution Rates

Nontronite dissolution rates at pH = 0.9, 1.7 and 3.0 were calculated for each steady state condition (Table S14) defined as the last three consecutive samples at each flow rate for which complete solution chemistry was available. For each steady state condition, elemental concentrations varied by less than 5%. Dissolution was stoichiometric at pH 0.9 and non-stoichiometric at pH 1.7 and 3.0 normalized to Si (Figure 10), note that Al and Fe concentrations were below detection. The very low concentrations within out-put solutions during clay mineral dissolution is commonly observed (Marty et al., 2011a). Nontronite dissolution rates were therefore calculated for each site (tetrahedral, octahedral and interlayer), based on the most abundant cation in that site (Si, Fe, and Ca, respectively), following the approach of Taylor et al. (2000a; 2000b). Although other cations may reside in these sites, they are minority constituents and their effect on the calculated dissolution rate is expected to be minimal. Cation site occupancies were taken from Keeling et al., (2000), who indicate that N Au-1 has the formula:  $M^{+1.05}[Si_{6.98}Al_{1.02}][Al_{0.29}Fe_{3.68}Mg_{0.04}]O_{20}(OH)_4$ . Steady state elemental release rates for Si, Fe and Ca were calculated after White and Brantley (1995):

$$R = \frac{(C_{out} - C_{in})Q}{Am}, \quad (Eq. 1)$$

where  $C_{out}$  (M) is the steady state elemental concentration (described above),  $C_{in}$  (M) is the input concentration (assumed to be zero),  $Q$  (L/s) is the average flow rate at the given

pH at steady state,  $m$  (g) is the mass of the unreacted material (0.7-0.8 g in each case) and  $A$  ( $\text{m}^2/\text{g}$ ) is the specific surface area of the reacted material determined by  $\text{N}_2$  sorptometry. The mineral dissolution rate was then calculated from the elemental release rate and the stoichiometry of the unreacted nontronite (described above).

Under the most acidic conditions (pH 0.9) dissolution rates measured from the tetrahedral and octahedral sites were approximately equal, with stoichiometric release of Fe relative to Si (Table S11). However, at pH conditions = 1.7 and 3.0, nontronite dissolution rates calculated from the tetrahedral sites were significantly faster than those calculated from the octahedral sites, indicating either non-stoichiometric release or precipitation of secondary Fe-bearing phases. We note that reflectance spectra of reacted and unreacted samples are qualitatively similar and showed no additional adsorption features at the wavelengths measured in this study that would indicate formation of precipitates other than amorphous silica (Figure 8 and 9). Our SEM-EDS observations of the reacted (exposed to both flow rates) nontronite also showed no evidence for secondary precipitates. However, we note that the strength of the Fe-OH vibrational features near  $\sim 2.28 \mu\text{m}$  are weaker in the samples at pH conditions 0.9 and 1.7, and the  $\text{H}_2\text{O}$  adsorption features near  $1.9 \mu\text{m}$  are also weaker in these samples, likely due to decreased availability in the interlayer region (Figure 9). These effects are most notable in the sample reacted at pH 0.9, although all diagnostic absorption features are still present and easily detected, suggesting Fe-OH bonds are still present in all nontronite samples. Nontronite dissolution rates calculated from Ca release rates from the interlayer site, when detectable, were more rapid than nontronite dissolution rates calculated from either the tetrahedral or the octahedral sites, indicating preferential loss of Ca. Where

steady state Ca release rates were below detection (BD), Ca concentrations showed high initial concentrations (Figure 4 – 6, Tables S11-S13), which presumably removed most of the Ca from the interlayer sites early in the experiments.

## DISCUSSION

### Solution Chemistry

Si concentrations show an initial decreasing trend over time (note initial Si concentrations are not available for the pH = 0.9 experiment). This observation is common for flow through dissolution experiments and may be the result of ultra-fine particles and high energy sites. Metz et al., (2005a) also observed similar behavior and concluded that the dissolution of a Si cement or coating may be responsible, which may act as a barrier to the protonation of the TOT structure, preventing the release of Al and Fe from the clay structure. Thermodynamic modeling in PHREEQC of steady state solutions suggest oversaturation with respect to amorphous silica in pH 0.9 experiments under both flow rates and under saturation in all other conditions (Parkhurst, 1995; Parkhurst and Appelo, 1999). The IR data also suggest the presence of amorphous silica in the reacted nontronite. Precipitation of amorphous silica within the columns also means that dissolution rates calculated from Si represent conservative, or minimum, dissolution rates.

In both pH = 0.9 and pH = 1.7 conditions, less Fe was released than Al relative to the mineral stoichiometry. Metz et al. (2005a) also observed that Fe concentrations were less than expected relative to Al and concluded that Fe is not released stoichiometrically as the result of preferential Fe reabsorption or precipitation. This may be due to the much

larger first hydrolysis constant of  $\text{Fe}^{3+}$  of  $2.5 \times 10^{-3}$  (Lamb and Jacques, 1938) than of  $\text{Al}^{3+}$  ( $1.05 \times 10^{-5}$ ) (Frink and Peech, 1963), which has previously been used to explain more rapid formation of Fe oxides (Hsu, 1975). Al and Fe from the octahedral (or tetrahedral) layers may also form oxides in the interlayer, altering smectite layers to chlorite (Barnhisel and Bertsch, 1989). This process would make the dissolution of the octahedral layer appear slower than that of the tetrahedral layer, as observed in the pH = 1.7 experiments. Secondary Al and Fe bearing phases were not detected with IR-spectroscopy or SEM, and when output concentrations of Fe and Al were above detection, solutions were undersaturated with respect to all Al- and Fe-bearing phases tested, although precipitation and adsorption may still occur despite undersaturation of the bulk solution (Ruiz-Agudo et al., 2012).

#### *Dissolution rates normalized to surface area and mass*

Nontronite dissolution rates were normalized to the total final surface areas of the reacted powders as well as the mass. As previously documented (Turpault and Trotignon, 1994; Bickmore et al., 2001; Dogan et al., 2006; Dogan et al., 2007b), solution phase adsorption and BET techniques used in the determination of clay mineral surface areas have significant sources of potential uncertainty. Molecules used during solution phase adsorption are generally large and may have preferred orientation producing erroneous results (Dogan et al., 2007b). Additionally, Bickmore et al. (2001) observed that nontronite dissolution is significantly more rapid on mineral edges than on basal surfaces, and some studies normalize to a fraction of the total BET surface area to account for this effect (Turpault and Trotignon, 1994; Taylor et al., 2000a; Taylor et al., 2000b; Hodson, 2006a; Hodson, 2006b). However, basal surfaces can be significant in

the dissolution process, as protons adsorb to them and then quickly diffuse to the reacting sites (Zysset and Schindler, 1996). Therefore, in this study, specific surface area was determined by N<sub>2</sub> adsorption and application of the BET isotherm (Brunauer et al., 1938) to both reacted and unreacted material, and rates have been normalized both to mass and final specific surface area for each condition (Table S14).

The surface area of the unreacted nontronite measured in this study (45-150 μm size fraction of N<sub>Au</sub>-1) ( $64.37 \pm 0.64 \text{ m}^2/\text{g}$ ) is slightly higher than the reported value for N<sub>Au</sub>-1 of  $52.8 \pm 1.06 \text{ m}^2/\text{g}$  (Dogan et al., 2007b). The specific surface area of nontronite N<sub>Au</sub>-1 has been considered a characteristic of the mineral regardless of particle size, due to the internal structures of clay minerals (in this case lamellar spaces) which comprise the majority of the specific surface area (Dogan et al., 2007b). Final surface areas in our experiments were slightly decreased relative to initial surface areas for pH = 1.7 ( $57.29 \pm 0.59 \text{ m}^2/\text{g}$ ) and 3.0 ( $60.77 \pm 0.62 \text{ m}^2/\text{g}$ ), and approximately doubled for pH = 0.9 ( $101.31 \pm 0.83 \text{ m}^2/\text{g}$ ). Past work by Bickmore et al. (2001) examined nontronite dissolution under acidic conditions with *in situ* atomic force microscopy. In that study, the authors observed the preferential dissolution of mineral edges. However, they concluded that the dissolution front slows along some of the crystal faces, potentially smoothing the crystals and reducing the surface area (Bickmore et al., 2001). This could explain the reduced surface area of the pH 1.7 and 3.0 experiments (Table S14). The large increase in surface area in our pH = 0.9 experiment may be the result of the formation of etch-pits along the mineral surfaces, disaggregation of the particles and/or a reduction of particle size (Metz et al., 2005b). Taylor et al. (2000b) similarly observe a doubling in surface area during phlogopite dissolution under acidic conditions.

### Dissolution rates and calculation of a rate law

Due to the changes in solution chemistry over time that are common in column dissolution experiments e.g. (Taylor et al., 2000a; Taylor et al., 2000b; Metz et al., 2005a; Rozalén et al., 2008b; Hausrath et al., 2009), and the nonstoichiometric dissolution discussed above, dissolution rates were measured from steady state concentrations of multiple elements corresponding to interlayer, octahedral and tetrahedral sites at each pH value and flow rate. Nontronite dissolution rates followed the order: interlayer > tetrahedral > octahedral sites when calculated from Ca, Si and Fe release rates respectively. Release from interlayer sites is interpreted as the replacement of Ca and Mg ions by protons (exchange reactions), which also causes the observed increase in pH (Stadler and Schindler, 1993; Madejová et al., 1998; Metz et al., 2005a). Bonds to ions in the interlayer tend to be weaker than to those ions in the tetrahedral and octahedral structures, and ions in the interlayer are subject to rapid replacement by protons. The nontronite dissolution rate calculated from Si release attributed to dissolution of the tetrahedral site is therefore assumed to represent the rate-limiting step along with the co-dissolution of the octahedral site (Marty et al., 2011a). Similarly, Bickmore et al. (2001) documents that the rate controlling step in nontronite dissolution is the breaking of oxygen bonds and the dissolution along edges. Although other cations such as Al may also be present in the tetrahedral site, Si is the dominant component, filling about 90 percent of the sites (Velde, 1995; Keeling et al., 2000), and the effect of Al substitution on the dissolution rate calculated from Si should therefore be minimal. Dissolution rates calculated from Si are therefore expected to be conservative (minimum dissolution rates) and were used to calculate the nontronite dissolution rate law.

Distance from equilibrium (degree of under-saturation) in mineral dissolution experiments is commonly determined through equation 2 for most minerals including smectites (Cama et al., 2000; Amram and Ganor, 2005; Metz et al., 2005a):

$$\Delta G_r = RT \ln(IAP/K_{eq}) \quad (Eq. 2)$$

where  $\Delta G_r$  is the change in Gibbs free energy of the reaction,  $IAP/K_{eq}$  is the reaction quotient over the equilibrium constant for dissolution,  $R$  is the universal gas constant and  $T$  is temperature in Kelvin. Although commonly used, the previous equation may not accurately predict the degree of under-saturation in dissolution experiments of smectites such as those presented here (May et al., 1986b). Currently, there is no experimentally determined equilibrium constant for nontronite, and calculated equilibrium constants produce differing degrees of under saturation (Delany and Lundeen, 1990; Wilson et al., 2006). In addition, the previous work of May et al. (1986b) suggests that the equilibrium constants and free energy estimates of smectites may not be justified due to their heterogeneous and variable nature. Therefore, in these experiments, where the dissolution rates show independence of flow rate, conditions are treated as far from equilibrium.

The two most acidic conditions (initial pH = 0.9 and 1.7) show no change in rate outside uncertainty between the two flow rates, indicating that pH and not distance from equilibrium (as affected by the change in flow rates) is likely controlling the dissolution rates. This would suggest far from equilibrium conditions, and that dissolution is occurring on the dissolution plateau (Burch et al., 1993; Marty et al., 2011a), and we therefore treat these experiments as far from equilibrium. In contrast, however, the

dissolution rate of the pH 3.0, 0.16 ml/h condition is much slower than the pH 3.0, 0.32 ml/hr rate. Due to the drastic change in outlet pH values of the pH 3.0, 0.16 ml/hr experiment, however, it cannot be determined if the change in rate between the two flow rates is a result of pH or degree of undersaturation (Al and Fe concentrations were below detection and therefore the Gibbs free energy of the reaction could not be calculated) (Burch et al., 1993).

Therefore, the dissolution rate law was calculated from all measured rates as a function of final pH, except the dissolution rate measured at initial pH = 3.0 and a flow rate of 0.16 ml/hr (Figure 11) in the form;

$$r = k_{H^+} \cdot 10^{-n \cdot pH_i} \quad (Eq. 3)$$

where  $r$  is the surface area normalized rate (mol mineral  $m^{-2}s^{-1}$ ),  $n$  is the reaction order with respect to  $H^+$  (0.297), and  $k_{H^+}$  is the rate constant for proton-promoted dissolution ( $-12.06 \log \text{ mol mineral } m^{-2}s^{-1}$ ). The dissolution rate constant and reaction order were determined by applying linear regression to log dissolution rates versus pH (Figure 11), and the strong linearity of these result is similar to many silicate minerals dissolved under acidic condition (Drever, 1997b). The measurement of a rate law allows its use in future kinetic modeling relevant to both Earth and Mars under acidic conditions.

### Implications for Mars

The dissolution rate law measured in this study represents, to our knowledge, the first rate law for nontronite dissolution under acidic or proton-promoted conditions, although previous work has examined the behavior and morphological alterations of nontronite during dissolution using Atomic Force Microscopy (Bickmore et al., 2001).



The dissolution of nontronite under acidic conditions is relevant to martian soils and sediments, which may have experienced acidic conditions on regional or global scales (Burns, 1987; Burns and Fisher, 1990; Burns, 1993; Elwood Madden et al., 2004; Bibring et al., 2006; Hurowitz et al., 2006; Hurowitz and McLennan, 2007; Tosca et al., 2008). The measurement of a dissolution rate law under far-from equilibrium, proton-promoted conditions such as these also means that dissolution rates can be calculated under conditions closer to equilibrium with higher concentrations of other ions in solution using, for example, transition state theory (Lasaga and Luttge, 2001; Lasaga and Lüttge, 2003; Amram and Ganor, 2005; Yang and Steefel, 2008). This approach is used in numerical reactive transport modeling (Drever, 2005; Maher et al., 2006; Navarre-Sitchler and Brantley, 2007; Hausrath et al., 2008b; Maher et al., 2009; Navarre-Sitchler et al., 2009; Hausrath and Olsen, 2013) which may have further relevance to natural conditions on Mars. In addition, this rate law will be useful for comparison to future work to specifically determine the effect of other factors on the dissolution of nontronite.

The nontronite dissolution rates measured in this study demonstrate the potential for long term stability of nontronite at the martian surface. These nontronite dissolution rates are significantly slower than the dissolution rates of the primary phases of basalt compiled by Brantley (2008), including apatite (Valsami-Jones et al., 1998; Welch et al., 2002; Guidry and Mackenzie, 2003), olivine (Brady and Walther, 1989; Wogelius and Walther, 1992; Pokrovsky and Schott, 2000; Rosso and Rimstidt, 2000; Oelkers, 2001), pyroxene (Eggleston et al., 1989; Knauss et al., 1993; Golubev et al., 2005), plagioclase (Holdren Jr and Speyer, 1987; Amrhein and Suarez, 1992; Hodson, 2003) and basalt glass (Gislason and Hans, 1987). Although dissolution rates measured in the laboratory

are generally faster than dissolution rates measured in the field (White and Brantley, 1995), relative dissolution rates generally follow the same order in the field as in the laboratory (Velbel, 1993b; Hausrath et al., 2008a; Hausrath et al., 2008b). Therefore, we can conclude from these laboratory experiments that once nontronite formed it would likely persist at the martian surface for prolonged periods relative to surrounding basaltic material.

Nontronite dissolution rates measured in this study are slightly faster and were performed closer to equilibrium than the montmorillonite dissolution rates reported by Rozalen et al. (2008b). In addition, Rozalen et al. (2008b) normalized their rates (plotted in Figure 12) to the reactive edge surface area (a much smaller surface area), whereas we normalize to the entire BET surface area. Therefore, our rates, if also normalized to an estimated reactive edge surface of  $6.5 \text{ m}^2\text{g}^{-1}$  (Rozalén et al., 2008b) would be 15-29 times faster, than montmorillonite. Taking into account the possible precipitation of amorphous silica, the difference between the rates reported is conservative (i.e. nontronite dissolution is potentially even more rapid relative to montmorillonite). Another study by Amram and Ganor (2005) on smectite dissolution (montmorillonite sample SAz-1) under acidic conditions and normalized to mass also documented slower rates of dissolution than the nontronite dissolution rates (normalized to mass) of this study. The dissolution rates of nontronite measured in this study were approximately 2 to 21 times faster than those of Amram and Ganor (2005) measured at the same pH. At pH ~ 1, our dissolution rates were approximately 8 to 20 times more rapid and at pH ~3.6 our dissolution rates were roughly 15 to 21 times faster, with the smallest difference occurring at a pH of 1.8 and 1.9, in which case, the rates were still an additional 2 to 6 time faster than Amram

and Ganor's (2005) dissolution rates. This is also likely to be a conservative estimate as more rapid flow rates (2-6x more rapid) were used in Amram and Ganor's (2005) studies. Due to the similar structure of these clays (montmorillonite and nontronite are both dioctahedral smectites which only differ in chemical composition) these results suggest Al-rich clays may be less susceptible to protonation and/or more susceptible to Al inhibition by mechanisms such as the formation of chlorites than ferric Fe-rich clays (Dixon and Weed, 1977).

The relative dissolution rates of nontronite and montmorillonite may also have implications for the stratigraphy of Mawrth Vallis, as previous work suggests that it consists of previously or currently mixed clay deposits based on the characteristics of the Al-Fe contact (Michalski et al., 2013). We hypothesize that the prolonged dissolution of a mixture of nontronite and montmorillonite under oxidizing and acidic conditions similar to these experiments would, over geologic time periods, enrich near surface environments in montmorillonite which is consistent with the observed mineral stratigraphy at Mawrth Vallis (Michalski et al., 2013; Smith et al., 2013). Both our IR measurements of the reacted nontronite, and the thermodynamic modeling of the output solutions suggest the precipitation of amorphous silica during reaction of the nontronite. Observations on Mars, in which phyllosilicates are generally in spatial association with amorphous silica (Murchie et al., 2009a), are therefore consistent with reaction by liquid water. Many previous studies have also shown that the weathering of smectite minerals produces kaolinite, e.g. Karathanasis and Hajek (1982), Srodon (1999) and Hausrath et al. (2011b), suggesting that the kaolinite at the land surface in the Mawrth Vallis region may also represent an alteration product resulting from the dissolution of nontronite.

Dissolution under soil-forming conditions may therefore represent a plausible formation mechanism for the mineralogic stratigraphy observed at Mawrth Vallis. Future work using these dissolution rates in reactive transport modeling may allow further constraints to be placed on the formation mechanisms and durations of the Mawrth Vallis stratigraphy.

## CONCLUSIONS

We have presented dissolution rates of the smectite nontronite, which has been identified at multiple locations on the martian surface, including Mawrth Vallis and Gale Crater (Loizeau et al., 2007b; Bishop et al., 2008b; Wray et al., 2009; Michalski et al., 2010c; Milliken et al., 2010a; Noe Dobrea et al., 2010b). Following the approach of Taylor et al., (2000a; 2000b), nontronite dissolution rates were calculated for each site (tetrahedral, octahedral and interlayer), based on the most abundant cation in that site (Si, Fe, and Ca, respectively). Stoichiometric dissolution was observed under conditions of initial pH = 0.9, and non-stoichiometric dissolution occurred under initial pH = 1.7 and 3.0 conditions. Mineral dissolution rates calculated from the cations follow the order interlayer > tetrahedral > octahedral. Dissolution rates calculated from the Si release rates yield the first rate law for nontronite dissolution:  $r = 10^{-12.06 (\pm 0.123)} \cdot 10^{-0.297 (\pm 0.058) \cdot pH}$ . When the dissolution rates measured in this study are compared to dissolution rates from the literature, dissolution of nontronite is orders of magnitude slower than dissolution of the primary phases in basalt. This result suggests that once nontronite formed it would persist on Mars for long periods of time relative to surrounding basaltic material. Nontronite dissolution rates are slightly faster than dissolution rates of montmorillonite (Rozalén et al., 2008b) and kaolinite (Huertas et al., 1999a), suggesting

that chemical weathering of a mixed clay deposit would enrich the deposit in montmorillonite and kaolinite through the preferential dissolution of nontronite. Amorphous silica precipitation, observed in our reacted nontronite, also suggests that weathered nontronite on Mars would likely contain amorphous silica. Therefore, chemical weathering of strata containing mixtures of montmorillonite, nontronite and kaolinite provides a potential formation mechanism for the mineralogic stratigraphy observed at Mawrth Vallis and other locations on Mars.

#### ACKNOWLEDGEMENTS

This material is based upon work supported by the National Aeronautics and Space Administration under Grant No. NNX12AH96G issued through the NASA Training Grant: National Space Grant College and Fellowship Program (Space Grant) and a Mars Fundamental Research Program grant NNX12AH96G to E. Hausrath and J. Hurowitz. The authors would like to express their appreciation to Valerie Tu, Chris Adcock, Oliver Tschauer and Brittany Myers and Michael Steiner for insightful conversations improving this paper, Paul Forster for aid in determining the surface area of the sample and William Abbey for aid and acquisition of spectra. We also thank Associate Editor Thomas McCollom, Joseph Michalski, and two anonymous reviewers for helpful comments that greatly improved this work.

## FIGURES

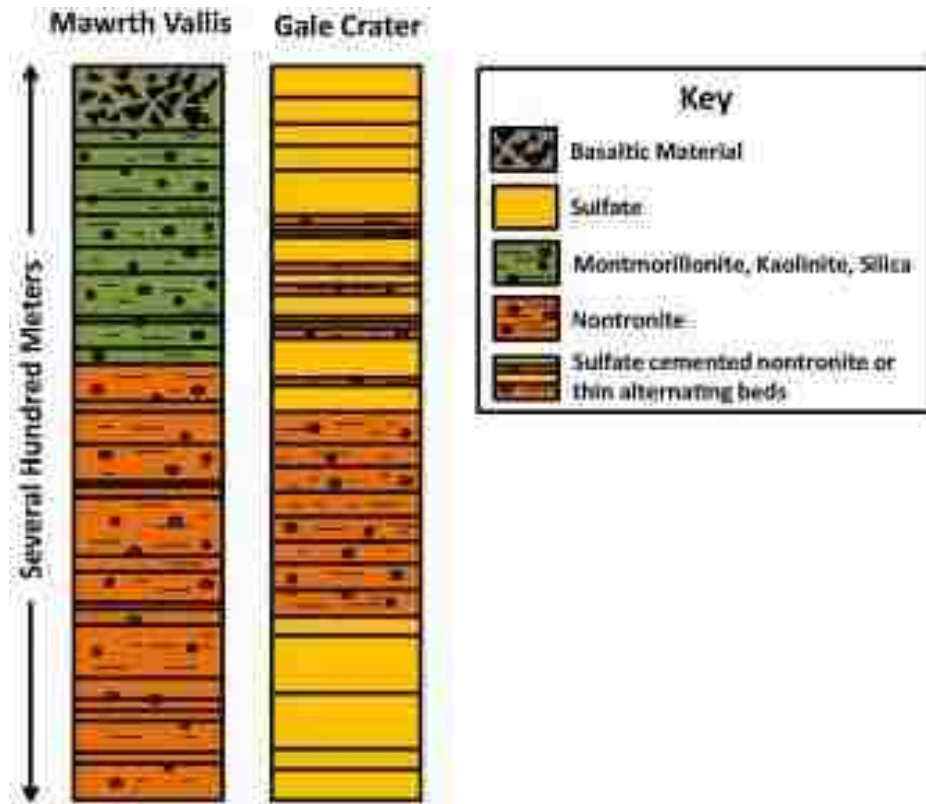


**Figure 3: (A) Stratigraphy of the Mawrth Vallis region, constructed from spectra taken by the Mars Reconnaissance and Mars Express Orbiters (Michalski et al., 2010b). (B) Stratigraphy of lower mound Gale Crater, constructed from CRISM data (Milliken et al., 2010b). Note the depicted stratigraphy for Gale Crater underlies several kilometers of unidentified dust covered materials (Milliken et al., 2010b). \*\*\*Strata are not to scale.**

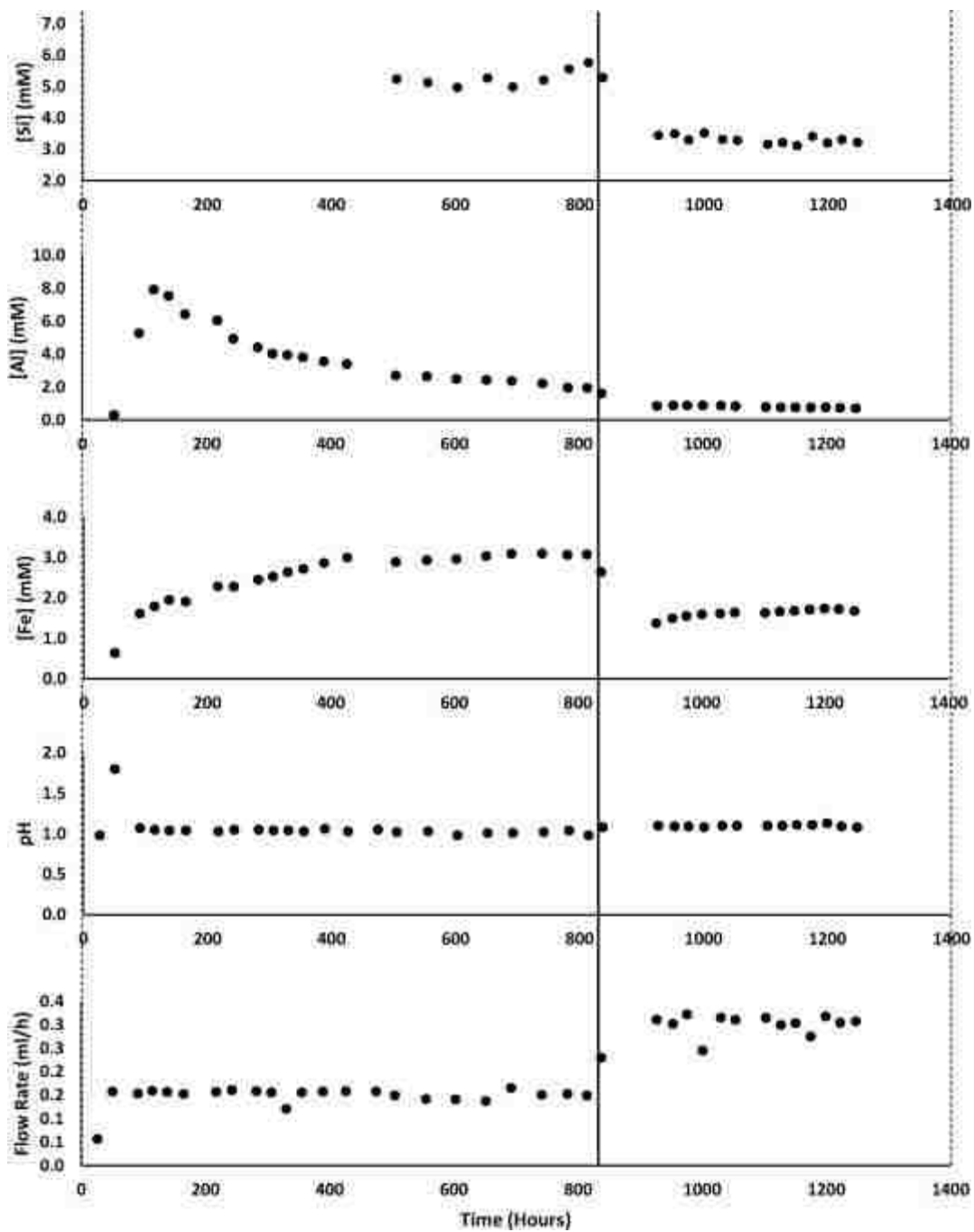


**Figure 4: Elemental concentrations, pH and flow rate of out-put solutions from nontronite dissolution experiments with initial pH = 0.9. The black vertical line represents the change in flow rate from 0.16 to 0.32 ml/h after 837 h.**

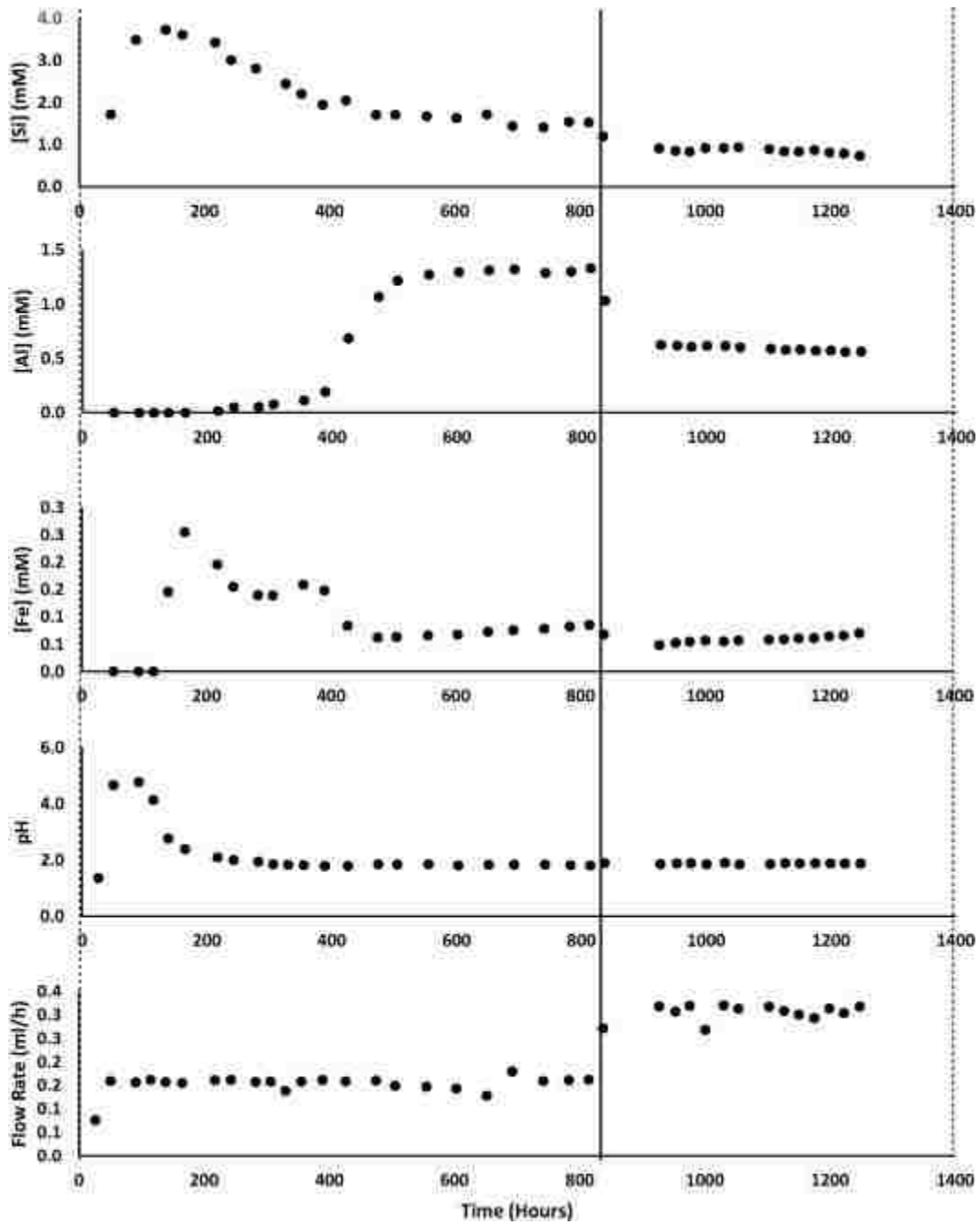


**Figure 5: Elemental concentrations, pH and flow rates of out-put solutions from nontronite dissolution experiments with initial pH = 1.7. The black vertical line represents the change in flow rate from 0.16 to 0.32 ml/h after 837 h.**



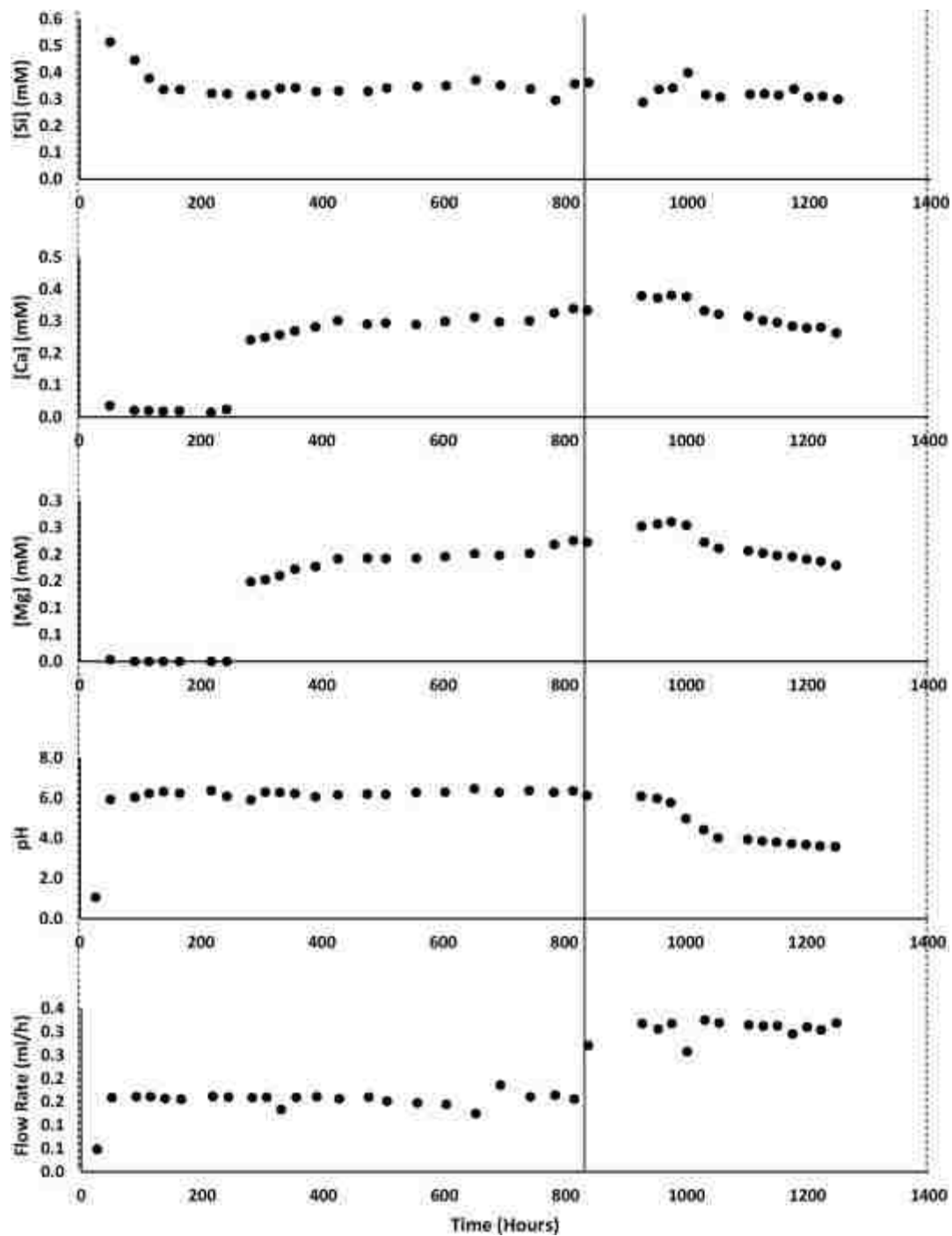


**Figure 6: Elemental concentrations, pH and flow rates of out-put solutions from nontronite dissolution experiments with initial pH = 3.0. The black vertical line represents the change in flow rate from 0.16 to 0.32 ml/h after 837 h.**

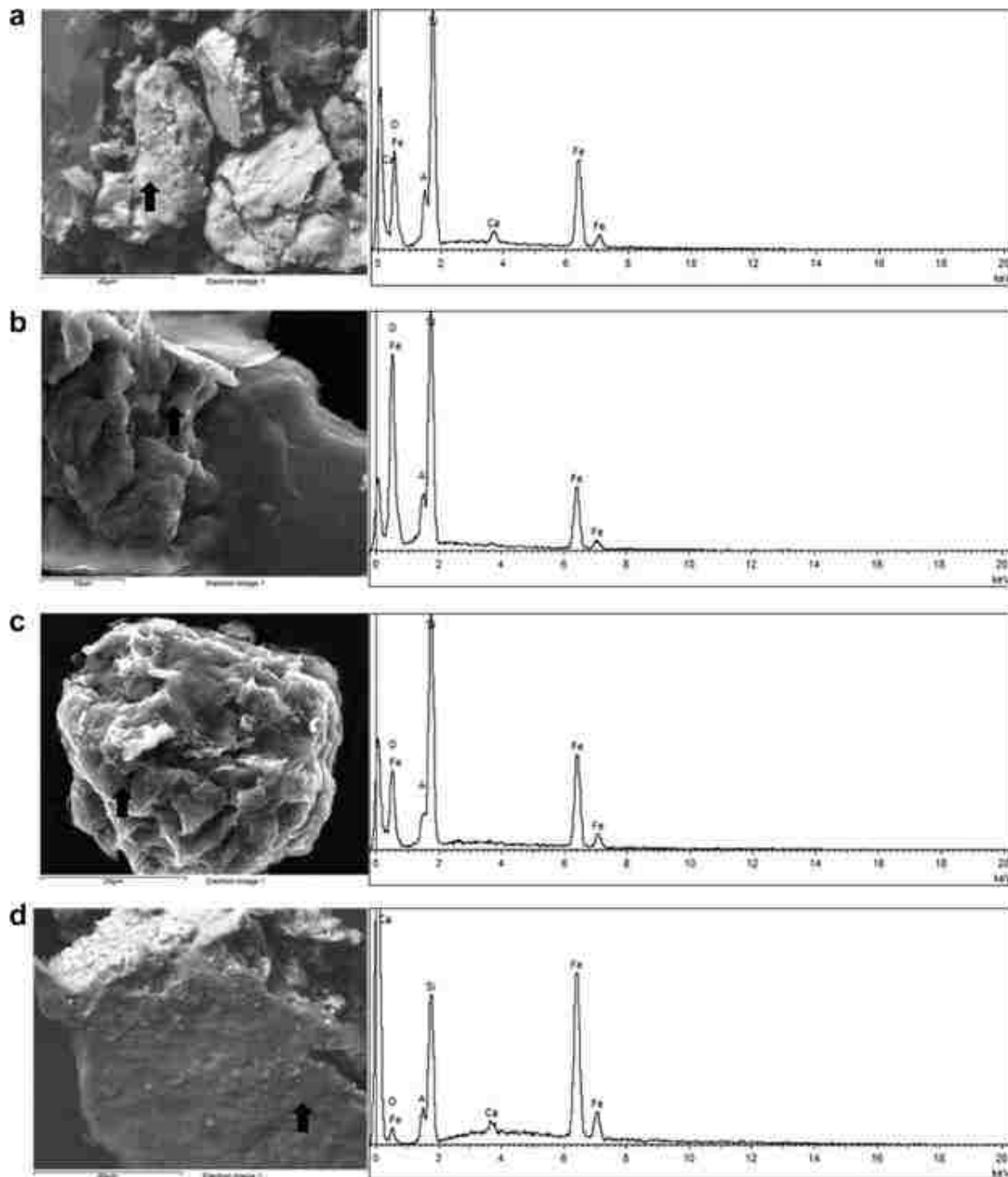


**Figure 7: SEM images and EDS spectra of Reacted and unreacted Nontronite.** SEM images and EDS spectra of (a) unreacted NAu-1, and reacted NAu-1 (from the end of the experiments) under initial pH conditions of (b) 0.9, (c) 1.7, and (d) 3.0. No unambiguous evidence of alteration is observed in SEM and EDS data except the depletion of Ca in the samples reacted at pH 0.9 and 1.7.

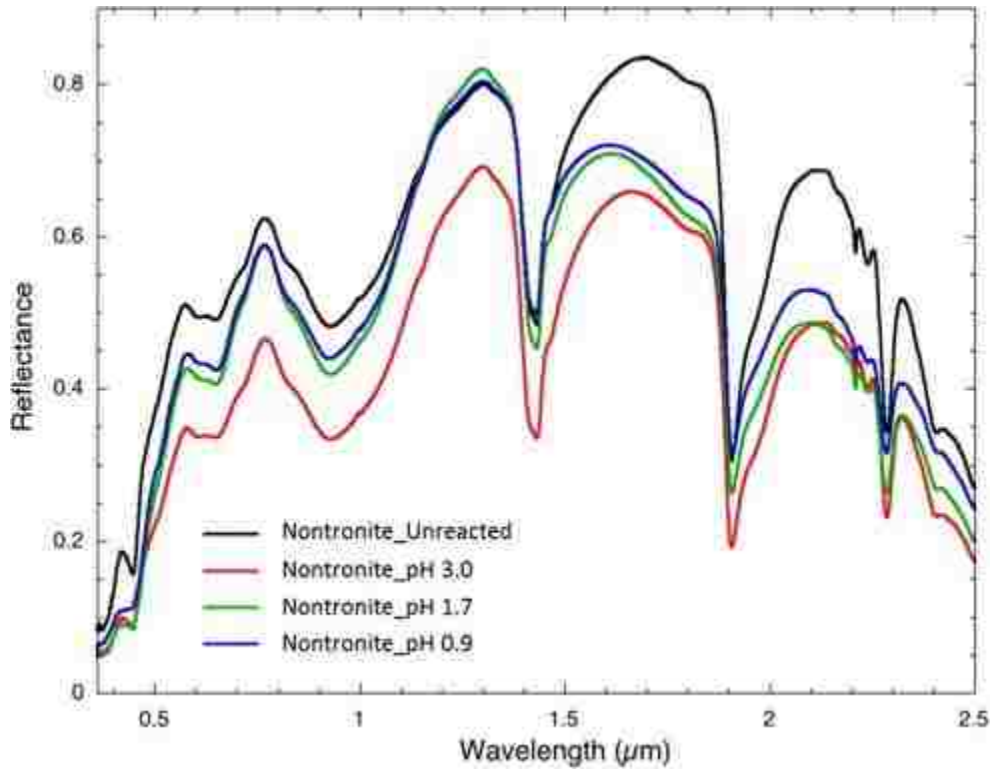


**Figure 8: Visible-near infrared and Fourier Transform Infrared spectra of unreacted and reacted nontronite.** Visible-near infrared (IR) range and Fourier Transform Infrared Spectroscopy (FTIR) spectra for the near infrared and mid-infrared (NIR-mid-IR) range of unreacted nontronite and final reacted material at pH = 0.9, 1.7 and 3.0.

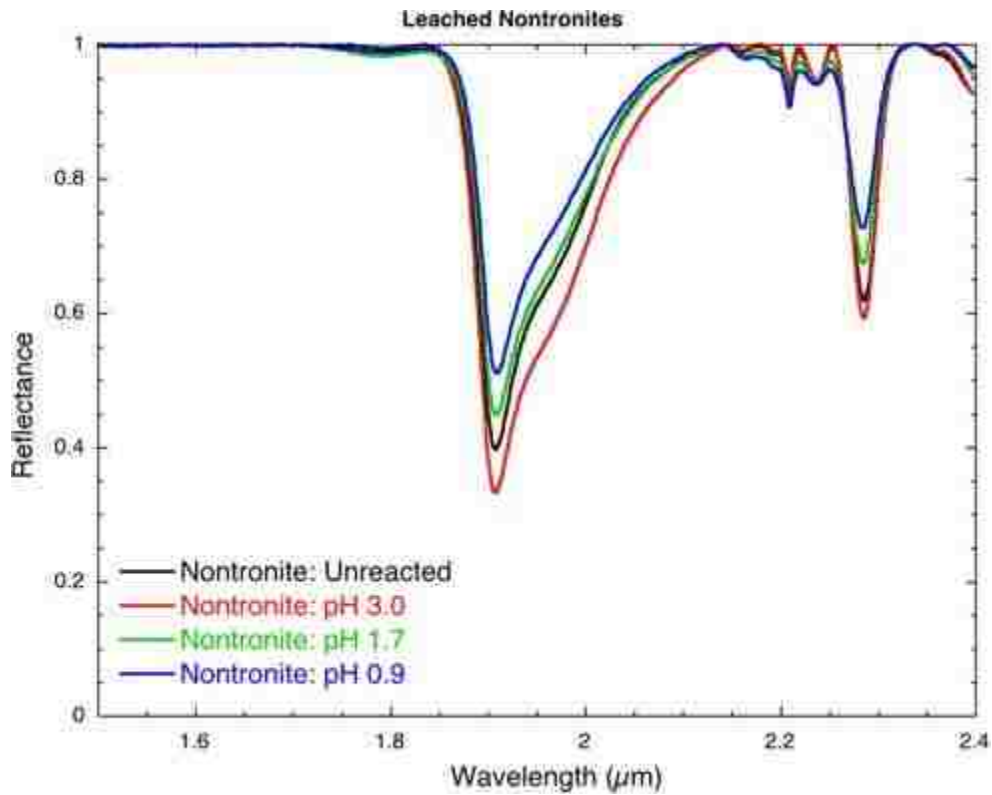


**Figure 9: Continuum removed spectra.** Note that the strength of the Fe-OH vibrational features near  $\sim 2.28 \mu\text{m}$  are weaker in the samples at pH conditions 0.9 and 1.7, and the H<sub>2</sub>O adsorption features near  $1.9 \mu\text{m}$  are also weaker in these samples, likely due to decreased availability in the interlayer region.

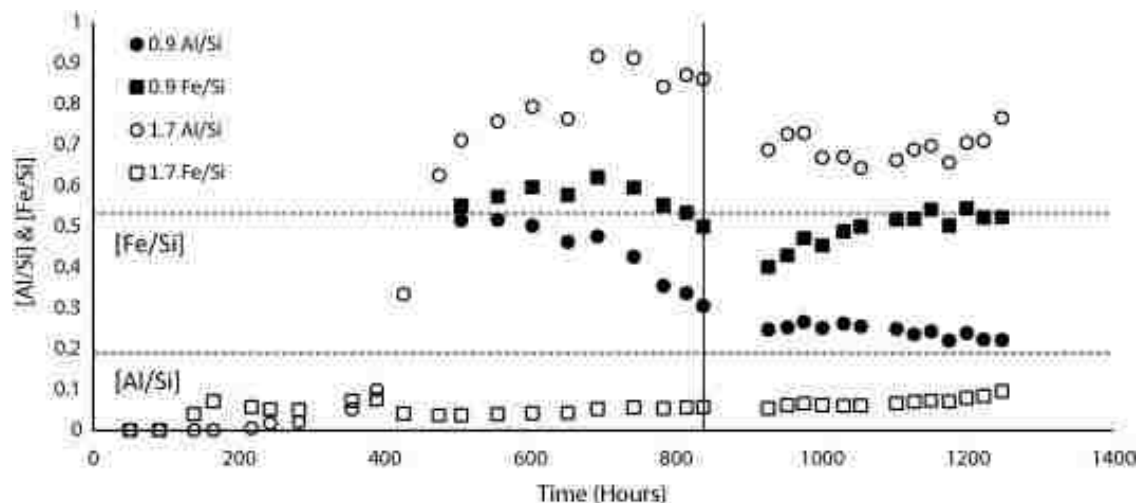


**Figure 10: Molar ratios of Fe and Al normalized to Si.** Elemental concentrations of Fe and Al normalized to Si for pH = 0.9 (filled points) and pH = 1.7 (open points). Solid lines represent the stoichiometric ratio of Al:Si and Fe:Si in the unreacted nontronite. Out-put concentrations are approximately stoichiometric or approach stoichiometric dissolution at pH 0.9 for both Al and Fe. In contrast, dissolution under the condition initial pH = 1.7 was nonstoichiometric, as was dissolution under condition initial pH = 3.0, not shown because Al and Fe concentrations were below detection. The black vertical line represents the change in flow rate from 0.16 to 0.32 ml/h after 837 h.

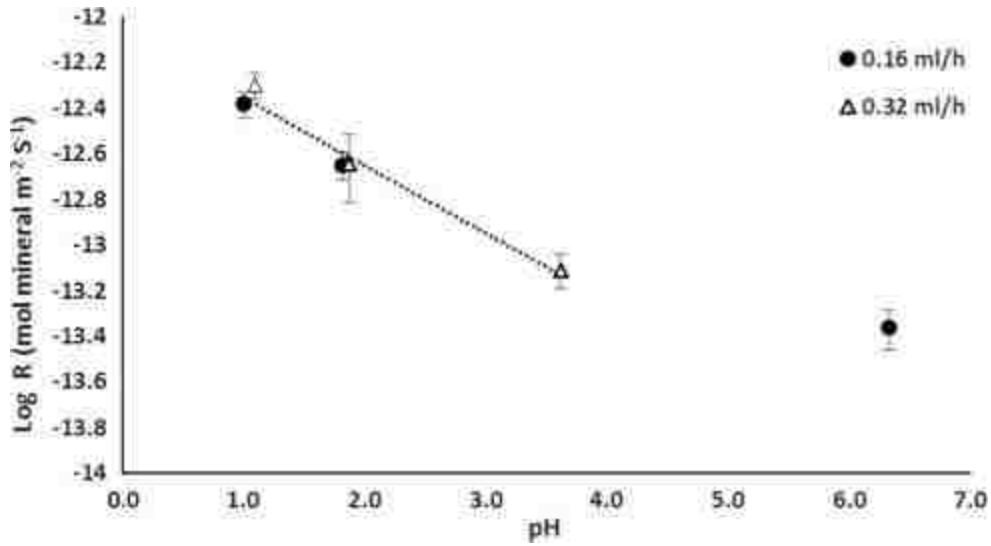


**Figure 11: Dissolution rate law for nontronite.** Log dissolution rates of nontronite with flow rates of 0.32 ml/h (open symbols) and flow rates of 0.16 ml/h (closed symbols). Dissolution rates are plotted versus final pH. All dissolution rates are shown, however the pH = 3.0, 0.16 ml/h flow rate is not included in the rate law,  $r = 10^{-12.06(\pm 0.123)} \cdot 10^{-0.297(\pm 0.058) \cdot \text{pH}}$  as discussed in text. Error bars represent two standard deviations.

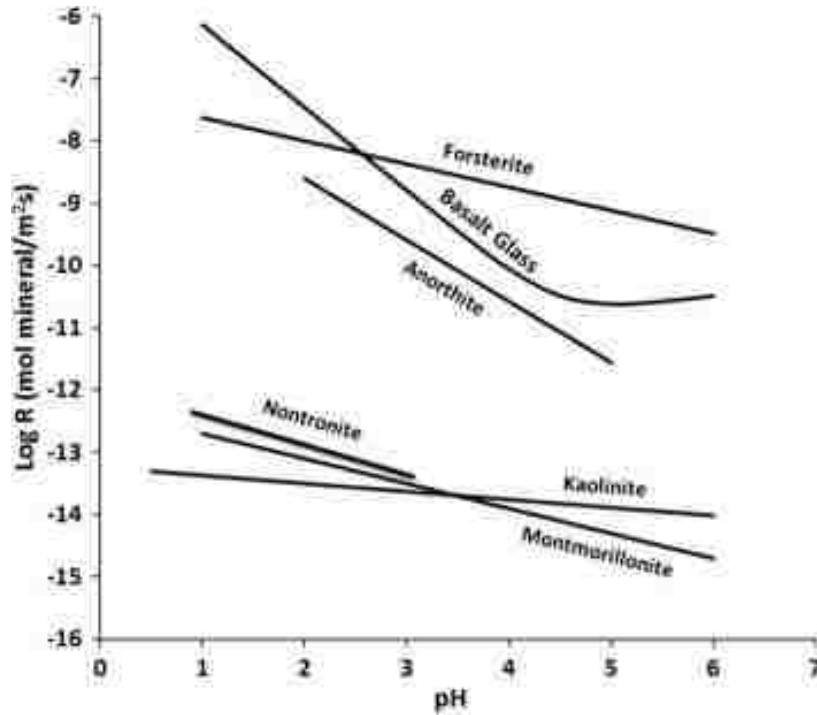


**Figure 12: Dissolution rate law of nontronite compared to the rate laws of the primary minerals in basalt and other clay minerals.** The nontronite dissolution rate law measured in this study compared to dissolution rate laws for primary minerals in mafic rocks (forsterite, basaltic glass and anorthite) as compiled by Brantley (2008), and dissolution rate laws of the clay minerals kaolinite (Huertas et al., 1999b) and montmorillonite (Rozalén et al., 2008a). Nontronite dissolution is much slower than the primary minerals in mafic rocks, suggesting its long term stability relative to basalt. However, nontronite dissolution is faster than montmorillonite and kaolinite, suggesting that preferred dissolution of nontronite at the surface of Mars could have produced the stratigraphy of the Mawrth Vallis region.

## CHAPTER FOUR

### WEATHERING PROFILES AT MAWRTH VALLIS YIELD INSIGHT INTO THE AQUEOUS HISTORY AND POTENTIAL HABITABILITY OF MARS

S. R. Gainey<sup>1</sup>, E. M. Hausrath<sup>1</sup>, J. A. Hurowitz<sup>2</sup>

<sup>1</sup>Department of Geoscience, University of Nevada, Las Vegas, 4505 S. Maryland Parkway, Las Vegas, NV 89154-4010, USA

<sup>2</sup>Department of Geosciences, Stony Brook University, 255 Earth and Space Building (ESS), Stony Brook, NY 11794-2100, USA.

#### ABSTRACT

Although abundant evidence exists for liquid water on Mars, the duration and characteristics of that liquid water remain under-constrained. The characteristics of liquid water can be preserved in its interactions with rock, soil or sediment when forming weathering profiles. On Earth, weathering profiles can be quantitatively modeled to interpret the conditions under which they formed, with inputs of measured geochemical parameters and known durations yielding observed profile characteristics. Putative weathering profiles also exist in rocks, soils and sediments on Mars. Of these, Mawrth Vallis is one of the largest in size, and is therefore critically important for understanding previous conditions that affected alteration on Mars. The stratigraphy of the Mawrth Vallis region is generally characterized by an Al-rich unit dominated spectrally by kaolinite and/or montmorillonite, overlying an Fe/Mg-rich unit spectrally composed of nontronite and/or saponite. In order to interpret the potential implications of the formation by weathering of Mawrth Vallis and other similar locations on Mars, we used the reactive transport code CrunchFlow to forward model alteration of (1) nontronite, (2)



nontronite and montmorillonite, (3) nontronite and saponite and (4) saponite to form a weathering profile that can be compared to Mawrth Vallis and other locations on Mars. Modeling results indicate the formation of an Al-rich upper unit formed from Fe/Mg-rich clay minerals under all conditions, which include the four parent material input scenarios as well as wide variations in model inputs such as temperature, flow rate, pH, porosity, solubilities and dissolution kinetics. Therefore, although the presence of clay minerals in general is indicative of aqueous alteration, the Al-rich unit overlying the Fe-Mg-rich unit may be suggestive of further alteration of the Fe/Mg-rich clay minerals. Because saponite weathers more rapidly than nontronite due to its higher solubility and faster dissolution kinetics, the formation of an Al-rich capping unit above saponite generally forms more rapidly than the same Al-rich capping unit above nontronite. An Al-rich capping unit above saponite may therefore be indicative of less water-rock alteration than the same Al-rich capping unit above nontronite. Increasing the flow rate and acidity of the reacting fluids resulted in more gradual transitions between the Fe-Mg-rich parent material and the Al-rich capping unit, whereas slower flow rates and/or decreasing pH values resulted in more abrupt transitions. The transition between the Al-rich capping unit and the parent mineral beneath it may therefore preserve properties of past fluid-flow and solution chemistry. Within the Al-rich capping unit, kaolinite occurred under conditions of greater aqueous alteration, due to either higher flow rates or more acidic conditions, whereas montmorillonite occurred under conditions of slower flow rates and more near-neutral conditions. The results of this study therefore suggest that locations which have experienced the most aqueous alteration would be characterized by a thick Al-rich capping unit composed of kaolinite and/or Fe-oxyhydr(oxide)s, overlying

predominately Fe<sup>3+</sup>-rich smectites (e.g. nontronite). Marwth Vallis, which is composed mostly of nontronite, with areas rich in kaolinite, may therefore represent a location exposed to one of the longest duration of weathering and/or the highest water-rock ratios. Characteristics of weathering profiles should be used to help inform scientists in the selection of the Mars 2020 landing site, to help choose a landing site that encountered liquid water with characteristics most conducive to habitability.

## INTRODUCTION

Observations from the Visible Near Infrared (VNIR) spectrometers Observatoire pour la Mineralogie, l'Eau, les Glaces, et l'Activité (OMEGA) and the Compact Reconnaissance Imaging Spectrometer for Mars (CRISM) have revealed the sequence of Al-rich phyllosilicates mixed with hydrated silica (potentially opal), overlying Fe/Mg clay minerals (spectrally resembling nontronite and/or saponite) in multiple location on the martian surface. This transition in clay mineral chemistry has been observed in the Mawrth Vallis region (Poulet et al., 2005b; Loizeau et al., 2007a; Michalski and Dobrea, 2007; Bishop et al., 2008a; Poulet et al., 2008a; Wray et al., 2008; Loizeau et al., 2010a; Michalski et al., 2010a; Michalski et al., 2010b; Carter et al., 2015), Noachis Terra (Wray et al., 2009), Nili Fossae (Ehlmann et al., 2009b; Carter et al., 2015), Vallis Marineris (Murchie et al., 2009a; Le Deit et al., 2010; Carter et al., 2015) and the Eridiana Basin (Noe Dobrea et al., 2010b). The transition is generally characterized by an Al-rich unit dominated spectrally by kaolinite and/or montmorillonite, overlying a Fe/Mg-rich unit dominated spectrally by nontronite and/or saponite (more nontronite-rich than saponite-rich at Mawrth Vallis) (Poulet et al., 2008b; Noe Dobrea et al., 2010a; Bishop et al., 2013). The collective occurrence of this stratigraphy has been interpreted to result from

wide-spread surficial weathering (Noe Dobrea and Swayze, 2010; Gaudin et al., 2011; Le Deit et al., 2012; Loizeau et al., 2013; Loizeau et al., 2014; Carter et al., 2015).

Large portions of the martian surface (up to one million square km in the greater Mawrth Vallis region (McKeown et al., 2009; Noe Dobrea et al., 2010b)) appear to be covered by this nearly identical stratigraphy and can be explained through wide-spread weathering of the martian surface (Badaut et al., 1985; Noe Dobrea and Swayze, 2010; Gaudin et al., 2011; Le Deit et al., 2012; Loizeau et al., 2013; Loizeau et al., 2014; Carter et al., 2015). Similar transitions in clay mineral chemistry are commonly observed in weathering profiles on Earth, where mafic and ultramafic materials form Fe/Mg-rich clay minerals which are subsequently weathered to an Al-rich clay unit containing Fe-oxyhydroxides and/or oxides (Delvigne et al., 1979; Elias et al., 1981; Nahon et al., 1982; Nahon and Colin, 1982; Colin et al., 1990; Ryan and Huertas, 2009; Yongue-Fouateu et al., 2009; Gaudin et al., 2011; Le Deit et al., 2012). Kaolinite is favored under acidic, well-drained conditions, whereas montmorillonite is dominant under near-neutral pH ranges and in environments with a lower Mean Annual Precipitation (MAP) (Allen and Scheid, 1946; Sherman, 1952; Barshad, 1966; Baker and Strawn, 2014). In addition to the observed chemical transition from Fe/Mg-rich to Al-rich phyllosilicates, the mineralogical transition from smectite to kaolinite caused by weathering has also been extensively documented (Craig and Loughnan, 1964; Delvigne et al., 1979; Elias et al., 1981; Herbillon, 1981; Nahon et al., 1982; Nahon and Colin, 1982; Colin et al., 1990; White, 2002; Fisher and Ryan, 2006; Ryan and Huertas, 2009; Yongue-Fouateu et al., 2009; Gaudin et al., 2011; Hausrath et al., 2011a). The weathering of Al-containing nontronite has been specifically suggested to lead to the precipitation of kaolinite and Fe-

oxides - although these experiments were conducted under acidic-hydrothermal conditions, the authors believed their results are applicable to weathering environments (Delvaux et al., 1989). Observations of the Mawrth Vallis region and other locations on the martian surface therefore suggest similar characteristics to weathering environments on Earth.

## BACKGROUND

Remote spectral observations have revealed phyllosilicate minerals at many locations on the martian surface (Bibring et al., 2005b; Poulet et al., 2005b; Bibring et al., 2006; Bishop et al., 2008a; Ehlmann et al., 2008a; Mustard et al., 2008a; Ehlmann et al., 2009b; Murchie et al., 2009a; Wray et al., 2009; Michalski et al., 2010a; Michalski et al., 2010b; Milliken et al., 2010b; Noe Dobrea et al., 2010b), which is significant as these minerals require liquid water to precipitate. Although liquid water is no longer present at the martian surface, the occurrence of minerals that require aqueous conditions to precipitate suggests that liquid water once occurred at or close to the martian surface. Therefore, the search for habitable environments is closely linked to the investigation of aqueous minerals on Mars. Phyllosilicates, in addition provide evidence of past environments in which the activity and pH of water may have been suitable for the presence of life (Poulet et al., 2005b; Murchie et al., 2009a; Grotzinger et al., 2014; Vaniman et al., 2014; Grotzinger et al., 2015). However, the mineralogy of these phyllosilicates is heterogeneous both laterally and vertically.

These heterogeneities or transitions in clay mineralogy may provide further evidence of the past aqueous conditions that once occurred at or near the martian surface. When rocks, sediment or soils interact with aqueous solutions, changes in mineralogy and

chemistry may occur with depth, ultimately forming weathering profiles. Weathering profiles can preserve the characteristics of the interacting solution and therefore further constrain the duration and conditions of aqueous alteration occurring at or near the martian surface. Weathering profiles consist of several components all of which are the direct result of the interacting solution and duration of alteration. The shape of the reaction front, or transition between the secondary minerals and the parental rock, constrains the relationship between dissolution and transport (Lichtner, 1988; White, 2002; Brantley, 2008; Brantley and White, 2009; Navarre-Sitchler et al., 2009; Maher, 2010; Navarre-Sitchler et al., 2011; Hausrath and Olsen, 2013). The depth of the reaction front results from aspects such as the duration of alteration, flow rate, and solubilities of the minerals (White et al., 2001; Sak et al., 2004; Fletcher et al., 2006; Hausrath et al., 2008b; Brantley and White, 2009). Although phyllosilicates provide evidence of near-neutral aqueous conditions, transitions in clay mineralogy (e.g. weathering) provide additional constraints on the duration and characteristics of alteration.

Transitions in clay mineral chemistry have been observed on Mars, including the Mawrth Vallis region (Loizeau et al., 2007a; Poulet et al., 2008b; Wray et al., 2008; Michalski et al., 2010b; Noe Dobrea et al., 2010b; Le Deit et al., 2012; Loizeau et al., 2012; Carter et al., 2013; Loizeau et al., 2013) and Nili Fossae (Ehlmann et al., 2009b; Murchie et al., 2009a; Le Deit et al., 2010; Gaudin et al., 2011; Carter et al., 2013; Carter et al., 2015) (Figure 13). Of these locations, the Mawrth Vallis region represents one of the largest exposures of putative weathering on Mars, encompassing an area of approximately one million square km (McKeown et al., 2009). Past work by Poulet et al., (2008b) and Vaviano and Moersch (2013), suggests that the upper Al-rich unit

contains between 20 to 40 percent phyllosilicates, and that the Fe, Mg-rich unit is composed of approximately 20 to 65 percent clay minerals (Poulet et al., 2008a; Viviano and Moersch, 2013). Another phase commonly detected in the Mawrth Vallis stratigraphy is Fe-oxyhydroxides and/or oxides (Loizeau et al., 2007a; Poulet et al., 2008a; Wray et al., 2008), which may potentially be more abundant in the Al-rich unit (McKeown et al., 2009), similar to weathered minerals in terrestrial environments on Earth (Birkeland, 1984).

In order to interpret these large potential weathering profiles, we used the reactive transport code, CrunchFlow, to forward model four alteration scenarios of (1) nontronite, (2) nontronite and montmorillonite, (3) nontronite and saponite and (4) saponite systems under soil-forming conditions to form a putative alteration front, such as that potentially observed in Mawrth Vallis and other locations on the martian surface. Result of these models suggest that pedogenic alteration of Fe/Mg-rich clay minerals is a viable mechanism in the formation of the observed transitions in clay mineral chemistry detected at or near the martian surface, with changes in the mineralogy and shape of the profile constraining aspects of the alteration conditions.

## METHODS

Mawrth Vallis, which we are interpreting using reactive transport modeling, is characterized by Al-rich clay minerals (potentially kaolinite and montmorillonite) mixed with hydrated silica (potentially opal), underlain by an Fe, Mg-rich smectite (spectrally more nontronite-rich than saponite-rich) (Michalski and Noe Dobrea, 2007; Bishop et al., 2008b; Wray et al., 2008; Bishop et al., 2010; Michalski et al., 2010c; Noe Dobrea et al., 2010b; Michalski et al., 2013). Although different formation scenarios are possible, this

sequence may represent a weathering front (McKeown et al., 2009; Michalski et al., 2010b; Gainey et al., 2014) in which Fe/Mg-rich smectites were altered to form Al-rich materials by leaching of Mg and Si from the system, followed by the reprecipitation Al-rich clays. In Mawrth Vallis, the thickness of the Al-rich layer is 30 to 60 m (Noe Dobrea et al., 2010a); the Fe/Mg rich smectite beneath it is at least several 100 m thick, as the bottom of the unit remains unexposed to remote observations. Here we modeled formation of a Mawrth Vallis-like weathering profile using the reactive transport code CrunchFlow to interpret the implications for the past climate and aqueous history of Mars.

### Reactive Transport Modeling

We used the reactive transport code, CrunchFlow (Steeffel and Maher, 2009), to forward model alteration of Mawrth Vallis under a variety of scenarios. CrunchFlow allows fully kinetic mineral dissolution and precipitation reactions; it incorporates advective, diffusive, or dispersive flow, including unsaturated transport with gas-aqueous exchange; and it contains reaction-induced porosity and permeability feedback. CrunchFlow also captures adsorption, after Dzombak and Morel (1990) with either a double layer or non-electrostatic model being possible. CrunchFlow utilizes a Global Implicit Transport Approach (GIMRT) that solves transport and multicomponent reactions concurrently (Steeffel and Lasaga, 1994; Steefel and MacQuarrie, 1996). After each time step (if convergence was achieved), CrunchFlow calculates the mineral volumes, surface area of minerals present and porosity. Changes in surface area due to mineral precipitation and/or dissolution are updated using a shrinking sphere model.

It has been previously been shown that laboratory rates generally exceed those extrapolated from field observations (Schnoor, 1990; Swoboda-Colberg and Drever, 1993; Velbel, 1993a; Drever, 1997a; Langmuir, 1997; White, 2002; Ganor et al., 2005; Brantley, 2008). This discrepancy results from multiple factors likely including distance from equilibrium, surface coatings and the surface area that interacts with the reacting fluid (Schnoor, 1990; Swoboda-Colberg and Drever, 1993; Velbel, 1993a; Drever, 1997a; Langmuir, 1997; White, 2002; Ganor et al., 2005; Brantley, 2008). CrunchFlow is additionally able to account for differences in solution chemistry between laboratory experiments and field environments (Steeffel, 2009a). CrunchFlow uses Transition State Theory (Lasaga, 1984), to model dissolution under near equilibrium conditions, which are likely much more representative of field conditions than far from equilibrium dissolution rate experiments.

CrunchFlow has been previously used to explore the physical and chemical discrepancies between laboratory and field-based rates and was shown to accurately model weathering processes and the precipitation of clay minerals with extreme accuracy (Maher et al., 2009). In addition, CrunchFlow has been successfully used to model weathering under a variety of conditions relevant to potential weathering of Mawrth Vallis on Mars, including weathering of terrestrial basaltic materials (Hausrath et al., 2008b; Navarre-Sitchler et al., 2009; Navarre-Sitchler et al., 2011), ocean floor sediments (Maher et al., 2006) as well as martian rocks (Hausrath et al., 2008; Hausrath and Olsen, 2013; Adcock et al., in revision).

### Model inputs



Because the stratigraphy at Mawrth Vallis is not fully constrained, we included four scenarios consistent with orbital observations of Mawrth Vallis and other clay-rich locations such as Nili Fossae: (1) alteration of a pure nontronite parent material (2) alteration of a mixed clay unit parent material consisting of nontronite and montmorillonite, (3) alteration of a parent material consisting of mixed nontronite and saponite and (4) alteration of a parent material consisting of pure saponite. For scenario 1, the starting parent material consisted of 65% nontronite, and 35% porosity. For scenario 2, the starting parent material consisted of 55% nontronite, 35% porosity, and 10% montmorillonite, which is an amount of montmorillonite that would likely be undetected by orbital remote observations. In addition, Scenario 2 is consistent with terrestrial observations in which weathering products may contain both nontronite and montmorillonite in a single unit (Claridge and Campbell, 1984; Gaudin et al., 2004; Gaudin et al., 2005). Scenario 3 is a mixture of equal proportions of nontronite (32.5%) and saponite (32.5%) with 35% porosity, and is based on remote spectral observations that the Fe/Mg clay minerals on Mars appear to consist of both nontronite and saponite (Ehlmann et al., 2008a; Mustard et al., 2008a). Similarly, scenario 4 consists of 65% saponite and 35% porosity, which tests the weathering behavior of pure saponite, widespread on the martian surface, and which may also be an initial phase in the weathering of basaltic and serpentine-bearing materials on Earth (Gaudin et al., 2011).

The simulated weathering profile consisted of a one-dimensional, 1000 cell column, representing a 100 meter stratigraphic column of phyllosilicate-rich rock, which was divided into 0.1 meter sub units. The model includes a flux boundary condition at the base of the profile, and a dirichlet boundary for aqueous and gaseous species at the

parent rock-atmosphere interface. The reactive solutions flow and diffuse from the top of the column to the base.

Due to the limited data constraining important characteristics of the Mawrth Vallis deposits such as porosity and tortuosity, these parameters were estimated from spectral observations and terrestrial analogs. Spectral deconvolution suggests the mineralogy of the Mawrth Vallis region is 40-65% phyllosilicates (Poulet et al., 2008a; Viviano and Moersch, 2013), which corresponds to either a bedded or laminated mud if nonindurated and a mudstone/mudshale if indurated (assuming the small grain size associated with clay minerals) (Boggs, 1995). Here, we used a quantitative evaluation of porosity in argillaceous sediments (Dzevanishir et al., 1986) to estimate the porosity of the Mawrth Vallis region. This model has been shown to accurately determine porosity of argillaceous sediments over a range of depths and time on Earth (Dzevanishir et al., 1986). The equation determining porosity in buried argillaceous sediments is as follows:

$$\phi = \phi_0 \exp[-0.014(13.3 \log A - 83.25 \log R + 2.79) \times 10^{-3} D] \quad (4)$$

where  $\phi$  is the porosity of the buried sediment (in percent),  $\phi_0$  is the initial porosity of the argillaceous sediment (in percent),  $A$  is the age in millions of years,  $R$  is the proportion of the clay unit(s) to the total thickness of the column, and  $D$  is the depth of burial in meters. In order to estimate the largest possible range of porosities for Mawrth Vallis, we use an initial porosity of 0.40 to 0.70  $\phi$  which is within the range of unconsolidated clays on Earth (Freeze and Cherry, 1979). We used the oldest (4.0Ga) and youngest (3.6Ga) published ages for Mawrth Vallis based on crater-counting, as well as including an age of 500Ma to represent the discontinuation of weathering and pedogenic processes occurring in the Mawrth Vallis region (Loizeau et al., 2012). We make the assumption that the

value of  $R$  is between 0.40 and 0.65 based on spectral deconvolution models (Poulet et al., 2008a; Viviano and Moersch, 2013). Depth of burial was constrained to the upper 100 meters, as the alteration front does not extent past 60 meters (e.g. the thickness of the Al-rich unit), and we are assuming minimal physical erosion (Golombek et al., 2006; Golombek et al., 2012). Using this broad range of input values, the porosity of the upper 100 meters ranged from 0.36 to 0.70  $\phi$ , and models were run and evaluated over this range to determine the effect of porosity on the modeled system.

Lithification would likely decrease this porosity, but we do not expect lithification near the surface of Mars. Similarly, the porosity range from weathering differs slightly (9.9-56.2%) (Valeton and Beißner, 1986), but our modeled range incorporates much of this variation, and our final porosity (35%) is a reasonably representative value of lithified mudstones, weathered soils, and surface sediments.

Similarly, the tortuosity of the Mawrth Vallis deposits was estimated assuming that the sedimentary material is mudstone or shale (i.e. composed of 33-65 percent clay-sized constituents which are bedded or laminated, respectively) (Boggs, 1995). Tortuosity as used in CrunchFlow is the relationship between the effective diffusion and the diffusion coefficient of pure water shown in the following equation (Steefel, 2009b):

$$\tau = \frac{D_{PM}}{D_W} \quad (5)$$

where  $\tau$  is tortuosity as used in CrunchFlow,  $D_W$  is the diffusion coefficient in pure water and  $D_{PM}$  is the effective diffusion coefficient in a porous medium (Steefel, 2009b).

Previous work by Barone et al. (1990; 1992) measured the tortuosity of mudstone and shale as 0.15 – 0.20 and Sato (1997) proposed values of 0.095 – 0.108. Here we chose to

use the range of values (0.15 to 0.20) from Barone et al. (1990; 1992) to evaluate the effect of tortuosity as pedogenic clays would likely have formed at or close to the martian surface and would have not experienced significant lithification without deep burial, which would result in tortuosities more similar to those presented by Sato (1997). Varying the tortuosity over this range had minimal effect on model results, and a tortuosity of 0.175 was used in final models.

Within CrunchFlow, dissolution rates must be normalized to mineral surface areas, generally using the Brunauer-Emmett-Teller (BET) method. However, clay minerals have been shown to preferentially dissolve along the clay mineral edges rather than the basal plane and therefore BET surface areas may not accurately represent the reactive surface area (Bickmore et al., 2001). Clay mineral dissolution rates are often normalized to only a fraction of the BET surface area to represent the surface area of the mineral edge. We have therefore normalized the dissolution rates of the clay minerals used in this study to the reactive edge surface area.

Previous work by Dogan et al. (2007a) documented that naturally occurring montmorillonite has a BET surface area between 41.0 – 65.3 m<sup>2</sup>/g, with nontronite having a BET surface area of 10.6 - 52.8 m<sup>2</sup>/g. Similarly, Gainey et al. (2014) measured a BET surface area of 64.2 m<sup>2</sup>/g for nontronite (Gainey et al., 2014). Previous work has suggested a reactive edge surface area of 4.9 m<sup>2</sup>/g for smectites, which was measured by Atomic Force Microscopy (AFM) (Metz et al., 2005b), and therefore this value was used as the reactive mineral surface area in this study for all smectites. Published BET surface areas for kaolinite range from 8.16 (Huertas et al., 1999b) to 24 (m<sup>2</sup>/g) (Madsen, 1977), with a reactive edge-surface area comprising only 18.2-30.0 percent of the total surface

area (Bickmore et al., 2002). Therefore, the total BET surface area would be reduced to 1.49 to 7.20 m<sup>2</sup>/g for the edge-surface area (i.e. 18.2 to 30.0 percent of the BET surface area stated above). A surface area of 3.81 m<sup>2</sup>/g was therefore used for kaolinite in our models, as this is the weighted average of the edge surface areas from Bickmore et al. (2002), which is in the range of previously determined edge-surface areas for kaolinite.

However, measured mineral surface areas may not accurately represent the area of the mineral in contact with the reactive fluid, which is considered one of the largest sources of uncertainty in terrestrial dissolution rates measured in the field (White, 2002). Previous work by Velbel (1993a) indicates that the mineral surface in contact with the weathering fluid in natural environments may be one to three orders of magnitude less than the total reactive surface area, resulting from a blocking effect by adjacent mineral grains. To account for this effect, we decreased the reactive surface area by two orders of magnitude in our final models (Table 2). To test the effect of varying mineral surface area on model results we ran models over a range of surface areas ( $\pm$  one order of magnitude). The change in surface area had an effect on the depth of the weathering profiles, but the overall results were the same.

Mineral molar volumes were sourced from Marini (2006), and are presented in Table 2. Due to the charge imbalance in smectites, cations, water and organic solvents can absorb onto the interlayer of these minerals, which can significantly change the mineral volume. Mineral volumes for the expanded form of the clay minerals were therefore used as this would be expected in contact with aqueous solutions. Mg<sup>2+</sup> was used as the interlayer cation for all smectites within the model, as data collected from

Sample Analysis at Mars (SAM) on board the *Curiosity* rover suggest interlayer cations with high hydration-energy at Gale Crater, e.g.  $Mg^{2+}$  (Vaniman et al., 2014).

### Mineral Dissolution Kinetics

In order to model relevant reactions in the Mawrth Vallis region, dissolution and precipitation rates for the initial and precipitated minerals must be included. The dissolution rates of many phyllosilicates have been previously measured (Huertas et al., 1999b; Cama et al., 2000; Metz et al., 2005a; Golubev et al., 2006; Rozalén et al., 2008a; Yang and Steefel, 2008; Marty et al., 2011b; Gainey et al., 2014) and are often expressed in the following form, where the neutral mechanism is not always included:

$$R = k_{H^+} \cdot a_{H^+}^n + k_N + k_{OH^-} \cdot a_{OH^-}^m \quad (6)$$

where  $R$  is the far from equilibrium rate ( $\text{mol m}^{-2} \text{s}^{-1}$ ),  $k_{H^+}$ ,  $k_N$  and  $k_{OH^-}$  are the proton-promoted, neutral and hydroxide-promoted dissolution rate constants, respectively,  $a_{H^+}$  and  $a_{OH^-}$  are the activity of the designated species, and  $n$  and  $m$  are the reaction orders with respect to those species.

Dissolution rate laws for the minerals modeled used in this study were compiled from the literature (Figure 14 and Table 2). The dissolution rate law for kaolinite used was from Brantley (2008), based on data from Carroll-Webb and Walther (1988). This kaolinite rate law was chosen because it used data conducted over a full pH range, and lies well within the range of other measured rates (see Supplementary Online Materials (SOM)). The dissolution rate law for montmorillonite was sourced from Rozalén et al. (2008a) because these rates were derived from both batch and flow through reactors, over a broad pH range, and this rate law falls between other measured values (SOM). The

acidic and neutral rate constants for nontronite dissolution were sourced from Gainey et al. (2014), as this is currently the only study measuring nontronite dissolution rates, with the neutral rate constant sourced from the dissolution rate above pH 6, which behaved differently from the proton-promoted dissolution rates and is therefore likely representative of the near-neutral dissolution rates of nontronite. A hydroxyl-promoted rate constant for the dissolution of an Fe-Mg-bearing smectite from Palandri and Kharaka (2004) (based on data from Novak and Cipel, (1978), Altaner (1986), Cama et al., (1994), Bauer and Berger, (1998) and Cama et al., (2000)) was combined with the acidic and neutral mechanisms from Gainey et al. (2014) to provide a rate law valid over a broad pH range. Dissolution rate constants for saponite over a broad pH range (Brigatti et al., 1999) were used to calculate dissolution rates through the initial rate method (Rimstidt and Newcomb, 1993), which were normalized to the surface area of a natural saponite (161 m<sup>2</sup>/g) (Vicente et al., 1996), and used to calculate a dissolution rate law (Table 2 and Figure S71).

A dissolution rate law for goethite, which was allowed to precipitate within the model but was not present initially, was also from Palandri and Kharaka (2004) based on data from Ruan and Gilkes (1996). All minerals allowed to dissolve were also allowed to precipitate, and dissolution and precipitation were calculated using transition state theory (TST) (Lasaga, 1984) within CrunchFlow.

### Solubilities

Here, we evaluated both solubilities calculated from thermodynamic data and experimentally determined solubilities for naturally occurring triple-layer clays (SOM), and during our modeling, we varied the input solubilities over the full range of values

observed (SOM). The thermodynamic properties of clay minerals such as smectites are difficult to measure due to their highly variable chemical compositions and crystallinities (Tardy and Fritz, 1981; May et al., 1986a; Sposito, 1986; Drever, 1997a; Langmuir, 1997). It has been previously shown that the solubility of clay minerals is dependent on the octahedral cation (most naturally occurring smectites may have several cations within the octahedral layer), with solubility decreasing in the following order:  $Mg > Fe^{2+} > Al > Fe^{3+}$  (Tardy and Garrels, 1974; Tardy and Fritz, 1981). Several methods of estimating the thermodynamic properties of clay minerals have been established (Karpov and Kashik, 1968; Eugster and Chou, 1973; Tardy and Garrels, 1974; Nriagu, 1975; Mattigod and Sposito, 1978; Tardy and Fritz, 1981). However, when calculating the thermodynamic properties of poorly crystalline clay minerals (e.g. smectites) from well-crystallized phyllosilicates (e.g. micas), the solubility products are low and therefore unrealistically stable (Table S15 and S16) (Tardy and Fritz, 1981). Fine-grained, poorly crystalline materials are less stable than their well-crystalline ordered counterparts resulting from higher surface-energy and decreased order (Sposito, 1986). Therefore, Tardy and Fritz (1981) suggest a correction is necessary when extrapolating the solubility of well crystalline phyllosilicates to poorly crystalline clay minerals in natural environments (Tardy and Fritz, 1981). Varying the solubilities over this range shifted the positions of the fronts and the abundance of Al-rich clay in the upper unit, but did not change the overall observations. In our final models, therefore, we used solubilities from Tardy and Fritz (1981) as indicated in Table 2, which incorporate the effect of the composition of the octahedral layer, the exchangeable cation, and a factor accounting for less crystalline natural clay minerals.



The clay mineral kaolinite has significantly less chemical variation and is generally more crystalline than smectites (Moore and Reynolds, 1989) and we therefore chose to use the solubility of kaolinite from the Lawrence Livermore National Laboratory database (Thermodynamic data from the database based on Lawrence Livermore National Laboratory thermodynamic modeling (Johnson et al., 2000)), which is in general agreement with the experimental work of Yang and Steefel (2008).

### Temperature and Solution Flow

In terrestrial environments the processes of laterization and the transition from 2:1 to 1:1 clay minerals generally requires a hydrologic cycle (e.g. the recycling of liquid water). Therefore, the transitions in clay mineral chemistry observed in the Mawrth Vallis region and other locations on the martian surface may be suggestive of an ancient hydrologic cycle. A hydrologic cycle is also supported by an abundance of martian geomorphic features, such as the wide-spread distribution of Noachian-aged valley systems and Amazonian-aged glacial features (Baker et al., 1991; Baker, 2001). The formation of these valleys and glacial features likely required a planet-wide and repetitive process, such as a hydrologic cycle resembling that on Earth (Baker et al., 1991; Moore et al., 1995). It is estimated the formation of the valleys on Alba Patera, Mars required a column of water approximately 250 km high, strongly supporting the dynamic cycling of martian water (Baker et al., 1991).

Models were run at the lowest temperature under which natural kaolinite formation has been observed on Earth, 5°C (Longstaffe, 1984). Kaolinitic, lateritic and bauxitic weathering has been generally associated with warm, wet conditions - however, it is not restricted to those environments (Bird and Chivas, 1988; Taylor et al., 1992).

Previous work by Taylor et al. (1992) suggests that lateritic weathering may also occur in wet cool to cold environments. This is further supported by the work of Bird and Chivas (1988), which reported that kaolinite could precipitate under cool temperate conditions based on the  $\delta D$  and  $\delta^{18}O$  of pedogenic kaolinites. The  $\delta D$  and  $\delta^{18}O$  values from Bird and Chivas (1988) are indicative of meteoric water of sub-polar to polar regions, potentially sourced from glacial melt waters. They suggest that high (tropical) temperatures are therefore not a pre-requisite for kaolinitic precipitation, but instead that thick kaolinitic profiles may develop from (1) high rainfall, effective leaching and subdued topography (low levels of relief to prevent the erosion of the profile) and (2) weathering time scales on the order of 0.01 to 10 Ma (Bird and Chivas, 1988).

The reacting solution contacting the parent material was a low ionic strength solution with the initial pH adjusted for each model over a range of 4 to 6. The partial pressures for  $O_2(g)$  and  $CO_2(g)$  were set to current martian atmospheric conditions. A final flow rate of 0.1 m per year was used, because that represents cold desert-like conditions on Earth, which are likely most relevant to Mars. However, to test the effect of flow rate we varied it based on observed clay mineralogy on Earth. On Earth smectite formation is favored when the Mean Annual Precipitation (MAP) is below 100 cm (Sherman, 1952; Birkeland, 1984). Kaolinite and halloysite are present over an array of conditions, but become significant above 50 cm and dominate above 100 cm (Barshad, 1966), and Fe and Al-oxhydroxides and/or oxides begin to form when the MAP is above 100 cm, and become dominant above 200 cm (Birkeland, 1984). Therefore, since the upper Al-rich unit of Mawrth Vallis is montmorillonite-rich (Noe Dobrea et al., 2010a) and may also be rich in kaolinite at other locations, we varied the flow rate between 10

and 75 cm per year (Barshad, 1966; Birkeland, 1984). Increasing flow rates were found to result in an increasing depth of the weathering profile, but the overall trend remained unaltered, justifying our use of cold desert-like flow rates.

## RESULTS AND DISCUSSION

### Results

As fluids interact with rock, sediment and/or soils, this can result in alterations to the chemistry and mineralogy with depth, which may produce weathering profiles (Brimhall and Dietrich, 1987; Anderson et al., 1997; Anderson et al., 2000; Anderson et al., 2002; White, 2002; Maher et al., 2006; Hausrath et al., 2008b; Brantley and White, 2009; Maher et al., 2009; Navarre-Sitchler et al., 2009) that can preserve the properties and the duration of the fluid-rock interaction (Maher et al., 2006; Hausrath et al., 2008b; Brantley and White, 2009; Maher et al., 2009; Maher, 2010; Navarre-Sitchler et al., 2011; Hausrath and Olsen, 2013). As discussed above, secondary minerals can record the environment of formation, with Fe and Al-oxyhydroxides and/or oxides representing highly leach and potentially acidic conditions (Birkeland, 1984; Moore and Reynolds, 1989; Gaudin et al., 2011), kaolinite indicating acidic and less leached profiles (Birkeland, 1984; Moore and Reynolds, 1989) and smectites representing near-neutral pH and poorly drained sediments and/or soils (Allen and Scheid, 1946; Birkeland, 1984; Moore and Reynolds, 1989; Gaudin et al., 2011). The shape of the reaction front or transition between the secondary minerals and the parent rock constrains the relationship between dissolution and transport (Lichtner, 1988; White, 2002). The depth of the reaction front results from the duration of weathering and fluid flow rates as well as the

mineral solubilities (White, 2002). Below we describe each of these aspects observed in our models.

### Mineralogy

An Al-rich capping unit that contained goethite formed under all scenarios, regardless of the initial input conditions used, including the initial parent minerals, solubilities, thermodynamics, pH and flow rate (Figure 15). The exact mineralogy of the Al-rich capping unit (percentages of kaolinite, montmorillonite and goethite, as well as the remaining parent smectite) differed with differing input conditions. The amount of Fe in the Al-rich capping unit was affected by the amount of Al and Fe in the parent unit (i.e. when more Fe was present, more goethite formed, whereas more Al produced a larger volume of Al-bearing clay minerals). Lower pH models (e.g. below 6) generally precipitated more kaolinite than their higher pH (e.g. 6) counterparts (Figure 16), which contained more montmorillonite, although increasing the amount of saponite in the parent material also resulted in more montmorillonite in the capping unit. Increasing the duration of weathering resulted in the increased thickness of the secondary Al-rich capping unit, and under very long durations under near-neutral conditions (e.g. pH 6) montmorillonite dissolved and was replaced by kaolinite, which was hastened under more acidic conditions. Therefore, kaolinite above nontronite is suggestive of long water-rock interactions. The ratio of kaolinite to montmorillonite also increased when the flow rate was increased from 0.1 m/y to 0.75 m/y.

### Advance Distance

The advance distance, generally considered to be the distance from the original land surface to the reaction front of weathering profiles, has been shown to record factors such as the duration of weathering, flow rate and solubilities (White, 2002; Sak et al., 2004; Fletcher et al., 2006; Hausrath et al., 2008b; Brantley and White, 2009). The advance distance in this study is also the thickness of the secondary Al-rich clay minerals and Fe-oxhydroxides and/or oxides formed, and was affected by the dissolution rates and solubilities of the parent minerals, the pH, temperature, and flow rates.

The parent material had a significant influence on the advance distance. The thickness of the secondary capping unit was not as thick when nontronite was the parent material (scenario 1 – Figure 15A) than saponite (scenario 4 – Figure 15D). In addition, the thickness of the capping unit increased when Al was present in the parent material (Figure 15B). These results are not unexpected - saponite was the most soluble and had the fastest dissolution rate of all the clay minerals used in this study, and therefore we would expect the advance rate to be fastest. In addition, the enhancement of dissolution when Al was present may be the result of the common ion effect where more soluble minerals can be replaced by less soluble minerals. In all scenarios decreasing the pH generally resulted in an increased advance distance or a depletion of Si within the Al-rich unit. When nontronite is the parental material (scenarios 1 and 2) the thickness of the kaolinite layer is greater under more acidic conditions (e.g. < pH 5), whereas the thickness of the montmorillonite unit is greater when the reacting fluid has higher pH (e.g. pH 6). Increasing the duration of time, flow rate, and temperature each increased the depth of the alteration front, as also expected.

#### *Shape of the reaction front*

In addition to the distance to the reaction front recording alteration conditions, the shape of the alteration front(s) also records weathering conditions, generally the interaction between dissolution and transport rates. When dissolution is faster than transport the alteration fronts are abrupt and when transport exceeds dissolution fronts are more gradual (Lichtner, 1988; White, 2002; Brantley, 2008; Brantley and White, 2009; Navarre-Sitchler et al., 2009; Maher, 2010; Navarre-Sitchler et al., 2011; Hausrath and Olsen, 2013). Here, the reaction front occurs between the secondary, Al-rich clay minerals (including Fe-oxyhydroxides and/or oxides) and the parent smectites, as well as between the two secondary Al-bearing clay minerals in the capping unit (Figure 15 and 16).

The transition between the parent material and the secondary Al-rich layer was always abrupt (Figure 15) (potentially only a few meters thick and therefore difficult to detect with the resolution of several of the current instruments onboard orbiters (Michalski et al., 2010b)), which may be partly due to the lower porosity of the parent material, similar to observations of low porosity basalt clasts on Earth (Hausrath et al., 2008b; Navarre-Sitchler et al., 2009; Navarre-Sitchler et al., 2011). Very acidic conditions (e.g. pH = 4) resulted in most abrupt transitions between the parent material and the Al-rich capping unit. More neutral conditions (e.g. pH = 5 and 6), although they still resulted in quite abrupt transitions, were more gradual than the more acidic scenarios. The transition between the two units remained sharp regardless of time and temperature. Increasing the flow rate and significantly increasing the surface area resulted in more gradual transitions.

In contrast, reaction fronts within the Al-rich capping unit between kaolinite and montmorillonite, when they occurred, were less abrupt (SOM). This is likely the result of the slower dissolution rates of montmorillonite and kaolinite relative to nontronite and saponite, as well as the increased porosity, allowing transport to be faster relative to dissolution (Lichtner, 1988; White, 2002; Hausrath et al., 2008b; Brantley and White, 2009; Navarre-Sitchler et al., 2009; Navarre-Sitchler et al., 2011; Hausrath and Olsen, 2013). Increasing the flow rate made the transition more gradual. The transition between kaolinite and montmorillonite was more evident when Al was more abundant in the parent material, which produced more Al-rich clays in the secondary layer (Scenario 2).

#### *Comparison to observations from Mars*

The results of this work suggest that the Al-rich capping unit observed in the Mawrth Vallis region can form from weathering of the Fe/Mg-rich underlying clay minerals – this result formed under all of the conditions in all of the models conducted in this study. This is supported by terrestrial observations as the chemical progression from Fe/Mg-rich to Al-rich clay minerals is common on Earth (Delvigne et al., 1979; Elias et al., 1981; Nahon et al., 1982; Nahon and Colin, 1982; Colin et al., 1990; Ryan and Huertas, 2009; Yongue-Fouateu et al., 2009; Gaudin et al., 2011; Le Deit et al., 2012). The mineralogical transition from smectite to kaolinite through weathering has also been extensively documented (Craig and Loughnan, 1964; Delvigne et al., 1979; Elias et al., 1981; Herbillon, 1981; Nahon et al., 1982; Nahon and Colin, 1982; White, 2002; Fisher and Ryan, 2006; Ryan and Huertas, 2009; Yongue-Fouateu et al., 2009; Gaudin et al., 2011; Hausrath et al., 2011a). The result of these models, which replicate observations of

Mawrth Vallis and other regions on Mars, are therefore also consistent with terrestrial observations of chemical weathering.

An Al-rich capping unit above Fe/Mg-rich smectites is therefore consistent with more aqueous alteration than Fe/Mg-clay minerals alone (i.e. without the Al-rich capping unit). Because kaolinite formed under acidic conditions and higher flow rates, and montmorillonite under near-neutral conditions and slower flow rates, the results of this study also suggest that a thick capping unit of kaolinite may imply greater weathering of the Fe/Mg-rich underlying unit than a thick capping unit of montmorillonite. This is in agreement with terrestrial observations in which kaolinite is found in environments with higher annual precipitation than montmorillonite (Sherman, 1952; Barshad, 1966), due to the loss of SiO<sub>2</sub> leached from the system (Hay and Jones, 1972). Ultimately, the formation of a thick Al-rich capping unit is the direct result of either increased temperature, increased mean annual precipitation (flow in the models), or an increased duration of exposure to aqueous alteration (Sherman, 1952; Barshad, 1966; Hay and Jones, 1972).

The formation of an Al-rich capping unit above nontronite may also be suggestive of greater water-rock alteration than the same Al-rich capping unit overlying saponite. Our results suggest that an Al-rich capping unit will form faster from a saponitic parent material rather than from nontronite (except under extremely acidic conditions where the Mg in saponite acts as a pH buffer). When the parent material consists of both nontronite and saponite, exposure to weathering will increase the Fe to Mg ratio of the underlying unit, as the Mg-rich saponite is more rapidly removed from the system, and therefore a progression from saponite to nontronite may be suggestive of weathering. This is



supported by previous work which has shown that the dissolution of saponite in laboratory experiments is significantly faster than that of nontronite (Brigatti et al., 1999; Gainey et al., 2014) (Figure 14). In addition, the solubility product of saponite has been shown to be significantly higher than that of nontronite under both calculated values from thermodynamic data and experimentally determined solubilities for naturally occurring saponites (SOM) natural conditions (e.g. observed) and in calculated values (Tardy and Fritz, 1981). Therefore, weathering profiles formed in locations rich in saponite may indicate less aqueous alteration than weathering profiles formed from nontronite.

Aqueous alteration, indicating potentially habitable environments, is an important criteria in the future selection of the Mars 2020 landing site. Previous studies have suggested that the stratigraphy in the Mawrth Vallis region may have formed through pedogenic processes (McKeown et al., 2009; Altheide et al., 2010; Michalski et al., 2010b; Noe Dobrea et al., 2010a; Noe Dobrea and Swayze, 2010; Le Deit et al., 2012; Gainey et al., 2014; Carter et al., 2015). Similar stratigraphy has been identified in multiple locations on the martian surface (Poulet et al., 2005b; Loizeau et al., 2007a; Michalski and Dobrea, 2007; Bishop et al., 2008a; Wray et al., 2008; Ehlmann et al., 2009b; Murchie et al., 2009a; Le Deit et al., 2010; Loizeau et al., 2010a; Michalski et al., 2010b; Noe Dobrea et al., 2010a; Carter et al., 2013; Carter et al., 2015). The results of this study suggest that locations which have experienced the most aqueous alteration would be characterized by a thick Al-rich capping unit rich in kaolinite with Fe-oxyhydroxides and/or oxides, overlying predominantly Ferric-rich smectites (e.g. nontronite). Therefore, Marwth Vallis, which is more nontronite-rich, and more kaolinite-rich than other locations on Mars containing this weathering sequence, may currently

represent the location that was exposed to the longest duration and/or the highest water-rock ratio and strongly suggests the presence of a hydrology cycle.

## CONCLUSIONS

Although evidence exists for ancient liquid water on Mars, the duration and characteristics of that water remain under-constrained. The characteristics of liquid water can be preserved in its interactions with rock, soil and/or sediment, forming weathering profiles. Here we use reactive transport modeling to interpret the implications of formation by weathering of the profiles observed in the Mawrth Vallis region and other locations abundant in the southern highlands of Mars.

Our models suggest that the Al-rich capping unit observed in the Mawrth Vallis region likely formed from the weathering of the underlying clay minerals, analogous to weathering profiles on Earth. The transition (e.g. Fe/Mg-rich clay underlying Al-rich phyllosilicates) occurred under all conditions, including all input scenarios and varying pH, time, temperature, and flow rates. Kaolinite was favored under acidic conditions when the parent material was nontronite or nontronite with montmorillonite. Montmorillonite was favored under near-neutral conditions or when saponite was present in the parent material. In all cases Fe-oxyhydroxides were present in the Al-rich unit.

These models suggest that the superimposed Al-rich unit would require additional alteration of the underlying clay minerals, similar to soils on Earth. The formation of an Al-rich capping unit above saponite generally occurs more rapidly than the same Al-rich capping unit above nontronite, due to the slower dissolution rates and lower solubility of nontronite and therefore may signify less aqueous alteration. Increasing the acidity of the

reacting fluid resulted in either a deeper alteration front or a decrease of Si in the Al-rich unit. In addition, increasing the flow rate, temperature and surface area also result in an increased depth of the alteration front.

The shape of the weathering profiles also provide characteristic of the interacting fluid. Within these models abrupt transitions occurred (e.g. between the Fe/Mg-rich parent material and the overlying Al-rich unit) when dissolution was faster relative to transport. Dissolution increased when there was a decrease in pH, the flow rate was reduced and/or when the surface area was increased.

The results of this study therefore indicate that locations which have experienced the most weathering would be characterized by deep clay bearing units, in addition to having a thick Al-rich capping unit containing Fe-oxyhydroxides and/or oxides. Therefore, Marwth Vallis, which is not only the thickest stratigraphic sequence of clay minerals, also contains one of the largest Al-rich capping units may represent the location that was exposed to the longest duration of aqueous alteration and weathering on the martian surface. Characteristics of weathering profiles should be used to help inform scientists in the selection of the Mars 2020 landing site, to help choose a landing site that encountered liquid water with the characteristics most conducive to habitability and the preservation of biosignatures.

#### ACKNOWLEDGEMENTS

This material is based upon work supported by the National Aeronautics and Space Administration under Grant No. NNX12AH96G issued through the NASA Training Grant: National Space Grant College and Fellowship Program (Space Grant)

and a Mars Fundamental Research Program grant NNX12AH96G to Elisabeth Hausrath and Joel Hurowitz. The authors would like to express their appreciation to Valerie Tu, Chris Adcock, Oliver Tschauner, Paul Forster, and Michael Steiner for insightful conversations improving this paper. We would additionally like to thank Carl Steefel for providing the code CrunchFlow.

## TABLES

**Table 2: Input parameters for reactive transport modeling**

Mineral <sup>A</sup>	Log K (298)	Log $k_{H^+}$	$n_{H^+}$	Log $k_{neutral}$	Log $k_{OH^-}$	$n_{OH^-}$	$E_{a_{H^+}}$ (kcal/mol)	$E_{a_{neutral}}$ (kcal/mol)	$E_{a_{OH^-}}$ (kcal/mol)	Mineral Volume (cm <sup>3</sup> /mol)	Reactive Surface Area (m <sup>2</sup> g <sup>-1</sup> )
Goethite	0.5345 <sup>L</sup>	-	-	-7.94 <sup>RG</sup>	-	-	-	20.55 <sup>P</sup>	-	20.82 <sup>L</sup>	0.940 <sup>VI-Ve</sup>
Kaolinite	7.4292 <sup>L</sup>	-12.37 <sup>BC</sup>	0.1290 <sup>BC</sup>	-	-10.32 <sup>BC</sup>	1.02 <sup>BC</sup>	10.3 <sup>Mt</sup>	-	11.0 <sup>Mt</sup>	98.56 <sup>Ma</sup>	0.038 <sup>B-Ve</sup>
Montmorillonite	3.136 <sup>T</sup>	-12.30 <sup>R</sup>	0.4000 <sup>R</sup>	-14.37 <sup>R</sup>	-13.05 <sup>R</sup>	0.270 <sup>R</sup>	12.29 <sup>Mt</sup>	15.1 <sup>Mt</sup>	14.6 <sup>Mt</sup>	272.82 <sup>Ma</sup>	0.049 <sup>M-Ve</sup>
Nontronite	-5.380 <sup>T</sup>	-11.76 <sup>G</sup>	0.2970 <sup>G</sup>	-13.06 <sup>G</sup>	-10.62 <sup>P*</sup>	0.400 <sup>P*</sup>	13.05 <sup>S</sup>	13.05 <sup>S</sup>	13.05 <sup>S</sup>	217.58 <sup>Ma</sup>	0.049 <sup>M-Ve</sup>
Saponite	15.642 <sup>T</sup>	-11.39 <sup>Br</sup>	0.0591 <sup>Br</sup>	-	-11.28 <sup>Br</sup>	0.0716 <sup>Br</sup>	5.64 <sup>P</sup>	-	14.077 <sup>P</sup>	180.10 <sup>Ma</sup>	0.049 <sup>M-Ve</sup>

<sup>A</sup>For dissolution reactions see supplementary Tables 1 and 2

<sup>L</sup>Thermodynamic data from the database based on Lawrence Livermore National Laboratory thermodynamic modeling (Thermo.com. V8.R6.230)

<sup>G</sup>Gainey et al., (2014)

<sup>D</sup>Dogan et al., (2007)

<sup>T</sup>Tardy and Fritz (1981)

<sup>M</sup>Metz et al., (2005)

<sup>B</sup>Bickmore et al., (2002)

<sup>VI</sup>Villalobos et al., (2009)

<sup>Ve</sup>Velbel (1993) - Denotes a surface area reduction of 100X, to replicate natural systems

<sup>S</sup>Steiner et al., (in prep)

<sup>BC</sup>Brantley et al., (2008) - Data sourced from Carroll-Webb and Walther (1999)

<sup>R</sup>Rozalen et al., (2008)

<sup>Br</sup>Brigatti et al., (1999)

<sup>V</sup>Vincent et al., (1996)

<sup>RG</sup>Raun and Gilkes, (1995)

<sup>Ma</sup>Marini, (2006)

<sup>P</sup>Palandri and Kharaka (2004) - Goethite data was sourced from Raun and Gilkes (1995) Smectite data sourced from Novak and Cecil, (1978); Altaner, (1986); Cama et al., (1994) Bauer and Berger, (1998) and Cama et al., (2000)

<sup>P\*</sup>Palandri and Kharaka, (2004) - Fe/Mg-bearing smectite used as the basic mechanism for nontronite -

Data was sourced from Novak and Cecil, (1978); Altaner, (1986); Cama et al., (1994); Bauer and Berger, (1998) and Cama et al., (2000)

<sup>Mt</sup>Marty et al., (2015) - Data was sourced from Sayed Hassan et al., (2006); Tournassat et al., (2003); Yokoyama et al., (2005); Bauer and Berger (1998); Nakayama et al., (2004), Cama et al., (2000), Amram and Ganor (2005), Yokoyama et al., (2005); Rozalen et al., (2008, 2009), Huertas et al., (2001); Metz et al., (2005); Zysset and Schindler (1996); Bosbach et al., (2000) and Golubev et al., (2006)

## FIGURES

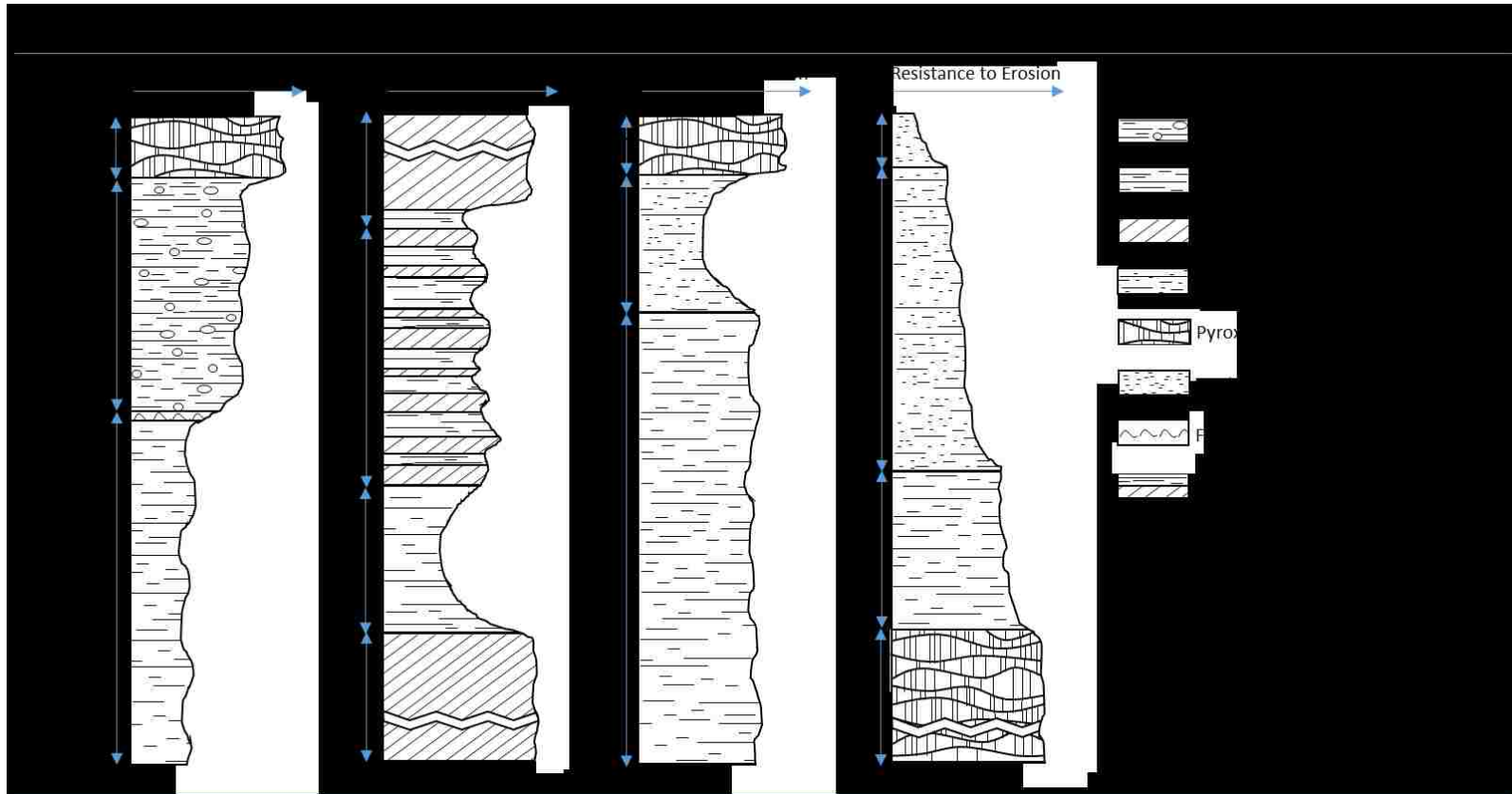


**Figure 13: Stratigraphic columns generated of Mawrth Vallis, Gale Crater, East Nili Fossae and Valles Marineris.**

Stratigraphic columns are based on data remote observations of Mawrth Vallis (Michalski and Dobreá, 2007; Noe Dobreá et al., 2010a), Gale Crater (Milliken et al., 2010b), East Nili Fossae (Ehlmann et al., 2009b) and Valles Marineris (Murchie et al., 2009a; Le Deit et al., 2010). The minerals within each stratigraphic column and resistance to erosion are indicated above.

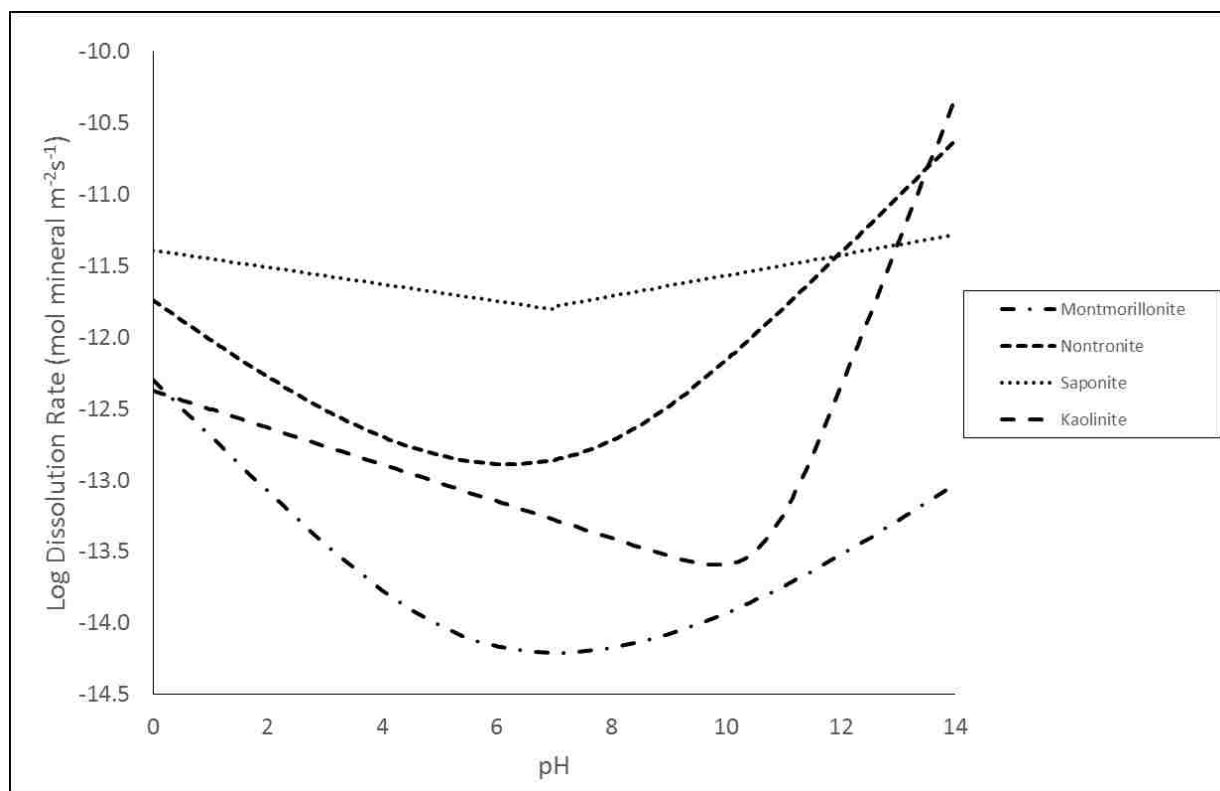


**Figure 14: Comparison of dissolution rate laws for kaolinite, montmorillonite, nontronite and saponite.** Dissolution rate laws for kaolinite from Brantley (2008) based on data from Carroll-Webb and Walther, (1988), montmorillonite (Rozalén et al., 2008a), nontronite (Novak and Cicek, 1978; Altaner, 1986; Cama et al., 1994; Bauer and Berger, 1998; Cama et al., 2000; Palandri and Kharaka, 2004; Gainey et al., 2014) and saponite (from data measured by Brigatti et al., (1999)). A comparison of the rate laws suggests that dissolution rates on Mars would follow the order saponite > nontronite > kaolinite > montmorillonite under most pH conditions. These relationships may help identify clay mineral assemblages that have been weathered by liquid water.

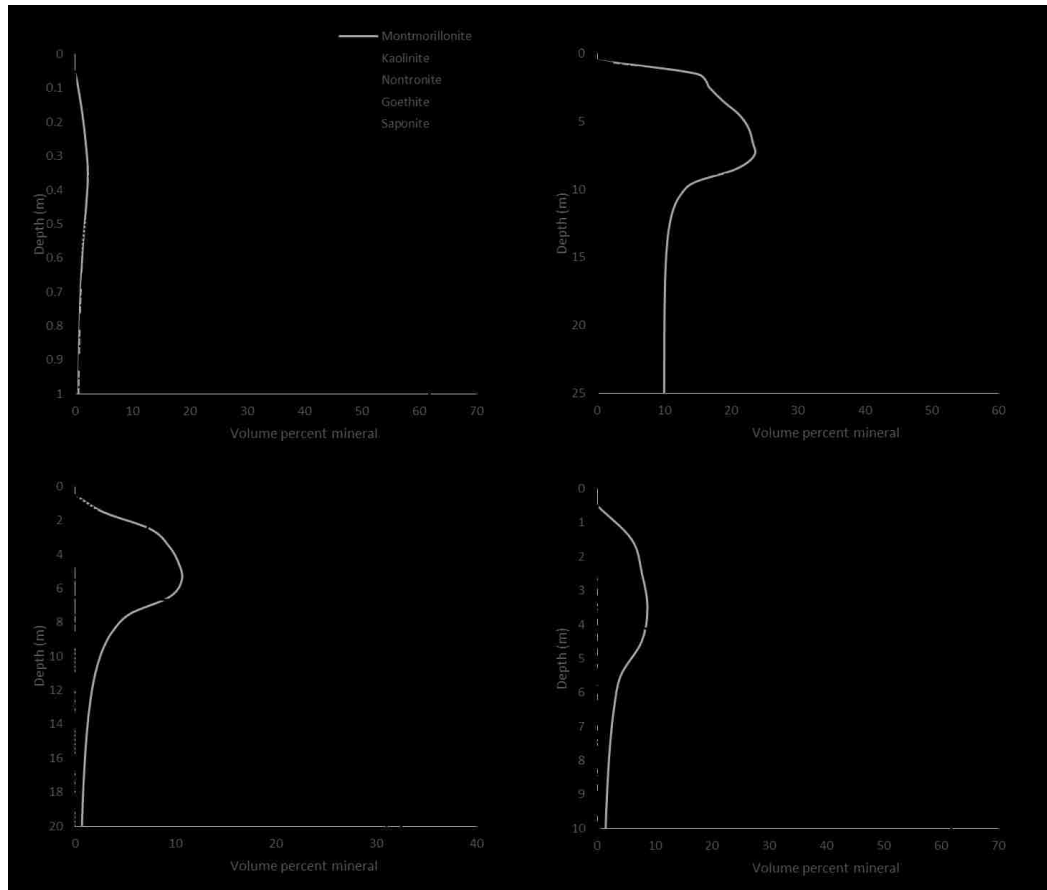


**Figure 15: Modeled weathering profiles of the four scenarios.** Weathering profiles with starting parent materials of (A.) nontronite, (B.) nontronite + 10% montmorillonite, (C.) nontronite + saponite in equal amounts and (D.) saponite. In all cases, an Al-rich layer formed on top of a Mg-Fe-rich layer, although differences were observed between the scenarios (A.) As the nontronite dissolves, montmorillonite becomes increasingly the more voluminous phase, and kaolinite also replaces montmorillonite (B.) Montmorillonite within the parent material resulted in a larger amount of Al-rich clays due to the increased Al from both montmorillonite and nontronite, with the kaolinite similarly replacing the montmorillonite (C.) Saponite is removed more rapidly than nontronite, which may suggest Mawrth Vallis has undergone abundant aqueous alteration due to the large amounts of nontronite. Therefore, nontronite above saponite might also be suggestive of weathering. (D.) The reaction front progressed rapidly and produced a clay rich unit of montmorillonite. The pH within the lower unit was higher than the other scenarios and may have contributed to the precipitation of montmorillonite.



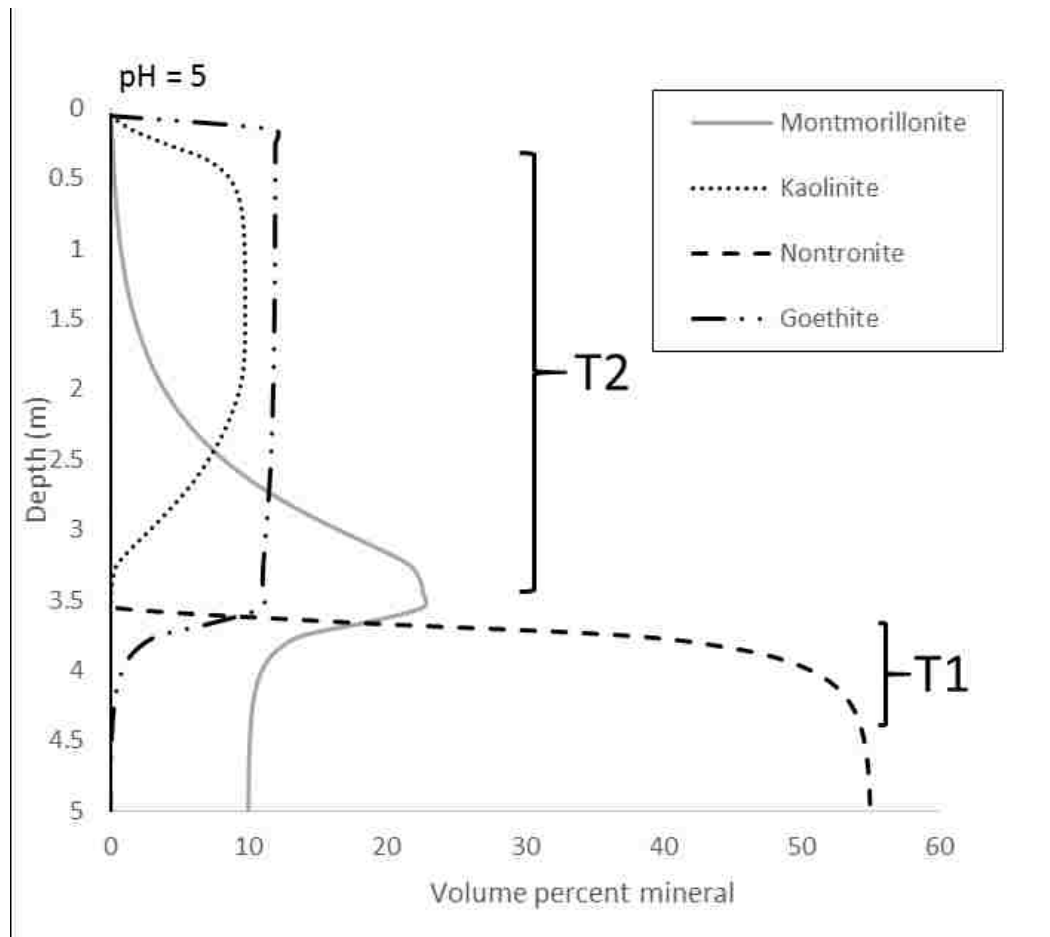


**Figure 16: Model results of weathered nontronite + montmorillonite at pH = 5 showing the two reaction fronts within the system.** Notice transition 1 (T1), from dominantly nontronite to dominantly montmorillonite, occurs over approximately 1 meter, which would be difficult to observe by remote observations. The thickness of transition 2 (T2), from dominantly montmorillonite to dominantly kaolinite, occurs over approximately 3 meters. The more graduate transition from montmorillonite to kaolinite is likely the result of the increased porosity within the weathered material and the slower dissolution kinetics of montmorillonite relative to nontronite. This feature is most pronounced in models with both nontronite and montmorillonite (Figure 15 and S74).

## APPENDIX A: SUPPLEMENTARY MATERIALS FOR CHAPTER TWO

### SUPPLEMENTARY EXPERIMENTAL METHODS

#### *Experimental Procedure - Synthesis*

In order to better determine clay mineral-forming environments on Mars and the potential for preservation of organic matter, we performed synthesis experiments of clay minerals with a range of chemical compositions, supplemented by alteration experiments of igneous materials, forming secondary clay minerals and other secondary phases.

Following a method similar to that of Mizutani et al.(1991), 4.35 g of sodium meta-silicate was dissolved in 420 mL of 18.2 MΩ water. The solution was then acidified with 0.5 M H<sub>2</sub>SO<sub>4</sub> to a pH of approximately 3. For the synthetic nontronite control, 4.2 g of sodium dithionite was dissolved in the solution to maintain reducing conditions. Various concentrations of reagent-grade Fe and Mg sulfates (mineralogy identified by X-Ray Diffraction (XRD) shown in Figures S1, S2 and S3) were then dissolved in the acidic solution (Table S1 and S2). The solution was then cleared with the addition of 19.8 mL of 5 M NaOH. The prepared solutions and suspensions were aged under ambient conditions for one day at approximately 20 °C (Table S1), then subsequently heated at either 150 °C for 48 hours in teflon lined Parr-vessels, or 100 °C (Table S2) in High Density PolyEthylene (HDPE) bottles for 60 days. At the end of the experiment the pH of the solution was recorded with an S20 SevenEasy pH meter using a two point calibration. Samples were then vacuum-filtered to obtain the solid particulate, using a Pyrex 47 mm Microfiltration all-glass assembly with a 300 mL funnel and 47 mm, 0.45 μm membrane disc filters. Samples were then dried in-vacuo in a desiccator.

Because the measurement of oxidation state is notoriously inaccurate (Becking et al., 1960; Langmuir, 1997), we calculated the minimum Eh of our experiments based on the Fe concentrations. It is likely that any ferrous Fe initially present as a contaminant in the reacting material would have been rapidly oxidized in the high pH (> 12) experimental conditions, which were open to the oxidizing terrestrial atmosphere. Previous experimental work has shown that the rate of oxidation of ferrous Fe is dramatically increased (several orders of magnitude) under basic conditions (Stumm and Lee, 1961; Millero et al., 1987) such as those in these synthesis experiments. As an extremely conservative upper limit of potential ferrous Fe contamination in our initial starting materials (which would have been rapidly oxidized during the experiments as described above), we used 3% based on XRD detection limits of a potential ferrous-Fe containing crystalline phase. When using 3% ferrous Fe as the upper limit, the calculated Eh from the ferric and ferrous Fe concentrations is 0.856 V, which, coupled with the rapid oxidation kinetics of ferrous Fe under these conditions, can be used as a minimum Eh in this system. In addition, the ferric state of Fe within the precipitates was confirmed by Synchrotron Mössbauer Spectroscopy (SMS) performed on select samples (Table S3).

#### *Experimental Procedure - Low temperature Synthesis*

Under oxidizing conditions at 20° and 60°C, 1L acid-washed plastic jars contained identical concentrations of Al, Fe, Mg and Si (from nitrate and sulfate salts) as used by Harder (1976, 1978b) in the precipitation of triple-layer silicates. We replicated 6 experiments from Harder's previous works (1972, 1976, 1978b) and expanded upon these to include higher concentration of Al, Fe and the incorporation of various concentrations of Mg.

Under anoxic (<5ppm dissolved O<sub>2</sub>) conditions 1L bottles contained identical concentration of Al, Fe, Mg, and Si as in the oxic experiments, to test the effect of reduced Fe on clay mineral precipitation. 18.2 MΩ water was placed into the 1L bottles after N<sub>2</sub> gas was bubbled through the water for 30 min to ensure minimal dissolved oxygen. 1L bottles were kept in a glove box with O<sub>2</sub> maintained below 5ppm. Samples were aged for 15 and 30 days, respectively. The low temperature precipitates were extremely difficult to characterize, due to the low sample quantity and amorphous and/or extremely-poorly crystalline nature of these samples. Therefore, these results are not discussed further.

#### *Experimental Procedure –Rock Alteration*

Previous experimental work on low-temperature rock alteration has been conducted to characterize the environmental-conditions required to precipitate clay minerals and zeolites (Tomita et al., 1993; Kawano and Tomita, 1997; Tomita and Kawano, 2002). Following a similar procedure to those previous experiments (Tomita et al., 1993; Kawano and Tomita, 1997; Tomita and Kawano, 2002), for both oxic and anoxic/reducing conditions, 150 mL acid-washed serum vials contained between 0.5-1.0 g of powdered sample, previously characterized with XRD to ensure the lack of clay minerals (Figures S4-S7). One of the powdered reference materials (DNC-1a) contained minor quantities of clay minerals – however, because not all products of the DNC-1A formed clay minerals, and because clay minerals were formed from BIR-1a, which initially contained no clay minerals, we consider the minor initial clay minerals if present to be negligible in the formation of clay minerals in these experiments. The bulk chemistry of these reference materials is presented in Table S4. Approximately 150 mL

of either 5, 0.5 or 0.05 M NaOH solutions (produced from 18.2 MΩ deionized water and reagent grade NaOH) was added to the serum vial and powdered material which were maintained at a constant temperature of 90 °C for 5, 10, 15, 20, 25, 30 and 35 days (Tables 5-8). At the end of the experiment the pH of the solution was recorded with a S20 SevenEasy pH meter, with a two point calibration. For oxic experiments, samples were then vacuum filtered under atmospheric conditions to obtain the solid particulate, using a Pyrex 47 mm Microfiltration all-glass assembly with a 300 mL funnel and 47 mm, 0.45 μm membrane disc filters. The particulate was then air dried at room temperature and stored in plastic bags.

Anoxic/reducing experiments were conducted in a similar manner to those described above except that for anoxic experiments, 2000 mL of either 5, 0.5 or 0.05 M NaOH was vigorously bubbled using perforated tubing for a minimum of one hour per liter with high-purity N<sub>2</sub> gas. To further ensure reducing conditions, sodium dithionite (1 g per 100 mL of solution) was added to the bubbled solution. The powdered material was then added to the serum vials and approximately 150 ml of solution was immediately added and capped. A syringe under N<sub>2</sub> pressure was inserted through the rubber cap into the head space and another syringe was then inserted to purge O<sub>2</sub> from the system. N<sub>2</sub> flowed through the head space for 30 seconds, before the output syringe was removed, followed by the input syringe (this was to ensure no O<sub>2</sub> entered the system). The bottles were aged for 35 days at 90 °C. Samples were then filtered under three different conditions to test the effects of re-oxidation. Samples were (1) filtered, rinsed with deoxygenated water, and dried, all within an O<sub>2</sub>-free glove box, preventing re-oxidation, (2) filtered and dried under atmospheric conditions and (3) filtered (to remove the

reducing agent) and re-inserted into serum vials with the addition of 100 mL of deionized water, and then bubbled for 1 hour every 24 hours for three days with air to re-oxygenate the solutions before filtering and drying under atmospheric conditions. To ensure air-free conditions during syntheses, experiments were performed in glass serum bottles.

Water-rock ratio and glass-free experiments were conducted in HDPE bottles. For oxic water-rock ratio experiments, one gram of powdered reference material was added to the bottle, followed by the addition of either 25, 50, 100 or 500 mL of 1 M NaOH. In order to replicate all oxic experiments performed in glass bottles, experiments were also conducted with 5, 0.5 and 0.05 M NaOH for 35 days in HDPE bottles to compare to their glass bottle counterparts. Samples were then vacuum-filtered and dried under atmospheric conditions.

Reducing experiments were also conducted in plastic bottles in which one gram of powdered material was added to HDPE bottles. Following a procedure similar to the reducing experiments performed in glass bottles; 5, 0.5 and 0.05M NaOH solutions were bubbled with N<sub>2</sub> (one hour per liter). Na-dithionite (1 g per 100 mL solution) was then added to the solution. 200 mL of the solution was decanted into to the bottles. As a redox indicator, 0.0001 g of resazurin-salt was added for every mL of solution. The head space was then purged with high-purity N<sub>2</sub> gas and sealed. The bottles were placed within two secondary plastic bags which were purged with N<sub>2</sub> to prevent the diffusion of O<sub>2</sub> into and H<sub>2</sub> out of the system. At the termination of the experiment, the products were then analyzed by X-ray diffraction (Tables 5-8).

## ANALYTICAL TECHNIQUES

## *X-Ray Diffraction*

Powder X-Ray Diffraction data were collected for the synthesized samples using a PANalytical X'Pert Pro X-Ray Diffractometer at 40 kV and 20 mA using CuK $\alpha$  radiation in the X-Ray Fluorescence and X-Ray Diffraction Laboratory (XXL) at the University of Nevada, Las Vegas. The samples produced in these experiments were prepared in a similar manner to the glass slide method illustrated by Moore and Reynolds(1989) in which samples were lightly ground in the presence of ethanol. The slurry was then poured onto a silicon wafer and dried at 60 °C. Patterns were taken under air dried conditions as well as after treatment with ethylene glycol vapor for a minimum of 24 hours to measure expansion and therefore identify the specific clay mineralogy.

Clay minerals are generally fine-grained, crystalline, hydrous phyllosilicates(Moore and Reynolds, 1989). Of these minerals, the smectite group is defined by their ability to expand and shrink when exposed to heat, water and polar organic compounds(Moore and Reynolds, 1989). The dioctahedral Fe end-member of the smectite group is nontronite, whereas the trioctahedral Mg end-member is either saponite or stevensite(Moore and Reynolds, 1989). However, significant Fe and Mg substitution can occur between these two end-members, leading to a semi-solid solution in Fe/Mg-smectites and other clay minerals(Grauby et al., 1993; Grauby et al., 1994). Previous work by Grauby et al.(1994) also suggests that di- and trioctahedral domains may occur within the same crystallite. Here we use the nomenclature used by Nickel(1992), in which the transition from end-members is marked at the midpoint of 50 mol percent of Fe and/or Mg for nontronite and saponite, respectively.

*Observations of clay minerals on Mars and comparisons to precipitates formed in this study*

Recently, the CheMin instrument onboard the Mars Science Laboratory (MSL) has used XRD to identify mineralogy at Gale Crater (Bish et al., 2013; Vaniman et al., 2014). Clay minerals have been inferred in both the John Klein and Cumberland samples taken at Yellowknife Bay based on low angle diffractions (Vaniman et al., 2014). The samples have been further classified as smectites due to their broad low-angle 001 peaks (9 – 13.2 Å) and lack of a 7 Å diffraction indicative of 1:1 phyllosilicates and chlorites (Vaniman et al., 2014). The di- and trioctahedral nature of these clay minerals could not be assessed by their 060 diffraction due to the  $2\theta$  range possible by CheMin (Vaniman et al., 2014). However, the use of the 020 reflection led to the conclusion that both samples (e.g. John Klein and Cumberland) were trioctahedral smectites and in particular saponite and/or Fe-rich saponites (Vaniman et al., 2014).

The diffraction patterns taken of the Fe-, Fe plus Mg- and Mg-bearing precipitates in this study also produced broad 001 peaks similar to those observed at Yellowknife Bay (Vaniman et al., 2014). The lack of a 7 Å peak suggests the absence of 1:1 phyllosilicates and chlorites within the sample, similar to the observation of the clay minerals detected at Yellowknife Bay (Vaniman et al., 2014). The 020 peaks, although present within the precipitates, are difficult to assess due to the poor crystallinity compared to more crystalline natural samples. However, the broad peaks are effectively within the same range as those observed in the John Klein and Cumberland samples (see Figure 1).

*Synchrotron Micro X-Ray Diffraction*



Select aliquots of powdered sample were placed in 1mm capillary tubes and examined with synchrotron micro X-Ray diffraction ( $\mu$ XRD). The  $\mu$ XRD was conducted at the 16-ID-D beamline of the Advanced Photon Source in the Argonne National Laboratory using monochromatic radiation with a wavelength of 0.860250 Å. The beam was focused to a 30 x 40  $\mu\text{m}^2$  spot at the sample position. A MAR165 area detector was used for collecting diffraction data. Sample detector distance and geometric distortions were determined based on a CeO<sub>2</sub> standard using GSE-ADA. The diffraction patterns were integrated using Fit2D (Hammersley, 1997).

#### *Synchrotron Mössbauer Spectroscopy*

In order to determine the oxidation state of the Fe within the precipitates, Synchrotron Mössbauer Spectra were collected on select samples (NAu-1, Exp-1, Exp-4 and Exp-5) at the 16-ID-D beamline of the Advanced Photon Source at Argonne National Laboratory using monochromatic radiation of 14.4 kV. Collection times were a minimum of one hour, using a 10  $\mu\text{m}$  steel foil to determine center shifts (Figure S8). In order to determine Mössbauer parameters, fitting was performed using the software CONUSS (Sturhahn, 2000) (Figures S9 – S13). Following previous Mössbauer studies of nontronite, spectra were modeled with two Mössbauer sites (Ribeiro et al., 2009; Vandenberghe and De Grave, 2013). The octahedral sites of clay minerals contain four oxygen ligands and the remaining two are hydroxyls, which maybe in either cis or trans configuration (Vandenberghe and De Grave, 2013) and therefore require two Mössbauer sites.

The results of the SMS indicate no evidence of Fe<sup>2+</sup> within the precipitates, as only one quantum bump/beat is present as well as relatively low isomer shifts, suggesting both sites' isomer shifts and quadrupole splittings occur within the single observed absorption which is consistent with the ferric-clay nontronite (Figures S9-S13)(Taylor et al., 1968; Ribeiro et al., 2009; Vandenberghe and De Grave, 2013). The quadrupole splitting of all samples are well below that of Fe<sup>2+</sup>-bearing clay minerals(Vandenberghe and De Grave, 2013), indicating that the samples do not contain measurable Fe<sup>2+</sup>. The Mössbauer parameters determined within the software CONUSS (Table S3)(Sturhahn, 2000) for all samples formed under oxidized conditions are also consistent with the ferric mineral nontronite (standard NAu-1) which was also analyzed and used as a reference in this investigation. Experiment 1 (*100 – Fe control – Subsequently Oxidized*) had slightly larger isomer shifts and quadrupole splitting than the other experiments (Table S3 and Figure S13), however the quadrupole splitting is still below that of Fe<sup>2+</sup> bearing clays(Vandenberghe and De Grave, 2013). In addition, Experiment 1 exactly replicated the previous work by Mizutani et al.(Mizutani et al., 1991), in which the result of their Mössbauer analysis also indicated that the clay mineral precipitates contained only Fe<sup>3+</sup>. The difference between Experiment 1 and the other samples may result from Experiment 1 requiring initially reducing conditions and therefore differences in Fe-coordination. In addition, consistent with our Mössbauer data, spectral observations are also indicative of ferric clay minerals rather than ferrous for all precipitates in this study (Figures S14 (150° C) and S15 (100° C))(Chemtob et al., 2015).

*Visible Near Infrared and Infrared Spectroscopy:*

Visible Near Infrared (VNIR) and Infrared (IR) reflectance spectra were measured for each sample, using an Analytical Spectra Devices (ASD) VNIR spectrometer and a Fourier Transform Infrared Spectrometer, respectively. Spectra were taken over the range of 0.4 – 2.5  $\mu\text{m}$  and 2.5 to 25  $\mu\text{m}$ . The spectra of our samples are similar to spectra measured by Observatoire pour la Mineralogie, l'Eau les Glaces et l'Activité (OMEGA), the Compact Reconnaissance Imaging Spectrometer for Mars (CRISM), the Thermal Emission Spectrometer (TES) and Mini-TES and are therefore comparable to remote and ground-based observation of the martian surface (Ehlmann et al., 2012). Band centers were determined from continuum-removed spectra.

*Remote observations of clay minerals on Mars and comparison to precipitates formed in this study:*

Observatoire pour la Mineralogie, l'Eau les Glaces et l'activité (OMEGA) and the Compact Reconnaissance Imaging Spectrometer for Mars (CRISM) allow for comparison of our synthetic products to clay mineral spectra taken from the Martian surface. The clay minerals are primarily identified using four different bands: (1) Fe electronic transitions which are present in Fe-rich clay minerals (such as nontronite) at approximately 1  $\mu\text{m}$ . (2) An overtone absorption related to metal-OH bonds which occur at 1.38 for saponite to 1.43  $\mu\text{m}$  for nontronite (3) An absorption due to water is located at  $\sim 1.9$   $\mu\text{m}$ , which is present in all smectites but is not used to differentiate clay mineral species and (4) another metal-OH absorption which occurs at 2.21 (montmorillonite) to 2.32  $\mu\text{m}$  (saponite), with the absorption for nontronite in between the previous two minerals (2.28-2.29  $\mu\text{m}$ ). This is one of the primary absorption features used to identify clay minerals from orbit.

### *Scanning Electron Microscopy and Energy Dispersive spectroscopy*

Scanning Electron Microscopy (SEM) was performed using a JEOL JSM-5610 scanning electron microscope equipped with an Oxford ISIS Energy Dispersive Spectrometer (EDS) capable of semi-quantitative chemical analysis. Samples were carbon-coated and examined for morphology and chemical composition. All SEM/EDS analyses were conducted at the University of Nevada, Las Vegas Electron Microanalysis and Imaging Laboratory (EMiL).

### *Microprobe*

Analysis by electron microprobe (EMP) wavelength-dispersive spectroscopy (WDS) was carried out on a Jeol JXA-8900 microprobe at the University of Nevada, Las Vegas EMiL laboratory on polished epoxy mounts. Analysis conditions were 20 keV and 10 nA using a 10  $\mu\text{m}$  beam.

The difficulties encountered when analyzing clay minerals by EMP analysis and the low totals observed (Table S9) have been previously documented (Treiman et al., 2014). Clay minerals may undergo dehydration under desiccation (during the carbon coating process and within the vacuum chamber of the microprobe itself) but retain structural OH, which may contain ~5 weight percent H<sub>2</sub>O (Treiman et al., 2014). In addition, EMP analysis relies on a relatively flat sample surface; this can be difficult to achieve due to etching and pitting during the polishing process, which was also observed by Treiman et al. (2014). Clay minerals are also highly porous, which may contribute to low totals observed by EMP analysis (Treiman et al., 2014).

## SUPPLEMENTARY RESULTS OF ALTERATION EXPERIMENTS

To further evaluate the effect of oxidation state on mineral synthesis, a range of igneous rocks (mafic to intermediate-felsic) were altered in initially-oxidizing or reducing alkaline solutions. Altered samples suggest 2:1 clay minerals (e.g. smectite) form in high SiO<sub>2</sub> solutions (within the glass bottles), whereas mafic materials produced 1:1 phyllosilicates (e.g. serpentines) under lower SiO<sub>2</sub> conditions (within the plastic bottles). Clay minerals were identified by XRD and morphology and chemical composition measured by SEM/EDS (Figures S16 – S17). 2:1 clay minerals were identified by broad low-angle peaks, which are indicative of hydrated smectite clay minerals. The 1:1 clay minerals (e.g. serpentines) were identified by the presence of 00 $l$  reflections in powder-XRD which likely correspond to the low temperature polymorphs chrysotile and/or lizardite. In addition SEM/EDS analyses suggest the potential presence Fe/Mg rich clay minerals (Figures S18 and S19). No clay minerals formed when felsic and intermediate materials were altered in the absence of additional SiO<sub>2</sub> (within plastic bottles).

## SUPPLEMENTARY RESULTS OF SYNTHESIS EXPERIMENTS

Results of experiments performed at 100 ° C and 150 ° C were very similar, and are therefore discussed together below.

### *Experiment-1(100-Fe Control - Subsequently Oxidized)*

Experiment 1 directly replicated the previous work of Mizutani et al. (1991), in which nontronite was synthesized under initially reducing conditions and subsequently oxidized through exposure to atmospheric conditions, with oxidation confirmed by Mössbauer spectroscopy (Mizutani et al., 1991). Trioctahedral ferrous smectites are very unstable

under oxidizing conditions and have been shown to oxidize during desiccation under laboratory conditions (Badaut et al., 1985). The initial 150° C precipitate was dark green in color and slowly became reddish brown in color, which may be an indicator of the oxidation from ferrous to ferric Fe (Figure S20). In contrast, the 100° C experiment appeared to be slightly greener in color (Figure S21). Diffraction patterns of the synthesized products included a broad low angle peak of approximately 12.5 Å, indicative of smectite clay (Figure S22 (150 ° C) and Figure S23 (100° C)). The lack of other peaks at or near 7 Å suggest the absence of other clay minerals such as kaolins and chlorites. The  $\mu$ XRD analyses of the 150 ° C synthesized material also show distinct reflections characteristic of clay minerals (e.g. 001, 020 and 060) (Figure S24 (150° C)). Treatment with ethylene glycol produced only a slight expansion more characteristic of high-charge smectite (expands very little when exposed to ethylene glycol vapor) (Decarreau et al., 2008) or vermiculite (Figure S22 (150° C) and Figure 23 (100° C)). A VNIR absorption feature at 0.975  $\mu$ m is due to Fe electronic transitions which have a distinctive overall continuum slope toward shorter wavelengths, distinct from the other samples (Figure S14 (150° C) and S15 (100° C)). The absorption feature at 1.422  $\mu$ m is characteristic of OH and H<sub>2</sub>O (2vOH) features of metal-hydroxyl bonds and structural and absorbed water. In addition, an absorption feature located at 1.914  $\mu$ m is indicative of H<sub>2</sub>O (VOH +  $\delta$ m-OH). The M-OH (2vOH) absorption feature was located at 2.294  $\mu$ m, a somewhat longer wavelength than expected for the Fe(III)-smectite nontronite (2.28-2.29  $\mu$ m).

*Experiment-2 (100-Fe<sup>3+</sup>)*

The initial precipitate was dark red in color (Figure S25 (150° C) and S26 (100° C)). Diffraction patterns of the synthesized products suggest the precipitate remained relatively amorphous (Figure S27 (150° C) and S28 (100° C)), which is supported by previous studies suggesting Fe-dioctahedral clay formation from ferric solutions is prohibitively slow and difficult (Harder, 1976; Decarreau et al., 2008). Treatment with ethylene glycol had little if any effect (Figure S27 (150° C)). An absorption feature at 1.013  $\mu\text{m}$  indicates Fe electronic transitions (Figure S14 (150° C) and S15 (100° C)). The absorption feature at 1.426  $\mu\text{m}$  is characteristic of OH and H<sub>2</sub>O (2vOH) features of metal-hydroxyl structural and absorbed water. This absorption feature is close to that of nontronite (1.43  $\mu\text{m}$ ). In addition, an absorption feature located at 1.925  $\mu\text{m}$  is indicative of H<sub>2</sub>O (VOH +  $\delta\text{m-OH}$ ). This absorption feature is broad and shallow, which may suggest a lack of Fe-OH structural elements and/or poorly crystalline components.

#### *Experiment-3 (100-Mg, High SiO<sub>2</sub>)*

The initial precipitate was white in color (Figure S29 (150° C) and S30 (100° C)). Diffraction patterns of the synthesized products contained broad low angle peaks (Figure S31 (150° C) and S32 (100° C)) that made it difficult to determine an accurate d-spacing of the 150° C experiment (Figure S31). After treatment with ethylene glycol, expansion occurred, although the exact expansion is difficult to determine in the 150° C experiment (Figure S31), the 100° C experiment expanded from approximately 12 to 19 Å (Figure S32). These data are suggestive of a Mg-trioctahedral smectite (e.g. saponite or stevensite). The VNIR spectra of the experiments contain several absorptions located at 0.945, 1.157 and 1.281  $\mu\text{m}$  that are likely due to structural H<sub>2</sub>O (Figure S14 (150° C) and S15 (100° C)). The absorption feature at 1.389 and 1.417  $\mu\text{m}$  is characteristic of Mg-OH

and H<sub>2</sub>O (2vOH) features of structural and absorbed water. An absorption feature located at 1.914 μm is indicative of H<sub>2</sub>O (VOH + δm-OH). The M-OH (2vOH) absorption feature is located at 2.314 μm, indicating Mg-OH. The spectral properties are also consistent with a Mg-trioctahedral smectite (e.g. saponite or stevensite).

*Experiment-4 (15-Mg 85-Fe<sup>3+</sup>)*

The initial precipitate was red-brown in color (Figure S33 (150° C) and S34 (100° C)). The diffraction pattern of the synthesized material contained a broad low-angle peak, indicative of a clay mineral and also showed other distinct reflections of clay minerals (e.g. 020 reflection) (Figure S35 (150° C) and S36 (100° C)). These results were also supported by μXRD for the 150 degree C experiment (Figure S37). In addition, treatment with ethylene glycol resulted in some expansion, which is a property of smectite, although due to the poor/nano crystallinity the exact expansion is difficult to determine (Figure S35 (150° C) and Figure 36 (100° C)). These data are indicative of a Fe-rich dioctahedral clay mineral, such as a high-charge nontronite (Decarreau et al., 2008). In the VNIR spectra, an absorption feature at 1.009 μm indicates Fe electronic transitions (Figure S14 (150° C) and S15 (100° C)). The absorption feature at 1.424 μm is characteristic of OH and H<sub>2</sub>O (2vOH) features of structural and absorbed water, and this absorption feature is suggestive of nontronite when at 1.43 μm, although band shifts may occur as a result of multiple cations within the mineral structure. An absorption feature located at 1.921 μm is indicative of H<sub>2</sub>O (VOH + δm-OH). The M-OH (2vOH) absorption feature is located at 2.295 μm. This absorption feature is closest to that of nontronite (2.28 -2.29 μm) but intermediate to that of smectite. The “L-shape” with a shoulder rather than a sharp absorption is a common characteristic of Fe/Mg



phyllosilicate-bearing terrain observed with CRISM and OMEGA (e.g. Poulet et al.(2005a)).

*Experiment-5 (50-Mg 50-Fe<sup>3+</sup>)*

The initial precipitate was red-brown in color (Figure S38 (150° C) and S39 (100° C)). Diffraction patterns of the synthesized products contained broad, low angle peaks at approximately 14 -15 Å, indicative of a smectite clay (Figure S40 (150° C) and Figure S41 (100° C)). These results were also supported by  $\mu$ XRD for the high temperature experiment indicating the presence of 020 and 060 reflections of clay minerals (Figure S42). Treatment with ethylene glycol produced an expansion to ~17 Å indicative of smectite (Figure S40 (150° C)). However, the 100° C precipitate only expanded to approximately 15 Å (Figure 41 (100° C)). These precipitates may contain domains of both Mg-trioctahedral and Fe-dioctahedral clays/smectites (Grauby et al., 1994). An absorption feature at 0.984  $\mu$ m is due to Fe electronic transitions (~1  $\mu$ m) (Figure S14 (150° C) and S15 (100° C)). The absorption feature at 1.420  $\mu$ m is characteristic of OH and H<sub>2</sub>O (2vOH) features of hydroxyl and structural and absorbed water. This absorption feature center wavelength is between montmorillonite and nontronite (1.41 and 1.43  $\mu$ m). In addition, an absorption feature located at 1.920  $\mu$ m is indicative of H<sub>2</sub>O (VOH +  $\delta$ m-OH). The M-OH (2vOH) absorption feature is located at 2.309  $\mu$ m, but is broad and ranges from 2.300 to 2.318  $\mu$ m. This absorption feature exists between that of nontronite (2.28 – 2.29  $\mu$ m) and saponite (2.31 – 2.32  $\mu$ m), although the absorption occurs closer to that of saponite.

*Experiment-6 (10-Mg 90-Fe<sup>3+</sup>) 150° C*

The initial precipitate was red-brown in color (Figure S43). Diffraction patterns of the synthesized product contained a broad, low angle peak, indicative of clay minerals (Figure S44). The diffraction pattern also contained a 020 reflection indicative of clay minerals. Treatment with ethylene glycol resulted in only a slight expansion of the basal plane. The diffraction data are similar to materials previously described as high-charge nontronites (Decarreau et al., 2008). A VNIR absorption feature at 0.975  $\mu\text{m}$  is due to Fe electronic transitions (Figure S14). The absorption feature at 1.433  $\mu\text{m}$  is characteristic of OH and H<sub>2</sub>O (2vOH) features of metal-hydroxyl bonds and structural and absorbed water and coincides with the absorption of nontronite. In addition, an absorption feature located at 1.914  $\mu\text{m}$  is indicative of H<sub>2</sub>O (VOH +  $\delta\text{m-OH}$ ). The M-OH (2vOH) absorption feature was located at 2.289  $\mu\text{m}$ , indicative of the clay mineral nontronite.

*Experiment-7 (5-Mg 95-Fe<sup>3+</sup>) 150° C*

The initial precipitate was red-brown in color (Figure S45). Diffraction patterns of the synthesized product contained a broad, low angle peak, indicative of a clay mineral (Figure S46). Although it was difficult to determine the exact position of the basal plane due to poor/nano crystallinity, when treated with ethylene glycol expansion likely occurred. The diffraction pattern also contained the 020 reflection which is indicative of clay minerals. Only 5% Mg was used in the synthesis of this precipitate, which therefore indicates that only very minor amounts of Mg are required in the formation of Fe-rich clay minerals such as this high-charge nontronite (Decarreau et al., 2008). Many naturally occurring nontronites contain a similar amount of Mg (Goodman et al., 1976; Tardy and Fritz, 1981; Keeling et al., 2000; Manceau et al., 2000a) (Table S10). A VNIR absorption feature at 0.975  $\mu\text{m}$  is due to Fe electronic transitions (Figure S14). The

absorption feature at 1.434  $\mu\text{m}$  is characteristic of OH and H<sub>2</sub>O (2vOH) features of metal-hydroxyl bonds and structural and absorbed water and coincides with the absorption on nontronite. In addition, an absorption feature located at 1.914  $\mu\text{m}$  is indicative of H<sub>2</sub>O (VOH +  $\delta\text{m-OH}$ ). The M-OH (2vOH) absorption feature was located at 2.287, indicative of the clay mineral nontronite.

*Experiment-8 (100-Al, Low SiO<sub>2</sub>)*

The initial precipitate was white in color (Figure S47 and S48). XRD results of the 150° C experiment, suggest boehmite precipitated in this experiment (Figure S49). The 100° C precipitate also remained relatively amorphous, but produced minor boehmite (Figure S50). The absorption feature at 1.420  $\mu\text{m}$  is characteristic of OH and H<sub>2</sub>O (2vOH) features of structural and absorbed water and/or metal-hydroxyls (Figure S14 and S15). In addition, an absorption feature located at 1.923  $\mu\text{m}$  is indicative of H<sub>2</sub>O (VOH +  $\delta\text{m-OH}$ ). The M-OH (2vOH) absorption feature is located at 2.206 – 2.266  $\mu\text{m}$ . This absorption feature is broad and shallow, and may indicate a hydrated silica phase or poorly crystalline Al-OH bearing phase. These absorptions are approximately equal to the lower temperature experiments.

*Experiment-9 (100-Mg, Low SiO<sub>2</sub>)*

The initial precipitate was white in color (Figure S51 and S52). The diffraction pattern of the 150° C synthesized product contained a broad low angle peak at approximately 7.7 Å, suggestive of a 1:1 clay, potentially serpentine (Figure S53). Additionally, the lack of a 19.3 – 19.4 Å diffraction peak suggests that this clay is lizardite and/or chrysotile, these same diffractions were also present in the 100° C

precipitate (Figure S54), which was chemically identical. The sharp absorption feature at 1.387  $\mu\text{m}$  with a shoulder is characteristic of Mg-OH with some H<sub>2</sub>O (2vOH). This absorption feature is consistent with that of serpentine (1.38 – 1.39) (Figure S14 and S15). In addition, an absorption feature located at 1.918  $\mu\text{m}$  is indicative of H<sub>2</sub>O (VOH +  $\delta\text{m-OH}$ ). The M-OH (2vOH) absorption feature is located at 2.321  $\mu\text{m}$ . This absorption feature again, coincides with that of the Mg-OH (2vOH) absorption of serpentine (2.31 – 2.32  $\mu\text{m}$ ). The VNIR spectra of the lower temperature precipitates were approximately equal.

#### *Experiment-10 (100-Al, High SiO<sub>2</sub>)*

The initial precipitate was white in color (Figure S55 and S56). The diffraction pattern of the 150° C synthesized product suggests an amorphous precipitate (Figure S57). However, the precipitate aged at 100° C, produced many sharp diffractions, which were suggestive of the zeolite faujasite (Figure S58). The sample was relatively homogeneous except for an amorphous component, such as hydrated silica. The absorption feature at 1.427  $\mu\text{m}$  is characteristic of OH and H<sub>2</sub>O (2vOH) features of structural and absorbed water. An absorption feature located at 1.925  $\mu\text{m}$  is indicative of H<sub>2</sub>O (VOH +  $\delta\text{m-OH}$ ) (Figure S14 and S15). The M-OH (2vOH) absorption feature is located at 2.237  $\mu\text{m}$  (2.233  $\mu\text{m}$  in the 100° C experiment). This absorption feature is broad and shallow suggesting an amorphous phase with Si-OH and/or Al-OH, such as a hydrated silica or allophane and faujasite in the low temperature experiment. These absorptions are approximately equal within the lower temperature experiments.

#### *Experiment-11 (44-Al 14-Mg 42-Fe<sup>3+</sup>)*

The initial precipitate was red-brown in color (Figure S59 and S60). The diffraction patterns of the 150° C synthesized product suggest a relatively amorphous precipitate, although some of the  $h00$  and  $0k0$  planes appear to be present, suggesting some crystalline development (Figure S61). However, the precipitate which was aged at 100° C was significantly more crystalline and had a broad basal reflection and other diffractions characteristic of clay minerals (Figure S62). Within the VNIR spectra, an absorption feature at 0.988  $\mu\text{m}$  represents Fe electronic transitions ( $\sim 1 \mu\text{m}$ ) (Figure S14 and S15). The absorption feature at 1.434  $\mu\text{m}$  is characteristic of Fe-OH and H<sub>2</sub>O (2vOH) features of structural and absorbed water. This absorption feature is closest to that of nontronite (1.43  $\mu\text{m}$ ). In addition, an absorption feature located at 1.924  $\mu\text{m}$  is indicative of H<sub>2</sub>O (VOH +  $\delta\text{m-OH}$ ). The M-OH (2vOH) absorption feature is located at 2.294  $\mu\text{m}$ . This absorption feature is closest to that of nontronite (2.28 -2.29  $\mu\text{m}$ ) but in a somewhat intermediate position, longward of typical nontronite. The VNIR spectra of the lower temperature precipitates were approximately equal.

#### *Experiment-12 (50-Al 50-Mg)*

The initial precipitate was white in color (Figure S63 and S64). The diffraction pattern of the 150° C synthesized product suggests a relatively amorphous product, although some of the  $h00$  and  $0k0$  planes appear to be present, suggesting some crystalline development (Figure S65). The precipitate aged at 100° C produced similar result (i.e. the presence of a 020 and 060 diffraction) (Figure S66). The absorption feature at 1.420  $\mu\text{m}$  is characteristic of the OH and H<sub>2</sub>O (2vOH) features of hydroxyl and structural and absorbed water (Figure S14 and S15). This absorption feature is near that of montmorillonite (1.41  $\mu\text{m}$ ). In addition, an absorption feature located at 1.918  $\mu\text{m}$  is

indicative of H<sub>2</sub>O (VOH + δ<sub>m</sub>-OH). M-OH (2νOH) absorption features are located at 2.243 and 2.315 μm. The 2.243 μm absorption feature is not consistent with montmorillonite (2.21 μm) but is similar to the location of the Al-OH feature in illite (although no potassium was present in our experiments) and perhaps MgAl-OH in Al-substituted Mg smectites and chlorites. The 2.315 μm absorption coincides with that of saponite (2.31 – 2.32 μm). These absorptions are approximately equal within the lower temperature experiments.

## SUPPLEMENTARY DISCUSSION

Synthesis experiments in which a divalent cation was present in a concentration of at least 5% led to the precipitation of clay minerals, marked by a low angle basal reflection in powder-XRD and supported by VNIR and IR absorptions for analyzed samples characteristic of clay minerals (Figures S46 and S14). The presence of Mg in at least 5% concentration is a common occurrence in many natural nontronites (Table S10) (Goodman et al., 1976; Tardy and Fritz, 1981; Keeling et al., 2000; Manceau et al., 2000a). The presence of solely trivalent cations in solution leads to a relatively amorphous product at both 150° C and 100° C as indicated by VNIR and XRD spectroscopy (Figure S14, S15, S27 and S28).

Previous experimental data also suggest that the incorporation of Al into precipitates may be kinetically slower due to the smaller size of this cation (Harder, 1977, 1978b). This is in agreement with the results of this study in which low Si:Al solutions precipitated boehmite and high Si:Al solution produced very-poorly crystalline materials lacking a definite 00l reflection (although these precipitates appear to contain a poor 060 reflection, which might incipient clay structure ) (Figures S49, S50 and 57). Our

experiments in which Al was the dominant cation remained relatively amorphous or poorly crystalline even when the ratio of Al: Mg was ~1:1. Previous experimental work has suggested that the precipitation of beidelite (an Al-endmember smectite, where the layer charge is derived from Al substitution for Si in the tetrahedral sheet) requires higher temperatures and pressures than those used in this study (Ewell and Insley, 1935; Granquist et al., 1972; Klopogge et al., 1990; Klopogge, 1998). Precipitation experiments performed by De Kimpe (1976) at 2.7-8.8 bars (significantly higher pressures than those used in this study) allowed for the precipitation of beidellite above 175 °C; below this temperature 2:1 clay minerals did not precipitate. This temperature (175 °C) is currently the lowest temperature under which beidellite has precipitated under laboratory conditions (Klopogge, 1998). Previous studies on the precipitation of synthetic montmorillonite were also generally conducted at elevated temperatures (Klopogge, 1998). The lowest temperature reported for the precipitation of montmorillonite under conditions similar to those within this study is 150-300° C, where the synthesis was performed in an autoclave in the presence of ZnO (the octahedral charge was derived from Zn substitution for Al). The precipitation of kaolinite was not expected to occur in our synthesis experiments, as it generally requires acidic to near-neutral conditions to precipitate (Nagy and Lasaga, 1993; Devidal et al., 1997; Yang and Steefel, 2008). The experiments of this study were also generally optimized for precipitation of Fe and Mg-containing smectites rather than Al-containing smectites.

Higher solution concentrations of Mg<sup>2+</sup> relative to Si (~16:10) produced 1:1 clay minerals (lizardite or chrysotile), whereas lower ratios (~7:10) produced 2:1 clay minerals (e.g. saponite). These results are consistent with previous work conducted by

Harder (1977) indicating that relatively high concentrations of Si (60 SiO<sub>2</sub> ppm with 1-2.5 ppm metal) favored the precipitation of 2:1 clay minerals, and relatively low concentrations of Si (5-20 ppm SiO<sub>2</sub> with 2 ppm metal) favored the precipitation of 1:1 clay minerals (Harder, 1978b).



SUPPLEMENTARY TABLES

**Table S1: Concentration of reagent grade chemicals that were incorporated into solution to produce the synthesized products at 150° C.**

**Experiment - 1 (100-Fe Control - Subsequently Oxidized)**

Chemical Name	Molecular Weight (g/mol)	Amount (g or mL)	Amount Cation (mol)
Sodium Metasilicate - Pentahydrate	212.7400	4.35	0.0204
Iron (II) Sulfate - Heptahydrate	278.0500	3.94	0.0142
Sodium Dithionite	174.1070	4.20	0.0241
<b>Fe:Mg ratio</b>	-	-	1:0

Solution Name	Molecular Weight (g/mol)	Amount (mL)	Amount Cation (mol)
Sodium Hydroxide (5 M)	-	19.80	-
H <sub>2</sub> O	18.0153	417.52	-
Sulfuric Acid (0.5 M)	-	41.00	-
<b>Ending pH</b>	-	-	12.49

**Experiment - 2 (100-Fe<sup>3+</sup>)**

Chemical Name	Molecular Weight (g/mol)	Amount (g or mL)	Amount (mol)
Sodium Metasilicate - Pentahydrate	212.7400	4.35	0.0204
Iron (III) Sulfate - Rhomboclase & Ferricopiapite	321.0340	4.02	0.0138
<b>Fe:Mg ratio</b>	-	-	1:0

Solution Name	Molecular Weight (g/mol)	Amount (mL)	Amount Cation (mol)
Sodium Hydroxide (5 M)	-	19.80	-
H <sub>2</sub> O	18.0153	419.96	-
Sulfuric Acid (0.5 M)	-	42.00	-
<b>Ending pH</b>	-	-	12.69

**Experiment - 3 (100-Mg, High SiO<sub>2</sub>)**

Chemical Name	Molecular Weight (g/mol)	Amount (g or mL)	Amount (mol)
Sodium Metasilicate - Pentahydrate	212.7400	4.36	0.0205
Magnesium Sulfate - Epsomite	246.4700	3.49	0.0142
<b>Fe:Mg ratio</b>	-	-	-

Solution Name	Molecular Weight (g/mol)	Amount (mL)	Amount Cation (mol)
Sodium Hydroxide (5 M)	-	19.80	-
H <sub>2</sub> O	18.0153	417.87	-
Sulfuric Acid (0.5 M)	-	42.00	-
<b>Ending pH</b>	-	-	12.88

**Experiment - 4 (15-Mg 85-Fe<sup>3+</sup>)**

Chemical Name	Molecular Weight (g/mol)	Amount (g or mL)	Amount (mol)
Sodium Metasilicate - Pentahydrate	212.7400	4.36	0.0205
Iron (III) Sulfate - Rhomboclase & Ferricopiapite	321.0340	3.42	0.0117
Magnesium Sulfate - Epsomite	246.4700	0.53	0.0022
<b>Fe:Mg ratio</b>	-	-	5:1

Solution Name	Molecular Weight (g/mol)	Amount (mL)	Amount Cation (mol)
Sodium Hydroxide (5 M)	-	19.80	-
H <sub>2</sub> O	18.0153	416.41	-
Sulfuric Acid (0.5 M)	-	42.00	-
<b>Ending pH</b>	-	-	12.76

**Experiment - 5 (50-Mg 50-Fe<sup>3+</sup>)**

Chemical Name	Molecular Weight (g/mol)	Amount (g or mL)	Amount (mol)
Sodium Metasilicate - Pentahydrate	212.7400	4.35	0.0204
Iron (III) Sulfate - Rhomboclase & Ferricopiapite	321.0340	2.02	0.0069
Magnesium Sulfate - Epsomite	246.4700	1.76	0.0071
<b>Fe:Mg ratio</b>	-	-	1:1

Solution Name	Molecular Weight (g/mol)	Amount (mL)	Amount Cation (mol)
Sodium Hydroxide (5 M)	-	19.80	-
H <sub>2</sub> O	18.0153	417.11	-
Sulfuric Acid (0.5 M)	-	42.00	-
<b>Ending pH</b>	-	-	12.79

**Experiment - 6 (10-Mg 90-Fe<sup>3+</sup>)**

Chemical Name	Molecular Weight (g/mol)	Amount (g or mL)	Amount (mol)
Sodium Metasilicate - Pentahydrate	212.7400	4.35	0.0204
Iron (III) Sulfate - Rhomboclase & Ferricopiapite	321.0340	3.90	0.0134
Magnesium Sulfate - Epsomite	246.4700	0.33	0.00134
<b>Fe:Mg ratio</b>	-	-	9:1

Solution Name	Molecular Weight (g/mol)	Amount (mL)	Amount Cation (mol)
Sodium Hydroxide (5 M)	-	19.80	-
H <sub>2</sub> O	18.0153	417.11	-
Sulfuric Acid (0.5 M)	-	42.00	-
<b>Ending pH</b>	-	-	12.71

**Experiment - 7 (5-Mg 95-Fe<sup>3+</sup>)**

Chemical Name	Molecular Weight (g/mol)	Amount (g or mL)	Amount (mol)
Sodium Metasilicate - Pentahydrate	212.7400	4.35	0.0204
Iron (III) Sulfate - Rhomboclase & Ferricopiapite	321.0340	4.25	0.0146
Magnesium Sulfate - Epsomite	246.4700	0.18	0.00073
<b>Fe:Mg ratio</b>	-	-	19:1

Solution Name	Molecular Weight (g/mol)	Amount (mL)	Amount Cation (mol)
Sodium Hydroxide (5 M)	-	19.80	-
H <sub>2</sub> O	18.0153	417.11	-
Sulfuric Acid (0.5 M)	-	42.00	-
<b>Ending pH</b>	-	-	12.64

**Experiment - 8 (100-Al, Low SiO<sub>2</sub>)**

Chemical Name	Molecular Weight (g/mol)	Amount (g or mL)	Amount (mol)
Sodium Metasilicate - Pentahydrate	212.7400	4.35	0.0204
Aluminum Sulfate - Alunogen	648.3900	9.75	0.0301
<b>Fe:Mg ratio</b>	-	-	-

Solution Name	Molecular Weight (g/mol)	Amount (mL)	Amount Cation (mol)
Sodium Hydroxide (5 M)	-	19.80	-
H <sub>2</sub> O	18.0153	416.42	-
Sulfuric Acid (0.5 M)	-	42.00	-
<b>Ending pH</b>	-	-	7.22

**Experiment - 9 (100-Mg, Low SiO<sub>2</sub>)**

Chemical Name	Molecular Weight (g/mol)	Amount (g or mL)	Amount (mol)
Sodium Metasilicate - Pentahydrate	212.7400	4.35	0.0204
Magnesium Sulfate - Epsomite	246.4700	8.00	0.0325
<b>Fe:Mg ratio</b>	-	-	-

Solution Name	Molecular Weight (g/mol)	Amount (mL)	Amount Cation (mol)
Sodium Hydroxide (5 M)	-	19.80	-
H <sub>2</sub> O	18.0153	416.84	-
Sulfuric Acid (0.5 M)	-	42.00	-
<b>Ending pH</b>	-	-	12.66

**Experiment - 10 (100-Al, High SiO<sub>2</sub>)**

Chemical Name	Molecular Weight (g/mol)	Amount (g or mL)	Amount (mol)
Sodium Metasilicate - Pentahydrate	212.7400	4.34	0.0204
Aluminum Sulfate - Alunogen	648.3900	4.71	0.0145
<b>Fe:Mg ratio</b>	-	-	-

Solution Name	Molecular Weight (g/mol)	Amount (mL)	Amount Cation (mol)
Sodium Hydroxide (5 M)	-	19.80	-
H <sub>2</sub> O	18.0153	417.10	-
Sulfuric Acid (0.5 M)	-	42.00	-
<b>Ending pH</b>	-	-	12.71

**Experiment - 11 (44-Al 14-Mg 42-Fe<sup>3+</sup>)**

Chemical Name	Molecular Weight (g/mol)	Amount (g or mL)	Amount (mol)
Sodium Metasilicate - Pentahydrate	212.7400	4.34	0.0204
Aluminum Sulfate - Alunogen	648.3900	2.01	0.0062
Iron (III) Sulfate - Rhomboclase & Ferricopiapite	321.0340	1.70	0.0058
Magnesium Sulfate - Epsomite	246.4700	0.50	0.0020
<b>Fe:Mg ratio</b>	-	-	3:1

Solution Name	Molecular Weight (g/mol)	Amount (mL)	Amount Cation (mol)
Sodium Hydroxide (5 M)	-	19.80	-
H <sub>2</sub> O	18.0153	418.48	-
Sulfuric Acid (0.5 M)	-	42.00	-
<b>Ending pH</b>	-	-	12.76

**Experiment - 12 (50-Al 50-Mg)**

Chemical Name	Molecular Weight (g/mol)	Amount (g or mL)	Amount (mol)
Sodium Metasilicate - Pentahydrate	212.7400	4.36	0.0205
Aluminum Sulfate - Alunogen	648.3900	2.35	0.0072
Magnesium Sulfate - Epsomite	246.4700	1.77	0.0072
<b>Fe:Mg ratio</b>	-	-	-

Solution Name	Molecular Weight (g/mol)	Amount (mL)	Amount Cation (mol)
Sodium Hydroxide (5 M)	-	19.80	-
H <sub>2</sub> O	18.0153	418.53	-
Sulfuric Acid (0.5 M)	-	42.00	-
<b>Ending pH</b>	-	-	12.81

**Table S2: Concentration of reagent grade chemicals that were incorporated into solution to produce the synthesized products at 100° C.**

**Experiment - 1 (100-Fe Control - Subsequently Oxidized)**

Chemical Name	Molecular Weight (g/mol)	Amount (g or mL)	Amount Cation (mol)
Sodium Metasilicate - Pentahydrate	212.7400	4.36	0.0205
Iron (II) Sulfate - Heptahydrate	278.0500	3.93	0.0141
Sodium Dithionite	174.1070	4.17	0.0240
<b>Fe:Mg ratio</b>	-	-	1:0

Solution Name	Molecular Weight (g/mol)	Amount (mL)	Amount Cation (mol)
Sodium Hydroxide (5 M)	NA	19.80	-
H <sub>2</sub> O	18.0153	417.74	-
Sulfuric Acid (0.5 M)	NA	41.00	-
<b>Ending pH</b>	-	-	12.58

**Experiment - 2 (100-Fe<sup>3+</sup>)**

Chemical Name	Molecular Weight (g/mol)	Amount (g or mL)	Amount (mol)
Sodium Metasilicate - Pentahydrate	212.7400	4.34	0.0204
Iron (III) Sulfate - Rhomboclase & Ferricopiapite	321.0340	4.04	0.0139
<b>Fe:Mg ratio</b>	-	-	1:0

Solution Name	Molecular Weight (g/mol)	Amount (mL)	Amount Cation (mol)
Sodium Hydroxide (5 M)	NA	19.80	-
H <sub>2</sub> O	18.0153	417.87	-
Sulfuric Acid (0.5 M)	NA	35.00	-
<b>Ending pH</b>	-	-	12.87

**Experiment - 3 (100-Mg, High SiO<sub>2</sub>)**

Chemical Name	Molecular Weight (g/mol)	Amount (g or mL)	Amount (mol)
Sodium Metasilicate - Pentahydrate	212.7400	4.34	0.0204
Magnesium Sulfate - Epsomite	246.4700	3.51	0.0142
<b>Fe:Mg ratio</b>	-	-	-

Solution Name	Molecular Weight (g/mol)	Amount (mL)	Amount Cation (mol)
Sodium Hydroxide (5 M)	-	19.80	-
H <sub>2</sub> O	18.0153	417.62	-
Sulfuric Acid (0.5 M)	-	35.00	-
<b>Ending pH</b>	-	-	12.98

**Experiment - 4 (15-Mg 85-Fe<sup>3+</sup>)**

Chemical Name	Molecular Weight (g/mol)	Amount (g or mL)	Amount (mol)
Sodium Metasilicate - Pentahydrate	212.7400	4.34	0.0204
Iron (III) Sulfate - Rhomboclase & Ferricopiapite	321.0340	3.41	0.0117
Magnesium Sulfate - Epsomite	246.4700	0.50	0.0020
<b>Fe:Mg ratio</b>	-	-	17:3

Solution Name	Molecular Weight (g/mol)	Amount (mL)	Amount Cation (mol)
Sodium Hydroxide (5 M)	-	19.80	-
H <sub>2</sub> O	18.0153	417.47	-
Sulfuric Acid (0.5 M)	-	35.00	-
<b>Ending pH</b>	-	-	12.89

**Experiment - 5 (50-Mg 50-Fe<sup>3+</sup>)**

Chemical Name	Molecular Weight (g/mol)	Amount (g or mL)	Amount (mol)
<i>Actual Experiment</i>			
Sodium Metasilicate - Pentahydrate	212.7400	4.33	0.0204
Iron (III) Sulfate - Rhomboclase & Ferricopiapite	321.0340	2.00	0.0069
Magnesium Sulfate - Epsomite	246.4700	1.76	0.0071
<b>Fe:Mg ratio</b>	-	-	1:1

Solution Name	Molecular Weight (g/mol)	Amount (mL)	Amount Cation (mol)
Sodium Hydroxide (5 M)	-	19.80	-
H <sub>2</sub> O	18.0153	416.62	-
Sulfuric Acid (0.5 M)	-	35.00	-
<b>Ending pH</b>	-	-	12.94

**Experiment - 8 (100-Al, Low SiO<sub>2</sub>)**

Chemical Name	Molecular Weight (g/mol)	Amount (g or mL)	Amount (mol)
Sodium Metasilicate - Pentahydrate	212.7400	4.37	0.0205
Aluminum Sulfate - Alunogen	648.3900	9.75	0.0301
<b>Fe:Mg ratio</b>	-	-	-

Solution Name	Molecular Weight (g/mol)	Amount (mL)	Amount Cation (mol)
Sodium Hydroxide (5 M)	-	19.80	-
H <sub>2</sub> O	18.0153	417.81	-
Sulfuric Acid (0.5 M)	-	35.00	-
<b>Ending pH</b>	-	-	7.52

**Experiment - 9 (100-Mg, Low SiO<sub>2</sub>)**

Chemical Name	Molecular Weight (g/mol)	Amount (g or mL)	Amount (mol)
Sodium Metasilicate - Pentahydrate	212.7400	4.37	0.0205
Magnesium Sulfate - Epsomite	246.4700	7.99	0.0324
<b>Fe:Mg ratio</b>	-	-	-

Solution Name	Molecular Weight (g/mol)	Amount (mL)	Amount Cation (mol)
Sodium Hydroxide (5 M)	-	19.80	-
H <sub>2</sub> O	18.0153	418.78	-
Sulfuric Acid (0.5 M)	-	35.00	-
<b>Ending pH</b>	-	-	12.84

**Experiment - 10 (100-Al, High SiO<sub>2</sub>)**

Chemical Name	Molecular Weight (g/mol)	Amount (g or mL)	Amount (mol)
Sodium Metasilicate - Pentahydrate	212.7400	4.36	0.0205
Aluminum Sulfate - Alunogen	648.3900	4.70	0.0145
<b>Fe:Mg ratio</b>	-	-	-

Solution Name	Molecular Weight (g/mol)	Amount (mL)	Amount Cation (mol)
Sodium Hydroxide (5 M)	-	19.80	-
H <sub>2</sub> O	18.0153	417.54	-
Sulfuric Acid (0.5 M)	-	35.00	-
<b>Ending pH</b>	-	-	12.87

**Experiment - 11 (44-Al 14-Mg 42-Fe<sup>3+</sup>)**

Chemical Name	Molecular Weight (g/mol)	Amount (g or mL)	Amount (mol)
Sodium Metasilicate - Pentahydrate	212.7400	4.35	0.0204
Aluminum Sulfate - Alunogen	648.3900	2.04	0.0063
Iron (III) Sulfate - Rhomboclase & Ferricopiapite	321.0340	1.70	0.0058
Magnesium Sulfate - Epsomite	246.4700	0.48	0.0019
<b>Fe:Mg ratio</b>	-	-	3:1

Solution Name	Molecular Weight (g/mol)	Amount (mL)	Amount Cation (mol)
Sodium Hydroxide (5 M)	-	19.80	-
H <sub>2</sub> O	18.0153	416.90	-
Sulfuric Acid (0.5 M)	-	35.00	-
<b>Ending pH</b>	-	-	12.90

**Experiment - 12 (50-Al 50-Mg)**

Chemical Name	Molecular Weight (g/mol)	Amount (g or mL)	Amount (mol)
Sodium Metasilicate - Pentahydrate	212.7400	4.34	0.0204
Aluminum Sulfate - Alunogen	648.3900	2.36	0.0073
Magnesium Sulfate - Epsomite	246.4700	1.74	0.0071
<b>Fe:Mg ratio</b>	-	-	-

Solution Name	Molecular Weight (g/mol)	Amount (mL)	Amount Cation (mol)
Sodium Hydroxide (5 M)	-	19.80	-
H <sub>2</sub> O	18.0153	417.27	-
Sulfuric Acid (0.5 M)	-	35.00	-
<b>Ending pH</b>	-	-	12.96

**Table S3: Mössbauer parameters for synthesized materials, precipitated at 150° C, as well as natural nontronites for comparison.**

Sample	Site	Weight	$\delta$ (Isomer Shift)	$\Delta$ (Quadrupole Splitting)	$\chi^2$	Source
*Nontronite N Au-1	Fe <sup>3+</sup>	0.61	0.35	0.24	2.10	This study
	Fe <sup>3+</sup>	0.39	0.60	0.68		
*Experiment 1 (100-Fe Control - Subsequently Oxidized)	Fe <sup>3+</sup>	0.60	0.81	1.09	5.57	This study
	Fe <sup>3+</sup>	0.40	0.67	0.46		
*Experiment 4 (15-Mg 85-Fe <sup>3+</sup> )	Fe <sup>3+</sup>	0.60	0.45	0.24	4.63	This study
	Fe <sup>3+</sup>	0.40	0.64	0.68		
*Experiment 5 (50-Mg 50-Fe <sup>3+</sup> )	Fe <sup>3+</sup>	0.54	0.33	0.24	2.35	This study
	Fe <sup>3+</sup>	0.46	0.58	0.68		
Nontronite (Garfield)	Fe <sup>3+</sup>	0.55	0.48	0.23	2.03	Ribeiro et al., 2009
	Fe <sup>3+</sup>	0.43	0.47	0.65		
Nontronite	Fe <sup>3+</sup>	NA	0.36-0.39	0.24-0.27	NA	Vandenberghé and De Grave, 2013
	Fe <sup>3+</sup>	NA	0.37-0.40	0.59-0.68		
Nontronite (Washington)	Fe <sup>3+</sup>	0.7	0.48	0.29	485	Goodman et al., 1976
	Fe <sup>3+</sup>	0.24	0.48	0.62		
	Fe <sup>3+</sup> <sub>tet</sub>	0.06	0.29	0.6		
Nontronite (Washington)	Fe <sup>3+</sup>	0.52	0.47	0.27	675	Goodman et al., 1976
	Fe <sup>3+</sup>	0.48	0.45	0.62		
Nontronite (Garfield)	Fe <sup>3+</sup>	0.54	0.5	0.27	437	Goodman et al., 1976
	Fe <sup>3+</sup>	0.37	0.5	0.62		
	Fe <sup>3+</sup> <sub>tet</sub>	0.09	0.3	0.47		
Nontronite (Garfield)	Fe <sup>3+</sup>	0.59	0.48	0.25	567	Goodman et al., 1976
	Fe <sup>3+</sup>	0.41	0.47	0.65		
Nontronite (Clausthal)	Fe <sup>3+</sup>	0.64	0.5	0.33	636	Goodman et al., 1976
	Fe <sup>3+</sup>	0.21	0.5	0.67		
	Fe <sup>3+</sup> <sub>tet</sub>	0.15	0.3	0.61		
Nontronite (Crocidolite)	Fe <sup>3+</sup>	0.59	0.49	0.34	469	Goodman et al., 1976
	Fe <sup>3+</sup>	0.22	0.49	0.67		
	Fe <sup>3+</sup> <sub>tet</sub>	0.19	0.29	0.56		
Nontronite (Koegas)	Fe <sup>3+</sup>	0.54	0.5	0.32	541	Goodman et al., 1976
	Fe <sup>3+</sup>	0.19	0.51	0.62		
	Fe <sup>3+</sup> <sub>tet</sub>	0.27	0.31	0.53		
Nontronite (Amosite)	Fe <sup>3+</sup>	0.51	0.49	0.34	556	Goodman et al., 1976
	Fe <sup>3+</sup>	0.21	0.5	0.64		
	Fe <sup>3+</sup> <sub>tet</sub>	0.28	0.31	0.54		
Nontronite (California)	Fe <sup>3+</sup>	0.44	0.5	0.33	475	Goodman et al., 1976
	Fe <sup>3+</sup>	0.24	0.5	0.6		
	Fe <sup>3+</sup> <sub>tet</sub>	0.32	0.31	0.48		
Nontronite (Riverside)	Fe <sup>3+</sup>	1	0.19	0.3	NA	Weldon et al., 1982
Nontronite (Washington)	Fe <sup>3+</sup>	1	0.5	0.4	NA	Taylor et al., 1968

\*Isomer shifts are reported relative to alpha-Fe.

**Table S4: Oxide weight percent of USGS standards used in this study.**

Oxide	AVG-2 <sup>A</sup>	BIR-1a <sup>B</sup>	DNC-1a <sup>C</sup>	GSP-2 <sup>D</sup>
SiO <sub>2</sub>	59.3 ± 0.7	47.96 ± 0.19	47.15 ± 0.21	66.6 ± 0.8
TiO <sub>2</sub>	1.05 ± 0.22	0.96 ± 0.01	0.48 ± 0.007	0.66 ± 0.02
Al <sub>2</sub> O <sub>3</sub>	16.91 ± 0.21	15.5 ± 0.15	18.34 ± 0.17	14.9 ± 0.2
FeO	-	8.34 ± 0.10	7.32 ± 0.06	-
Fe <sub>2</sub> O <sub>3</sub>	-	2.06 ± 0.10	1.79 ± 0.11	-
Fe <sub>2</sub> O <sub>3</sub> TOT	6.69 ± 0.1	-	-	4.90 ± 0.16
MnO	-	0.175 ± 0.003	0.15 ± 0.003	-
CaO	5.20 ± 0.13	13.3 ± 0.12	11.49 ± 0.07	2.10 ± 0.06
MgO	1.79 ± 0.03	9.70 ± 0.079	10.13 ± 0.11	0.96 ± 0.03
K <sub>2</sub> O	2.88 ± 0.11	0.030 ± 0.003	0.234 ± 0.009	5.38 ± 0.14
Na <sub>2</sub> O	4.19 ± 0.13	1.82 ± 0.045	1.89 ± 0.057	2.78 ± 0.09
P <sub>2</sub> O <sub>5</sub>	0.48 ± 0.02	0.021 ± 0.001	0.07 ± 0.005	0.29 ± 0.02
<b>Total</b>	<b>98.49</b>	<b>100.77</b>	<b>99.91</b>	<b>98.57</b>

<sup>A</sup>AVG-2 Andesite from the eastern side of Guano Valley, Oregon, USA (Flanagan, 1967; Flanagan, 1969).

<sup>B</sup>BIR-1a Basalt collected from interglacial lava flows (Reykjavik dolerites), Iceland (Flanagan, 1984).

<sup>C</sup>DNC-1a Dolerite collected from Braggtown Quarry near Durham, North Carolina, USA (Flanagan, 1984; Gladney and Roelandts, 1987; Govindaraju et al., 1994).

<sup>D</sup>GSP-2 Granodiorite from the Silver Plume Quarry, Colorado, USA (Wilson, 1998).



**Table S5: Results of alteration experiments of andesite (AVG-2) under alkaline conditions.**

Andesite (AVG-2)										
Sample ID	Bottle Material	Duration (Days)	Temperature (°C)	NaOH (M)	pH (End)	Oxidizing / Reducing	Drying Conditions	Sample (g)	Reaction Product (XRD)	
AVG-2 5M NaOH 5D	Glass	5	90	5.00	12.80	Oxidizing	Air Dried	0.66	Apophyllite, Hydroxy-Sodalite	
AVG-2 5M NaOH 10D	Glass	10	90	5.00	13.12	Oxidizing	Air Dried	0.67	Apophyllite, Hydroxy-Sodalite	
AVG-2 5M NaOH 15D	Glass	15	90	5.00	13.56	Oxidizing	Air Dried	0.87	Hydroxy-Sodalite	
AVG-2 5M NaOH 20D	Glass	20	90	5.00	13.15	Oxidizing	Air Dried	0.59	Erionite, Hydroxy-Sodalite	
AVG-2 5M NaOH 25D	Glass	25	90	5.00	13.09	Oxidizing	Air Dried	0.71	Erionite, Hydroxy-Sodalite	
AVG-2 5M NaOH 30D	Glass	30	90	5.00	13.25	Oxidizing	Air Dried	0.79	Erionite, Hydroxy-Sodalite	
AVG-2 5M NaOH 35D ***	Glass	35	90	5.00	13.09	Oxidizing	Air Dried	0.95	Erionite, Smectite-Hydroxy, Sodaite	
AVG-2 5M NaOH AIR	Glass	35	90	5.00	13.68	Reducing	Air Dried	0.76	Apophyllite, Erionite, Hydroxy-Sodalite, Smectite	
AVG-2 5M NaOH BOX ***	Glass	35	90	5.00	13.66	Reducing	Glove Box	0.65	Apophyllite, Erionite, Hydroxy-Sodalite, Smectite, Nahcolite	
AVG-2 5M NaOH BUB	Glass	35	90	5.00	13.69	Reducing	Bubbled / Air Dried	0.61	Apophyllite, Erionite, Hydroxy-Sodalite, Smectite	
AVG-2 5M NaOH 1:500	Plastic	21	90	5.00	13.96	Oxidizing	Air Dried	1.01	Magnesite, Kaoite, brucite, Ferrihydrite, <i>Serpentine</i>	
AVG-2 5M NaOH 1:2000 ***	Plastic	35	90	5.00	13.97	Oxidizing	Air Dried	1.01	Andradite, Kaoite, <i>Magnesite</i> , Magnetite, Brucite	
AVG-2 2M NaOH 1:1000 7D	Plastic	7	100	2.00	13.76	Oxidizing	Air Dried	1.01	Hematite, Magnetite, Katoite, Maghemite	
AVG-2 2M NaOH 1:1000 16D ***	Plastic	16	100	2.00	13.58	Oxidizing	Air Dried	1.00	Magnesium Fe Oxide, Katoite, Magnesite, Maghemite	
AVG-2 1M NaOH 1:500 ***	Plastic	21	90	1.00	13.66	Oxidizing	Air Dried	1.01	Magnetite, <i>Dolomite</i>	
AVG-2 1M NaOH 1:250 ***	Plastic	21	90	1.00	13.68	Oxidizing	Air Dried	0.99	Very Little alteration if any	
AVG-2 1M NaOH 1:167 ***	Plastic	21	90	1.00	13.60	Oxidizing	Air Dried	1.00	<i>Tobermorite</i>	
AVG-2 1M NaOH 1:125 ***	Plastic	21	90	1.00	13.67	Oxidizing	Air Dried	1.00	Tobermorite, Magnesioferrite, Magnetite	
AVG-2 1M NaOH 1:100 ***	Plastic	21	90	1.00	13.64	Oxidizing	Air Dried	1.00	Tobermorite, <i>Magnetite</i>	
AVG-2 1M NaOH 1:50 ***	Plastic	21	90	1.00	13.66	Oxidizing	Air Dried	1.01	None	
AVG-2 1M NaOH 1:25 ***	Plastic	21	90	1.00	13.71	Oxidizing	Air Dried	1.00	None	
AVG-2 1M NaOH 1:10 ***	Plastic	21	90	1.00	13.71	Oxidizing	Air Dried	0.99	None	
AVG-2 0.5M NaOH 5D	Glass	5	90	0.50	12.49	Oxidizing	Air Dried	0.64	None	
AVG-2 0.5M NaOH 10D	Glass	10	90	0.50	12.38	Oxidizing	Air Dried	0.65	Garronite, Phillipsite	
AVG-2 0.5M NaOH 15D	Glass	15	90	0.50	12.10	Oxidizing	Air Dried	0.75	Garronite, Phillipsite	
AVG-2 0.5M NaOH 20D	Glass	20	90	0.50	12.82	Oxidizing	Air Dried	0.63	Garronite, Phillipsite	
AVG-2 0.5M NaOH 25D	Glass	25	90	0.50	12.66	Oxidizing	Air Dried	0.70	Garronite, Phillipsite	
AVG-2 0.5M NaOH 30D	Glass	30	90	0.50	12.89	Oxidizing	Air Dried	0.78	Garronite, Phillipsite	
AVG-2 0.5M NaOH 35D ***	Glass	35	90	0.50	12.68	Oxidizing	Air Dried	0.93	Garronite, Smectite, Phillipsite	
AVG-2 0.5M NaOH AIR	Glass	35	90	0.50	12.39	Reducing	Air Dried	0.73	Garronite, Phillipsite	
AVG-2 0.5M NaOH BOX ***	Glass	35	90	0.50	12.52	Reducing	Glove Box	0.66	Garronite, Phillipsite	
AVG-2 0.5M NaOH BUB	Glass	35	90	0.50	12.55	Reducing	Bubbled / Air Dried	0.87	Garronite, Phillipsite	
AVG-2 0.5M NaOH 1:500	Plastic	21	90	0.50	13.44	Oxidizing	Air Dried	0.98	Hematite, Magnetite, Magnesioferrite, <i>Antigorite</i> , Maghemite	
AVG-2 0.5M NaOH 1:200 ***	Plastic	35	90	0.50	13.42	Oxidizing	Air Dried	0.98	Tobermorite	
AVG-2 0.05M NaOH 5D	Glass	5	90	0.05	11.88	Oxidizing	Air Dried	0.80	None	
AVG-2 0.05M NaOH 10D	Glass	10	90	0.05	12.13	Oxidizing	Air Dried	0.60	None	
AVG-2 0.05M NaOH 15D	Glass	15	90	0.05	12.07	Oxidizing	Air Dried	0.75	Garronite/Phillipsite	
AVG-2 0.05M NaOH 20D	Glass	20	90	0.05	12.25	Oxidizing	Air Dried	0.63	Garronite, Phillipsite	
AVG-2 0.05M NaOH 25D	Glass	25	90	0.05	11.64	Oxidizing	Air Dried	0.65	Garronite, Phillipsite	
AVG-2 0.05M NaOH 30D	Glass	30	90	0.05	11.99	Oxidizing	Air Dried	0.64	Garronite, Phillipsite	
AVG-2 0.05M NaOH 35D ***	Glass	35	90	0.05	11.55	Oxidizing	Air Dried	0.62	Garronite, Phillipsite	
AVG-2 0.05M NaOH AIR	Glass	35	90	0.05	8.12	Reducing	Air Dried	0.64	None	
AVG-2 0.05M NaOH BOX ***	Glass	35	90	0.05	8.05	Reducing	Glove Box	0.66	None	
AVG-2 0.05M NaOH BUB	Glass	35	90	0.05	8.09	Reducing	Bubbled / Air Dried	0.76	None	
AVG-2 0.05M NaOH 1:500	Plastic	21	90	0.05	12.72	Oxidizing	Air Dried	1.02	None	
AVG-2 0.05M NaOH 1:200 ***	Plastic	35	90	0.05	12.80	Oxidizing	Air Dried	1.00	Little to no alteration	

Products in italics are tentatively identified

**Table S6: Results of alteration experiments of basalt (BIR-1a) under alkaline conditions.**

Basalt (BIR-1a)									
Sample ID	Bottle Material	Duration (Days)	Temperature (°C)	NaOH (M)	pH (End)	Oxidizing / Reducing	Drying Conditions	Sample (g)	Reaction Product (XRD)
BIR-1a 5M NaOH 5D	Glass	5	90	5.00	13.80	Oxidizing	Air Dried	0.81	Apophyllite, Erionite
BIR-1a 5M NaOH 10D	Glass	10	90	5.00	13.83	Oxidizing	Air Dried	0.72	Apophyllite, Erionite
BIR-1a 5M NaOH 15D	Glass	15	90	5.00	13.80	Oxidizing	Air Dried	0.78	Apophyllite, Erionite
BIR-1a 5M NaOH 20D	Glass	20	90	5.00	13.95	Oxidizing	Air Dried	0.71	Apophyllite, Erionite, Smectite, Hydroxy-Soalдите
BIR-1a 5M NaOH 25D	Glass	25	90	5.00	13.95	Oxidizing	Air Dried	0.82	Apophyllite, Erionite, Smectite, Hydroxy-Soalдите
BIR-1a 5M NaOH 30D	Glass	30	90	5.00	13.74	Oxidizing	Air Dried	0.77	Apophyllite, Erionite, Smectite, Hydroxy-Soalдите
BIR-1a 5M NaOH 35D ***	Glass	35	90	5.00	13.89	Oxidizing	Air Dried	0.65	Apophyllite, Erionite, Smectite, Hydroxy-Soalдите
BIR-1a 5M NaOH AIR	Glass	35	90	5.00	-	Reducing	Air Dried	0.80	Apophyllite, Erionite, Hydroxy-Sodalite, Smectite
BIR-1a 5M NaOH BOX ***	Glass	35	90	5.00	13.68	Reducing	Glove Box	0.84	Apophyllite, Erionite, Hydroxy-Sodalite, Smectite, Nahcolite
BIR-1a 5M NaOH BUB	Glass	35	90	5.00	13.52	Reducing	Bubbled / Air Dried	0.84	Apophyllite, Erionite, Hydroxy-Sodalite, Smectite
BIR-1a 5M NaOH 1:500	Plastic	21	90	5.00	13.94	Oxidizing	Air Dried	1.00	Brucite, Hydro-Andradite, Magnetite, <i>Halloysite</i> , <i>Dolomite</i>
BIR-1a 5M NaOH 1:200 ***	Plastic	35	90	5.00	14.04	Oxidizing	Air Dried	1.00	Katoite, Brucite, Bayerite, Magnetite
BIR-1a 2M NaOH 1:1000 7D	Plastic	7	100	2.00	13.73	Oxidizing	Air Dried	1.01	Magnetite, Katoite, Tobermorite
BIR-1a 2M NaOH 1:1000 16D ***	Plastic	16	100	2.00	13.70	Oxidizing	Air Dried	1.01	Serpentine, Magnetite, Katoite
BIR-1a 1M NaOH 1:500 ***	Plastic	21	90	1.00	13.42	Oxidizing	Air Dried	1.00	Tobermorite
BIR-1a 1M NaOH 1:250 ***	Plastic	21	90	1.00	13.66	Oxidizing	Air Dried	1.00	Tobermorite, Magnetite
BIR-1a 1M NaOH 1:167 ***	Plastic	21	90	1.00	13.54	Oxidizing	Air Dried	1.00	Tobermorite
BIR-1a 1M NaOH 1:125 ***	Plastic	21	90	1.00	13.63	Oxidizing	Air Dried	1.00	Tobermorite, Magnetite, Magnesferrite
BIR-1a 1M NaOH 1:100 ***	Plastic	21	90	1.00	13.68	Oxidizing	Air Dried	1.00	Tobermorite Magnesioferrite, Magnetite
BIR-1a 1M NaOH 1:50 ***	Plastic	21	90	1.00	13.72	Oxidizing	Air Dried	0.98	Tobermorite, Magnetite
BIR-1a 1M NaOH 1:25 ***	Plastic	21	90	1.00	13.80	Oxidizing	Air Dried	0.99	Tobermorite
BIR-1a 1M NaOH 1:10 ***	Plastic	21	90	1.00	13.78	Oxidizing	Air Dried	0.98	Manetite, <i>Serpentine</i>
BIR-1a 0.5M NaOH 5D	Glass	5	90	0.50	13.43	Oxidizing	Air Dried	0.71	None
BIR-1a 0.5M NaOH 10D	Glass	10	90	0.50	13.33	Oxidizing	Air Dried	0.75	Garronite, Phillipsite
BIR-1a 0.5M NaOH 15D	Glass	15	90	0.50	13.25	Oxidizing	Air Dried	0.76	Garronite, Phillipsite
BIR-1a 0.5M NaOH 20D	Glass	20	90	0.50	13.24	Oxidizing	Air Dried	0.88	Garronite, Phillipsite
BIR-1a 0.5M NaOH 25D	Glass	25	90	0.50	13.14	Oxidizing	Air Dried	0.71	Garronite, Phillipsite
BIR-1a 0.5M NaOH 30D	Glass	30	90	0.50	13.04	Oxidizing	Air Dried	0.69	Garronite, Phillipsite
BIR-1a 0.5M NaOH 35D ***	Glass	35	90	0.50	12.88	Oxidizing	Air Dried	0.74	Garronite, Smectite, Phillipsite
BIR-1a 0.5M NaOH AIR	Glass	35	90	0.50	12.66	Reducing	Air Dried	0.78	Garronite, Phillipsite
BIR-1a 0.5M NaOH BOX ***	Glass	35	90	0.50	12.71	Reducing	Glove Box	0.96	Garronite, Phillipsite
BIR-1a 0.5M NaOH BUB	Glass	35	90	0.50	12.72	Reducing	Bubbled / Air Dried	0.94	Garronite, Phillipsite
BIR-1a 0.5M NaOH 1:500	Plastic	31	90	0.50	12.87	Oxidizing	Air Dried	1.01	Magnetite, Tobermorite, <i>Calcite</i> , <i>Kanoite</i>
BIR-1a 0.5M NaOH 1:200 ***	Plastic	35	90	0.50	13.54	Oxidizing	Air Dried	1.02	Tobermorite, Magnetite
BIR-1a 0.05M NaOH 5D	Glass	5	90	0.05	11.57	Oxidizing	Air Dried	0.76	None
BIR-1a 0.05M NaOH 10D	Glass	10	90	0.05	12.20	Oxidizing	Air Dried	0.75	None
BIR-1a 0.05M NaOH 15D	Glass	15	90	0.05	12.19	Oxidizing	Air Dried	0.76	None
BIR-1a 0.05M NaOH 20D	Glass	20	90	0.05	13.11	Oxidizing	Air Dried	0.78	None
BIR-1a 0.05M NaOH 25D	Glass	25	90	0.05	12.88	Oxidizing	Air Dried	0.74	Garronite/Phillipsite
BIR-1a 0.05M NaOH 30D	Glass	30	90	0.05	12.44	Oxidizing	Air Dried	0.79	Garronite, Phillipsite
BIR-1a 0.05M NaOH 35D ***	Glass	35	90	0.05	12.22	Oxidizing	Air Dried	0.94	Garronite, Phillipsite
BIR-1a 0.05M NaOH AIR (BS)	Glass	35	90	0.05	5.23	Reducing	Air Dried	0.68	None
BIR-1a 0.05M NaOH BOX ***	Glass	35	90	0.05	8.13	Reducing	Glove Box	0.65	None
BIR-1a 0.05M NaOH BUB	Glass	35	90	0.05	8.21	Reducing	Bubbled / Air Dried	0.83	None
BIR-1a 0.05M NaOH 1:500	Plastic	21	90	0.05	12.87	Oxidizing	Air Dried	1.01	<i>Kanoite</i> Magnetite, <i>Chrysotile</i>
BIR-1a 0.05M NaOH 1:200 ***	Plastic	35	90	0.05	12.90	Oxidizing	Air Dried	0.98	Tobermorite

Products in italics are tentatively identified.

**Table S7: Results of alteration experiments of diabase (DNC-1a) under alkaline conditions.**

Diabase (DNC-1a)										
Sample ID	Bottle Material	Duration (Days)	Temperature (°C)	NaOH (M)	pH (End)	Oxidizing / Reducing	Drying Conditions	Sample (g)	Reaction Product (XRD)	
DNC-1a 5M NaOH 5D	Glass	5	90	5.00	12.65	Oxidizing	Air Dried	0.95	Apophyllite	
DNC-1a 5M NaOH 10D	Glass	10	90	5.00	13.84	Oxidizing	Air Dried	0.52	Apophyllite, Hydroxy-Sodalite	
DNC-1a 5M NaOH 15D	Glass	15	90	5.00	12.86	Oxidizing	Air Dried	0.71	Apophyllite, Hydroxy-Sodalite	
DNC-1a 5M NaOH 20D	Glass	20	90	5.00	13.34	Oxidizing	Air Dried	0.71	Apophyllite, Hydroxy-Sodalite	
DNC-1a 5M NaOH 25D	Glass	25	90	5.00	13.14	Oxidizing	Air Dried	0.71	Apophyllite, Hydroxy-Sodalite	
DNC-1a 5M NaOH 30D	Glass	30	90	5.00	13.27	Oxidizing	Air Dried	0.94	Erionite, Smectite, Hydroxy-Sodalite	
DNC-1a 5M NaOH 35D ***	Glass	35	90	5.00	NA	Oxidizing	Air Dried	0.83	Erionite, Smectite, Hydroxy-Sodalite	
DNC-1a 5M NaOH AIR	Glass	35	90	5.00	13.71	Reducing	Air Dried	0.82	Apophyllite, Erionite, Hydroxy-Sodalite, Smectite	
DNC-1a 5M NaOH BOX ***	Glass	35	90	5.00	13.68	Reducing	Glove Box	0.73	Apophyllite, Erionite, Hydroxy-Sodalite, Smectite, Nahcolite	
DNC-1a 5M NaOH BUB	Glass	35	90	5.00	13.88	Reducing	Bubbled / Air Dried	0.75	Apophyllite, Erionite, Hydroxy-Sodalite, Smectite	
DNC-1a 5M NaOH 1:500	Plastic	21	90	5.00	13.90	Oxidizing	Air Dried	0.99	Katoite, Brucite, Magnesite, Magnetite, <i>Serpentine</i>	
DNC-1a 5M NaOH 1:200 ***	Plastic	35	90	5.00	13.90	Oxidizing	Air Dried	0.99	Andradite, Katoite, Antigorite, Lizardite, Magnetite	
DNC-1a 2M NaOH 1:1000 7D	Plastic	7	100	2.00	13.75	Oxidizing	Air Dried	1.01	Hematite, Katoite, Tobermorite, Lizardite, Magnetite	
DNC-1a 2M NaOH 1:1000 16D ***	Plastic	16	100	2.00	13.55	Oxidizing	Air Dried	0.99	Tobermorite, Serpentine Minerals (Lizardite, Crystolite), Smect	
DNC-1a 1M NaOH 1:500 ***	Plastic	21	90	1.00	13.56	Oxidizing	Air Dried	1.00	Tobermorite, <i>Serpentine</i>	
DNC-1a 1M NaOH 1:250 ***	Plastic	21	90	1.00	13.57	Oxidizing	Air Dried	0.99	Tobermorite, Magnetite, <i>Serpentine</i>	
DNC-1a 1M NaOH 1:167 ***	Plastic	21	90	1.00	13.60	Oxidizing	Air Dried	1.00	Tobermorite, <i>Serpentine</i>	
DNC-1a 1M NaOH 1:125 ***	Plastic	21	90	1.00	13.46	Oxidizing	Air Dried	1.00	Magnetite, Magnesioferrite, <i>Serpentine</i>	
DNC-1a 1M NaOH 1:100 ***	Plastic	21	90	1.00	13.70	Oxidizing	Air Dried	1.00	Tobermorite, <i>Serpentine minerals</i>	
DNC-1a 1M NaOH 1:50 ***	Plastic	21	90	1.00	13.65	Oxidizing	Air Dried	1.03	Tobermorite, <i>Serpentine</i>	
DNC-1a 1M NaOH 1:25 ***	Plastic	21	90	1.00	13.67	Oxidizing	Air Dried	1.02	None	
DNC-1a 1M NaOH 1:10 ***	Plastic	21	90	1.00	13.59	Oxidizing	Air Dried	1.01	None	
DNC-1a 0.5M NaOH 5D	Glass	5	90	0.50	12.56	Oxidizing	Air Dried	0.78	Phillipsite, Thompsonite	
DNC-1a 0.5M NaOH 10D	Glass	10	90	0.50	12.46	Oxidizing	Air Dried	0.68	Phillipsite, Thompsonite	
DNC-1a 0.5M NaOH 15D	Glass	15	90	0.50	12.20	Oxidizing	Air Dried	0.63	Phillipsite, Thompsonite	
DNC-1a 0.5M NaOH 20D	Glass	20	90	0.50	12.85	Oxidizing	Air Dried	0.60	Analcime, Phillipsite, Thompsonite	
DNC-1a 0.5M NaOH 25D	Glass	25	90	0.50	12.72	Oxidizing	Air Dried	0.64	Analcime, Phillipsite, Thompsonite	
DNC-1a 0.5M NaOH 30D	Glass	30	90	0.50	12.74	Oxidizing	Air Dried	0.82	Analcime, Phillipsite, Thompsonite	
DNC-1a 0.5M NaOH 35D ***	Glass	35	90	0.50	12.74	Oxidizing	Air Dried	0.64	Analcime, Phillipsite, Smectite, Thompsonite	
DNC-1a 0.5M NaOH AIR	Glass	35	90	0.50	12.54	Reducing	Air Dried	0.95	Analcime, Garnonite, Phillipsite, Thompsonite, Smectite	
DNC-1a 0.5M NaOH BOX ***	Glass	35	90	0.50	12.62	Reducing	Glove Box	0.79	Analcime, Garnonite, Phillipsite, Thompsonite, Smectite	
DNC-1a 0.5M NaOH BUB	Glass	35	90	0.50	12.68	Reducing	Bubbled / Air Dried	0.66	Analcime, Garnonite, Phillipsite, Thompsonite, Smectite	
DNC-1a 0.5M NaOH 1:500	Plastic	21	90	0.50	13.49	Oxidizing	Air Dried	0.98	Tobermorite, Maghemite, <i>Serpentine</i>	
DNC-1a 0.5M NaOH 1:200 ***	Plastic	35	90	0.50	13.51	Oxidizing	Air Dried	0.98	Magnetite, Tobermorite	
DNC-1a 0.05M NaOH 5D	Glass	5	90	0.05	11.72	Oxidizing	Air Dried	0.97	None	
DNC-1a 0.05M NaOH 10D	Glass	10	90	0.05	12.20	Oxidizing	Air Dried	0.71	None	
DNC-1a 0.05M NaOH 15D	Glass	15	90	0.05	11.71	Oxidizing	Air Dried	0.85	None	
DNC-1a 0.05M NaOH 20D	Glass	20	90	0.05	11.81	Oxidizing	Air Dried	0.83	None	
DNC-1a 0.05M NaOH 25D	Glass	25	90	0.05	12.11	Oxidizing	Air Dried	0.83	None	
DNC-1a 0.05M NaOH 30D	Glass	30	90	0.05	12.31	Oxidizing	Air Dried	0.83	None	
DNC-1a 0.05M NaOH 35D ***	Glass	35	90	0.05	12.16	Oxidizing	Air Dried		None	
DNC-1a 0.05M NaOH AIR	Glass	35	90	0.05	8.18	Reducing	Air Dried	0.69	None	
DNC-1a 0.05M NaOH BOX ***	Glass	35	90	0.05	8.14	Reducing	Glove Box	0.68	None	
DNC-1a 0.05M NaOH BUB	Glass	35	90	0.05	8.15	Reducing	Bubbled / Air Dried	0.79	None	
DNC-1a 0.05M NaOH 1:500	Plastic	21	90	0.05	12.84	Oxidizing	Air Dried	1.01	None	
DNC-1a 0.05M NaOH 1:200 ***	Plastic	35	90	0.05	12.81	Oxidizing	Air Dried	0.98	Tobermorite, Antigorite	

Products in italics are tentatively identified

**Table S8: Results of alteration experiments of grandodiorite (GSP-2) under alkaline conditions.**

Grandodiorite (GSP-2)										
Sample ID	Bottle Material	Duration (Days)	Temperature (°C)	NaOH (M)	pH (End)	Oxidizing / Reducing	Drying Conditions	Sample (g)	Reaction Product (XRD)	
GSP-2 5M NaOH 5D	Glass	5	90	5.00	12.94	Oxidizing	Air Dried	0.54	None	
GSP-2 5M NaOH 10D	Glass	10	90	5.00	13.59	Oxidizing	Air Dried	0.62	Hydroxy-Sodalite	
GSP-2 5M NaOH 15D	Glass	15	90	5.00	13.55	Oxidizing	Air Dried	0.87	Hydroxy-Sodalite	
GSP-2 5M NaOH 20D	Glass	20	90	5.00	13.32	Oxidizing	Air Dried	0.66	Hydroxy-Sodalite	
GSP-2 5M NaOH 25D	Glass	25	90	5.00	12.94	Oxidizing	Air Dried	0.79	Hydroxy-Sodalite	
GSP-2 5M NaOH 30D	Glass	30	90	5.00	13.29	Oxidizing	Air Dried	0.62	Hydroxy-Sodalite	
GSP-2 5M NaOH 35D ***	Glass	35	90	5.00	13.18	Oxidizing	Air Dried	0.76	Erionite, Smectite, Hydroxy-Sodalite	
GSP-2 5M NaOH AIR	Glass	35	90	5.00	13.55	Reducing	Air Dried	0.80	Apophyllite, Hydroxy-Sodalite, Smectite	
GSP-2 5M NaOH BOX	Glass	35	90	5.00	13.66	Reducing	Glove Box	0.71	Apophyllite, Hydroxy-Sodalite, Smectite, Nahcolite	
GSP-2 5M NaOH BUB	Glass	35	90	5.00	13.54	Reducing	Bubbled / Air Dried	0.68	Apophyllite, Hydroxy-Sodalite, Smectite	
GSP-2 5M NaOH 1:500	Plastic	21	90	5.00	14.03	Oxidizing	Air Dried	0.99	Katoite	
GSP-2 5M NaOH 1:200 ***	Plastic	35	90	5.00	13.97	Oxidizing	Air Dried	1.02	Andradtite, Katoite	
GSP-2 2M NaOH 1:1000 7D	Plastic	7	100	2.00	13.61	Oxidizing	Air Dried	1.00	<i>Tobermorite</i>	
GSP-2 2M NaOH 1:1000 16D ***	Plastic	16	100	2.00	13.64	Oxidizing	Air Dried	1.00	Tobermorite, Magnetite, Katotie	
GSP-2 1M NaOH 1:500 ***	Plastic	21	90	1.00	13.72	Oxidizing	Air Dried	0.98	Tobermorite	
GSP-2 1M NaOH 1:250 ***	Plastic	21	90	1.00	13.69	Oxidizing	Air Dried	1.00	Tobermorite	
GSP-2 1M NaOH 1:167 ***	Plastic	21	90	1.00	13.49	Oxidizing	Air Dried	1.00	None	
GSP-2 1M NaOH 1:125 ***	Plastic	21	90	1.00	13.58	Oxidizing	Air Dried	1.00	None	
GSP-2 1M NaOH 1:100 ***	Plastic	21	90	1.00	13.64	Oxidizing	Air Dried	1.00	None	
GSP-2 1M NaOH 1:50 ***	Plastic	21	90	1.00	13.70	Oxidizing	Air Dried	0.99	None	
GSP-2 1M NaOH 1:25 ***	Plastic	21	90	1.00	13.64	Oxidizing	Air Dried	0.98	None	
GSP-2 1M NaOH 1:10 ***	Plastic	21	90	1.00	13.60	Oxidizing	Air Dried	0.98	None	
GSP-2 0.5M NaOH 5D	Glass	5	90	0.50	12.27	Oxidizing	Air Dried	0.69	None	
GSP-2 0.5M NaOH 10D	Glass	10	90	0.50	12.61	Oxidizing	Air Dried	0.66	Garronite, Phillipsite	
GSP-2 0.5M NaOH 15D	Glass	15	90	0.50	12.45	Oxidizing	Air Dried	0.67	Garronite, Phillipsite	
GSP-2 0.5M NaOH 20D	Glass	20	90	0.50	12.86	Oxidizing	Air Dried	0.72	Garronite, Phillipsite	
GSP-2 0.5M NaOH 25D	Glass	25	90	0.50	12.66	Oxidizing	Air Dried	0.57	Garronite, Phillipsite	
GSP-2 0.5M NaOH 30D	Glass	30	90	0.50	12.81	Oxidizing	Air Dried	0.70	Garronite, Phillipsite	
GSP-2 0.5M NaOH 35D ***	Glass	35	90	0.50	12.67	Oxidizing	Air Dried	0.79	Garronite, Smectite, Phillipsite	
GSP-2 0.5M NaOH 1:500	Plastic	21	90	0.50	13.52	Oxidizing	Air Dried	0.99	Tobermorite, Hematite, Hauyne	
GSP-2 0.5M NaOH 1:200 ***	Plastic	35	90	0.50	13.42	Oxidizing	Air Dried	1.00	<i>Altered Mica</i>	
GSP-2 0.05M NaOH 5D	Glass	5	90	0.05	11.57	Oxidizing	Air Dried	0.75	None	
GSP-2 0.05M NaOH 10D	Glass	10	90	0.05	12.20	Oxidizing	Air Dried	0.97	None	
GSP-2 0.05M NaOH 15D	Glass	15	90	0.05	12.19	Oxidizing	Air Dried	0.89	None	
GSP-2 0.05M NaOH 20D	Glass	20	90	0.05	12.49	Oxidizing	Air Dried	0.95	None	
GSP-2 0.05M NaOH 25D	Glass	25	90	0.05	12.03	Oxidizing	Air Dried	0.89	None	
GSP-2 0.05M NaOH 30D	Glass	30	90	0.05	12.34	Oxidizing	Air Dried	1.00	None	
GSP-2 0.05M NaOH 35D ***	Glass	35	90	0.05	12.33	Oxidizing	Air Dried	0.91	None	
GSP-2 0.05M NaOH 1:500	Plastic	21	90	0.05	12.79	Oxidizing	Air Dried	0.98	None	
GSP-2 0.05M NaOH 1:200 ***	Plastic	35	90	0.05	12.94	Oxidizing	Air Dried	0.99	None	

Products in italics are tentatively identified

**Table S9: Compositions of synthesized material determined through microprobe analysis.**

<b>Weight Percent</b>	<b>Experiment 1</b>	<b><math>\sigma</math></b>	<b>Experiment 2</b>	<b><math>\sigma</math></b>	<b>Experiment 3</b>	<b><math>\sigma</math></b>	<b>Experiment 4</b>	<b><math>\sigma</math></b>	<b>Experiment 5</b>	<b><math>\sigma</math></b>
<b>Na<sub>2</sub>O</b>	2.974	1.168	5.553	1.239	1.766	0.601	4.083	1.081	3.041	0.583
<b>Cr<sub>2</sub>O<sub>3</sub></b>	0.011	0.009	0.010	0.015	0.017	0.022	0.012	0.016	0.019	0.020
<b>Cl</b>	0.022	0.016	0.031	0.012	0.024	0.012	0.018	0.016	0.014	0.014
<b>M<sub>g</sub>O</b>	0.012	0.011	0.067	0.023	25.633	9.036	4.789	0.998	17.384	0.634
<b>SiO<sub>2</sub></b>	39.066	1.097	23.578	0.359	42.078	3.866	32.060	2.033	41.958	1.063
<b>TiO<sub>2</sub></b>	0.021	0.026	0.015	0.017	0.015	0.014	0.024	0.020	0.015	0.019
<b>K<sub>2</sub>O</b>	0.399	0.135	0.656	0.130	0.208	0.041	0.627	0.263	0.383	0.162
<b>Al<sub>2</sub>O<sub>3</sub></b>	0.078	0.021	0.144	0.050	0.090	0.059	0.117	0.046	0.113	0.033
<b>MnO</b>	0.035	0.017	0.034	0.021	0.014	0.015	0.041	0.024	0.033	0.024
<b>CaO</b>	0.042	0.030	0.117	0.030	0.039	0.014	0.070	0.027	0.054	0.022
<b>F</b>	0.020	0.057	0.000	0.000	0.074	0.097	0.018	0.036	0.011	0.023
<b>FeO</b>	48.383	1.286	65.221	1.068	0.052	0.027	54.699	2.549	31.758	0.981
<b>P<sub>2</sub>O<sub>5</sub></b>	0.452	0.133	1.464	0.272	0.277	0.198	0.547	0.151	0.406	0.189
<b>*Total</b>	<b>91.502</b>	<b>1.315</b>	<b>96.881</b>	<b>2.148</b>	<b>70.251</b>	<b>11.770</b>	<b>97.094</b>	<b>2.050</b>	<b>95.181</b>	<b>1.129</b>

\*Low totals, characteristic of many clay minerals, are due to dehydration under desiccation and significant structural OH. In addition, EMP analysis relies on a relatively flat sample surfaces; this can be difficult to achieve, due to etching and pitting during the polishing process. Clay minerals are also highly porous, which may contribute to low totals observed in this study and within the literature by EMP analysis (Treiman et al., 2014).

**Table S10: Compositions of naturally occurring nontronites, all of which contain at least minor concentrations of Mg.**

Name	Equation	Source
NAU-1 - Nontronite	$M^{2+}_{0.5025}[Al_{1.02}Si_{6.98}][Fe_{3.68}Mg_{0.04}Al_{0.29}]O_{20}(OH)_4$	Keeling et al., 2000
NAU-2 - Nontronite	$M^{2+}_{0.36}[Al_{0.45}Si_{7.55}][Fe_{3.83}Mg_{0.05}]O_{20}(OH)_4$	Keeling et al., 2000
Garfield - Nontronite	$M^{2+}_{0.405}[Al_{0.780}Si_{7.22}][Al_{0.31}Fe^{3+}_{3.64}Fe^{2+}_{0.01}Mg_{0.04}]O_{20}(OH)_4$	Manceau et al., 2000
PV - Nontronite	$Mg_{0.445}[Al_{0.43}Si_{7.57}][Al_{0.65}Fe^{3+}_{2.87}Fe^{2+}_{0.01}Mg_{0.47}]O_{20}(OH)_4$	Manceau et al., 2000
SWA-1 - Nontronite	$M^{2+}_{0.435}[Al_{0.623}Si_{7.38}][Al_{1.08}Fe^{3+}_{2.67}Fe^{2+}_{0.01}Mg_{0.23}]O_{20}(OH)_4$	Manceau et al., 2000
NG-1 - Nontronite	$M^{2+}_{0.35}[Fe^{3+}_{0.63}Al_{0.08}Si_{7.29}][Al_{0.88}Fe^{3+}_{3.08}Fe^{2+}_{0.01}Mg_{0.06}]O_{20}(OH)_4$	Manceau et al., 2000
Chad - Nontronite	$M^{2+}_{0.22}[Al_{0.17}Si_{3.83}][Fe_{1.77}Mg_{0.21}]O_{10}(OH)_2$	Tardy and Fritiz, 1981
Caledonia - Nontronite	$M^{2+}_{0.135}[Al_{0.27}Si_{3.73}][Al_{0.07}Fe_{1.72}Mg_{0.315}]O_{10}(OH)_2$	Tardy and Fritiz, 1981
CLA - Nontronite	$M^{2+}_{0.52}[Al_{0.13}Si_{6.81}Fe_{1.06}][Fe_{4.01}Mg_{0.07}]O_{20}(OH)_4$	Goodman et al., 1976
CRO - Nontronite	$M^{2+}_{0.535}[Al_{0.063}Si_{6.75}Fe_{1.19}][Fe_{3.90}Mg_{0.24}]O_{20}(OH)_4$	Goodman et al., 1976
CAL - Nontronite	$M^{2+}_{0.625}[Al_{0.14}Si_{6.21}Fe_{1.65}][Fe_{4.04}Mg_{0.21}]O_{20}(OH)_4$	Goodman et al., 1976
AMO - Nontronite	$M^{2+}_{0.37}[Al_{0.04}Si_{6.84}Fe_{1.12}][Fe_{4.04}Mg_{0.15}]O_{20}(OH)_4$	Goodman et al., 1976
GAR - Nontronite	$M^{2+}_{0.6}[Al_{1.05}Si_{6.84}Fe_{0.11}][Fe_{3.96}Mg_{0.04}]O_{20}(OH)_4$	Goodman et al., 1976
WAS - Nontronite	$M^{2+}_{0.405}[Al_{0.70}Si_{7.30}][Al_{1.06}Fe_{2.73}Mg_{0.26}]O_{20}(OH)_4$	Goodman et al., 1976
KOE - Nontronite	$M^{2+}_{0.505}[Al_{0.08}Si_{6.61}Fe_{1.31}][Fe_{4.06}Mg_{0.10}]O_{20}(OH)_4$	Goodman et al., 1976

## SUPPLEMENTARY FIGURES

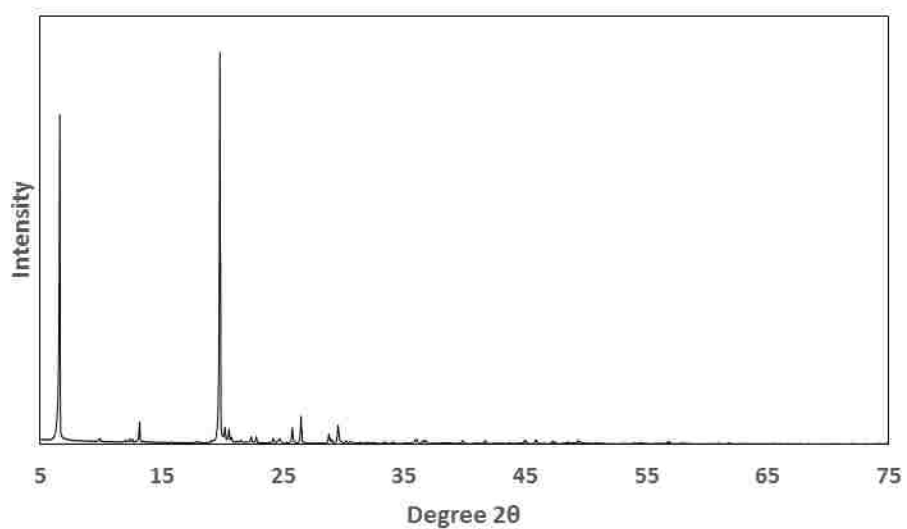


**Figure S1: Diffraction pattern taken of the reagent grade Al-sulfate, to characterize its hydration state.** This diffraction pattern is indicative of the Al-sulfate alunogen –  $\text{Al}_2(\text{SO}_4)_3 \cdot 17(\text{H}_2\text{O})$ .

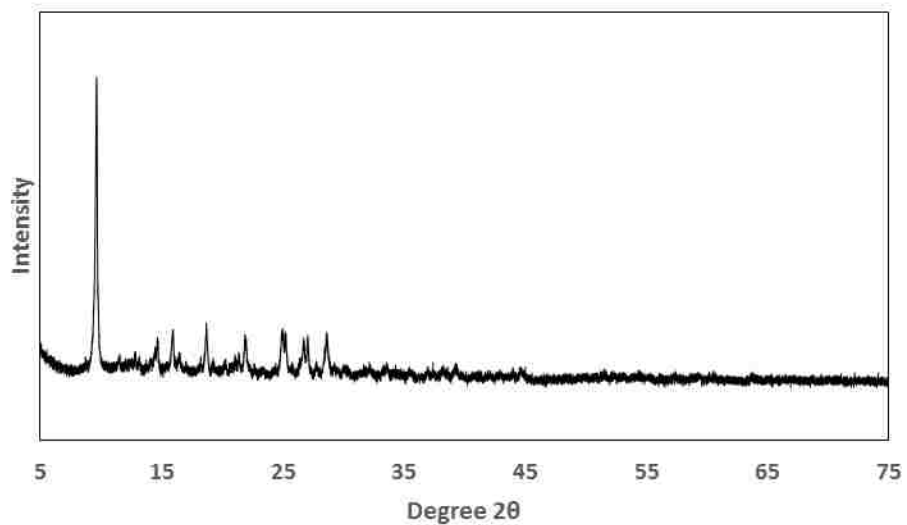


**Figure S2: Diffraction pattern of the reagent grade Fe<sup>3+</sup>-sulfate, to characterize its hydration state.** This diffraction pattern is indicative of the Fe-sulfates rhomboclase – HFe<sup>3+</sup>(SO<sub>4</sub>)<sub>2</sub>·4(H<sub>2</sub>O) and ferricopiapite – Fe<sup>3+</sup><sub>0.66</sub>Fe<sup>3+</sup><sub>4</sub>(SO<sub>4</sub>)<sub>6</sub>(OH)<sub>2</sub>·20(H<sub>2</sub>O).



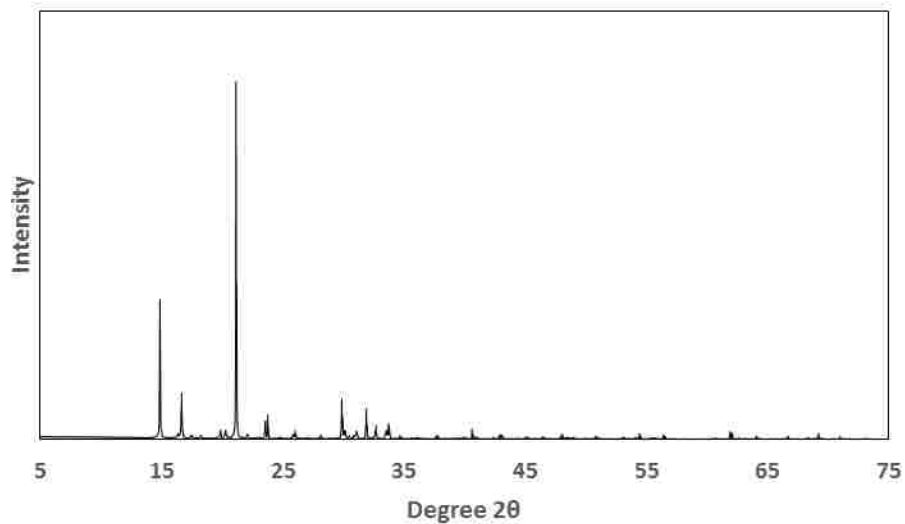


**Figure S3: Diffraction pattern taken of the Mg-sulfate, to characterize its hydration state.** This diffraction pattern is indicative of the Mg-sulfate epsomite –  $\text{MgSO}_4 \cdot 7(\text{H}_2\text{O})$ .

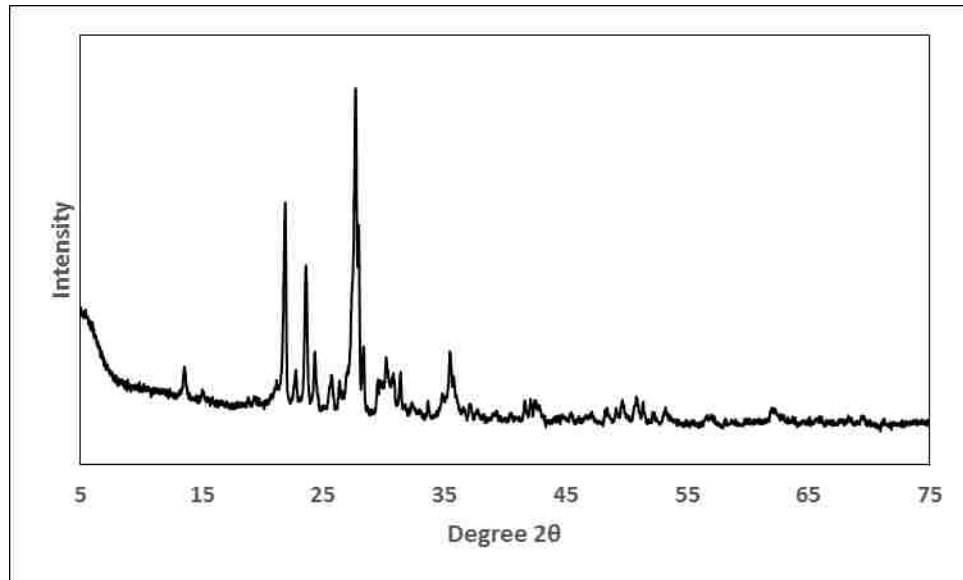


**Figure S4: Diffraction pattern taken of the reference powder AVG-1 (andesite) indicating the presence of plagioclase and K-feldspar. The lack of a low angle basal reflection suggests the absence of clay minerals.**

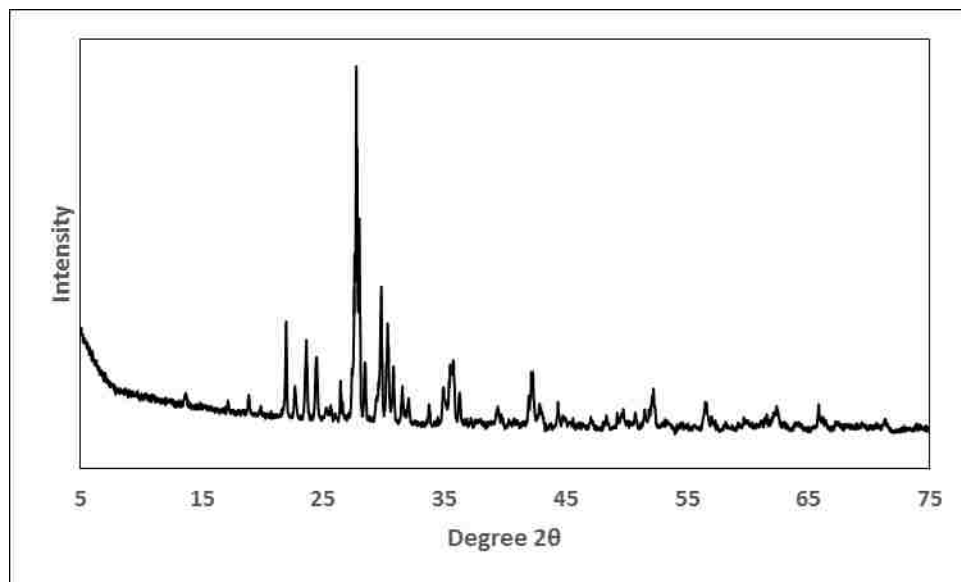


**Figure S5: Diffraction pattern of the reference powder BIR-1a (basalt).** XRD diffraction suggests the presence of plagioclase, pyroxene and olivine. The lack of a low angle basal reflection suggests the absence of clay minerals.

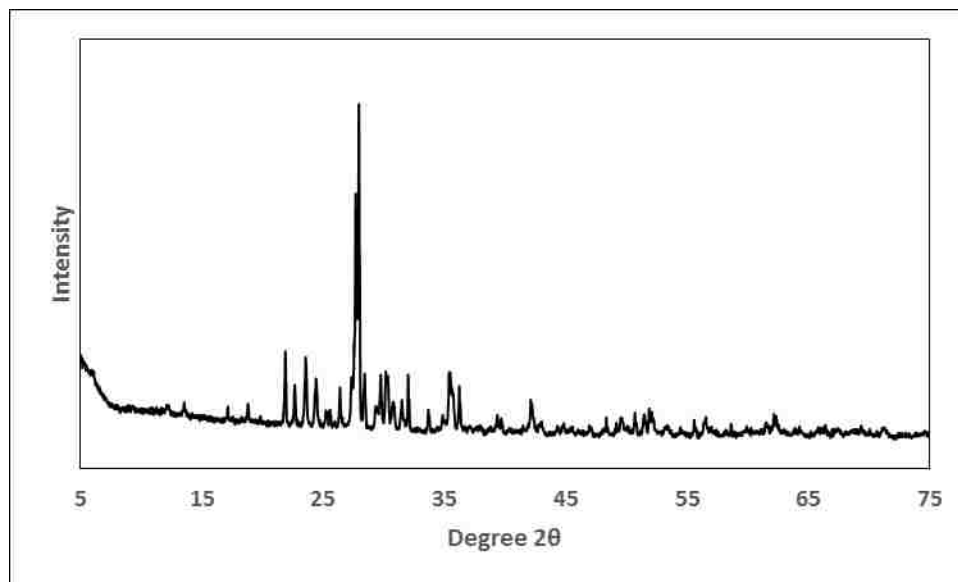


**Figure S6: Diffraction pattern of the reference powder DNC-1a (diabase/dolerite).** XRD suggests the presence of plagioclase, pyroxene and olivine. The small diffraction peak at approximately 6 degrees may suggest the minor presence of clay minerals. However, because not all products of the DNC-1A formed clay minerals, and because clay minerals were formed from BIR-1a, which initially contained no clay minerals, we consider the minor initial clay minerals if present to be negligible in the formation of clay minerals during these experiments.

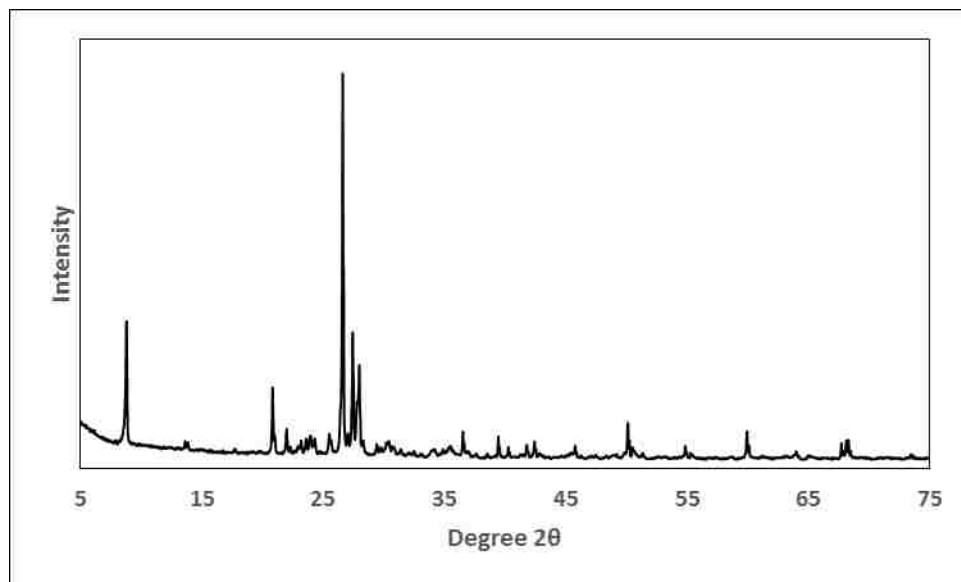


**Figure S7: Diffraction pattern of the reference powder GSP-2 (granodiorite).** XRD suggests the presence of plagioclase, quartz and mica. The lack of a low angle basal reflection suggests the absence of clay minerals.

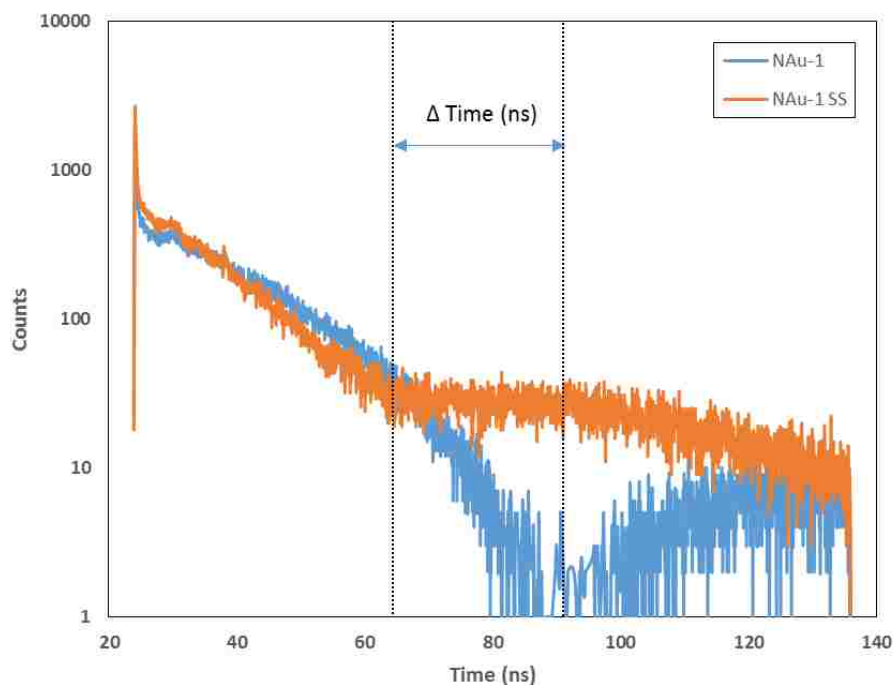


**Figure S8: Synchrotron Mössbauer data of NAu-1 and NAu-1 with 10 $\mu$ m stainless steel foil.** SMS of NAu-1 (blue) and NAu-1 with a 10 $\mu$ m stainless steel foil (orange) to determine center shifts (blue arrow). Note the increased abundance of  $^{57}\text{Fe}$  results in a shift to lower time for the sample with stainless steel foil. The isomer shifts and quadrupole splittings of both  $\text{Fe}^{3+}$  sites occur within the single observed absorption which is consistent with the ferric-clay nontronite (Taylor et al., 1968; Ribeiro et al., 2009; Vandenberghe and De Grave, 2013).

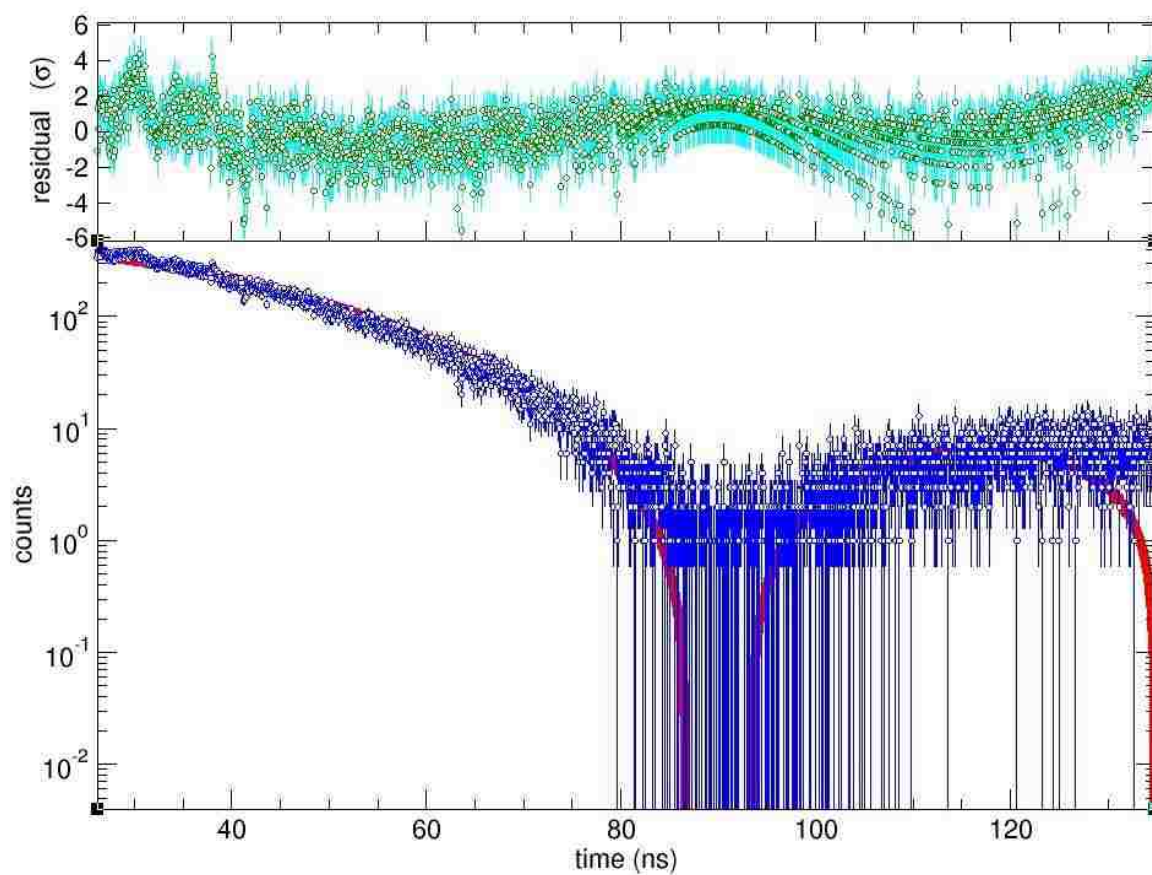


**Figure S9: Synchrotron Mössbauer data of NAu-1 without stainless steel foil.** The plot was fitted in CONUSS (Sturhahn, 2000). Blue lines represent the error of the analysis.

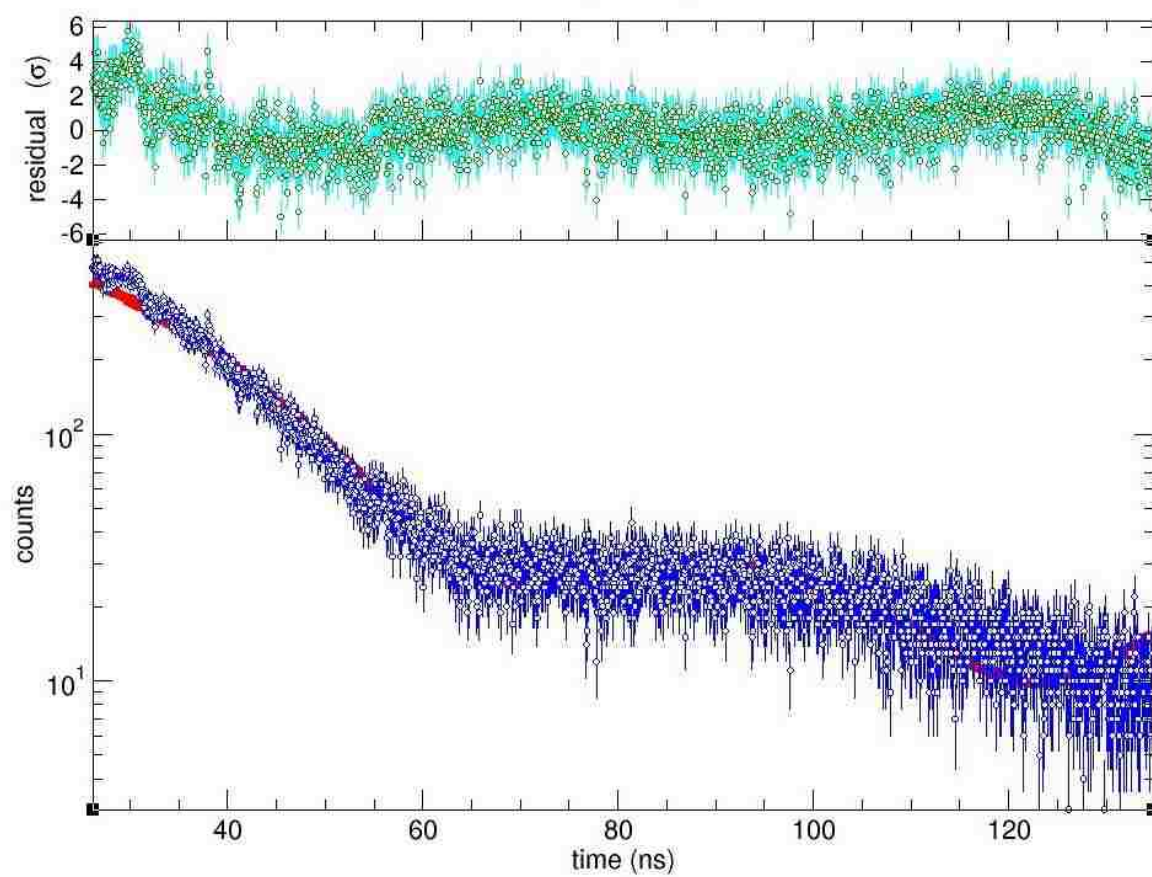


**Figure S10: Synchrotron Mössbauer data of NAu-1 with stainless steel foil.** The plot was fitted in CONUSS (Sturhahn, 2000). Blue lines represent the error of the analysis.



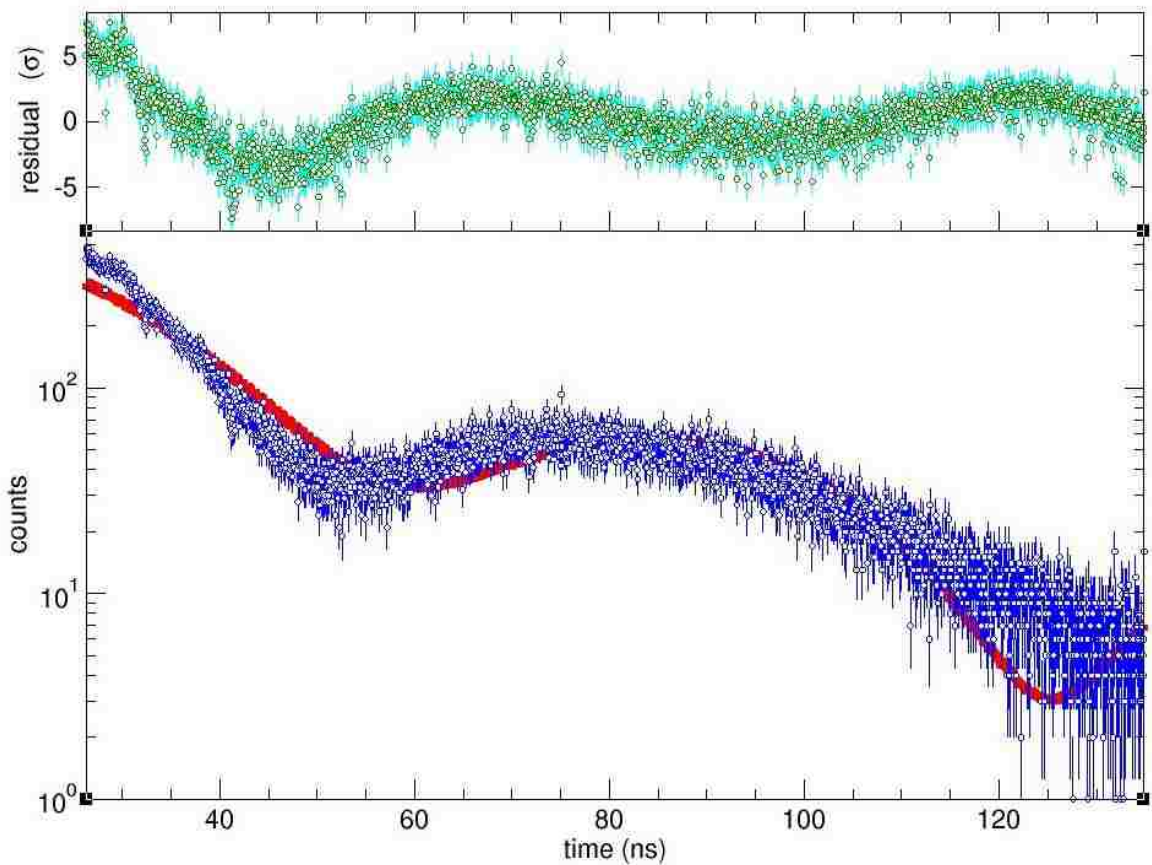


**Figure S11: Synchrotron Mössbauer data of *Experiment-4* ( $^{15}\text{Mg } ^{85}\text{Fe}^{3+}$ ) with stainless steel foil.** The plot was fitted in CONUSS (Sturhahn, 2000). Blue lines represent the error of the analysis. The variation between the fit produced within CONUSS and the actual data is likely due to the low number of counts towards higher time. However, the very low number of counts in this time-range contribute little to the over-all spectra.

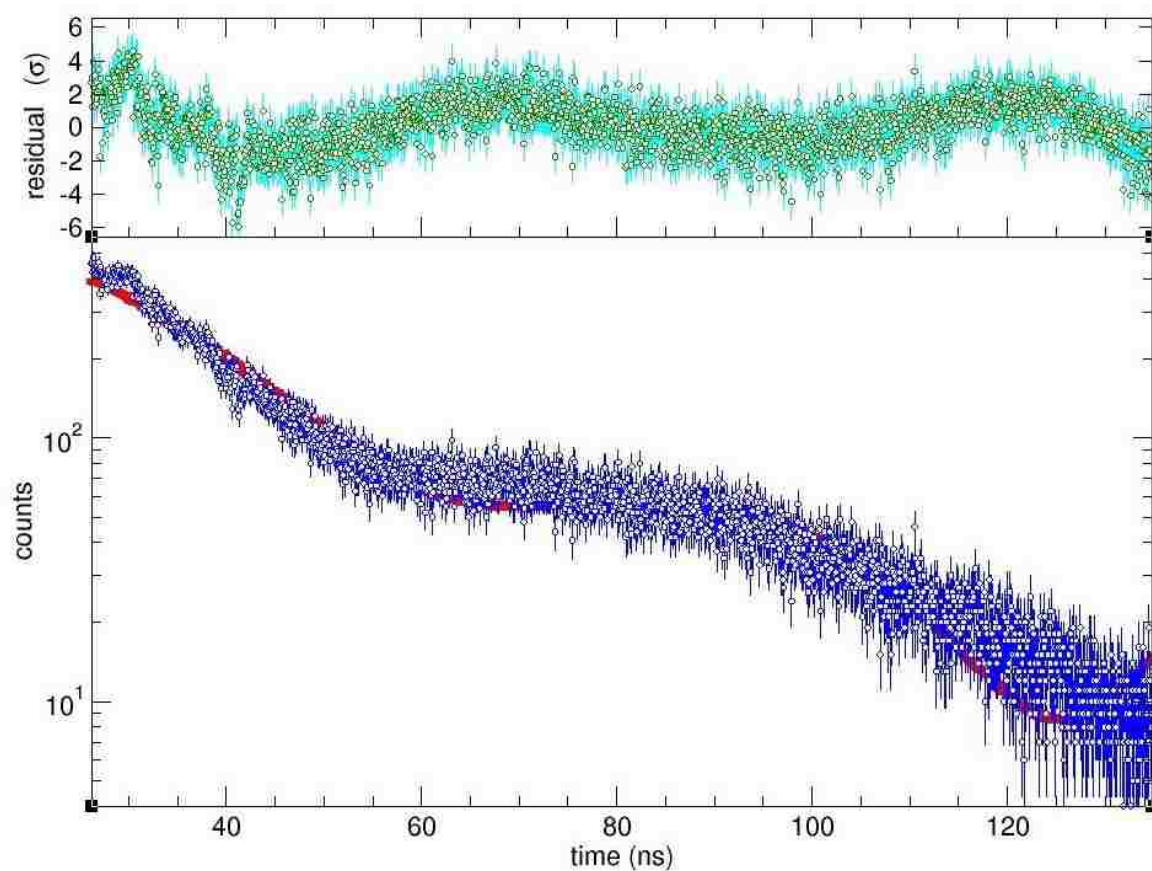


**Figure S12: Synchrotron Mössbauer data of *Experiment-5* ( $50\text{-Mg } 50\text{-Fe}^{3+}$ ) with stainless steel foil.** The plot was fitted in CONUSS (Sturhahn, 2000). Blue lines represent the error of the analysis. The variation between the fit produced within CONUSS and the actual data is likely due to the low number of counts towards higher time. However, the very low number of counts in this time-range contribute little to the over-all spectra.

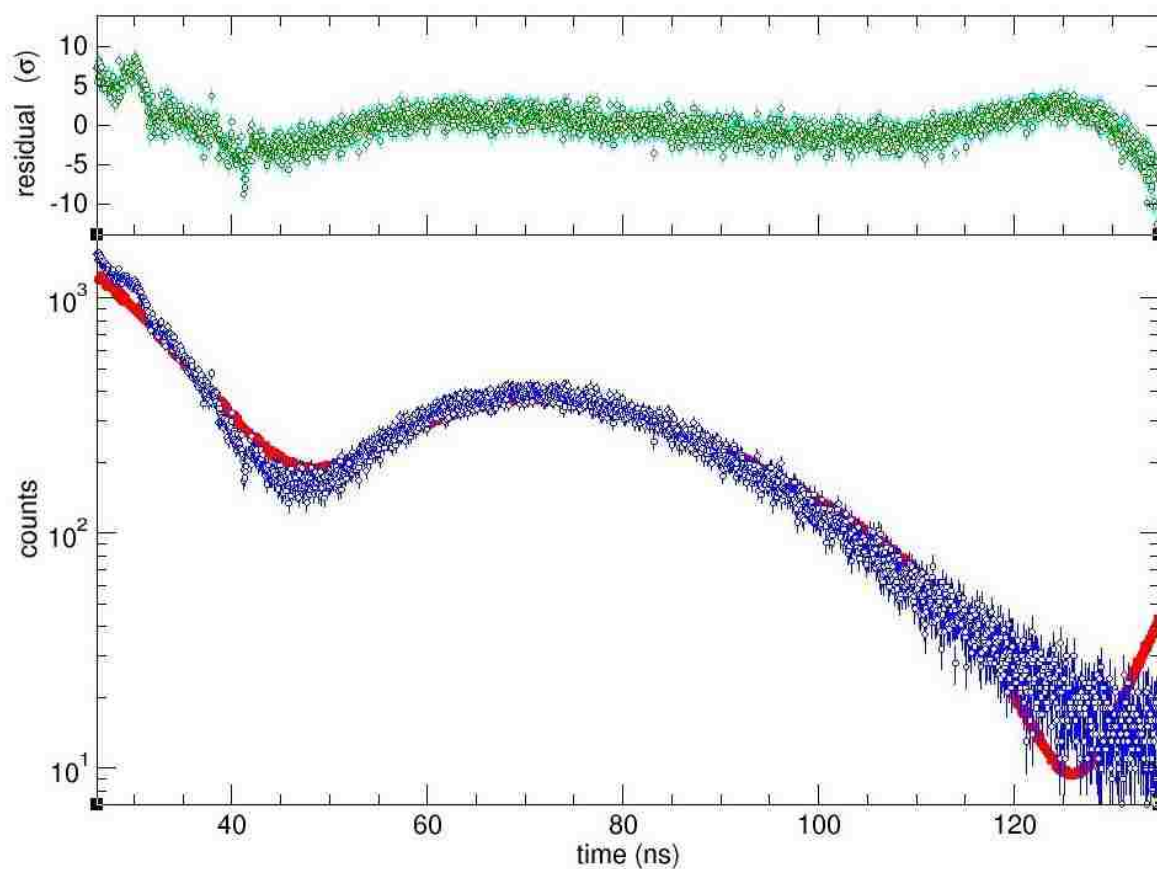


**Figure S13: Synchrotron Mössbauer data of *Experiment-1(100-Fe Control - Subsequently Oxidized)* with stainless steel foil.** The plot was fit in CONUSS (Sturhahn, 2000). Blue lines represent the error of the analysis. The variation between the fit produced within CONUSS and the actual data is likely due to the low number of counts towards higher time. However, the very low number of counts in this time-range contribute little to the over-all spectra.

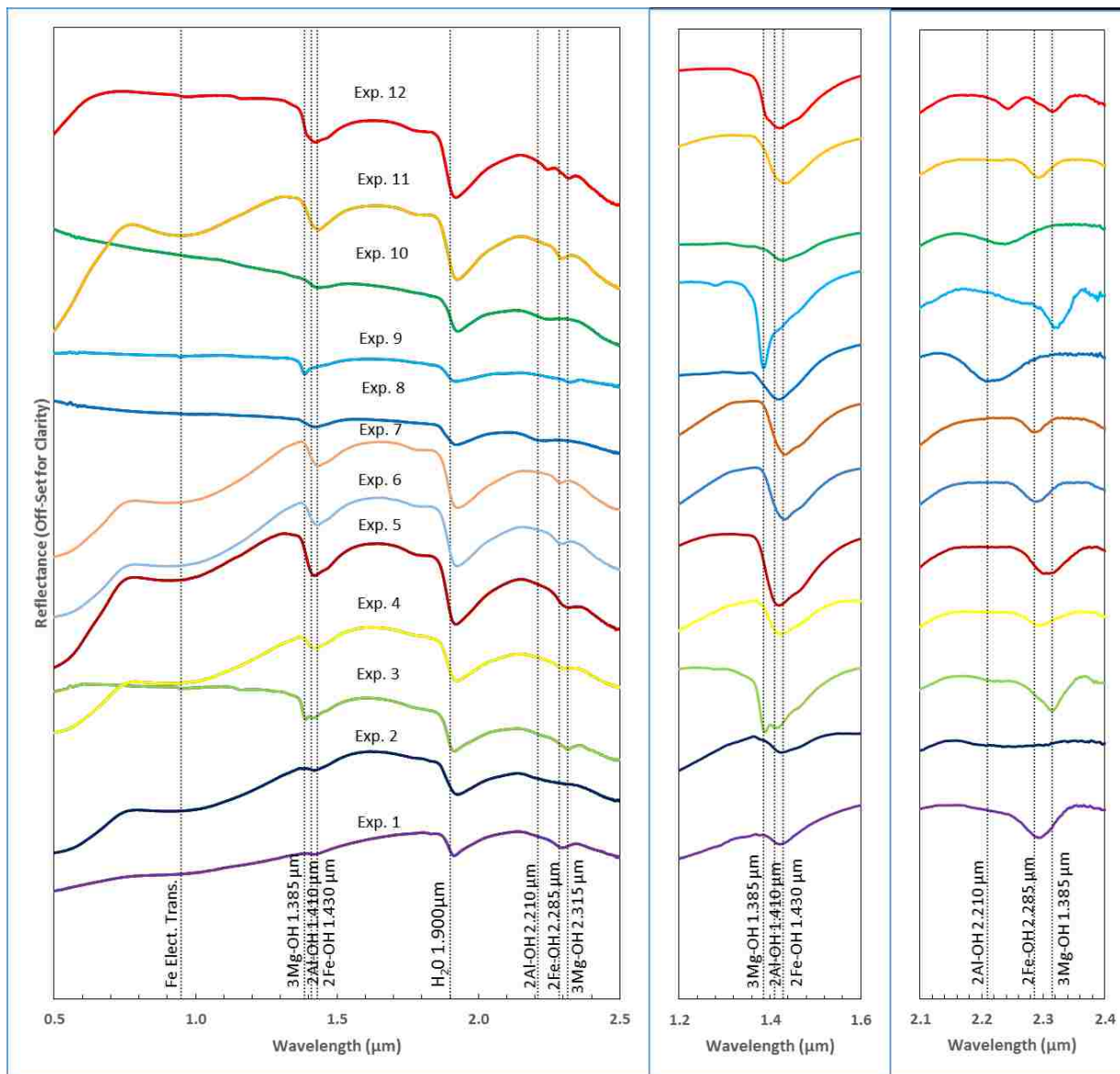


**Figure S14: Visible Near Infrared (VNIR) spectra of the synthesized clay minerals precipitated at 150° C.** For complete information regarding the compositions see table 1. Spectra were collected with an Analytical Spectra Devices (ASD) VNIR spectrometer. The continuum has been removed in the right columns.

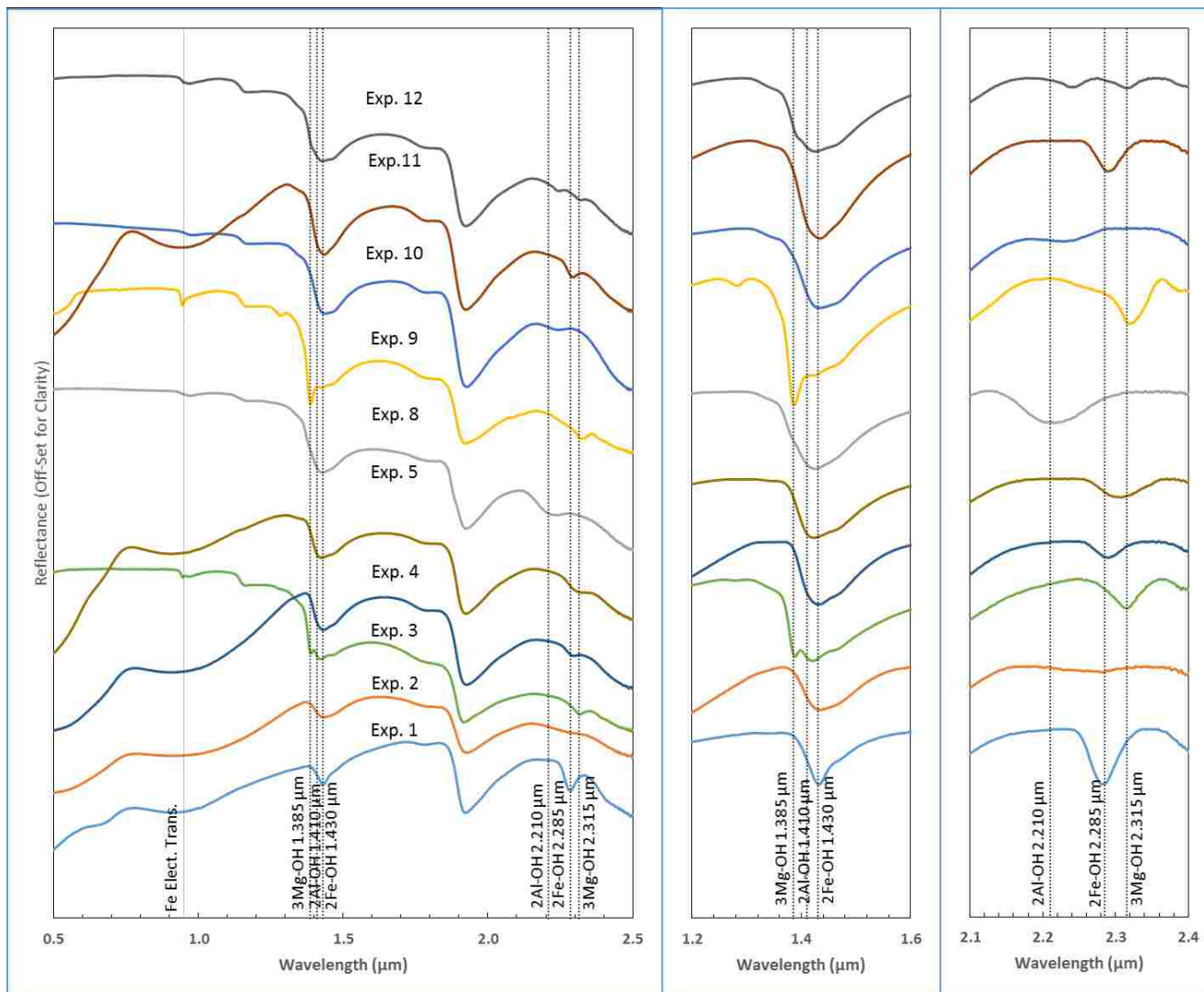


**Figure S15: Visible Near Infrared (VNIR) spectra of the synthesized clay minerals precipitated at 100° C.** For complete information regarding the compositions see table 2. Spectra were collected with an Analytical Spectra Devices (ASD) VNIR spectrometer. The continuum has been removed in the right two columns.

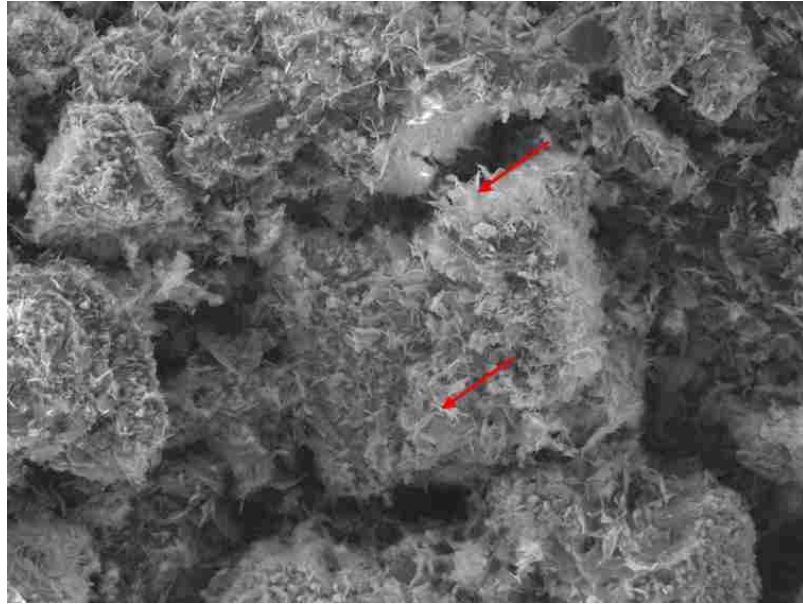


**Figure S16: SEM image of altered Icelandic basalt (BIR-1a).** Red arrows indicate the platy morphology suggestive of clay minerals.

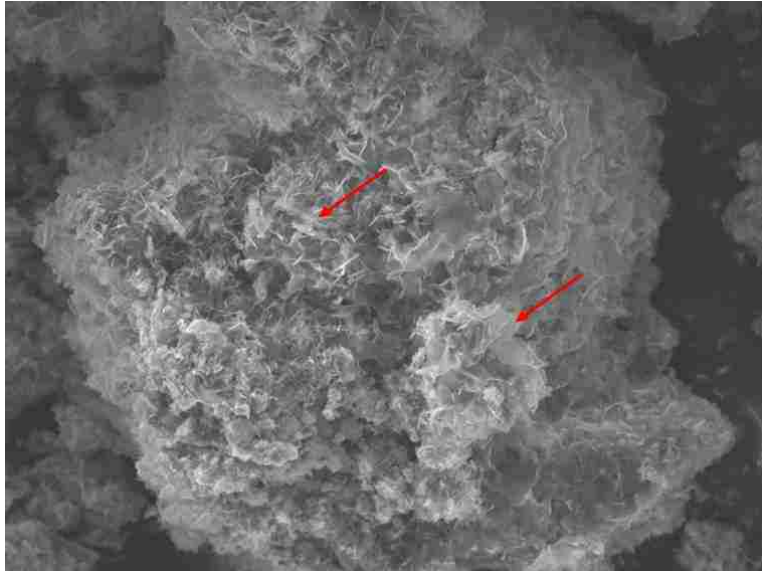


**Figure S17: SEM image of altered dolerite (DNC-1a).** Red arrows indicate the platy morphology suggestive of clay minerals.

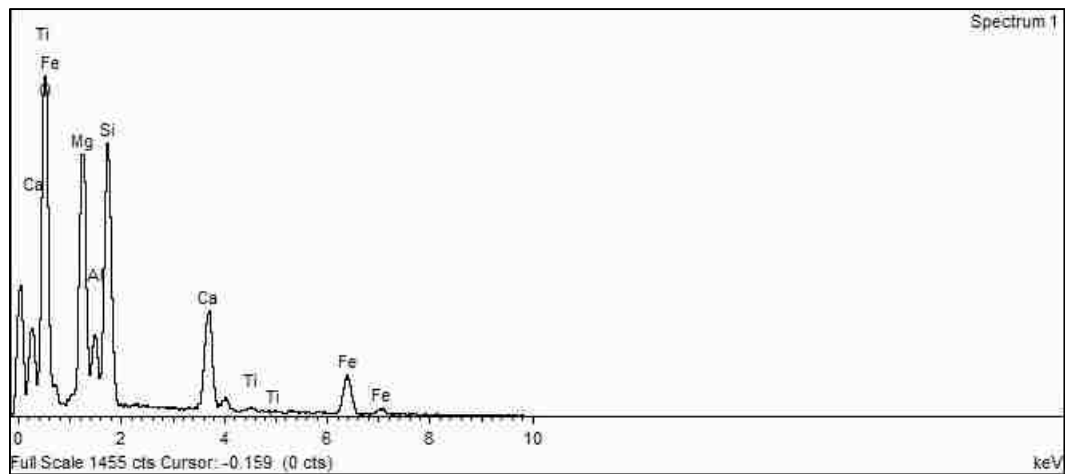
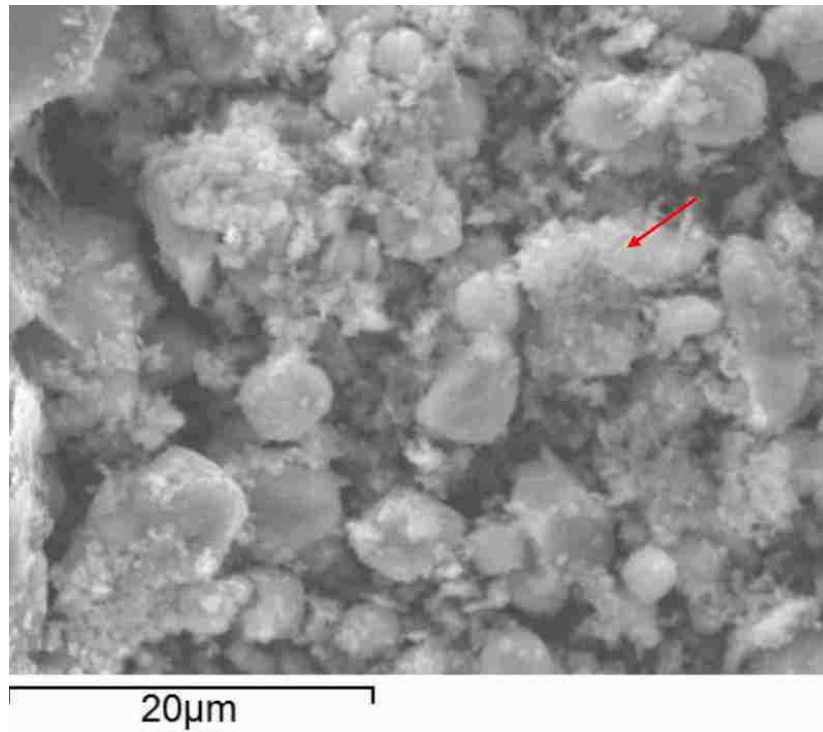


**Figure S18: SEM image of altered mafic rock and the accompanying EDS-spectra.** The combined SEM/EDS data (location marked with a red arrow) are consistent with the Fe/Mg-bearing clay minerals that were identified by powder-XRD.



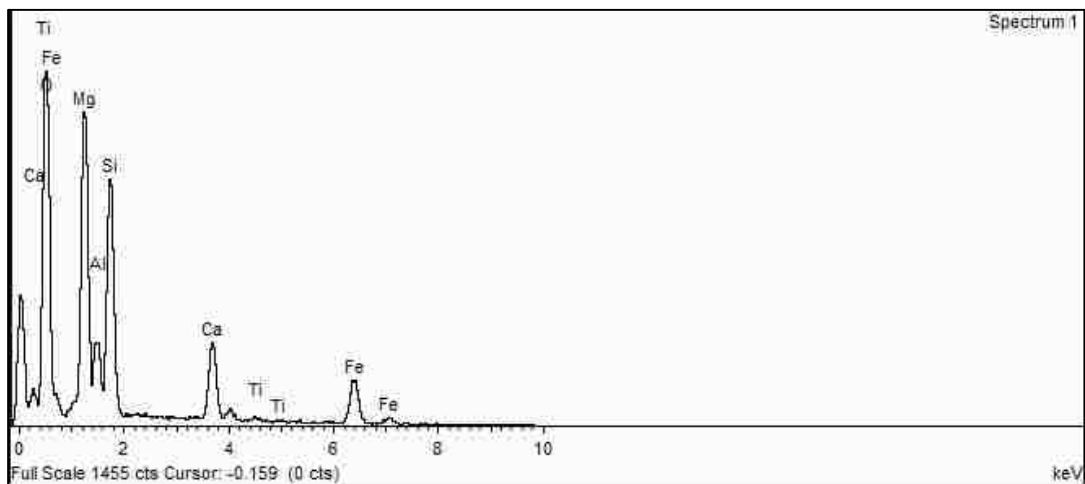
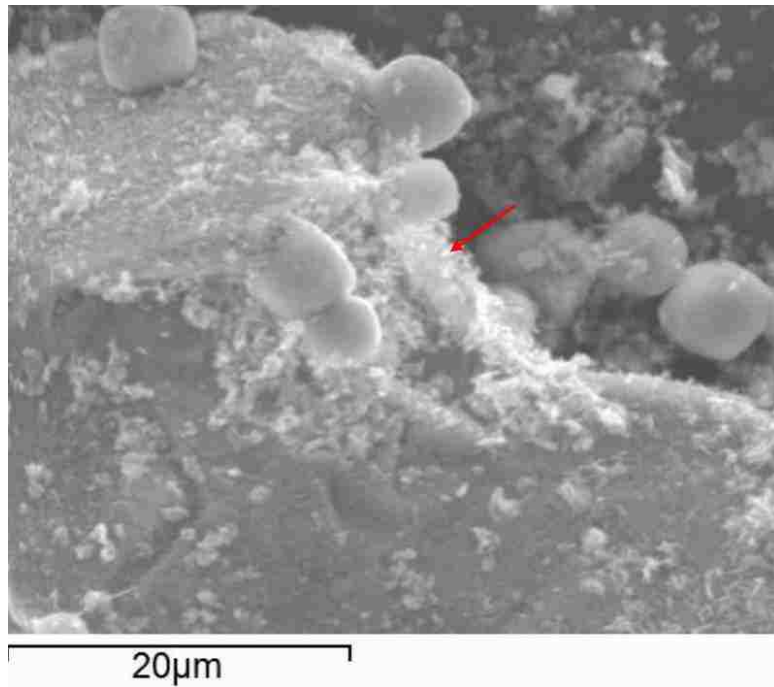


**Figure S19: SEM image of altered mafic rock and the accompanying EDS-spectra.** The combined SEM/EDS data (location marked with a red arrow) are consistent with the Fe/Mg-bearing clay minerals that were identified by powder-XRD.



**Figure S20: Photograph of the synthetic nontronite control - *Experiment-1(100-Fe Control - Subsequently Oxidized)* precipitated at 150° C.** The precipitate was dried in-vacuo and ground to a fine powder in a mortar and pestle. The reddish color is likely due to the oxidation of the ferrous precursor into nontronite as indicated by our Mössbauer data (Table S3 and S13), as well as the Mössbauer spectroscopy data collected by Mizutani et al. (1991) on material previously produced by this method.



**Figure S21: Photograph of the synthetic nontronite control - *Experiment-1(100-Fe Control - Subsequently Oxidized)* precipitated at 100° C.** The precipitate was dried in-vacuo and ground to a fine powder in a mortar and pestle. The reddish color is likely due to the oxidation of the ferrous precursor into nontronite. This is supported by the Mössbauer spectroscopy data collected by Mizutani et al. (1991) on material synthesized in an identical manner, as well as our Mössbauer data of the corresponding 150 ° C experiment (Table S3 and Figure S13).

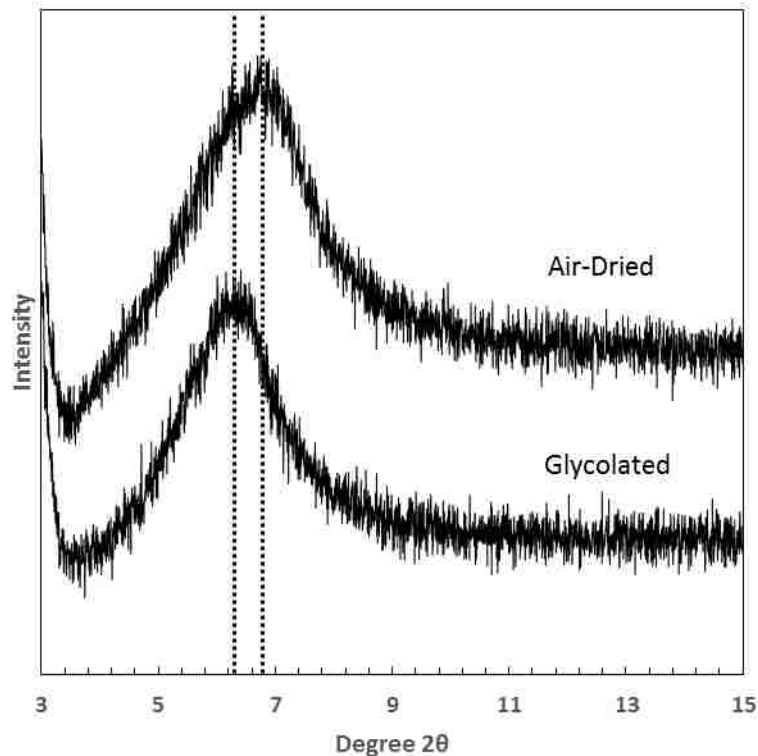


**Figure S22: X-Ray diffraction pattern of *Experiment-1(100-Fe Control - Subsequently Oxidized)*, precipitated at 150° C.** Note the slight expansion when exposed to ethylene glycol vapor for over 24 hours. The clay mineral did not expand to the diagnostic 17 Å of smectite, but only to approximately 14 Å which is consistent with previous descriptions of material synthesized in this manner as a high-charge (expands very little during exposure to ethylene glycol vapor) nontronite (Decarreau et al., 2008).

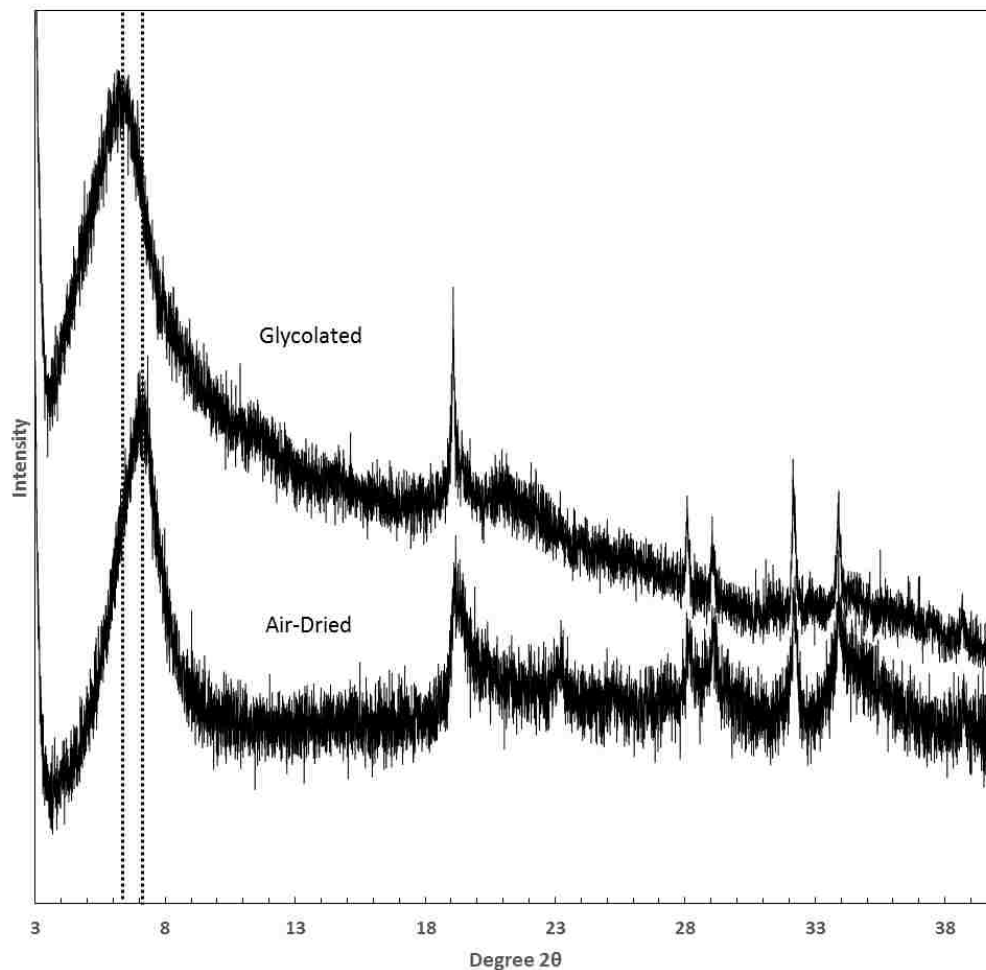


**Figure S23: X-Ray diffraction pattern of *Experiment-1(100-Fe Control - Subsequently Oxidized)* precipitated at 100° C.** Note the low angle broad reflection, which is indicative of clay minerals. In addition, the diffractions occurring at approximately 20 degrees (020 reflection) characterizes the b dimension of the unit cell and is also indicative of clay minerals, having been used to identify clay mineralogy on Mars (Treiman et al., 2014). Material synthesized in this manner has been previously characterized as high-charge (e.g. expands very little when exposed to ethylene glycol vapor) nontronite (Decarreau et al., 2008).

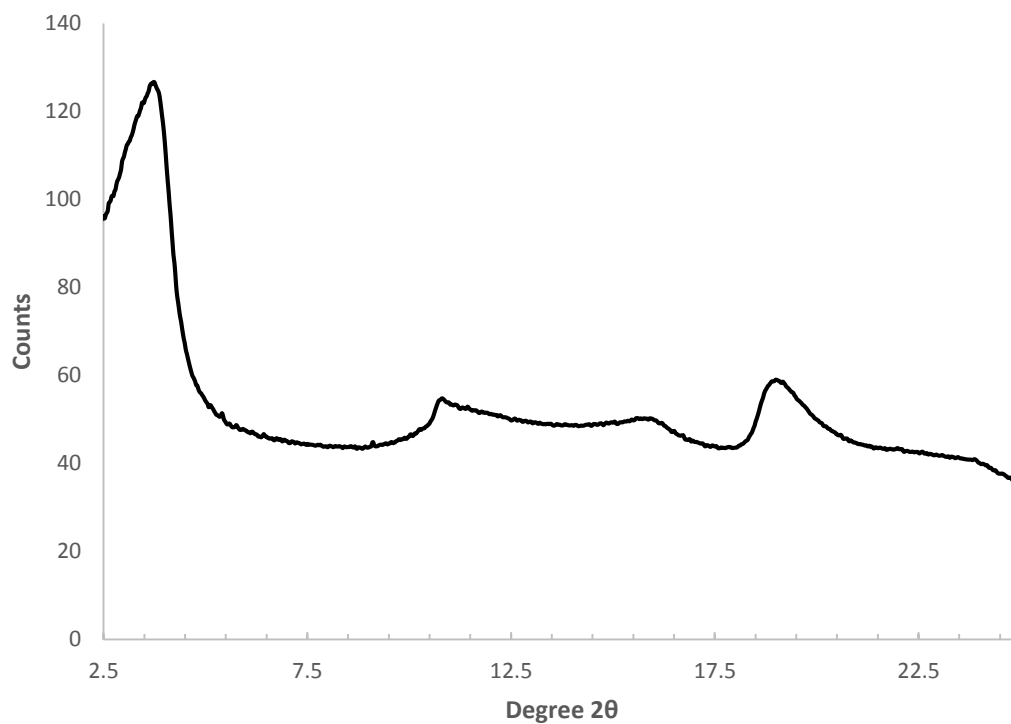


**Figure S24: Synchrotron  $\mu$ -XRD (0.86 Å wavelength) pattern for *Experiment-1(100-Fe Control - Subsequently Oxidized)* precipitated at 150° C.** Notice the multiple peaks produced as the direct result of crystallinity. This diffraction pattern is consistent with a clay structure in that the diffraction peaks are produced through the 001 (large low-angle reflection) 020 and 060 reflections.



**Figure S25: Photograph of *Experiment-2* ( $100\text{-Fe}^{3+}$ ) precipitated at  $150^\circ\text{C}$ .** The precipitate was dried in-vacuo and ground to a fine powder in a mortar and pestle. Notice the reddish color likely from the presence of  $\text{Fe}^{3+}$ .



**Figure S26: Photograph of the *Experiment-2* ( $100\text{-Fe}^{3+}$ ) precipitated at  $100^\circ\text{C}$ .** The precipitate was dried in-vacuo and ground to a fine powder in a mortar and pestle. Notice the reddish color likely from the presence of  $\text{Fe}^{3+}$ .



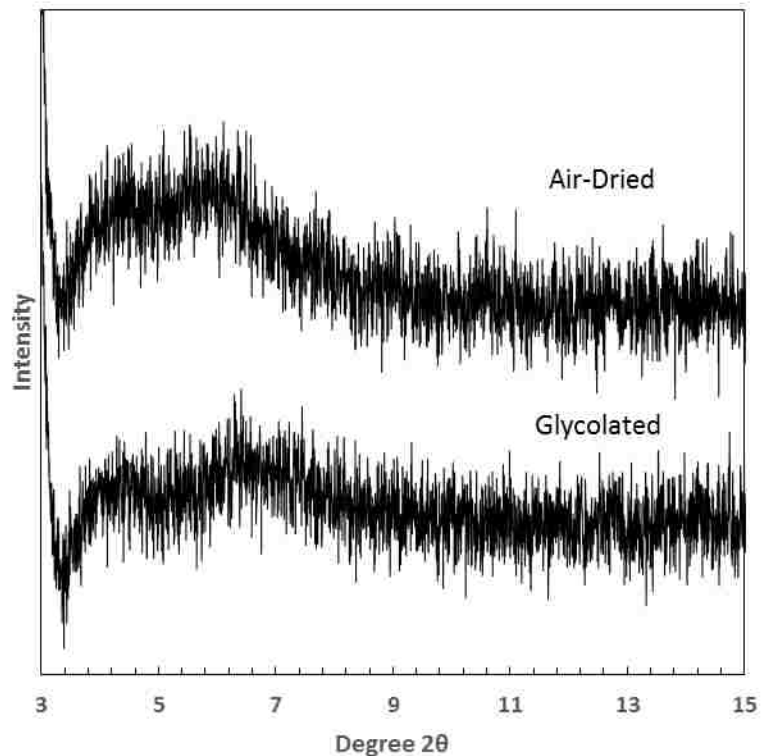


**Figure S27: X-Ray diffraction pattern of *Experiment-2* ( $100\text{-Fe}^{3+}$ ) precipitated at  $150^\circ\text{C}$ .** Note the lack of crystallinity of this relatively amorphous sample, which indicates the importance of a divalent cation and is consistent with previous studies (Harder, 1976; Mizutani et al., 1991; Decarreau et al., 2008). In addition, no expansion occurred when exposing the sample to ethylene glycol vapor for over 24 hours.

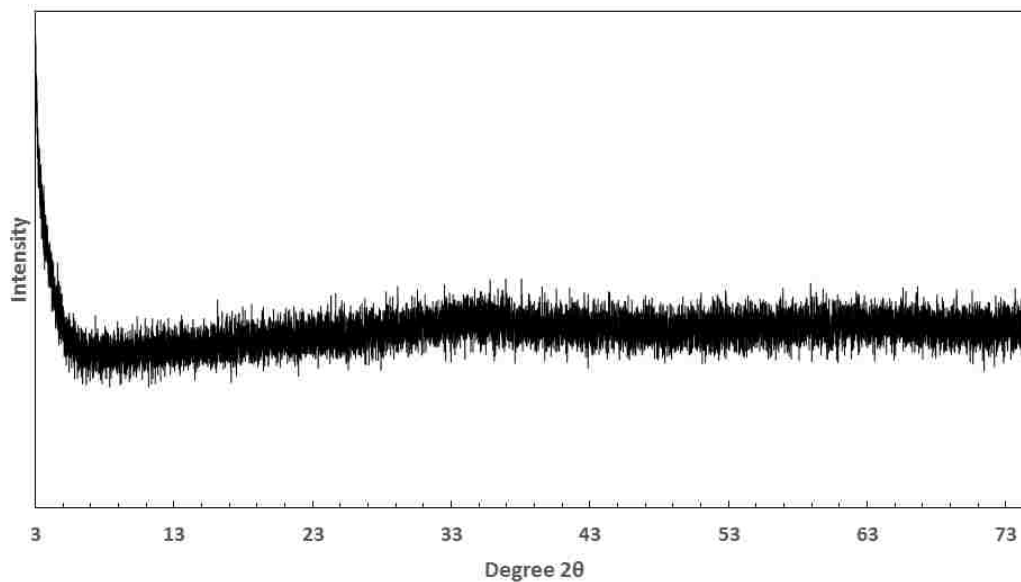


**Figure S28: X-Ray diffraction pattern of *Experiment-2* ( $100\text{-Fe}^{3+}$ ) precipitated at  $100^\circ\text{C}$ .** Note the lack of crystallinity of this amorphous sample which indicates the importance of a divalent cation and is consistent with previous studies (Harder, 1976; Mizutani et al., 1991; Decarreau et al., 2008).



**Figure S29: Photograph of *Experiment-3 (100-Mg, High SiO<sub>2</sub>)* precipitated at 150° C.** The precipitate was dried in-vacuo and ground to a fine powder in a mortar and pestle.



**Figure S30: Photograph of the *Experiment-3 (100-Mg, High SiO<sub>2</sub>)* precipitated at 100° C.** The precipitate was dried in-vacuo and ground to a fine powder in a mortar and pestle.

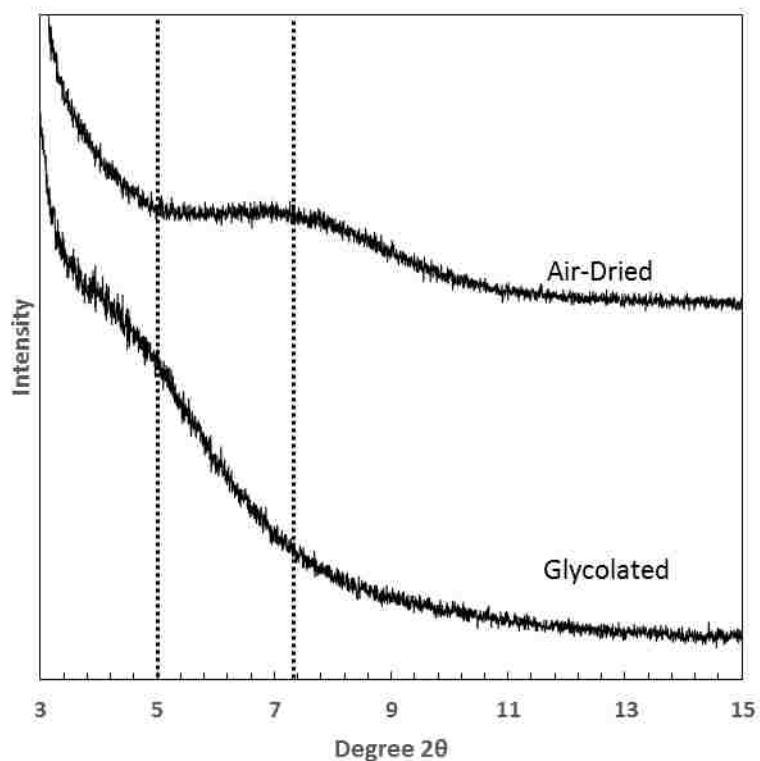


**Figure S31: X-Ray diffraction pattern of *Experiment-3 (100-Mg, High SiO<sub>2</sub>) precipitated at 150° C*.** Note the diffraction peak shift when exposed to ethylene glycol for over 24 hours. This material lacks crystal coherency in the c-axis which makes it difficult to determine the exact peak positions. This pattern is indicative of a trioctahedral Mg-clay/smectite such as saponite or stevensite.

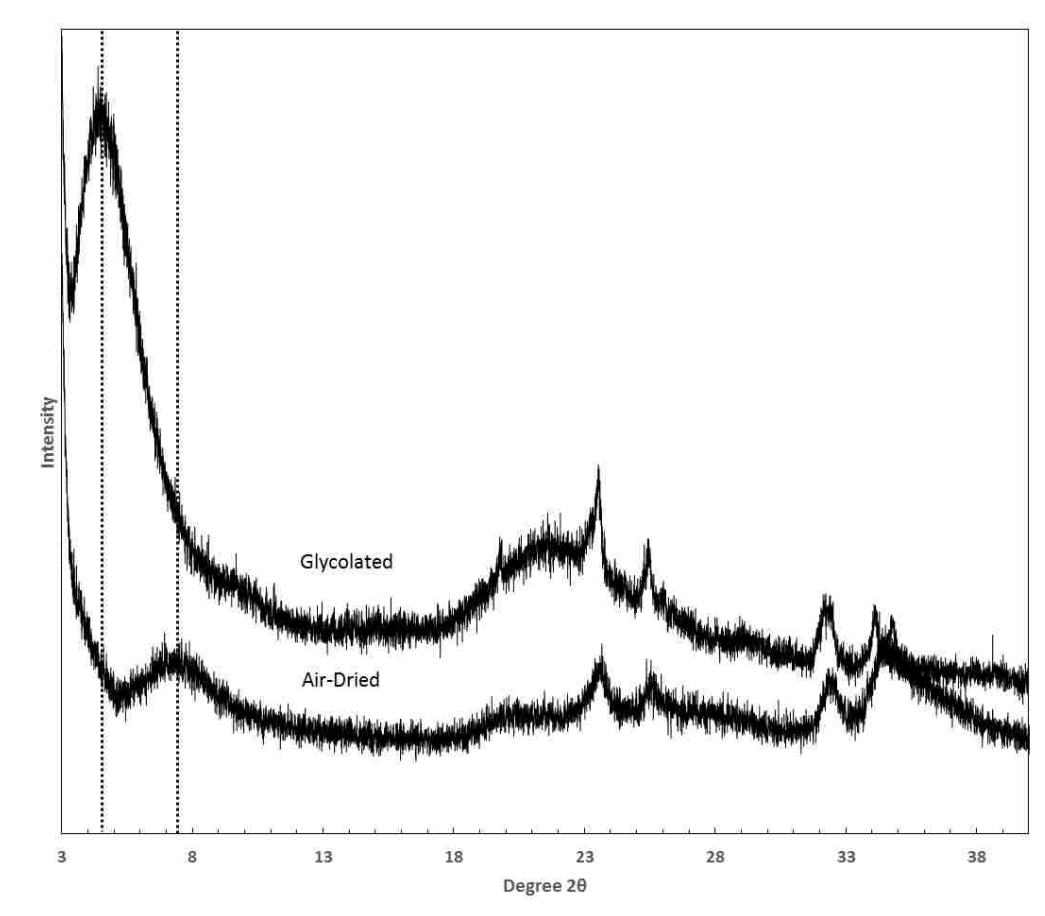


**Figure S32: X-Ray diffraction pattern of *Experiment-3 (100-Mg, High SiO<sub>2</sub>) precipitated at 100° C*.** Note the low angle broad reflection, which is indicative of clay minerals. Exposure to ethylene glycol resulted in an expansion of the basal 001 reflection to approximately 20 Å. In addition, the broad-diffraction occurring at approximately 20 degrees characterizes the b-dimension of the unit cell and is used to identify clay mineralogy on Mars (Treiman et al., 2014). This pattern is indicative of a trioctahedral Mg-smectite such as saponite or stevensite.



**Figure S33: Photograph of the *Experiment-4* ( $15\text{-Mg } 85\text{-Fe}^{3+}$ ) precipitated at  $150^\circ\text{C}$ .** The precipitate was dried in-vacuo and ground to a fine powder in a mortar and pestle. Notice the reddish color likely due to the presence of  $\text{Fe}^{3+}$ .



**Figure S34: Photograph of the *Experiment-4* ( $15\text{-Mg } 85\text{-Fe}^{3+}$ ) precipitate at  $100^\circ\text{C}$ .** The precipitate was dried in-vacuo and ground to a fine powder in a mortar and pestle. Notice the reddish color likely due to the presence of  $\text{Fe}^{3+}$ .



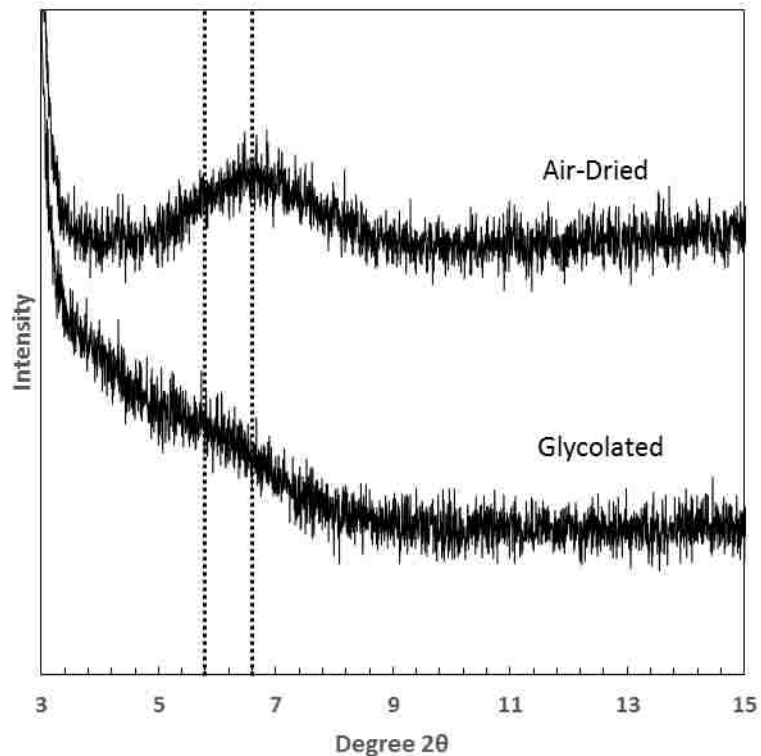


**Figure S35: X-Ray diffraction pattern of *Experiment-4* ( $15\text{-Mg } 85\text{-Fe}^{3+}$ ) precipitated at  $150^\circ\text{C}$ .** Note the low angle basal reflection under air-dried conditions and the subsequent result when exposed to ethylene glycol vapor for over 24 hours. Do to the loss of a strong basal resolution, which may be due to the low angle background, it is difficult to determine the exact peak position. However, exposure likely produced an expansion within the clay mineral along the c-axis. The data are consistent with a dioctahedral Fe-rich clay.

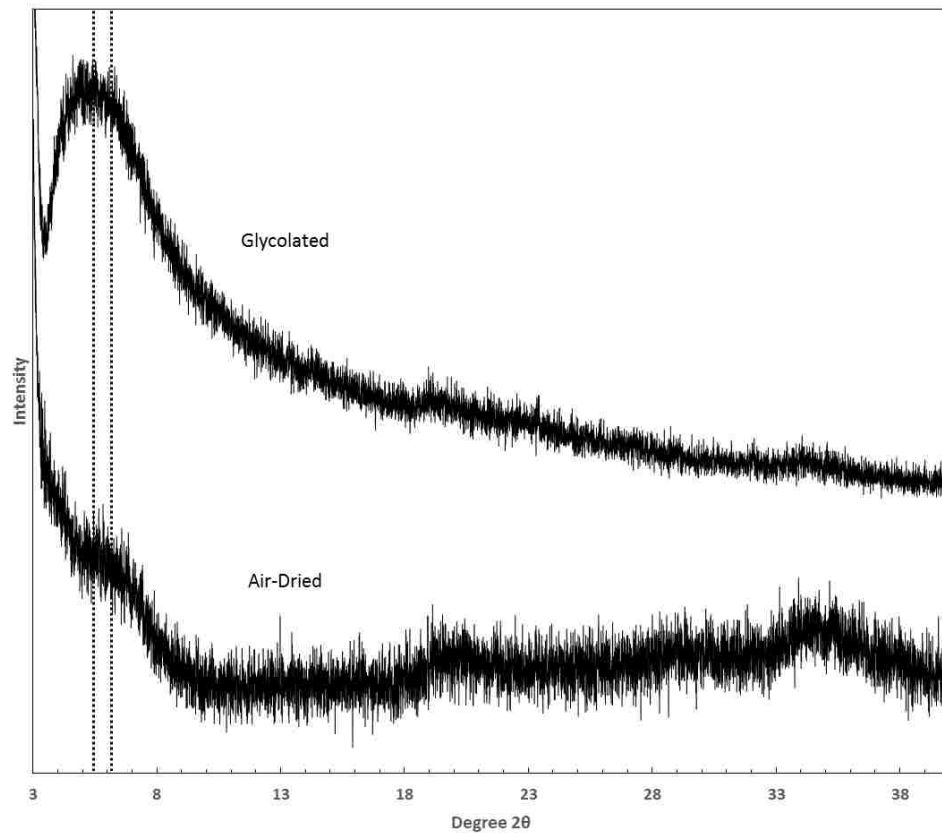


**Figure S36: X-Ray diffraction pattern of *Experiment-4* ( $15\text{-Mg } 85\text{-Fe}^{3+}$ ) precipitated at  $100^\circ\text{C}$ .** Note the low angle reflection (although not prominent, diffraction is occurring at approximately 6 degrees  $2\theta$ ), which is indicative of clay minerals. In addition, the diffractions occurring at approximately 20 degrees characterize the b dimension of the unit cell have been used to identify clay mineralogy on Mars (Treiman et al., 2014). These data are consistent with a high-charge nontronite (Decarreau et al., 2008).

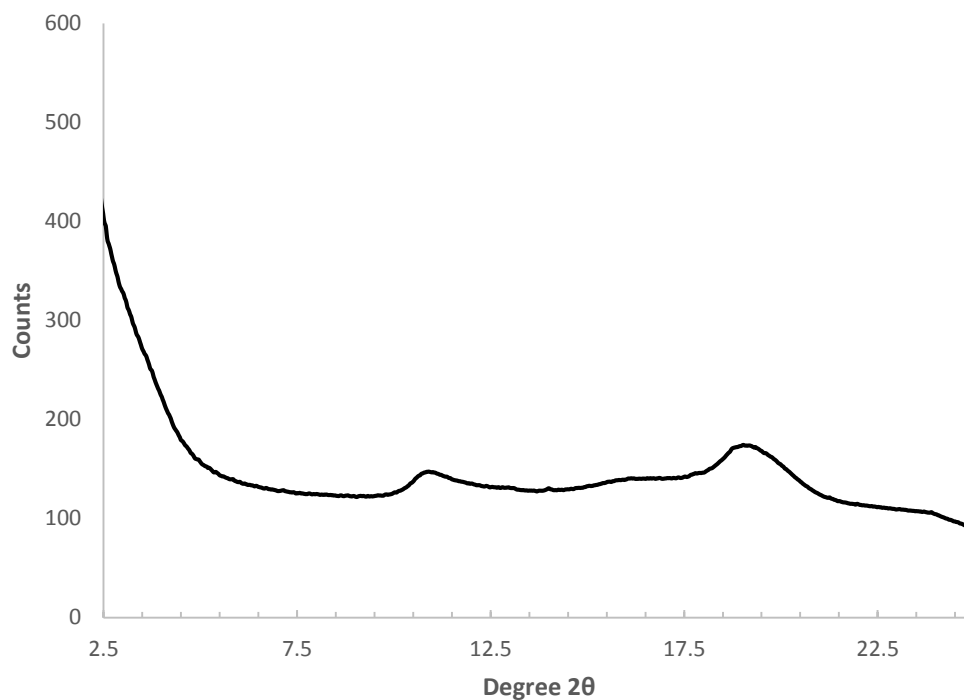


**Figure S37: Synchrotron  $\mu$ -XRD (0.86 Å wavelength) pattern for *Experiment-4* (15-Mg 85-Fe<sup>3+</sup>) precipitated at 150° C.** Note the multiple peaks produced due to crystallinity. This diffraction pattern indicates a clay structure, in that the diffraction peaks are produced through the 020 and 060 reflections.



**Figure S38: Photograph of the *Experiment-5* ( $50\text{-Mg } 50\text{-Fe}^{3+}$ ) precipitated at  $150^\circ\text{C}$ . The precipitate was dried in-vacuo and ground to a fine powder in a mortar and pestle. Notice the reddish color likely from the presence of  $\text{Fe}^{3+}$ .**



**Figure S39: Photograph of the *Experiment-5* (50-Mg 50-Fe<sup>3+</sup>) precipitated at 100° C.** The precipitate was dried in-vacuo and ground to a fine powder in a mortar and pestle. Notice the reddish color likely from the presence of Fe<sup>3+</sup>.

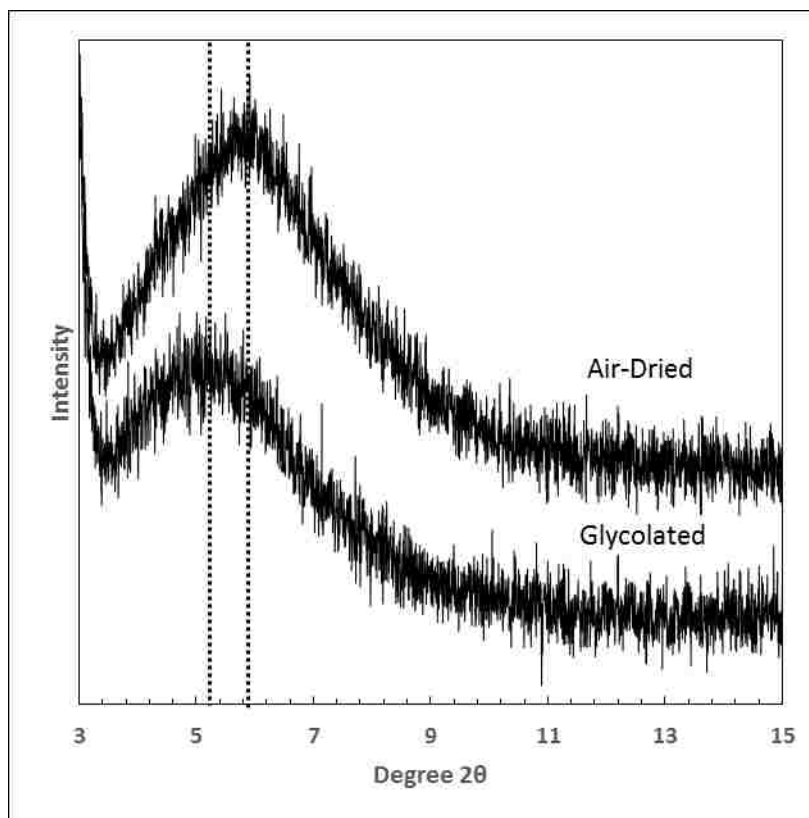


**Figure S40: X-Ray diffraction pattern of *Experiment-5* (50-Mg 50-Fe<sup>3+</sup>) precipitated at 150° C.** Note the expansion between the air-dried and ethylene glycol treated samples (exposed to vapor for over 24 hours). This expansion to approximately 17 Å is indicative of a smectite clay mineral.

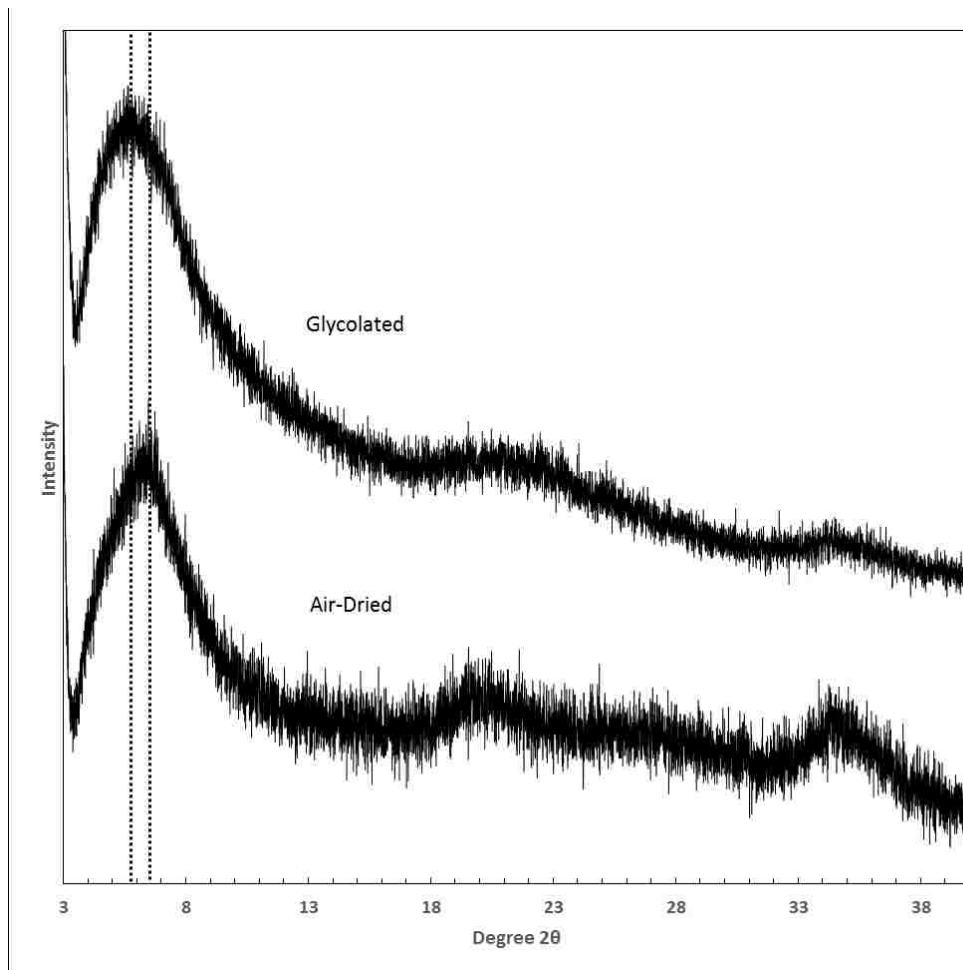


**Figure S41: X-Ray diffraction pattern of *Experiment-5* (50-Mg 50-Fe<sup>3+</sup>) precipitated at 100° C.** Note the low angle broad reflection, which is indicative of clay minerals. Exposure to ethylene glycol result in a slight expansion from approximately 14 to 15 Å. In addition, the diffractions occurring at approximately 20 degrees characterize the lateral dimension of the b plane and have been used to determine clay mineralogy on Mars (Treiman et al., 2014). This material may contain domains of both dioctahedral and trioctahedral Fe/Mg clay minerals (Grauby et al., 1994).

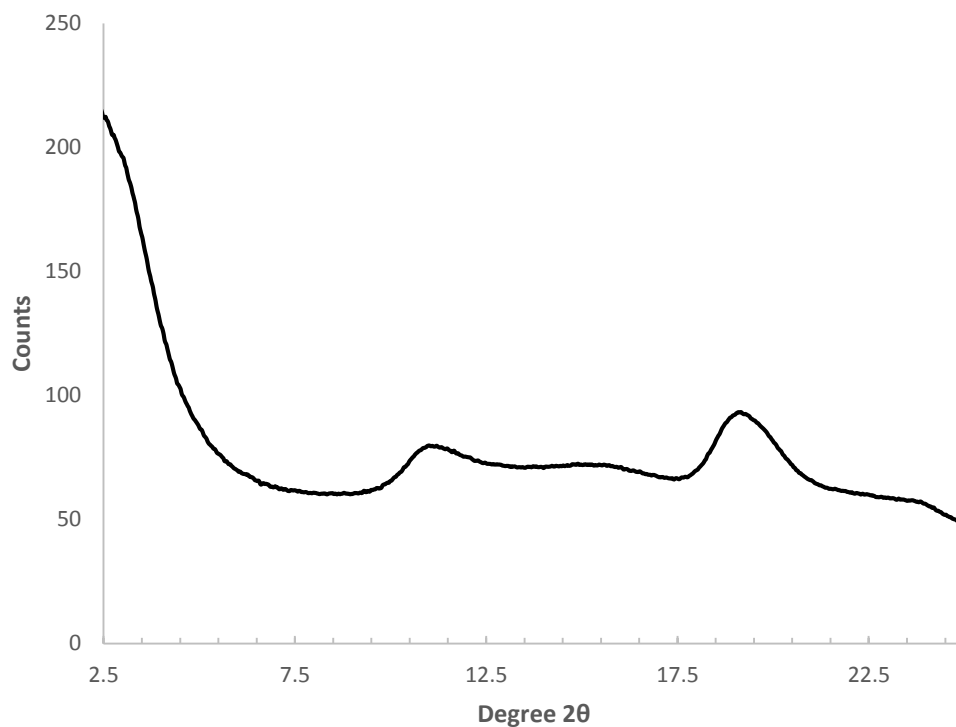


**Figure S42: Synchrotron  $\mu$ -XRD (0.86 Å wavelength) pattern for *Experiment-5* (50-Mg 50-Fe<sup>3+</sup>) precipitated at 150° C.** Note the multiple peaks produced due to crystallinity. This diffraction pattern is consistent with a clay structure, in that the diffraction peaks are produced through the 020 and 060 reflections.





**Figure S43: Photograph of the *Experiment-6* ( $10\text{-Mg } 90\text{-Fe}^{3+}$ ) precipitated at  $150^\circ\text{C}$ .** The precipitate was dried in-vacuo and ground to a fine powder in a mortar and pestle. Notice the reddish color likely from the presence of  $\text{Fe}^{3+}$ .

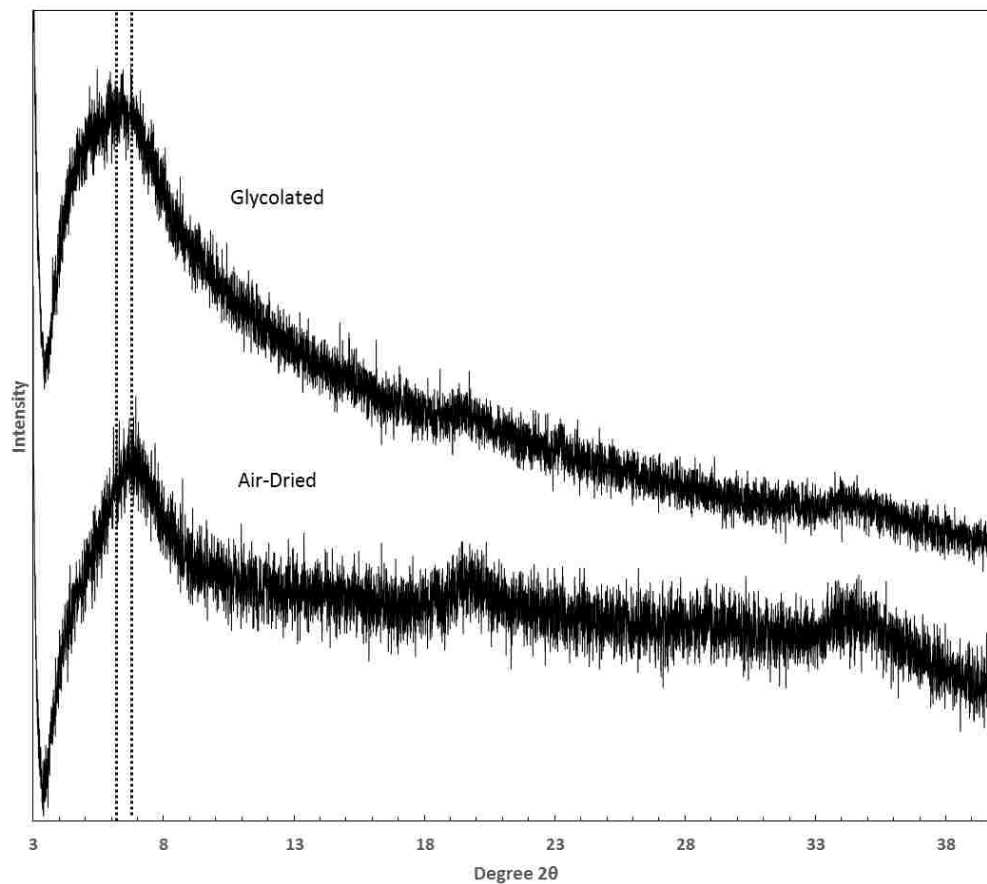


**Figure S44: X-Ray diffraction pattern of *Experiment-6* ( $10\text{-Mg } 90\text{-Fe}^{3+}$ ) precipitated at  $150^\circ\text{C}$ .** The broad low angle diffraction is indicative of a clay mineral. Note the little to no expansion that occurred between the air-dried and ethylene glycol treated samples (exposed to vapor for over 24 hours). This material is similar to the previously synthesized high-charge nontronites produced by Mizutani et al. (1991), and Decreau et al. (2008).



**Figure S45: Photograph of the *Experiment-7* ( $5\text{-Mg } 95\text{-Fe}^{3+}$ ) precipitated at  $150^\circ\text{C}$ .** The precipitate was dried in-vacuo and ground to a fine powder in a mortar and pestle. Note the reddish color likely from the presence of  $\text{Fe}^{3+}$ .

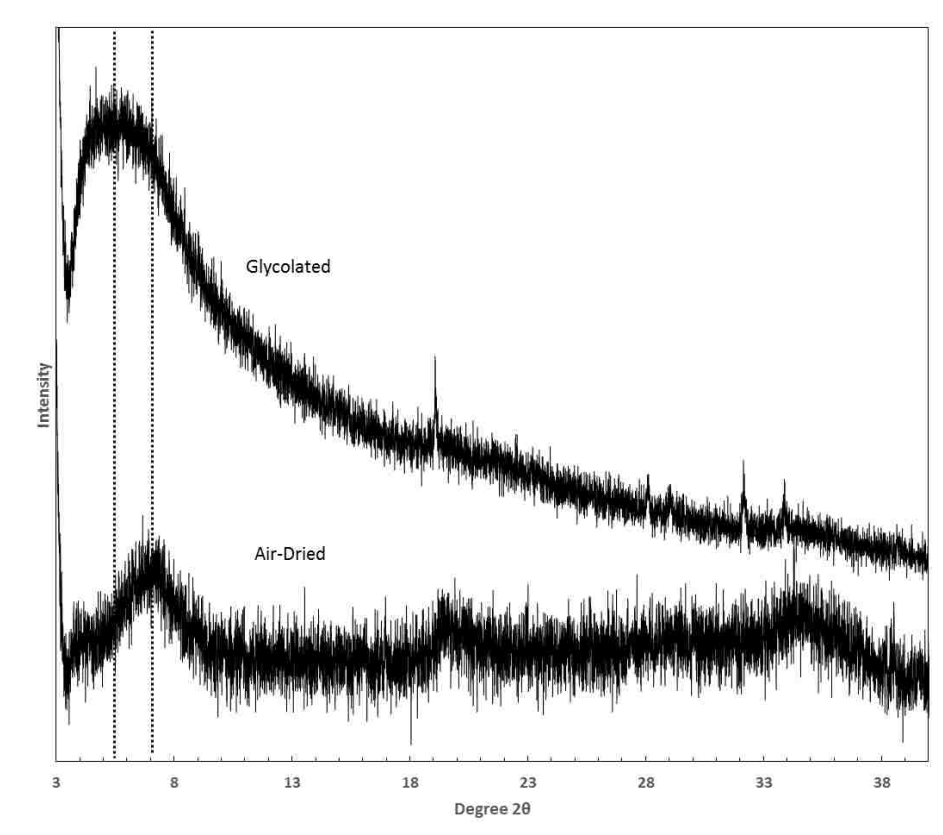


**Figure S46: X-Ray diffraction pattern of *Experiment-7* ( $5\text{-Mg } 95\text{-Fe}^{3+}$ ) precipitated at  $150^\circ\text{C}$ .** The diffraction pattern of the product is consistent with a poorly crystalline clay mineral. This indicates that Fe-rich clay minerals can precipitate with very minor concentrations of Mg. Note that the expansion which occurred between the air-dried and ethylene glycol treated samples (exposed to vapor for over 24 hours), did not expand to the characteristic  $17\text{ \AA}$  of smectite. However, this material is similar to previously studied materials which were characterized as high-charge (e.g. does not fully expand when exposed to ethylene-glycol vapor) nontronites (Harder, 1976; Decarreau et al., 2008).



**Figure S47: Photograph of the *Experiment-8 (100-Al, Low SiO<sub>2</sub>)* precipitated at 150° C. The precipitate was dried in-vacuo and ground to a fine powder in a mortar and pestle.**



**Figure S48: Photograph of the *Experiment-8 (100-Al, Low SiO<sub>2</sub>)* precipitated at 100° C.** The precipitate was dried in-vacuo and ground to a fine powder in a mortar and pestle.

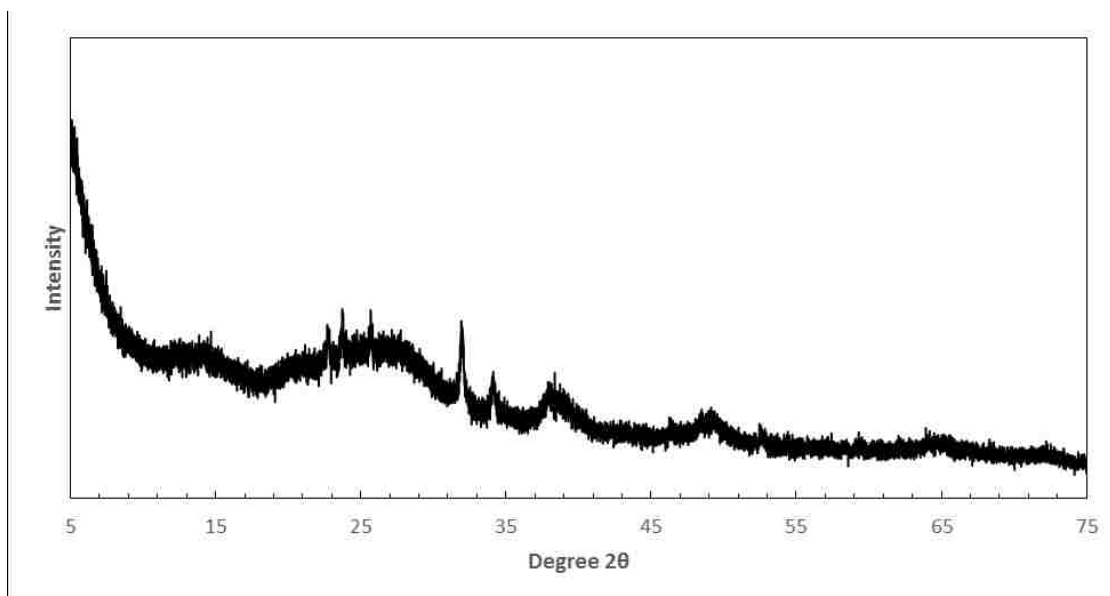


**Figure S49: X-Ray diffraction pattern of *Experiment-8 (100-Al, Low SiO<sub>2</sub>)* precipitated at 150° C.** Note the lack of crystallinity of this relatively amorphous sample. The peaks present are not indicative of clay minerals, but rather boehmite.

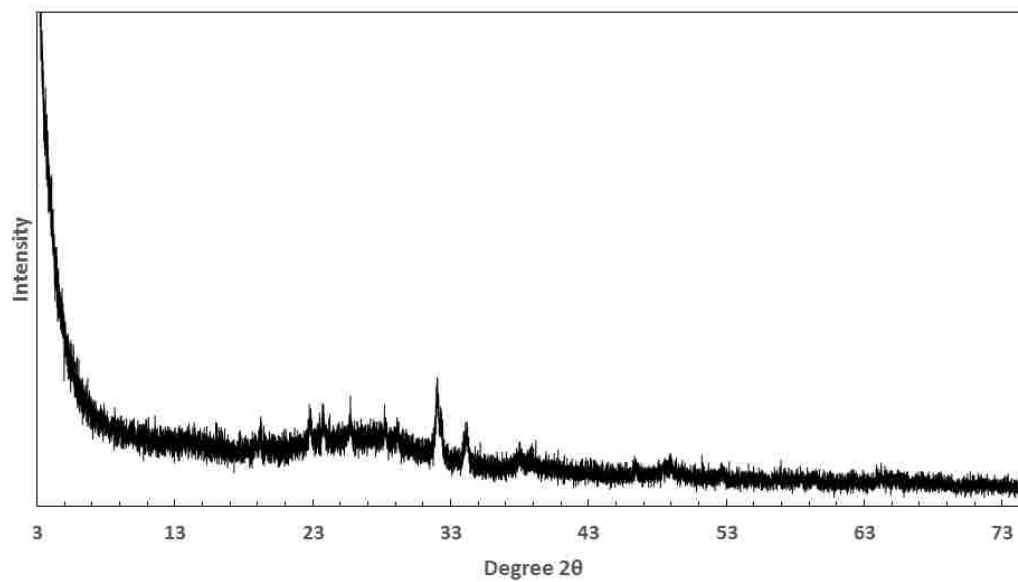


**Figure S50: X-Ray diffraction pattern of *Experiment-8 (100-Al, Low SiO<sub>2</sub>)* precipitated at 100° C.** Note the lack of crystallinity of this relatively amorphous sample. The peaks are the result of minor boehmite.





**Figure S51: Photograph of the *Experiment-9 (100-Mg, Low SiO<sub>2</sub>)* precipitated at 150° C. The precipitate was dried in-vacuo and ground to a fine powder in a mortar and pestle.**



**Figure S52: Photograph of the *Experiment-9 (100-Mg, Low SiO<sub>2</sub>)* precipitated at 100° C. The precipitate was dried in-vacuo and ground to a fine powder in a mortar and pestle.**

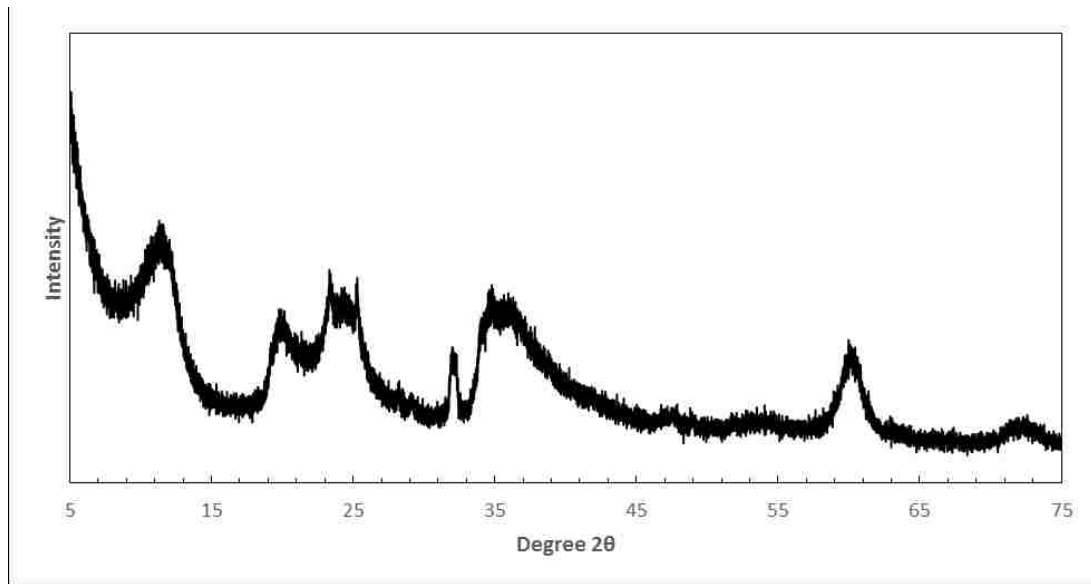


**Figure S53: X-Ray diffraction pattern of *Experiment-9* (100-Mg, Low SiO<sub>2</sub>) precipitated at 150° C. Note the low-angle peak indicative of chrysotile and/or lizardite. The other diffraction peaks are strong indicators of chrysotile and/or lizardite.**

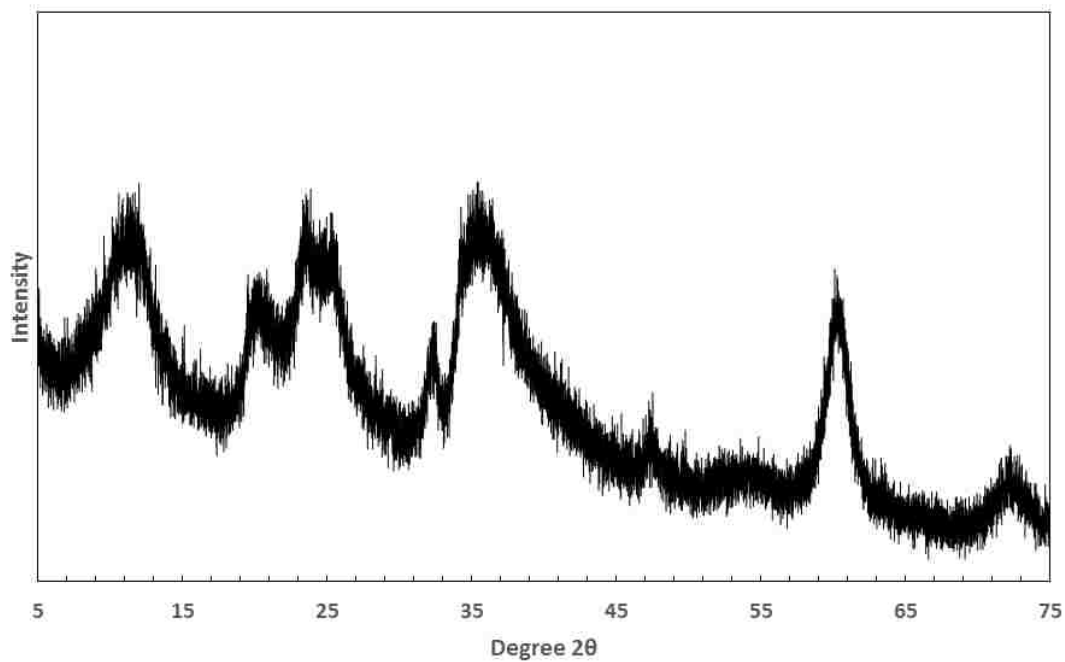


**Figure S54: X-Ray diffraction pattern of *Experiment-9* (100-Mg, Low SiO<sub>2</sub>) precipitated at 100° C.** Note the low-angle peak indicative of chrysotile and/or lizardite. The other diffraction peaks are also strong indicators of chrysotile and/or lizardite. This diffraction pattern is identical to the 150° C precipitate.



**Figure S55: Photograph of the *Experiment-10* (100-Al, High SiO<sub>2</sub>) precipitated at 150° C. The precipitate was dried in-vacuo and ground to a fine powder in a mortar and pestle.**



**Figure S56: Photograph of the *Experiment-10 (100-Al, High SiO<sub>2</sub>)* precipitated at 100° C. The precipitate was dried in-vacuo and ground to a fine powder in a mortar and pestle.**

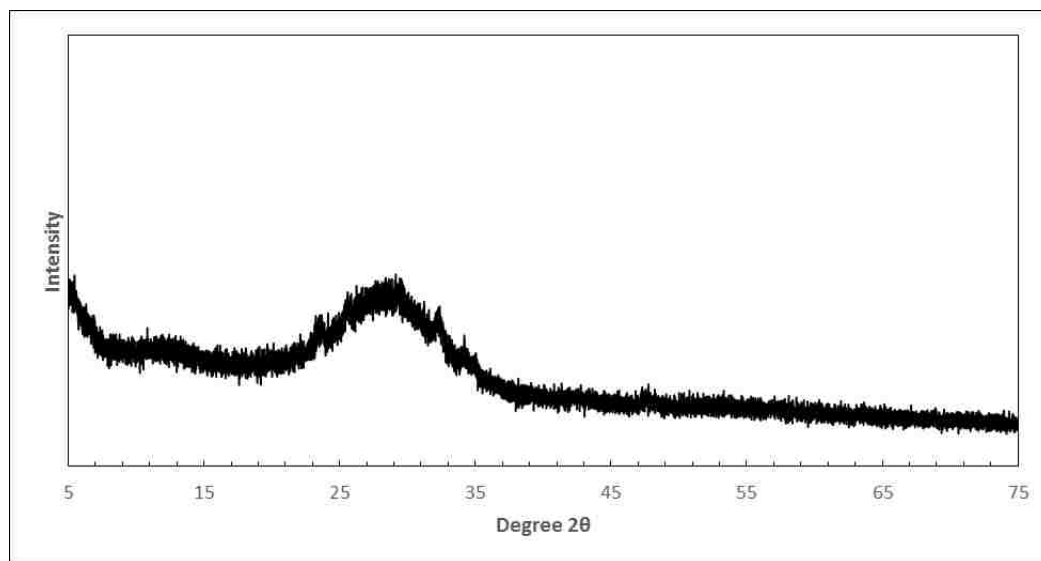


**Figure S57: X-Ray diffraction pattern of *Experiment-10* (100-Al, High SiO<sub>2</sub>) precipitated at 150° C.** This diffraction pattern is consistent with an amorphous product. Some weak diffractions are likely from boehmite.

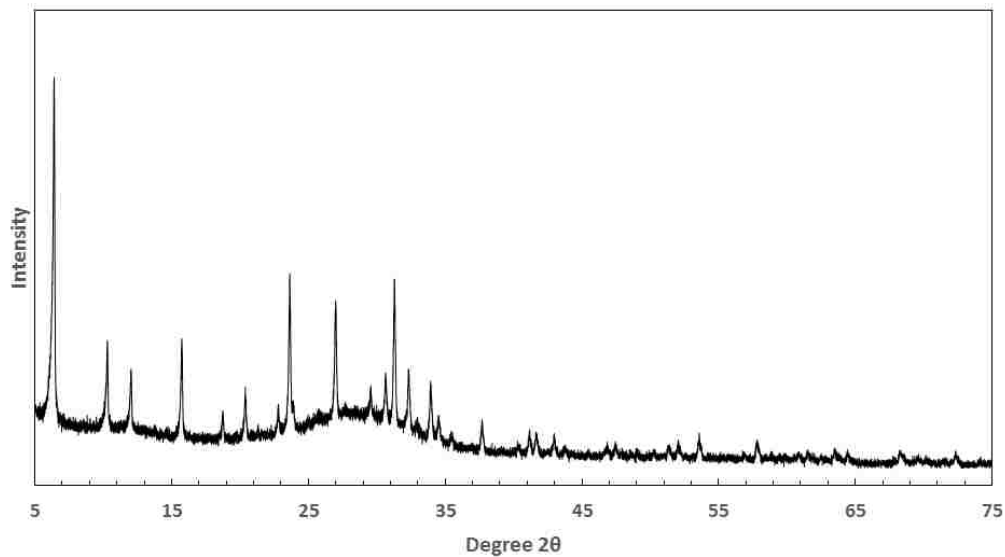


**Figure S58: X-Ray diffraction pattern of *Experiment-10 (100-Al, High SiO<sub>2</sub>)* precipitated at 100° C.** This diffraction pattern is consistent with the zeolite faujasite. The sample is virtually homogeneous, except for the amorphous hump located at approximately 30 degrees 2θ, this is suggestive of hydrated silica.





**Figure S59: Photograph of the *Experiment-11* (44-Al 14-Mg 42-Fe<sup>3+</sup>) precipitated at 150° C.** The precipitate was dried in-vacuo and ground to a fine powder in a mortar and pestle. Note the reddish color likely from the presence of Fe<sup>3+</sup>.



**Figure S60: Photograph of the *Experiment-11* (44-Al 14-Mg 42-Fe<sup>3+</sup>) precipitated at 100° C.** The precipitate was dried in-vacuo and ground to a fine powder in a mortar and pestle. Note the reddish color likely from the presence of Fe<sup>3+</sup>.

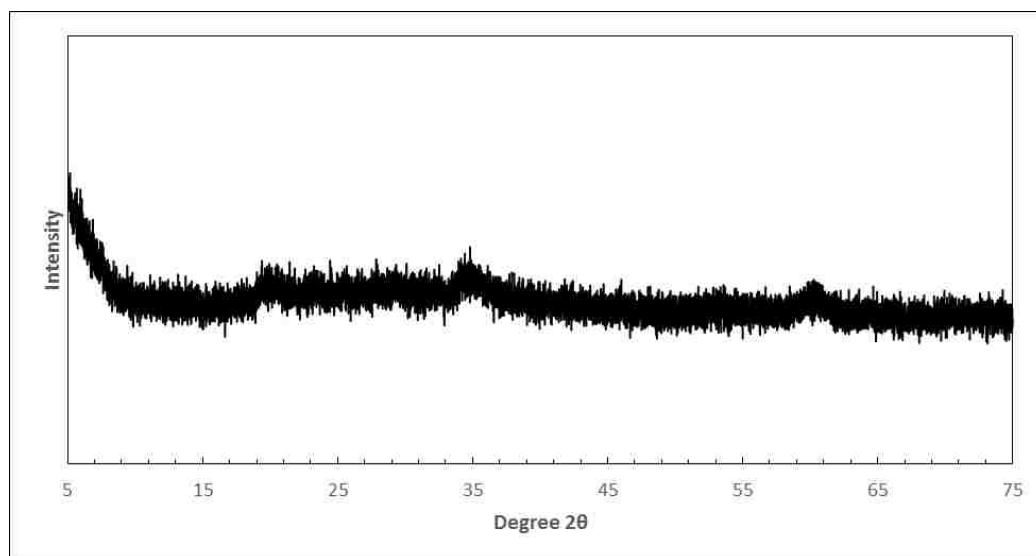


**Figure S61: X-Ray diffraction pattern of *Experiment-11* (44-Al 14-Mg 42-Fe<sup>3+</sup>) precipitated at 150° C.** The diffraction pattern of this product suggest a relatively amorphous precipitate. Some of the *h00* and *0k0* planes appear to be present, suggesting some crystallinity consistent with clay minerals.

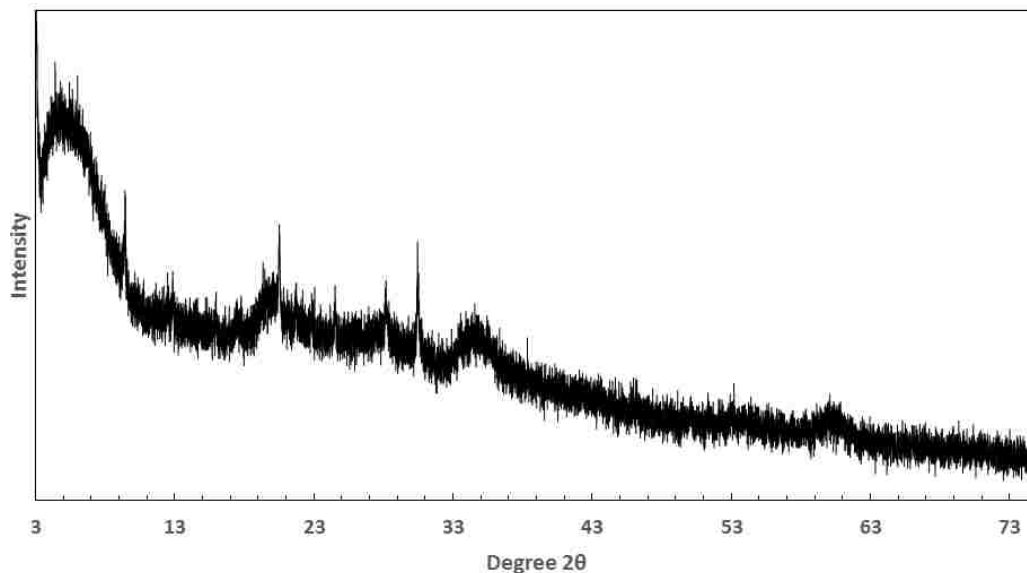


**Figure S62: X-Ray diffraction pattern of *Experiment-11* (44-Al 14-Mg 42-Fe<sup>3+</sup>) precipitated at 100° C.** Note the low angle broad reflection, which is indicative of clay minerals. In addition the diffractions occurring at approximately 19 and 60 degrees characterize the a and b directions of the unit cell and are also indicative of clay minerals. Also a slight shift occurs in the 060 (~60 degree 2θ) peak which maybe suggestive of the incorporation of Al into the structure.



**Figure S63: Photograph of the *Experiment-12 (50-Al 50-Mg)* precipitated at 150° C.**  
The precipitate was dried in-vacuo and ground to a fine powder in a mortar and pestle.



**Figure S64: Photograph of the *Experiment-12 (50-Al 50-Mg)* precipitated at 100° C.**  
The precipitate was dried in-vacuo and ground to a fine powder in a mortar and pestle.

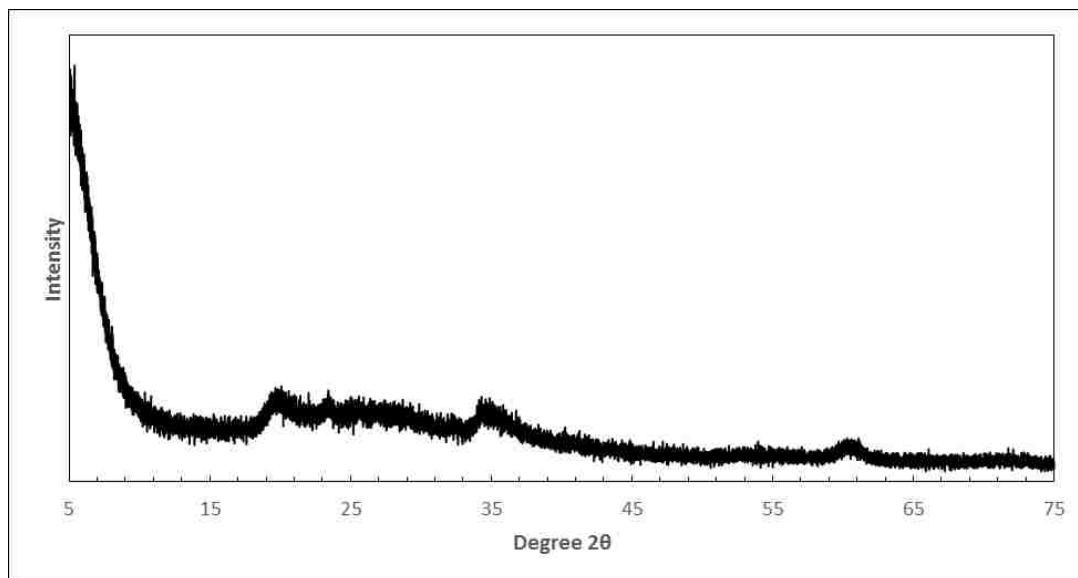


**Figure S65: X-Ray diffraction pattern of *Experiment-12 (50-Al 50-Mg)* precipitated at 150° C.** The diffraction pattern of the product suggests a relatively amorphous precipitate. Some of the  $h00$  and  $0k0$  planes appear to be present, suggesting some crystallinity.

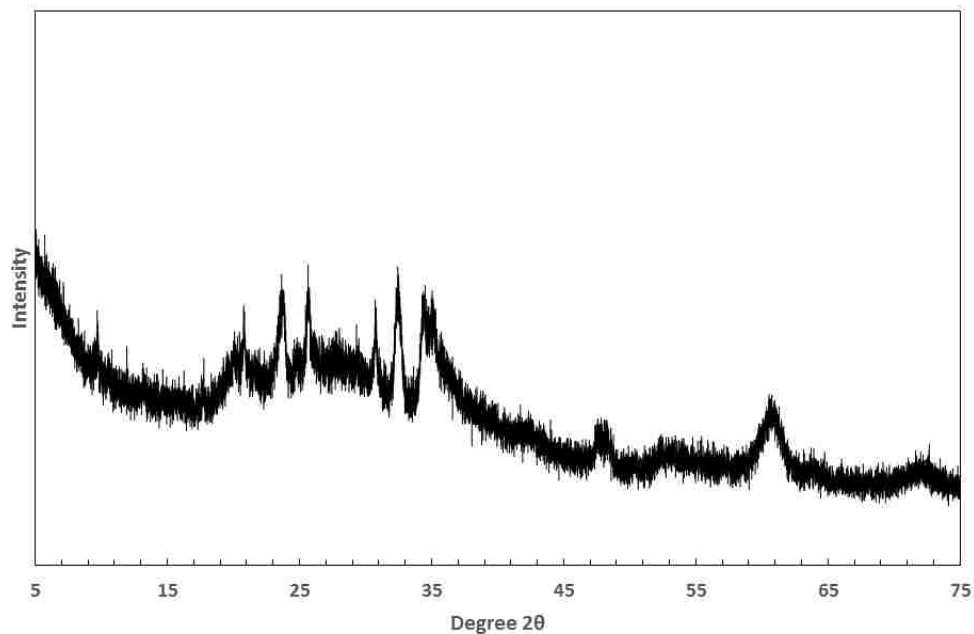


**Figure S66: X-Ray diffraction pattern of *Experiment-12* (50-Al 50-Mg) precipitated at 100° C.** The diffraction patterns of the product suggest a poorly crystalline clay and other secondary phases. Some of the  $h00$  and  $0k0$  planes appear to be present, suggesting some crystallinity.



APPENDIX B: SUPPLEMENTARY MATERIALS FOR CHAPTER THREE

SUPPLEMENTARY TABLES

**Table S11: Flow rate, pH elemental concentration of pH 0.9 experiments at 26°C.**

Sample	Time (h)	Flow Rate		[Si]	[Al]	[Fe]	[Ca]	[Mg]	[Na]
		(mL/h)	pH	(mol/m <sup>3</sup> )	(mol/m <sup>3</sup> )	(mol/m <sup>3</sup> )	(mol/m <sup>3</sup> )	(mol/m <sup>3</sup> )	(mol/m <sup>3</sup> )
R0	0	0.000	-	-	-	-	-	-	-
R1	26.08	0.057	0.98	-	-	-	-	-	-
R2	50.52	0.158	1.80	-	0.30	0.64	-	17.72	0.06
R3	90.87	0.154	1.07	-	5.27	1.61	4.59	3.39	-
R4	114.48	0.159	1.05	-	7.92	1.79	0.01	0.67	-
R5	138.33	0.157	1.04	-	7.54	1.95	-	0.59	-
R6	165.05	0.152	1.04	-	6.43	1.91	-	0.50	-
R7	217.27	0.157	1.03	-	6.05	2.28	-	0.51	-
R8	242.93	0.161	1.05	-	4.94	2.28	-	0.42	-
R9	282.40	0.159	1.05	-	4.41	2.45	-	0.40	-
R10	306.27	0.156	1.04	-	4.03	2.53	-	0.37	-
R11	330.25	0.121	1.04	-	3.95	2.64	-	0.39	-
R12	355.30	0.156	1.03	-	3.81	2.72	-	0.36	-
R13	389.15	0.158	1.06	-	3.55	2.87	-	0.31	-
R14	426.30	0.158	1.03	-	3.39	2.99	-	0.31	-
R15	474.75	0.158	1.05	-	-	-	-	0.25	-
R16	505.20	0.149	1.02	5.24	2.70	2.89	-	0.23	-
R17	555.38	0.142	1.03	5.13	2.65	2.94	-	0.20	-
R18	603.05	0.141	0.98	4.97	2.49	2.96	-	0.20	-
R19	651.60	0.137	1.01	5.27	2.43	3.04	-	0.16	-

R20	692.45	0.165	1.01	4.99	2.37	3.09	-	0.14	-
R21	742.02	0.151	1.02	5.21	2.21	3.10	-	0.14	-
R22	782.95	0.153	1.04	5.55	1.96	3.07	-	0.14	-
R23	814.47	0.149	0.98	5.76	1.94	3.07	-	0.13	-
R24	837.43	0.230	1.08	5.29	1.61	2.64	-	0.11	-
R25	926.90	0.311	1.10	3.44	0.85	1.38	-	0.04	-
R26	953.13	0.302	1.09	3.49	0.88	1.50	-	0.04	-
R27	975.72	0.322	1.09	3.30	0.88	1.55	-	0.03	-
R28	1000.88	0.245	1.08	3.52	0.88	1.59	-	0.04	-
R29	1030.25	0.315	1.10	3.31	0.87	1.61	-	0.02	-
R30	1053.88	0.310	1.10	3.28	0.84	1.64	-	0.02	-
R31	1102.88	0.315	1.10	3.16	0.78	1.63	-	0.01	-
R32	1126.88	0.300	1.10	3.21	0.76	1.66	-	0.01	-
R33	1150.33	0.304	1.11	3.11	0.75	1.68	-	0.01	-
R34	1175.17	0.275	1.11	3.41	0.75	1.71	-	0.01	-
R35	1199.22	0.318	1.13	3.20	0.76	1.74	-	-	-
R36	1222.42	0.304	1.09	3.31	0.74	1.73	-	-	-
R37	1247.72	0.307	1.08	3.22	0.71	1.68	-	-	-

**Table S12: Flow rate, pH elemental concentration of pH 1.7 experiments at 26°C.**

Sample	Time (h)	Flow Rate (mL/h)	pH	[Si] (mol/m <sup>3</sup> )	[Al] (mol/m <sup>3</sup> )	[Fe] (mol/m <sup>3</sup> )	[Ca] (mol/m <sup>3</sup> )	[Mg] (mol/m <sup>3</sup> )	[Na] (mol/m <sup>3</sup> )
O0	0	0.000	-	-	-	-	-	-	-
O1	26.08	0.076	1.36	-	-	-	-	-	-
O2	50.52	0.159	4.67	1.72	-	-	4.98	3.43	2.40
O3	90.87	0.157	4.78	3.49	-	-	6.08	4.32	-
O4	114.48	0.162	4.14	-	-	-	5.62	4.11	-
O5	138.33	0.157	2.77	3.73	-	0.146	5.02	3.66	-
O6	165.05	0.155	2.39	3.62	-	0.255	4.26	3.09	-
O7	217.27	0.161	2.10	3.43	0.016	0.196	3.45	2.25	-
O8	242.93	0.162	2.00	3.01	0.050	0.155	2.59	1.59	-
O9	282.40	0.157	1.94	2.81	0.055	0.140	2.02	1.21	-
O10	306.27	0.158	1.85	-	0.077	0.139	1.44	0.923	-
O11	330.25	0.138	1.83	2.45	-	-	0.114	-	-
O12	355.30	0.158	1.82	2.21	0.113	0.159	0.598	0.652	-
O13	389.15	0.161	1.79	1.95	0.192	0.148	0.143	0.500	-
O14	426.30	0.159	1.79	2.05	0.685	0.084	0.004	0.211	-
O15	474.75	0.160	1.85	1.71	1.07	0.062	-	0.130	-
O16	505.20	0.149	1.84	1.71	1.22	0.063	-	0.118	-
O17	555.38	0.147	1.85	1.68	1.27	0.066	-	0.110	-
O18	603.05	0.143	1.81	1.63	1.30	0.068	-	0.104	-
O19	651.60	0.128	1.83	1.72	1.31	0.073	-	0.105	-
O20	692.45	0.180	1.83	1.44	1.32	0.076	-	0.100	-
O21	742.02	0.159	1.84	1.41	1.29	0.078	-	0.080	-

O22	782.95	0.161	1.82	1.54	1.30	0.082	-	0.083	-
O23	814.47	0.162	1.81	1.53	1.33	0.085	-	0.082	-
O24	837.43	0.272	1.89	1.20	1.03	0.068	-	0.060	-
O25	926.90	0.319	1.86	0.91	0.626	0.048	-	0.031	-
O26	953.13	0.308	1.88	0.85	0.619	0.053	-	0.028	-
O27	975.72	0.320	1.89	0.83	0.607	0.055	-	0.027	-
O28	1000.88	0.268	1.85	0.92	0.617	0.057	-	0.028	-
O29	1030.25	0.321	1.90	0.92	0.615	0.055	-	0.018	-
O30	1053.88	0.314	1.85	0.94	0.601	0.057	-	0.014	-
O31	1102.88	0.318	1.86	0.89	0.590	0.058	-	0.014	-
O32	1126.88	0.309	1.89	0.84	0.579	0.059	-	0.012	-
O33	1150.33	0.301	1.88	0.84	0.582	0.061	-	0.013	-
O34	1175.17	0.294	1.89	0.87	0.572	0.061	-	0.012	-
O35	1199.22	0.314	1.88	0.81	0.573	0.065	-	0.011	-
O36	1222.42	0.304	1.88	0.79	0.560	0.066	-	-	-
O37	1247.72	0.318	1.88	0.74	0.563	0.070	-	0.011	-

**Table S13: Flow rate, pH elemental concentration of pH 3.0 experiments at 26°C.**

Sample	Time (h)	Flow Rate (mL/h)	pH	[Si] (mol/m <sup>3</sup> )	[Al] (mol/m <sup>3</sup> )	[Fe] (mol/m <sup>3</sup> )	[Ca] (mol/m <sup>3</sup> )	[Mg] (mol/m <sup>3</sup> )	[Na] (mol/m <sup>3</sup> )
G0	0	0.000	-	-	-	-	-	-	-
G1	26.08	0.076	1.06	-	-	-	-	-	-
G2	50.52	0.159	5.93	0.515	-	-	0.035	0.003	1.074
G3	90.87	0.157	6.04	0.447	-	-	0.021	-	1.047
G4	114.48	0.162	6.23	0.378	-	-	0.020	-	1.008
G5	138.33	0.157	6.32	0.336	-	-	0.018	-	1.020
G6	165.05	0.155	6.24	0.336	-	-	0.019	-	0.997
G7	217.27	0.161	6.37	0.322	-	-	0.014	-	0.995
G8	242.93	0.162	6.08	0.320	-	-	0.024	-	0.946
G9	282.40	0.157	5.91	0.315	-	-	0.242	0.149	0.007
G10	306.27	0.158	6.29	0.319	-	-	0.249	0.153	0.000
G11	330.25	0.138	6.28	0.341	-	-	0.257	0.160	-
G12	355.30	0.158	6.22	0.342	-	-	0.270	0.172	-
G13	389.15	0.161	6.06	0.329	-	-	0.282	0.177	-
G14	426.30	0.159	6.16	0.331	-	-	0.302	0.192	-
G15	474.75	0.160	6.20	0.330	-	-	0.291	0.193	-
G16	505.20	0.149	6.18	0.342	-	-	0.294	0.192	-
G17	555.38	0.147	6.28	0.348	-	-	0.289	0.193	-
G18	603.05	0.143	6.29	0.350	-	-	0.299	0.196	-
G19	651.60	0.128	6.46	0.372	-	-	0.312	0.201	-
G20	692.45	0.180	6.28	0.352	-	-	0.297	0.198	-
G21	742.02	0.159	6.37	0.338	-	-	0.301	0.202	-

G22	782.95	0.161	6.28	0.296	-	-	0.326	0.218	-
G23	814.47	0.162	6.35	0.358	-	-	0.339	0.226	-
G24	837.43	0.272	6.12	0.362	-	-	0.334	0.223	-
G25	926.90	0.319	6.09	0.288	-	-	0.379	0.252	-
G26	953.13	0.308	5.98	0.337	-	-	0.373	0.256	-
G27	975.72	0.320	5.77	0.342	-	-	0.381	0.261	-
G28	1000.88	0.268	4.97	0.400	-	-	0.377	0.254	-
G29	1030.25	0.321	4.42	0.317	-	-	0.333	0.222	-
G30	1053.88	0.314	4.01	0.308	-	-	0.322	0.211	-
G31	1102.88	0.318	3.94	0.319	-	-	0.316	0.207	-
G32	1126.88	0.309	3.86	0.321	-	-	0.302	0.202	-
G33	1150.33	0.301	3.80	0.315	-	-	0.296	0.198	-
G34	1175.17	0.294	3.72	0.338	-	-	0.284	0.196	-
G35	1199.22	0.314	3.68	0.308	-	-	0.279	0.191	-
G36	1222.42	0.304	3.61	0.311	-	-	0.281	0.187	-
G37	1247.72	0.318	3.58	0.300	-	-	0.263	0.179	-

**Table S14: Steady state nontronite dissolution rates at 26 °C calculated from Si, Fe and Ca release rates assumed to be from the tetrahedral, octahedral and interlayer sites, respectively.** Dissolution rates were normalized to the reacted mineral surface area and sample weight, and used the bulk chemistry of the unreacted nontronite (Keeling et al., 2000).

Input pH	Steady state pH	Flow rate (ml/h)	Dissolution rates normalized to surface area (mol/m <sup>2</sup> s) × 10 <sup>-13</sup>			Dissolution rates normalized to mass (mol/kg s) × 10 <sup>-8</sup>		
			Tetrahedral (Si)	Octahedral (Fe)	Interlayer (Ca)	Tetrahedral (Si)	Octahedral (Fe)	Interlayer (Ca)
0.88	1.01	0.1509 ± 0.0036	4.14 ± 0.27	4.39 ± 0.29	Below Detection	4.19 ± 0.27	4.44 ± 0.29	Below Detection
1.69	1.82	0.1609 ± 0.0029	2.25 ± 0.15	0.234 ± 0.06	Below Detection	1.29 ± 0.08	0.134 ± 0.04	Below Detection
3.01	6.33	0.1602 ± 0.0084	0.432 ± 0.04	Below Detection	2.80 ± 0.24	0.263 ± 0.03	Below Detection	1.70 ± 0.14
0.88	1.10	0.3099 ± 0.0144	5.00 ± 0.35	5.02 ± 0.35	Below Detection	5.07 ± 0.35	5.08 ± 0.34	Below Detection
1.69	1.88	0.3123 ± 0.0143	2.28 ± 0.13	0.371 ± 0.13	Below Detection	1.31 ± 0.07	0.212 ± 0.07	Below Detection
3.01	3.62	0.3111 ± 0.0148	0.777 ± 0.07	Below Detection	4.63 ± 0.35	0.472 ± 0.04	Below Detection	2.81 ± 0.21

SUPPLEMENTARY FIGURES

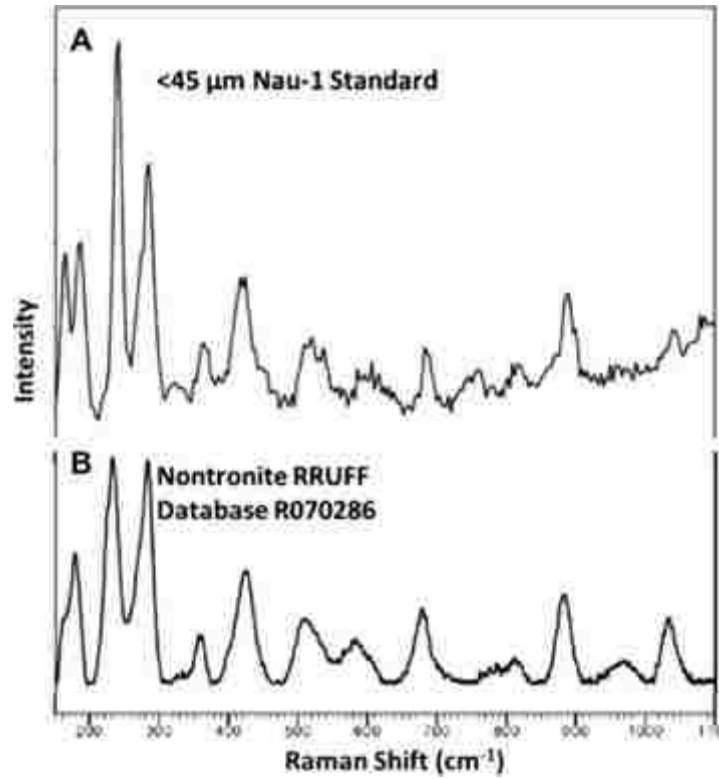


**Figure S67: Raman spectra of Nontronite standard NAu-1.** Raman spectra of (A) the powdered <45 μm NAu-1 standard used in these experiments and (B) a reference spectra of the Andreasberg, Saxony, Germany Nontronite from the RRUFF database (Downs, 2006) measured using a Horiba Jobin Yvon LabRam HR confocal Raman microscope.



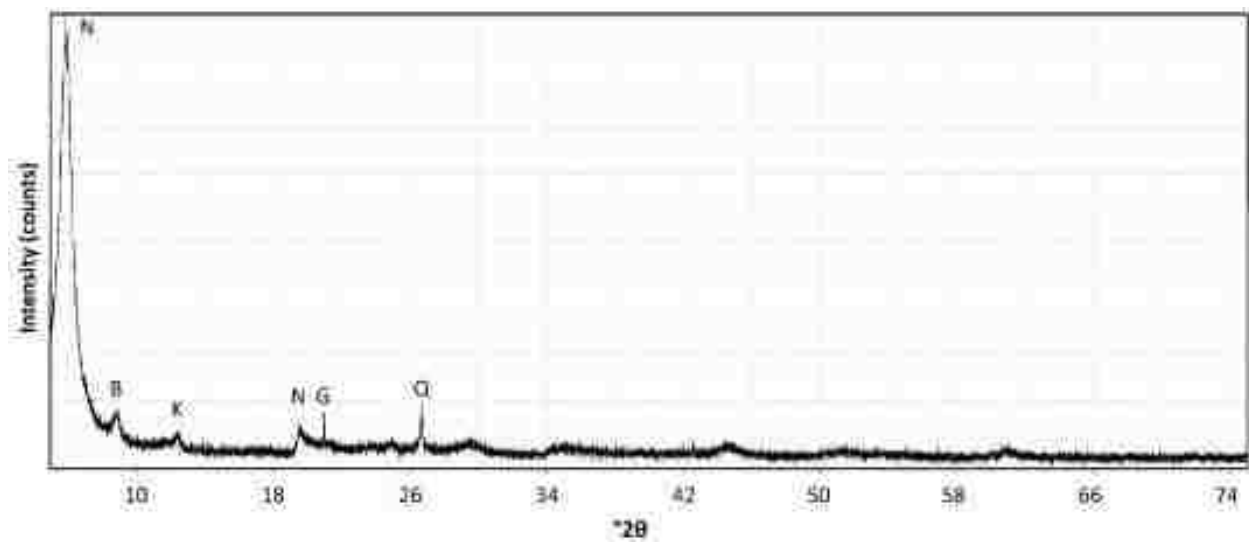


**Figure S68:** XRD pattern of the 45–150  $\mu\text{m}$  size fraction of NAu-1. N-nontronite, B-biotite, G-Goethite, K-Kaolinite, Q-Quartz.

APPENDIX C: SUPPLEMENTARY MATERIALS FOR CHAPTER FOUR

SUPPLEMENTARY TABLES

**Table S15: Observed and calculated solubilities based on chemical analysis on naturally occurring nontronites.**

Name	Equation	Log K <sub>sp</sub>	Source
NAU-1 - Nontronite	$Mg_{0.5025}[Al_{1.02}Si_{6.98}][Fe_{3.68}Mg_{0.04}Al_{0.29}]O_{20}(OH)_4 + 16.08H^+ \leftrightarrow 0.5425Mg^{2+} + 1.31Al^{3+} + 6.98SiO_2 + 3.68Fe^{3+} + 10.04H_2O$	-12.311	Keeling et al., 2000
NAU-2 - Nontronite	$Mg_{0.36}[Al_{0.45}Si_{7.55}][Fe_{3.83}Mg_{0.05}]O_{20}(OH)_4 + 13.8H^+ \leftrightarrow 0.41Mg^{2+} + 0.45Al^{3+} + 7.55SiO_2 + 3.83Fe^{3+} + 8.9H_2O$	-22.143	Keeling et al., 2000
Garfield - Nontronite	$Mg_{0.405}[Al_{0.780}Si_{7.22}][Al_{0.31}Fe^{3+}_{3.64}Fe^{2+}_{0.01}Mg_{0.04}]O_{20}(OH)_4 + 2H^+ \leftrightarrow 0.445Mg^{2+} + 1.09Al^{3+} + 7.22SiO_2 + 3.64Fe^{3+} + 0.01Fe^{2+} + 9.56H_2O$	-14.570	Manceau et al., 2000
PV - Nontronite	$Mg_{0.445}[Al_{0.43}Si_{7.57}][Al_{0.65}Fe^{3+}_{2.87}Fe^{2+}_{0.01}Mg_{0.47}]O_{20}(OH)_4 + 13.72H^+ \leftrightarrow 0.915Mg^{2+} + 1.08Al^{3+} + 7.57SiO_2 + 2.87Fe^{3+} + 0.01Fe^{2+} + 8.86H_2O$	-10.399	Manceau et al., 2000
SWA-1 - Nontronite	$Mg_{0.435}[Al_{0.623}Si_{7.38}][Al_{1.08}Fe^{3+}_{2.67}Fe^{2+}_{0.01}Mg_{0.23}]O_{20}(OH)_4 + 14.48H^+ \leftrightarrow 0.665Mg^{2+} + 1.7Al^{3+} + 7.38SiO_2 + 2.67Fe^{3+} + 0.01Fe^{2+} + 9.24H_2O$	-9.182	Manceau et al., 2000
NG-1 - Nontronite	$Mg_{0.35}[Fe^{3+}_{0.63}Al_{0.08}Si_{7.29}][Al_{0.88}Fe^{3+}_{3.08}Fe^{2+}_{0.01}Mg_{0.06}]O_{20}(OH)_4 + 14.84H^+ \leftrightarrow 0.41Mg^{2+} + 0.96Al^{3+} + 7.29SiO_2 + 3.71Fe^{3+} + 0.01Fe^{2+} + 9.42H_2O$	-14.882	Manceau et al., 2000
Chad - Nontronite	$Mg_{0.22}[Al_{0.17}Si_{3.83}][Fe_{1.77}Mg_{0.21}]O_{10}(OH)_2 + 6.68H^+ \leftrightarrow 0.43Mg^{2+} + 0.17Al^{3+} + 3.83SiO_2 + 1.77Fe^{3+} + 4.34H_2O$	-14.918	Tardy and Fritiz, 1981
Caledonia - Nontornite	$Mg_{0.135}[Al_{0.27}Si_{3.73}][Al_{0.07}Fe_{1.72}Mg_{0.315}]O_{10}(OH)_2 + 7.08H^+ \leftrightarrow 0.45Mg^{2+} + 0.34Al^{3+} + 3.73SiO_2 + 1.72Fe^{3+} + 4.54H_2O$	-11.760	Tardy and Fritz, 1981
CLA - Nontornite	$Mg_{0.52}[Al_{0.13}Si_{6.81}Fe_{1.06}][Fe_{4.01}Mg_{0.07}]O_{20}(OH)_4 + 14.8H^+ \leftrightarrow 0.59Mg^{2+} + 0.13Al^{3+} + 6.81SiO_2 + 5.07Fe^{3+} + 10.38H_2O$	-18.372	Goodman et al., 1976
CRO - Nontronite	$Mg_{0.535}[Al_{0.063}Si_{6.75}Fe_{1.19}][Fe_{3.90}Mg_{0.24}]O_{20}(OH)_4 + 14.48H^+ \leftrightarrow 0.775Mg^{2+} + 0.06Al^{3+} + 6.75SiO_2 + 5.15Fe^{3+} + 10.5H_2O$	-18.922	Goodman et al., 1976
CAL - Nontornite	$Mg_{0.625}[Al_{0.14}Si_{6.21}Fe_{1.65}][Fe_{4.04}Mg_{0.21}]O_{20}(OH)_4 + 19.16H^+ \leftrightarrow 0.835Mg^{2+} + 0.14Al^{3+} + 6.21SiO_2 + 5.69Fe^{3+} + 11.58H_2O$	-16.228	Goodman et al., 1976
AMO - Nontronite	$Mg_{0.37}[Al_{0.04}Si_{6.84}Fe_{1.12}][Fe_{4.04}Mg_{0.15}]O_{20}(OH)_4 + 19.16H^+ \leftrightarrow 0.52Mg^{2+} + 0.04Al^{3+} + 6.84SiO_2 + 5.16Fe^{3+} + 10.32H_2O$	-18.381	Goodman et al., 1976
GAR - Nontronite	$Mg_{0.6}[Al_{1.05}Si_{6.84}Fe_{0.11}][Fe_{3.96}Mg_{0.04}]O_{20}(OH)_4 + 16.64H^+ \leftrightarrow 0.64Mg^{2+} + 1.05Al^{3+} + 6.84SiO_2 + 4.07Fe^{3+} + 10.32H_2O$	-13.532	Goodman et al., 1976
WAS - Nontornite	$Mg_{0.405}[Al_{0.70}Si_{7.30}][Al_{1.06}Fe_{2.73}Mg_{0.26}]O_{20}(OH)_4 + 14.8H^+ \leftrightarrow 0.915Mg^{2+} + 1.76Al^{3+} + 7.30SiO_2 + 2.73Fe^{3+} + 9.4H_2O$	-8.918	Goodman et al., 1976
KOE - Nontronite	$Mg_{0.505}[Al_{0.08}Si_{6.61}Fe_{1.31}][Fe_{4.06}Mg_{0.10}]O_{20}(OH)_4 + 17.56H^+ \leftrightarrow 0.605Mg^{2+} + 0.08Al^{3+} + 6.61SiO_2 + 5.37Fe^{3+} + 10.78H_2O$	-18.067	Goodman et al., 1976
Chad - Nontronite	$Mg_{0.22}[Al_{0.17}Si_{3.83}][Fe_{1.77}Mg_{0.21}]O_{10}(OH)_2 + 6.68H^+ \leftrightarrow 0.43Mg^{2+} + 0.17Al^{3+} + 3.83SiO_2 + 1.77Fe^{3+} + 4.34H_2O$	-8.440	Tardy and Fritiz, 1981
Caledonia - Nontornite	$Mg_{0.135}[Al_{0.27}Si_{3.73}][Al_{0.07}Fe_{1.72}Mg_{0.315}]O_{10}(OH)_2 + 7.08H^+ \leftrightarrow 0.45Mg^{2+} + 0.34Al^{3+} + 3.73SiO_2 + 1.72Fe^{3+} + 4.54H_2O$	-6.157	Tardy and Fritz, 1981

\*\*\*Chemical formulae for nontronites were sourced from the literature (Goodman et al., 1976; Tardy and Fritz, 1981; Keeling et al., 2000; Manceau et al., 2000b) and solubilities calculated (black) using the method proposed by Tardy and Garrels (1974), values were calculated per O<sub>10</sub>(OH)<sub>2</sub> unit cell. Notice the broad range of solubilities with this method, many of which are extremely insoluble. Tardy and Fritiz (1981) revised a method to account for the poor crystallinity of clay mineral, making clay minerals significantly more soluble. The solubilities presented in red, are the observed solubilities from Tardy and Fritz (1981).

**Table 16: Observed and calculated solubility based on chemical analysis on naturally occurring montmorillonites.**

Name	Equation	Log K <sub>sp</sub>	Source
Chi - Montmorillonite	$Mg_{0.445}[Al_{0.09}Si_{7.91}][Al_{3.11}Fe_{0.09}Mg_{0.80}]O_{20}(OH)_4 + 6.76 H^+ \leftrightarrow 1.245Mg^{2+} + 3.2Al^{3+} + 7.91SiO_2 + 0.09Fe^{3+} + 8.18H_2O$	2.676	Vantelon et al., 2003
STx1 - Montmorillonite	$Mg_{0.42}[Al_{0.09}Si_{7.91}][Al_{3.12}Fe_{0.14}Mg_{0.75}]O_{20}(OH)_4 + 6.76 H^+ \leftrightarrow 1.17Mg^{2+} + 3.21Al^{3+} + 7.91SiO_2 + 0.14Fe^{3+} + 8.18H_2O$	6.016	Vantelon et al., 2003
NAf - Montmorillonite	$Mg_{0.5}[Al_{0.17}Si_{7.83}][Al_{2.88}Fe^{3+}_{0.29}Fe^{2+}_{0.07}Mg_{0.81}]O_{20}(OH)_4 + 6.76 H^+ \leftrightarrow 1.31Mg^{2+} + 3.05Al^{3+} + 7.83SiO_2 + 0.29Fe^{3+} + 0.07Fe^{2+} + 8.34H_2O$	2.722	Vantelon et al., 2003
Mil - Montmorillonite	$Mg_{0.39}[Al_{0.23}Si_{7.77}][Al_{3.02}Fe^{3+}_{0.43}Fe^{2+}_{0.02}Mg_{0.53}]O_{20}(OH)_4 + 6.76 H^+ \leftrightarrow 0.92Mg^{2+} + 3.25Al^{3+} + 7.77SiO_2 + 0.43Fe^{3+} + 0.02Fe^{2+} + 8.46H_2O$	1.475	Vantelon et al., 2003
BAV - Montmorillonite	$Mg_{0.39}[Al_{0.17}Si_{7.83}][Al_{2.78}Fe_{0.53}Fe_{0.03}Mg_{0.66}]O_{20}(OH)_4 + 6.76 H^+ \leftrightarrow 1.05Mg^{2+} + 2.95Al^{3+} + 7.83SiO_2 + 0.43Fe^{3+} + 0.03Fe^{2+} + 8.34H_2O$	0.680	Vantelon et al., 2003
Wyoming - Montmorillonite	$Mg_{0.365}[Al_{0.24}Si_{7.76}][Al_{3.09}Fe_{0.46}Mg_{0.49}]O_{20}(OH)_4 + 6.76 H^+ \leftrightarrow 0.855Mg^{2+} + 3.33Al^{3+} + 7.76SiO_2 + 0.46Fe^{3+} + 8.48H_2O$	-0.699	Tardy and Fritz, 1981
Aberdeen - Montmorillonite	$Mg_{0.275}[Al_{0.18}Si_{3.82}][Al_{1.29}Fe_{0.335}Mg_{0.445}]O_{10}(OH)_2 + 6.72 H^+ \leftrightarrow 0.72Mg^{2+} + 1.47Al^{3+} + 3.82SiO_2 + 0.335Fe^{3+} + 4.36H_2O$	4.338	Tardy and Fritz, 1981
Belle - Montmorillonite	$Mg_{0.14}[Al_{0.065}Si_{3.935}][Al_{1.51}Fe_{0.225}Mg_{0.29}]O_{10}(OH)_2 + 6.26 H^+ \leftrightarrow 0.43Mg^{2+} + 1.575Al^{3+} + 3.935SiO_2 + 0.225Fe^{3+} + 4.13H_2O$	-0.302	Tardy and Fritz, 1981
Caslte - Montmorillonite	$Mg_{0.21}[Al_{0.32}Si_{3.68}][Al_{1.52}Fe_{0.14}Mg_{0.46}]O_{10}(OH)_2 + 7.28 H^+ \leftrightarrow 0.67Mg^{2+} + 1.84Al^{3+} + 3.68SiO_2 + 0.14Fe^{3+} + 4.64H_2O$	0.122	Tardy and Fritz, 1981
Upton - Montmorillonite	$Mg_{0.17}[Al_{0.07}Si_{3.93}][Al_{1.55}Fe_{0.20}Mg_{0.24}]O_{10}(OH)_2 + 6.28 H^+ \leftrightarrow 0.41Mg^{2+} + 1.62Al^{3+} + 3.93SiO_2 + 0.20Fe^{3+} + 4.14H_2O$	6.425	Tardy and Fritz, 1981
Colony 1 - Montmorillonite	$Mg_{0.185}[Al_{0.20}Si_{3.80}][Al_{1.58}Fe_{0.19}Mg_{0.26}]O_{10}(OH)_2 + 6.8 H^+ \leftrightarrow 0.445Mg^{2+} + 1.78Al^{3+} + 3.80SiO_2 + 0.19Fe^{3+} + 4.4H_2O$	2.130	Tardy and Fritz, 1981
Colony 2 - Montmorillonite	$Mg_{0.195}[Al_{0.19}Si_{3.81}][Al_{1.52}Fe_{0.22}Mg_{0.29}]O_{10}(OH)_2 + 6.76 H^+ \leftrightarrow 0.485Mg^{2+} + 1.71Al^{3+} + 3.81SiO_2 + 0.22Fe^{3+} + 4.38H_2O$	1.970	Tardy and Fritz, 1981
Arizona - Montmorillonite	$Mg_{0.145}[Al_{0.07}Si_{3.93}][Al_{1.52}Fe_{0.14}Mg_{0.33}]O_{10}(OH)_2 + 7.28 H^+ \leftrightarrow 0.475Mg^{2+} + 1.59Al^{3+} + 3.93SiO_2 + 0.14Fe^{3+} + 4.14H_2O$	9.630	Tardy and Fritz, 1981
Wyoming - Montmorillonite	$Mg_{0.365}[Al_{0.24}Si_{7.76}][Al_{3.09}Fe_{0.46}Mg_{0.49}]O_{20}(OH)_4 + 6.76 H^+ \leftrightarrow 0.855Mg^{2+} + 3.33Al^{3+} + 7.76SiO_2 + 0.46Fe^{3+} + 8.48H_2O$	6.879	Tardy and Fritz, 1981
Aberdeen - Montmorillonite	$Mg_{0.275}[Al_{0.18}Si_{3.82}][Al_{1.29}Fe_{0.335}Mg_{0.445}]O_{10}(OH)_2 + 6.72 H^+ \leftrightarrow 0.72Mg^{2+} + 1.47Al^{3+} + 3.82SiO_2 + 0.335Fe^{3+} + 4.36H_2O$	2.753	Tardy and Fritz, 1981
Belle - Montmorillonite	$Mg_{0.14}[Al_{0.065}Si_{3.935}][Al_{1.51}Fe_{0.225}Mg_{0.29}]O_{10}(OH)_2 + 6.26 H^+ \leftrightarrow 0.43Mg^{2+} + 1.575Al^{3+} + 3.935SiO_2 + 0.225Fe^{3+} + 4.13H_2O$	0.280	Tardy and Fritz, 1981
Caslte - Montmorillonite	$Mg_{0.21}[Al_{0.32}Si_{3.68}][Al_{1.52}Fe_{0.14}Mg_{0.46}]O_{10}(OH)_2 + 7.28 H^+ \leftrightarrow 0.67Mg^{2+} + 1.84Al^{3+} + 3.68SiO_2 + 0.14Fe^{3+} + 4.64H_2O$	6.224	Tardy and Fritz, 1981
Upton - Montmorillonite	$Mg_{0.17}[Al_{0.07}Si_{3.93}][Al_{1.55}Fe_{0.20}Mg_{0.24}]O_{10}(OH)_2 + 6.28 H^+ \leftrightarrow 0.41Mg^{2+} + 1.62Al^{3+} + 3.93SiO_2 + 0.20Fe^{3+} + 4.14H_2O$	3.220	Tardy and Fritz, 1981
Colony 1 - Montmorillonite	$Mg_{0.185}[Al_{0.20}Si_{3.80}][Al_{1.58}Fe_{0.19}Mg_{0.26}]O_{10}(OH)_2 + 6.8 H^+ \leftrightarrow 0.445Mg^{2+} + 1.78Al^{3+} + 3.80SiO_2 + 0.19Fe^{3+} + 4.4H_2O$	2.858	Tardy and Fritz, 1981
Colony 2 - Montmorillonite	$Mg_{0.195}[Al_{0.19}Si_{3.81}][Al_{1.52}Fe_{0.22}Mg_{0.29}]O_{10}(OH)_2 + 6.76 H^+ \leftrightarrow 0.485Mg^{2+} + 1.71Al^{3+} + 3.81SiO_2 + 0.22Fe^{3+} + 4.38H_2O$	2.847	Tardy and Fritz, 1981
Arizona - Montmorillonite	$Mg_{0.145}[Al_{0.07}Si_{3.93}][Al_{1.52}Fe_{0.14}Mg_{0.33}]O_{10}(OH)_2 + 7.28 H^+ \leftrightarrow 0.475Mg^{2+} + 1.59Al^{3+} + 3.93SiO_2 + 0.14Fe^{3+} + 4.14H_2O$	10.263	Tardy and Fritz, 1981

\*\*\*Chemical formulae for montmorillonities were sourced from the literature (Tardy and Fritz, 1981; Vantelon et al., 2003) and solubilities calculated (black) using the method proposed by Tardy and Garrels (1974), values were calculated per O<sub>10</sub>(OH)<sub>2</sub> unit cell. The solubilities presented in red, are the observed solubilities from Tardy and Fritz (1981).

SUPPLEMENTARY FIGURES

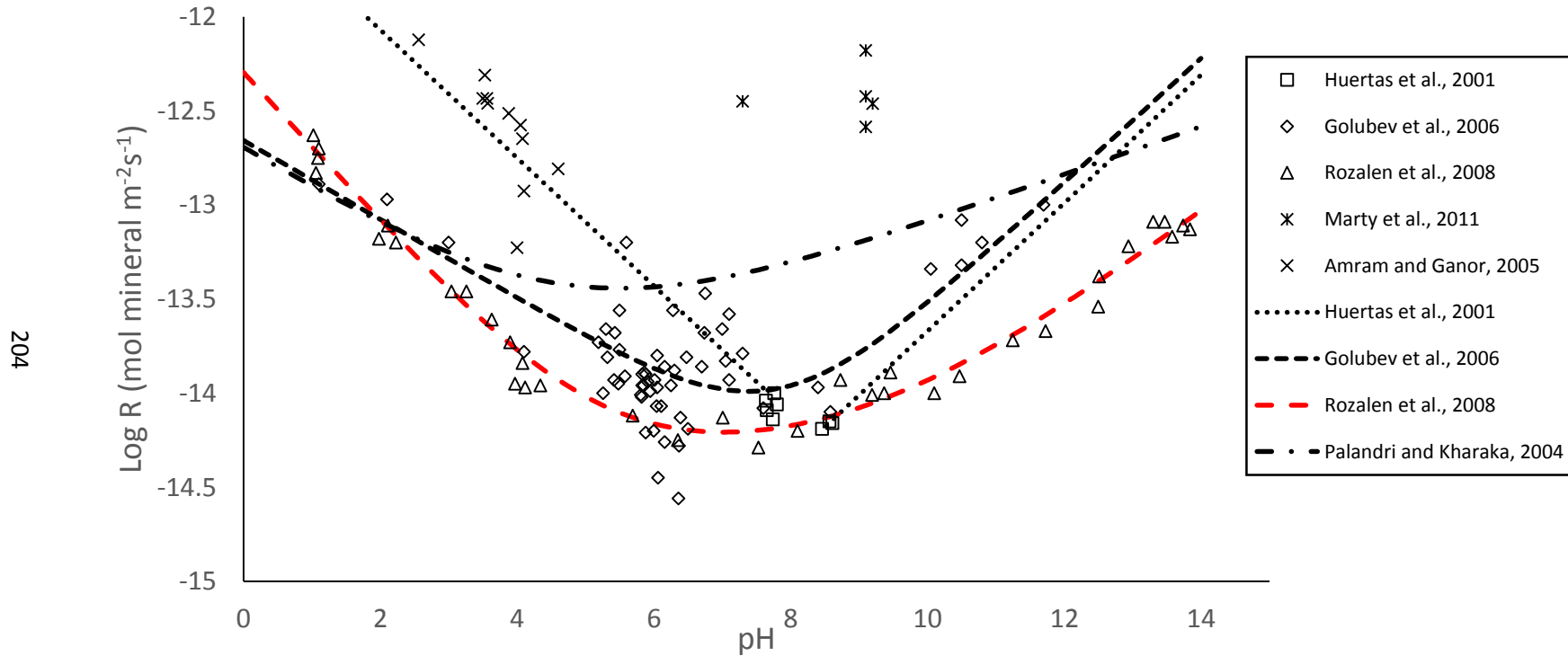


**Figure S69: Comparison of dissolution rates and rate laws for montmorillonite.** Comparison of dissolution rates (marked by single points) for montmorillonite, sourced from the literature (Huertas et al., 2001; Amram and Ganor, 2005; Golubev et al., 2006; Rozalén et al., 2008a; Marty et al., 2011b). Dissolution rate laws marked by dashed lines, were sourced from Huertas et al., (2001); Golubev et al., (2006); Rozalen et al., (2008a) and Palandri and Kharaka, (2004). The rate law from Rozalen et al., (2008a), was chosen for the final models (marked in red).

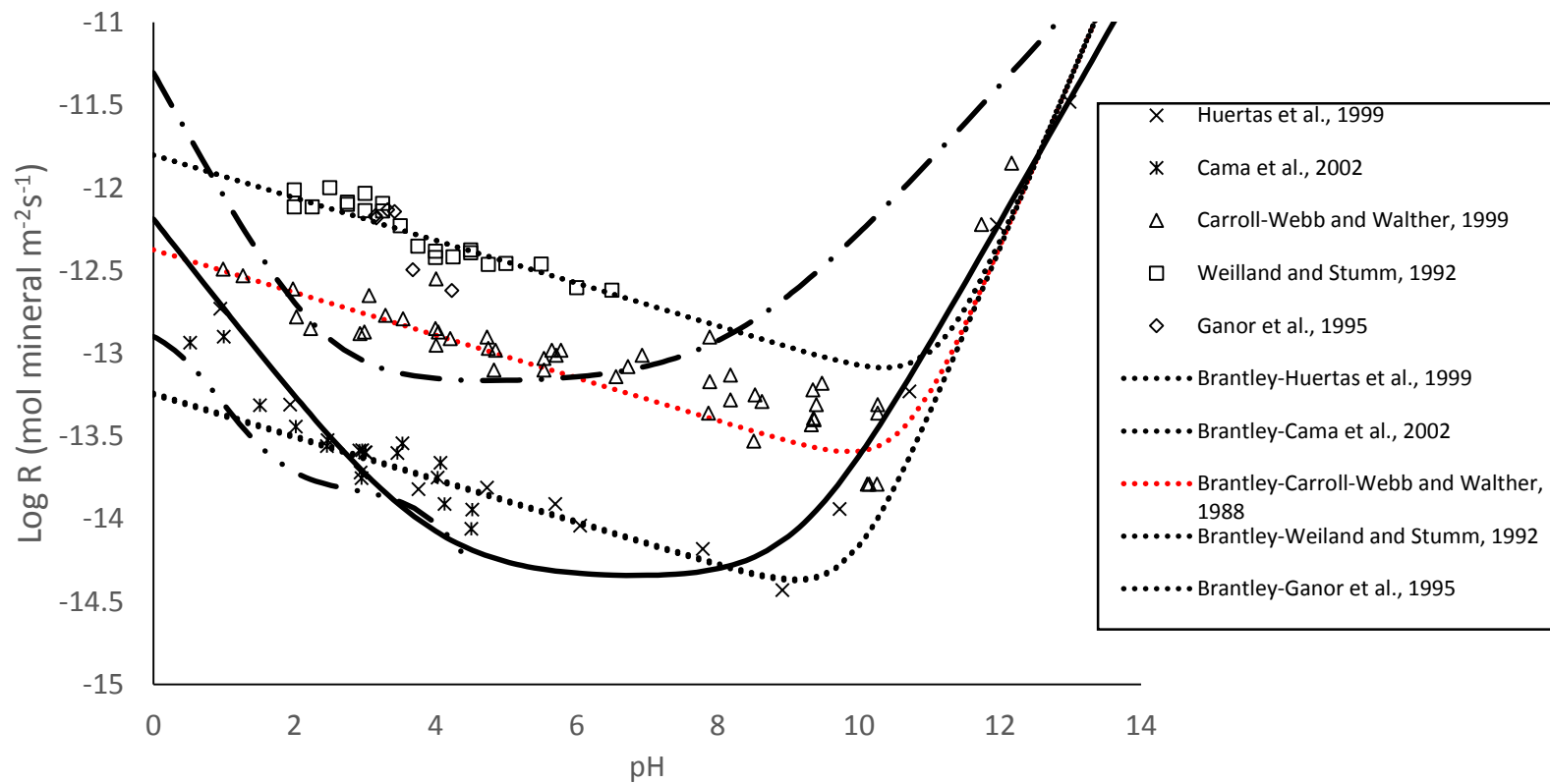


**Figure S70: Comparison of dissolution rates and rate laws for kaolinite.** Comparison of dissolution rates (marked by single points) for kaolinite, sourced from the literature (Carroll-Webb and Walther, 1988; Weiland and Stumm, 1992; Ganor et al., 1995; Huertas et al., 1999a; Cama et al., 2002). Dissolution rate laws marked by dashed lines, were sourced from Brantley (2008) – data was sourced from Huertas et al., (1999a); Cama et al., (2002); Carroll-Webb and Walther (1988); Weiland and Stumm, (1992) and Ganor et al., (1995). Additional rate laws were sourced from Palandri and Kharaka (2004) – based on data from Carroll and Walther (1988); Ganor et al., (1995); Huertas et al., (1999a); Huertas et al., (1999c); Nagay et al., (1991); Soong (1993). In addition the experimental rate laws of; Huertas et al, (1999a) and Cama et al., (2002). The rate law from Brantley (2008), based on data from Carroll-Webb and Walther (1988) was chosen for the final models (marked in red).

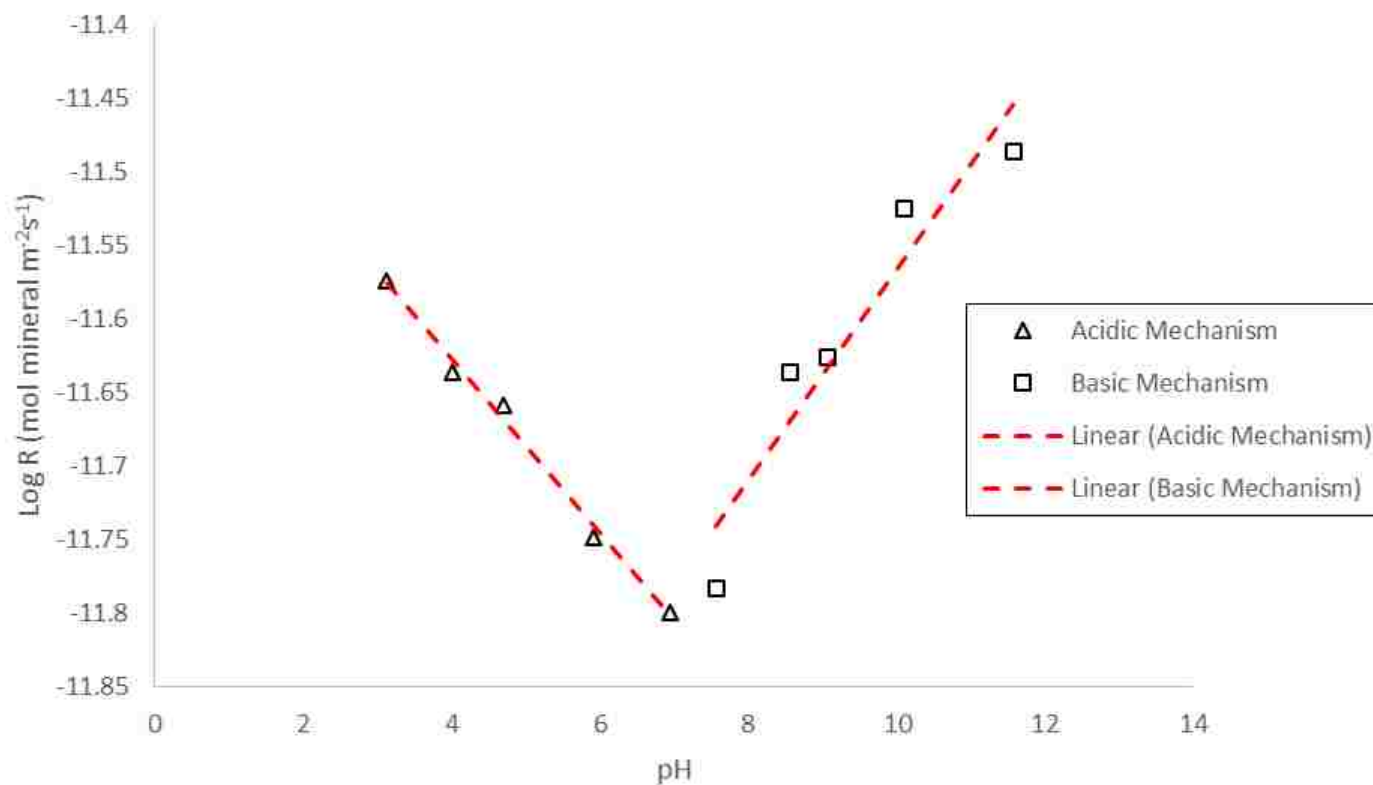


**Figure S71: Dissolution rates and the determined rate law for saponite.** Dissolution rate constants for saponite over a broad pH range (Brigatti et al., 1999) were used to calculate dissolution rates marked by single points) through the initial rate method (Rimstidt and Newcomb, 1993), which were normalized to the surface area of a natural saponite (161 m<sup>2</sup>/g) (Vicente et al., 1996), and used to calculate a dissolution rate law (marked in red).

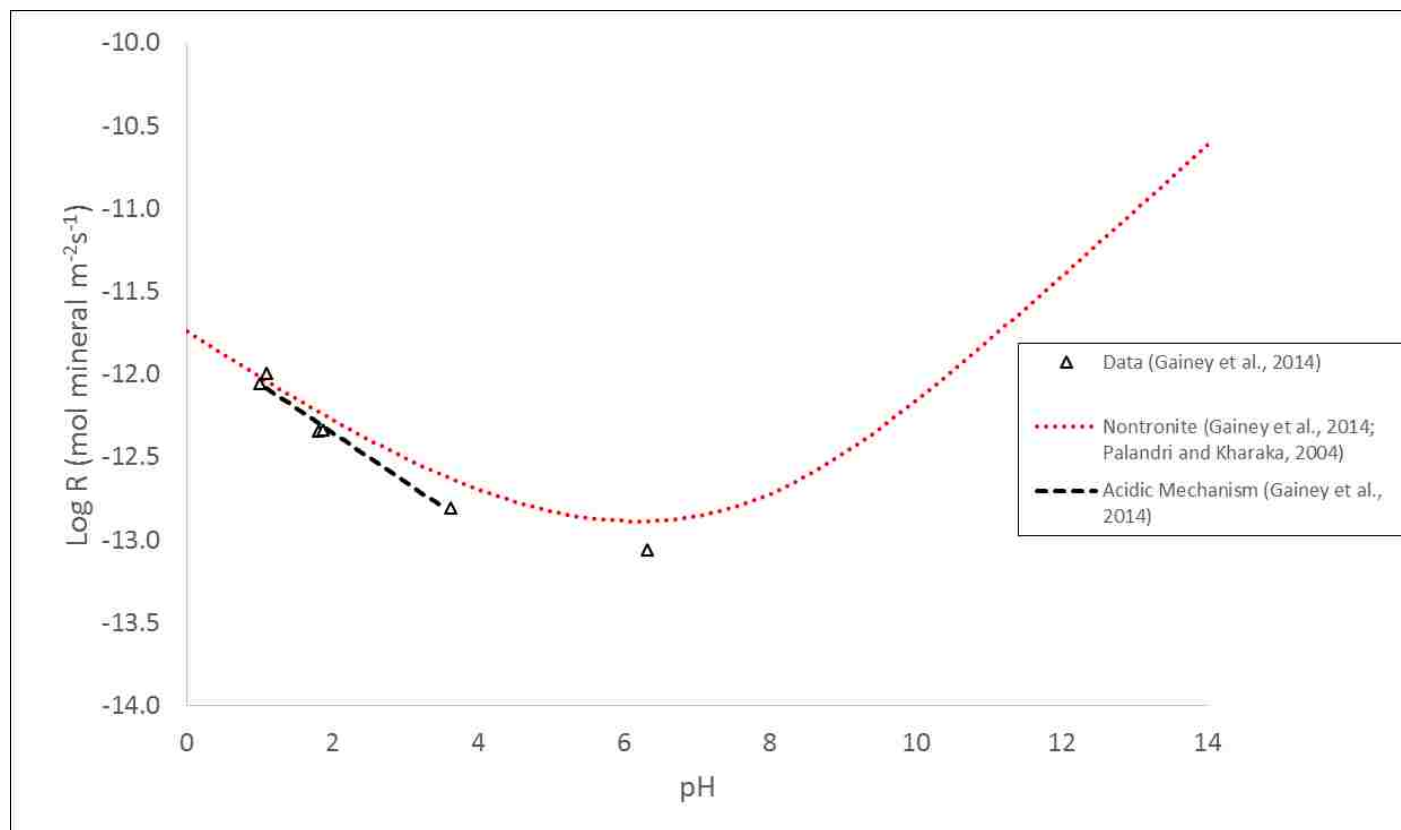


**Figure S72: Dissolution rates and the determined rate law for nontronite.** Dissolution rates (marked by single points) for nontronite, sourced from the literature (Gainey et al., 2014). Dissolution rate laws marked by dashed lines were sourced from Gainey et al., (2014) for the acidic and neutral mechanisms. The basic mechanism was sourced from Palandri and Kharaka, (2004) – data was sourced from Bauer and Berger, (1998); Huertas et al., (2001); Sverdrup (1990) and Zysset and Schindler (1996).

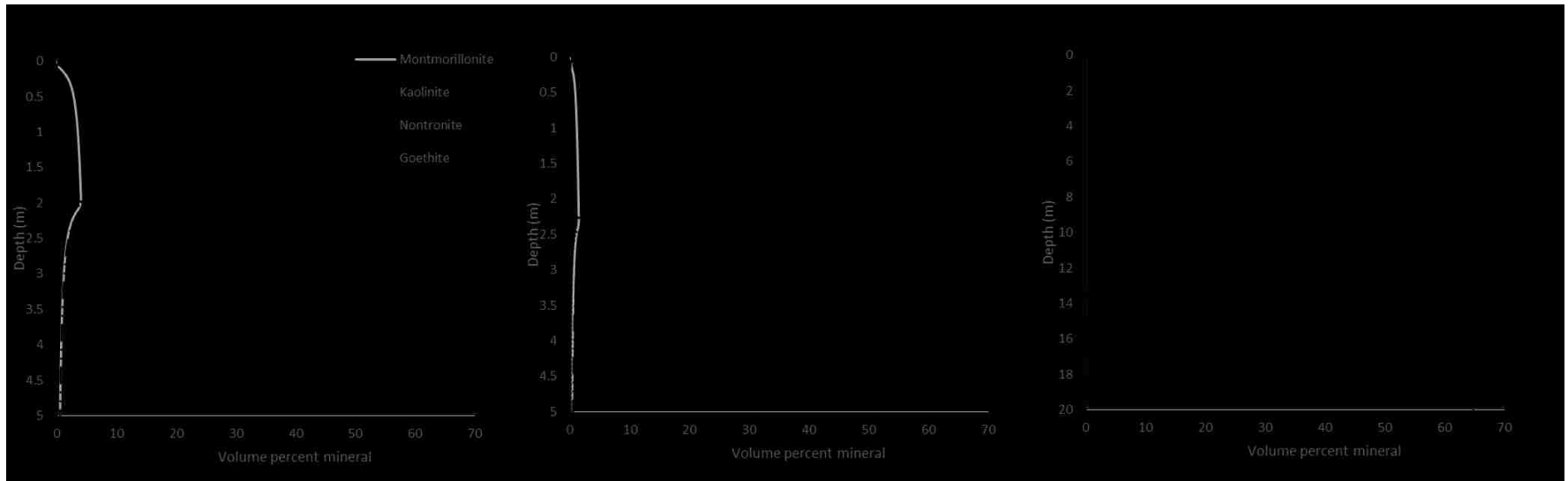


**Figure S73: Modeling result for scenario 1.** Note that decreasing the pH results in an increased thickness of the weathering profile. In addition lowering the pH increases the presence of kaolinite over montmorillonite. Goethite is present throughout the upper Al-rich unit. Increasing acidity also results in more abrupt transitions between the upper Al-rich unit and the under-lying unit of nontronite.



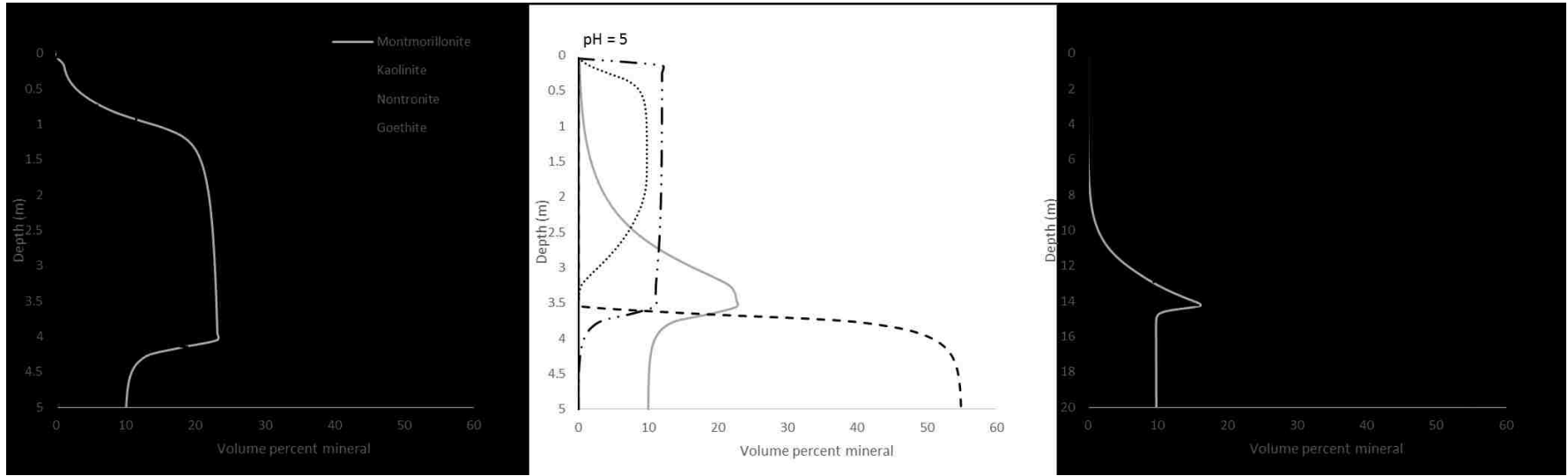


**Figure S74: Modeling result for scenario 2.** Note that decreasing the pH generally results in an increased thickness of the weathering profile or increases the depletion of Si in the Al-rich unit (the Al-rich unit and the nontronite contact are not as deep at pH 5, where the presence of montmorillonite acts as a buffer in the alteration of nontronite). In addition lowering the pH increases the presence of kaolinite over montmorillonite. Goethite is present throughout the upper Al-rich unit. Increasing acidity results in more abrupt transitions between the upper Al-rich unit and the under-lying unit of nontronite.

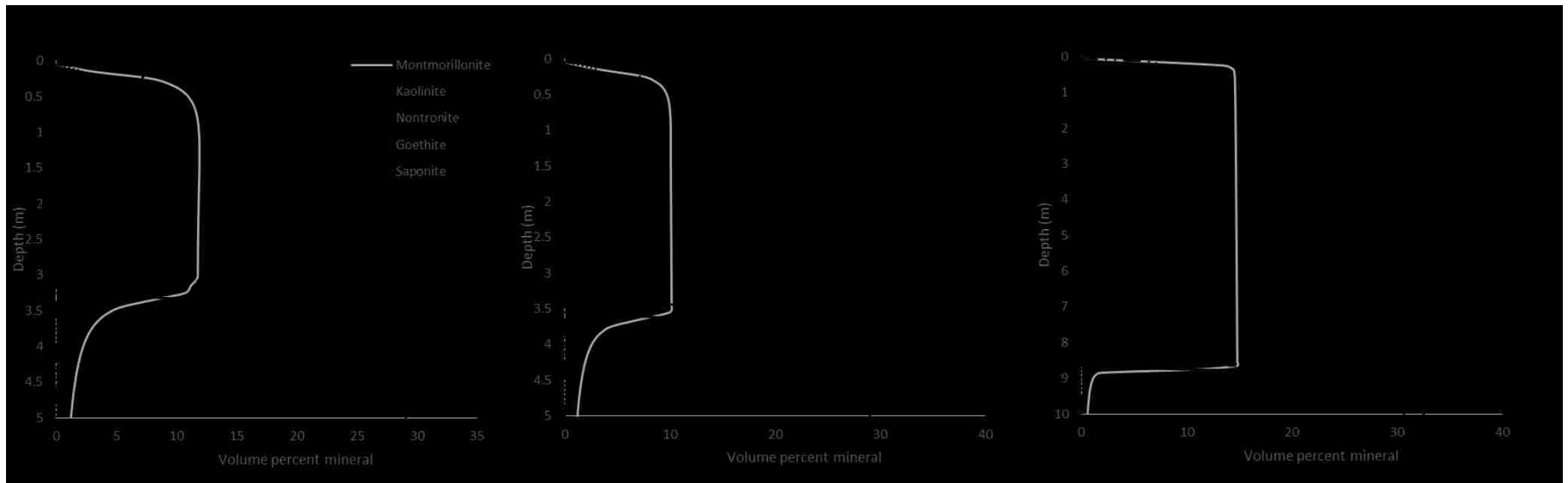


**Figure S75: Modeling result for scenario 3.** Note that decreasing the pH results in an increased thickness of the weathering profile. Note that the depth of the saponite contact is below that of nontronite for all pH conditions. Saponite overlying nontronite may therefore also indicate weathering. Goethite is present throughout the upper Al-rich unit. Increasing acidity results in more abrupt transitions between the upper Al-rich unit and the under-lying unit of saponite.

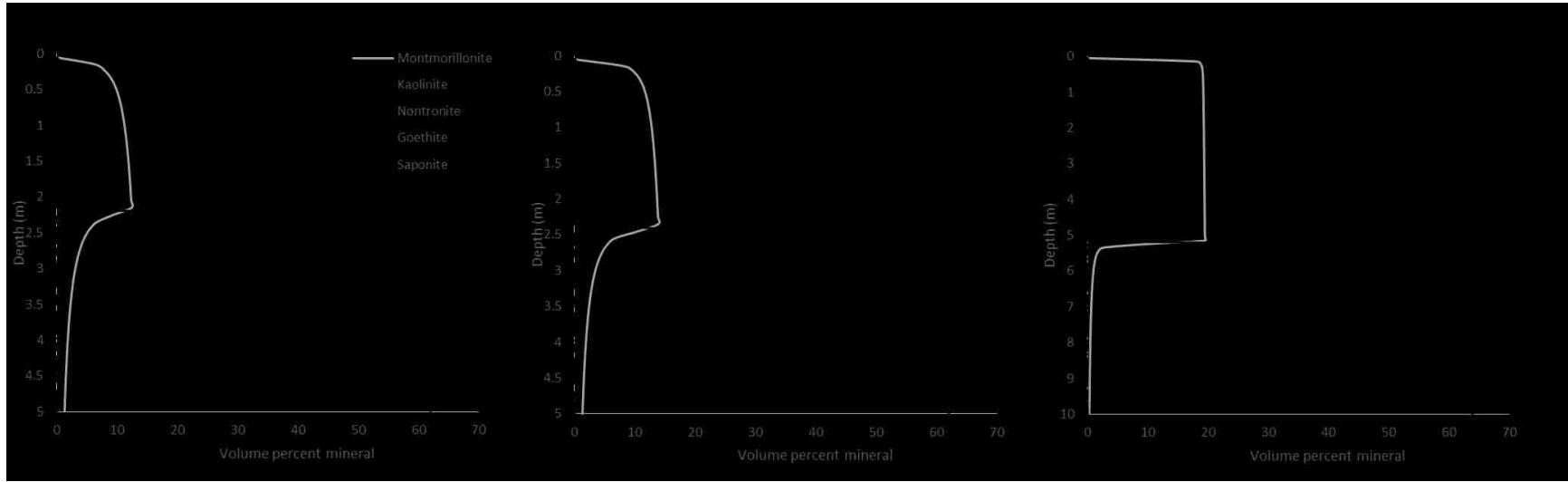


**Figure S76: Modeling result for scenario 4.** Note that decreasing the pH results in an increased thickness of the weathering profile. Goethite is not as abundant when saponite is the parental material and therefore may be an indicator of the original parent material. Increasing acidity results in more abrupt transitions between the upper Al-rich unit and the under-lying unit of saponite. Montmorillonite is more abundant when saponite is the parent material.

## REFERENCES

- Adcock, C.T., Hausrath, E.M., (In Review). Weathering Profiles in Phosphorus-rich Rocks at Gusev Crater, Mars, Suggest Dissolution of Phosphate Minerals into Potentially Habitable Near-Neutral Waters.
- Allen, V.T., Scheid, V.E., 1946. Nontronite in the Columbia River region. *American Mineralogist* 31, 294-312.
- Altaner, S.P., 1986. Comparison of rates of smectite illitization with rates of K-feldspar dissolution. *Clays and Clay minerals* 34, 608-611.
- Altheide, T.S., Chevrier, V.F., Dobrea, E.N., 2010. Mineralogical characterization of acid weathered phyllosilicates with implications for secondary Martian deposits. *Geochimica et Cosmochimica Acta* 74, 6232-6248.
- Amram, K., Ganor, J., 2005. The combined effect of pH and temperature on smectite dissolution rate under acidic conditions. *Geochimica et Cosmochimica Acta* 69, 2535-2546.
- Amrhein, C., Suarez, D.L., 1992. Some factors affecting the dissolution kinetics of anorthite at 25°C. *Geochimica et Cosmochimica Acta* 56, 1815-1826.
- Anderson, S.P., Dietrich, W.E., Brimhall, G.H., 2002. Weathering profiles, mass-balance analysis, and rates of solute loss: Linkages between weathering and erosion in a small, steep catchment. *Geological Society of America Bulletin* 114, 1143-1158.
- Anderson, S.P., Drever, J.I., Frost, C.D., Holden, P., 2000. Chemical weathering in the foreland of a retreating glacier. *Geochimica et Cosmochimica Acta* 64, 1173-1189.

- Anderson, S.P., Drever, J.I., Humphrey, N.F., 1997. Chemical weathering in glacial environments. *Geology* 25, 399-402.
- Badaut, D., Besson, G., Decarreau, A., Rautureau, R., 1985. Occurrence of a ferrous, trioctahedral smectite in recent sediments of Atlantis II Deep, Red Sea. *Clay Minerals* 20, 389-404.
- Baker, L.L., Strawn, D.G., 2014. Temperature Effects on the Crystallinity of Synthetic Nontronite and Implications for Nontronite Formation in Columbia River Basalts. *Clays and Clay minerals* 62, 89-101.
- Baker, V., Strom, R., Gulick, V., Kargel, J., Komatsu, G., Kale, V., 1991. Ancient oceans, ice sheets and the hydrological cycle on Mars.
- Baker, V.R., 2001. Water and the Martian landscape. *Nature* 412, 228-236.
- Bandfield, J.L., Glotch, T.D., Christensen, P.R., 2003. Spectroscopic identification of carbonate minerals in the Martian dust. *Science* 301, 1084-1087.
- Barnhisel, R.I., Bertsch, P.M., 1989. Chlorites and hydroxy-interlayered vermiculite and smectite. *Minerals in soil environments*, 729-788.
- Barone, F., Rowe, R., Quigley, R., 1992. Estimation of chloride diffusion coefficient and tortuosity factor for mudstone. *Journal of geotechnical engineering* 118, 1031-1045.
- Barone, F., Rowe, R., Quigley, R.M., 1990. Laboratory determination of chloride diffusion coefficient in an intact shale. *Canadian Geotechnical Journal* 27, 177-184.

- Barshad, I., 1966. The effect of a variation in precipitation on the nature of clay mineral formation in soils from acid and basic igneous rocks, Proc. Int. Clay Conf, pp. 167-173.
- Bauer, A., Berger, G., 1998. Kaolinite and smectite dissolution rate in high molar KOH solutions at 35 and 80 C. Applied Geochemistry 13, 905-916.
- Becking, L.B., Kaplan, I.R., Moore, D., 1960. Limits of the natural environment in terms of pH and oxidation-reduction potentials. The Journal of Geology, 243-284.
- Benner, S.A., Devine, K.G., Matveeva, L.N., Powell, D.H., 2000. The missing organic molecules on Mars. Proceedings of the National Academy of Sciences 97, 2425-2430.
- Bibring, J.-P., Langevin, Y., Gendrin, A., Gondet, B., Poulet, F., Berthe, M., Soufflot, A., Arvidson, R., Mangold, N., Mustard, J., Drossart, P., the OMEGA team, 2005a. Mars Surface Diversity as Revealed by the OMEGA/Mars Express Observations. Science 307, 1576-1581.
- Bibring, J.-P., Langevin, Y., Mustard, J.F., Poulet, F., Arvidson, R., Gendrin, A., Gondet, B., Mangold, N., Pinet, P., Forget, F., 2006. Global mineralogical and aqueous Mars history derived from OMEGA/Mars Express data. Science 312, 400-400-404.
- Bibring, J.P., Langevin, Y., Anonymous, 2005b. Mars surface diversity as observed by the OMEGA/Mars Express investigation. Lunar and Planetary Science Conference, Houston, TX, United States (USA), United States (USA), pp. @unpaginated-@unpaginated.

- Bickmore, B.R., Bosbach, D., Hochella, M.F., Jr., Charlet, L., Rufe, E., 2001. In situ atomic force microscopy study of hectorite and nontronite dissolution: Implications for phyllosilicate edge surface structures and dissolution mechanisms. *American Mineralogist* 86, 411-423.
- Bickmore, B.R., Nagy, K.L., Sandlin, P.E., Crater, T.S., 2002. Quantifying surface areas of clays by atomic force microscopy. *American Mineralogist* 87, 780-783.
- Biemann, K., Oro, J., Toulmin, P., Orgel, L., Nier, A., Anderson, D., Simmonds, P., Flory, D., Diaz, A., Rushneck, D., 1977. The search for organic substances and inorganic volatile compounds in the surface of Mars. *Journal of Geophysical Research* 82, 4641-4658.
- Bird, M.I., Chivas, A.R., 1988. Stable-isotope evidence for low-temperature kaolinitic weathering and post-formational hydrogen-isotope exchange in Permian kaolinites. *Chemical Geology: Isotope Geoscience section* 72, 249-265.
- Birkeland, P.W., 1984. *Soils and geomorphology*. Oxford University Press.
- Bish, D.L., Blake, D., Vaniman, D., Chipera, S., Morris, R., Ming, D., Treiman, A., Sarrazin, P., Morrison, S., Downs, R., 2013. X-ray diffraction results from Mars Science Laboratory: Mineralogy of Rocknest at Gale crater. *Science* 341, 1238932.
- Bishop, J., Murad, E., Dyar, M., 2002. The influence of octahedral and tetrahedral cation substitution on the structure of smectites and serpentines as observed through infrared spectroscopy. *Clay minerals* 37, 617-628.
- Bishop, J.L., Dobrea, E.Z.N., McKeown, N.K., Parente, M., Ehlmann, B.L., Michalski, J.R., Milliken, R.E., Poulet, F., Swayze, G.A., Mustard, J.F., 2008a. Phyllosilicate

- diversity and past aqueous activity revealed at Mawrth Vallis, Mars. *Science* 321, 830-833.
- Bishop, J.L., Dobrea, E.Z.N., McKeown, N.K., Parente, M., Ehlmann, B.L., Michalski, J.R., Milliken, R.E., Poulet, F., Swayze, G.A., Mustard, J.F., Murchie, S.L., Bibring, J.-P., 2008b. Phyllosilicate Diversity and Past Aqueous Activity Revealed at Mawrth Vallis, Mars. *Science* 321, 830-833.
- Bishop, J.L., Loizeau, D., McKeown, N.K., Saper, L., Dyar, M.D., Des Marais, D.J., Parente, M., Murchie, S.L., 2013. What the ancient phyllosilicates at Mawrth Vallis can tell us about possible habitability on early Mars. *Planetary and Space Science* 86, 130-149.
- Bishop, J.L., McKeown, N.K., Rossi, C.M., Michalski, J.R., Heinlein, C., Hanus, V., Poulet, F., Mustard, R.J.F., Murchie, S.L., McEwen, A.S., Swayze, G.A., Bibring, J.P., Malaret, E., Hash, C., 2010. Mineralogy and stratigraphy of phyllosilicate-bearing and dark mantling units in the greater Mawrth Vallis/west Arabia Terra area; constraints on geological origin. *Journal of Geophysical Research* 115, @Citation E00D19-@Citation E00D19.
- Boggs, S., 1995. *Principles of sedimentology and stratigraphy*. Prentice Hall New Jersey.
- Botta, O., Bada, J.L., 2002. Extraterrestrial organic compounds in meteorites. *Surveys in Geophysics* 23, 411-467.
- Brady, N.C., Weil, R.R., 1999. *The nature and properties of soils*. Prentice Hall, Upper Saddle River, NJ, Upper Saddle River, NJ, United States (USA).
- Brady, P.V., Walther, J.V., 1989. Controls on silicate dissolution rates in neutral and basic pH solutions at 25°C. *Geochimica et Cosmochimica Acta* 53, 2823-2830.



- Brantley, S.L., 2008. Kinetics of mineral dissolution, Kinetics of water-rock interaction. Springer, pp. 151-210.
- Brantley, S.L., White, A.F., 2009. Approaches to modeling weathered regolith. Reviews in Mineralogy and Geochemistry 70, 435-484.
- Brigatti, M., Lugli, C., Poppi, L., Venturelli, G., 1999. Iron-rich saponite: dissolution reactions and Cr uptake. Clay Minerals 34, 637-637.
- Brimhall, G.H., Dietrich, W.E., 1987. Constitutive mass balance relations between chemical composition, volume, density, porosity, and strain in metasomatic hydrochemical systems: results on weathering and pedogenesis. Geochimica et Cosmochimica Acta 51, 567-587.
- Bristow, T.F., Milliken, R.E., 2011. Terrestrial perspective on authigenic clay mineral production in ancient martian lakes. Clays and Clay minerals 59, 339-358.
- Brunauer, S., Emmett, P.H., Teller, E., 1938. Adsorption of gases in multimolecular layers. Journal of the American Chemical Society 60, 309-319.
- Burch, T.E., Nagy, K.L., Lasaga, A.C., 1993. Free energy dependence of albite dissolution kinetics at 80°C and pH 8.8. Chemical Geology 105, 137-162.
- Burns, R.G., 1987. Ferric sulfates on Mars. Journal of Geophysical Research: Solid Earth (1978–2012) 92, E570-E574.
- Burns, R.G., 1993. Rates and mechanisms of chemical weathering of ferromagnesian silicate minerals on Mars. Geochimica et Cosmochimica Acta 57, 4555-4574.
- Burns, R.G., Fisher, D.S., 1990. Iron-sulfur mineralogy of Mars: Magmatic evolution and chemical weathering products. Journal of Geophysical Research: Solid Earth (1978–2012) 95, 14415-14421.

- Cama, J., Ganor, J., Ayora, C., Lasaga, C.A., 2000. Smectite dissolution kinetics at 80 C and pH 8.8. *Geochimica et Cosmochimica Acta* 64, 2701-2717.
- Cama, J., Ganor, J., Lasaga, A., 1994. The kinetics of smectite dissolution. *Mineral. Mag. A* 58, 140-141.
- Cama, J., Metz, V., Ganor, J., 2002. The effect of pH and temperature on kaolinite dissolution rate under acidic conditions. *Geochimica et Cosmochimica Acta* 66, 3913-3926.
- Carroll-Webb, S.A., Walther, J.V., 1988. A surface complex reaction model for the pH-dependence of corundum and kaolinite dissolution rates. *Geochimica et Cosmochimica Acta* 52, 2609-2623.
- Carter, J., Loizeau, D., Mangold, N., Poulet, F., Bibring, J.-P., 2015. Widespread surface weathering on early Mars: A case for a warmer and wetter climate. *Icarus* 248, 373-382.
- Carter, J., Poulet, F., Bibring, J.P., Mangold, N., Murchie, S., 2013. Hydrous minerals on Mars as seen by the CRISM and OMEGA imaging spectrometers: Updated global view. *Journal of Geophysical Research: Planets* 118, 831-858.
- Chemtob, S.M., Nickerson, R.D., Morris, R.V., Agresti, D.G., Catalano, J.G., 2015. Synthesis and structural characterization of ferrous trioctahedral smectites: Implications for clay mineral genesis and detectability on Mars. *Journal of Geophysical Research: Planets*.
- Chevrier, V.F., Altheide, T.S., 2008. Low temperature aqueous ferric sulfate solutions on the surface of Mars. *Geophysical Research Letters* 35.

- Christensen, P., Morris, R., Lane, M., Bandfield, J., Malin, M., 2001. Global mapping of Martian hematite mineral deposits: Remnants of water-driven processes on early Mars. *Journal of Geophysical Research: Planets* (1991–2012) 106, 23873-23885.
- Claridge, G., Campbell, I., 1984. Mineral transformation during the weathering of dolerite under cold arid conditions in Antarctica. *New Zealand journal of geology and geophysics* 27, 537-545.
- Clark, B.C., III, Arvidson, R.E., Gellert, R., Morris, R.V., Ming, D.W., Richter, L., Ruff, S.W., Michalski, J.R., Farrand, W.H., Yen, A., Herkenhoff, K.E., Li, R., Squyres, S.W., Schröder, C., Klingelhöfer, G., Bell, J.F., III, 2007a. Evidence for montmorillonite or its compositional equivalent in Columbia Hills, Mars. *J. Geophys. Res.* 112, E06S01.
- Clark, R.N., Swayze, G.A., Wise, R., Livo, K.E., Hoefen, T.M., Kokaly, R.F., Sutley, S.J., 2007b. USGS digital spectral library splib06a. US Geological Survey Reston, VA.
- Colin, F., Nahon, D., Trescases, J.-J., Melfi, A., 1990. Lateritic weathering of pyroxenites at Niquelandia, Goias, Brazil; the supergene behavior of nickel. *Economic Geology* 85, 1010-1023.
- Craig, D., Loughnan, F., 1964. Chemical and mineralogical transformations accompanying the weathering of basic volcanic rocks from New South Wales. *Soil Research* 2, 218-234.
- Davis, W.L., McKay, C.P., 1996. Origins of life; a comparison of theories and application to Mars. *Origins of Life and Evolution of the Biosphere* 26, 61-73.

- De Kimpe, C., 1976. Formation of phyllosilicates and zeolites from pure silica-alumina gels. *Clays and Clay minerals* 24, 200-207.
- Decarreau, A., Petit, S., Martin, F., Farges, F., Vieillard, P., Joussein, E., 2008. Hydrothermal synthesis, between 75 and 150 C, of high-charge, ferric nontronites. *Clays and Clay minerals* 56, 322-337.
- Delany, J., Lundeen, S., 1990. The LLNL thermodynamic database. Lawrence Livermore National Laboratory.
- Delvaux, B., Dufey, J.E., Vielvoye, L., Herbillon, A.J., 1989. Potassium exchange behavior in a weathering sequence of volcanic ash soils. *Soil Science Society of America Journal* 53, 1679-1684.
- Delvigne, J., Bisdorf, E., Sleeman, J., Stoops, G., 1979. Olivines, their pseudomorphs and secondary products. *Stiboka*.
- Devidal, J.-L., Schott, J., Dandurand, J.-L., 1997. An experimental study of kaolinite dissolution and precipitation kinetics as a function of chemical affinity and solution composition at 150 C, 40 bars, and pH 2, 6.8, and 7.8. *Geochimica et Cosmochimica Acta* 61, 5165-5186.
- Dixon, J.B., Weed, S.B., 1977. *Minerals in soil environments*. Soil Sci. Soc. Am., Madison, Wis., Madison, Wis., United States (USA).
- Dogan, A.U., Dogan, M., Onal, M., Sarikaya, Y., Aburub, A., Wurster, D.E., 2006. Baseline Studies of the Clay Minerals Society Source Clays: Specific Surface Area by the Brunauer Emmett Teller (BET) Method. *Clays and Clay Minerals* 54, 62-66.

Dogan, M., Dogan, A.U., Yesilyurt, F.I., Alaygut, D., Buckner, I., Wurster, D.E., 2007a.

Baseline studies of The Clay Minerals Society special clays: specific surface area by the Brunauer Emmett Teller (BET) method. *Clays and Clay minerals* 55, 534-541.

Dogan, M., Dogan, A.U., Yesilyurt, F.I., Alaygut, D., Buckner, I., Wurster, D.E., 2007b.

Baseling Studies of the Clay Minerals Society Special Calys: Specific Surface Area by the Brunauer Emmett Teller (BET) Method. *Clays and Clay Minerals* 55, 534-541.

Downs, R., 2006. *The RRUFF Project: An Integrated Study of the Chemistry.*

*Crystallography, Raman and Infrared Spectroscopy of Minerals* [Online].

Drever, J.I., 1997a. *The geochemistry of natural waters: surface and groundwater environments.*

Drever, J.I., 1997b. *The geochemistry of natural waters; surface and groundwater environments.* Prentice Hall, Upper Saddle River, NJ, Upper Saddle River, NJ, United States (USA).

Drever, J.I., 2005. *Surface and Ground Water, Weathering, and Soils: Treatise on Geochemistry.* Access Online via Elsevier.

Dzevanishir, R.D., Buryakovskiy, L.A., Chilingarian, G.V., 1986. Simple quantitative evaluation of porosity of argillaceous sediments at various depths of burial. *Sedimentary geology* 46, 169-175.

Dzombak, D.A., Morel, F.M.M., 1990. *Surface Complexation Modeling: Hydrated Ferric Oxide.* John Wiley & Sons, Inc., New York.

- Eggleston, C.M., Hochella Jr, M.F., George, P.A., 1989. Sample preparation and aging effects on the dissolution rate and surface composition of diopside. *Geochimica et Cosmochimica Acta* 53, 797-804.
- Ehlmann, B., Bish, D., Ruff, S., Mustard, J., 2012. Mineralogy and chemistry of altered Icelandic basalts: Application to clay mineral detection and understanding aqueous environments on Mars. *Journal of Geophysical Research: Planets* (1991–2012) 117.
- Ehlmann, B.L., Mustard, J.F., Fassett, C.I., Schon, S.C., Head, J.W., III, De Marais, D.J., Grant, J.A., Murchie, S.L., 2008a. Clay minerals in delta deposits and organic preservation potential on Mars. *Nature Geoscience* 1, 355-355-358.
- Ehlmann, B.L., Mustard, J.F., Murchie, S.L., Bibring, J.-P., Meunier, A., Fraeman, A.A., Langevin, Y., 2011. Subsurface water and clay mineral formation during the early history of Mars. *Nature* 479, 53-60.
- Ehlmann, B.L., Mustard, J.F., Murchie, S.L., Poulet, F., Bishop, J.L., Brown, A.J., Calvin, W.M., Clark, R.N., Des Marais, D.J., Milliken, R.E., 2008b. Orbital identification of carbonate-bearing rocks on Mars. *Science* 322, 1828-1832.
- Ehlmann, B.L., Mustard, J.F., Swayze, G.A., Clark, R.N., Bishop, J.L., Poulet, F., Des Marais, D.J., Roach, L.H., Milliken, R.E., Wray, J.J., 2009a. Identification of hydrated silicate minerals on Mars using MRO-CRISM: Geologic context near Nili Fossae and implications for aqueous alteration. *Journal of Geophysical Research* 114, E00D08.
- Ehlmann, B.L., Mustard, J.F., Swayze, G.A., Clark, R.N., Bishop, J.L., Poulet, F., Des Marais, D.J., Roach, L.H., Milliken, R.E., Wray, J.J., 2009b. Identification of

- hydrated silicate minerals on Mars using MRO-CRISM: Geologic context near Nili Fossae and implications for aqueous alteration. *Journal of Geophysical Research: Planets* (1991–2012) 114.
- Elias, M., Donaldson, M., Giorgetta, N., 1981. Geology, mineralogy, and chemistry of lateritic nickel-cobalt deposits near Kalgoorlie, Western Australia. *Economic Geology* 76, 1775-1783.
- Elwood Madden, M.E., Bodnar, R.J., Rimstidt, J.D., 2004. Jarosite as an indicator of water-limited chemical weathering on Mars. *Nature* 431, 821-823.
- Eugster, H.P., Chou, I.-M., 1973. The depositional environments of Precambrian banded iron-formations. *Economic Geology* 68, 1144-1168.
- Ewell, R.H., Insley, H., 1935. Hydrothermal synthesis of kaolinite, dickite, beidellite and nontronite. *Journal of Research of the National Bureau of Standards* 15, 173-186.
- Ferris, J.P., 2005. Mineral Catalysis and Prebiotic Synthesis: Montmorillonite-Catalyzed Formation of RNA. *Elements* 1, 145-149.
- Fisher, G.B., Ryan, P.C., 2006. The smectite-to-disordered kaolinite transition in a tropical soil chronosequence, Pacific Coast, Costa Rica. *Clays and Clay minerals* 54, 571-586.
- Flanagan, F., 1969. US Geological Survey standards—II. First compilation of data for the new USGS rocks. *Geochimica et Cosmochimica Acta* 33, 81-120.
- Flanagan, F.J., 1967. US Geological Survey silicate rock standards. *Geochimica et Cosmochimica Acta* 31, 289-308.
- Flanagan, F.J., 1984. Three USGS mafic rock reference samples, W-2, DNC-1, and BIR-1.

- Fletcher, R., Buss, H., Brantley, S., 2006. A spheroidal weathering model coupling porewater chemistry to soil thicknesses during steady-state denudation. *Earth and Planetary Science Letters* 244, 444-457.
- Flynn, G.J., 1996. The delivery of organic matter from asteroids and comets to the early surface of Mars. *Earth, Moon, and Planets* 72, 469-474.
- Freeze, R.A., Cherry, J., 1979. *Groundwater*, 604 pp. Prentice-Hall, Englewood Cliffs, NJ.
- Freissinet, C., Glavin, D.P., Mahaffy, P.R., Miller, K.E., Eigenbrode, J.L., Summons, R.E., Brunner, A.E., Buch, A., Szopa, C., Archer, P.D., Franz, H.B., Atreya, S.K., Brinckerhoff, W.B., Cabane, M., Coll, P., Conrad, P.G., Des Marais, D.J., Dworkin, J.P., Fairén, A.G., François, P., Grotzinger, J.P., Kashyap, S., ten Kate, I.L., Leshin, L.A., Malespin, C.A., Martin, M.G., Martin-Torres, F.J., McAdam, A.C., Ming, D.W., Navarro-González, R., Pavlov, A.A., Prats, B.D., Squyres, S.W., Steele, A., Stern, J.C., Sumner, D.Y., Sutter, B., Zorzano, M.P., the M.S.L.S.T., 2015. Organic molecules in the Sheepbed Mudstone, Gale Crater, Mars. *Journal of Geophysical Research: Planets*, 2014JE004737.
- Frink, C., Peech, M., 1963. Hydrolysis of the aluminum ion in dilute aqueous solutions. *Inorganic Chemistry* 2, 473-478.
- Frost, R.L., Klopogge, J.T., Ding, Z., 2002. The Garfield and Uley nontronites--an infrared spectroscopic comparison. *Spectrochimica Acta Part A: Molecular and Biomolecular Spectroscopy* 58, 1881-1894.
- Gainey, S., Hausrath, E., Hurowitz, J., Milliken, R., 2014. Nontronite dissolution rates and implications for Mars. *Geochimica et Cosmochimica Acta* 126, 192-211.



- Ganor, J., Mogollón, J.L., Lasaga, A.C., 1995. The effect of pH on kaolinite dissolution rates and on activation energy. *Geochimica et Cosmochimica Acta* 59, 1037-1052.
- Ganor, J., Roueff, E., Erel, Y., Blum, J.D., 2005. The dissolution kinetics of a granite and its minerals—implications for comparison between laboratory and field dissolution rates. *Geochimica et Cosmochimica Acta* 69, 607-621.
- Gaudin, A., Decarreau, A., Noack, Y., Grauby, O., 2005. Clay mineralogy of the nickel laterite ore developed from serpentinised peridotites at Murrin Murrin, Western Australia. *Australian Journal of Earth Sciences* 52, 231-241.
- Gaudin, A., Dehouck, E., Mangold, N., 2011. Evidence for weathering on early Mars from a comparison with terrestrial weathering profiles. *Icarus* 216, 257-268.
- Gaudin, A., Grauby, O., Noack, Y., Decarreau, A., Petit, S., 2004. Accurate crystal chemistry of ferric smectites from the lateritic nickel ore of Murrin Murrin (Western Australia). I. XRD and multi-scale chemical approaches. *Clay Minerals* 39, 301-315.
- Gendrin, A., Mangold, N., Bibring, J.-P., Langevin, Y., Gondet, B., Poulet, F., Bonello, G., Quantin, C., Mustard, J., Arvidson, R., 2005. Sulfates in Martian layered terrains: the OMEGA/Mars Express view. *Science* 307, 1587-1591.
- Gislason, S.R., Hans, P.E., 1987. Meteoric water-basalt interactions. I: A laboratory study. *Geochimica et Cosmochimica Acta* 51, 2827-2840.
- Gladney, E.S., Roelandts, I., 1987. Compilation of boron concentration data for NBS, USGS and CCRMP reference materials. *Geostandards Newsletter* 11, 167-185.

- Golombek, M., Grant, J., Crumpler, L., Greeley, R., Arvidson, R., Bell, J., Weitz, C., Sullivan, R., Christensen, P., Soderblom, L., 2006. Erosion rates at the Mars Exploration Rover landing sites and long-term climate change on Mars. *Journal of Geophysical Research: Planets* (1991–2012) 111.
- Golombek, M., Grant, J., Kipp, D., Vasavada, A., Kirk, R., Fergason, R., Bellutta, P., Calef, F., Larsen, K., Katayama, Y., 2012. Selection of the Mars Science Laboratory landing site. *Space science reviews* 170, 641-737.
- Golubev, S.V., Bauer, A., Pokrovsky, O.S., 2006. Effect of pH and organic ligands on the kinetics of smectite dissolution at 25 C. *Geochimica et Cosmochimica Acta* 70, 4436-4451.
- Golubev, S.V., Pokrovsky, O.S., Schott, J., 2005. Experimental determination of the effect of dissolved CO<sub>2</sub> on the dissolution kinetics of Mg and Ca silicates at 25 °C. *Chemical Geology* 217, 227-238.
- Goodman, B., Russell, J., Fraser, A., Woodhams, F., 1976. A Mössbauer and IR spectroscopic study of the structure of nontronite. *Clays and Clay Minerals* 24, 53-59.
- Govindaraju, K., POTTS, P.J., WEBB, P.C., WATSON, J.S., 1994. 1994 REPORT ON WHIN SILL DOLERITE WS-E FROM ENGLAND AND PITSCURRIE MICROGABBRO PM-S FROM SCOTLAND: ASSESSMENT BY ONE HUNDRED AND FOUR INTERNATIONAL LABORATORIES. *Geostandards Newsletter* 18, 211-300.

- Granquist, W., Hoffmann, G., Boteler, R., 1972. Clay mineral synthesis III. Rapid hydrothermal crystallization of an aluminian smectite. *Clays and Clay minerals* 20, 323-329.
- Grauby, O., Petit, S., Decarreau, A., Baronnet, A., 1993. The beidellite-saponite series: an experimental approach. *European Journal of Mineralogy* 5, 623-635.
- Grauby, O., Petit, S., Decarreau, A., Baronnet, A., 1994. The nontronite-saponite series: an experimental approach. *European Journal of Mineralogy* 6, 99-112.
- Grotzinger, J.P., Crisp, J.A., Vasavada, A.R., 2015. Curiosity's Mission of Exploration at Gale Crater, Mars. *Elements* 11, 19-26.
- Grotzinger, J.P., Sumner, D., Kah, L., Stack, K., Gupta, S., Edgar, L., Rubin, D., Lewis, K., Schieber, J., Mangold, N., 2014. A habitable fluvio-lacustrine environment at Yellowknife Bay, Gale Crater, Mars. *Science* 343, 1242777.
- Guidry, M.W., Mackenzie, F.T., 2003. Experimental study of igneous and sedimentary apatite dissolution: Control of pH, distance from equilibrium, and temperature on dissolution rates. *Geochimica et Cosmochimica Acta* 67, 2949-2963.
- Hammersley, A., 1997. FIT2D: an introduction and overview. European Synchrotron Radiation Facility Internal Report ESRF97HA02T.
- Harder, H., 1972. The role of magnesium in the formation of smectite minerals. *Chemical Geology* 10, 31-39.
- Harder, H., 1976. Nontronite synthesis at low temperatures. *Chemical Geology* 18, 169-180.
- Harder, H., 1977. Clay mineral formation under lateritic weathering conditions. *Clay Minerals* 12, 281-288.

- Harder, H., 1978a. Synthesis of iron layer silicate minerals under natural conditions. *Clays and Clay Minerals* 26, 65-72.
- Harder, H., 1978b. Synthesis of iron layer silicate minerals under natural conditions. *Clays Clay Miner* 26, 65-72.
- Hassler, D.M., Zeitlin, C., Wimmer-Schweingruber, R.F., Ehresmann, B., Rafkin, S., Eigenbrode, J.L., Brinza, D.E., Weigle, G., Böttcher, S., Böhm, E., 2014. Mars' surface radiation environment measured with the Mars Science Laboratory's Curiosity Rover. *Science* 343, 1244797.
- Hausrath, E., Navarre-Sitchler, A., Sak, P., Williams, J., Brantley, S., 2011a. Soil profiles as indicators of mineral weathering rates and organic interactions for a Pennsylvania diabase. *Chemical Geology* 290, 89-100.
- Hausrath, E., Treiman, A., Vicenzi, E., Bish, D., Blake, D., Sarrazin, P., Hoehler, T., Midtkandal, I., Steele, A., Brantley, S., 2008a. Short-and long-term olivine weathering in Svalbard: Implications for Mars. *Astrobiology* 8, 1079-1092.
- Hausrath, E.M., Navarre-Sitchler, A.K., Sak, P.B., Steefel, C.I., Brantley, S.L., 2008b. Basalt weathering rates on Earth and the duration of liquid water on the plains of Gusev Crater, Mars. *Geology* 36, 67-70.
- Hausrath, E.M., Navarre-Sitchler, A.K., Sak, P.B., Williams, J.Z., Brantley, S.L., 2011b. Soil profiles as indicators of mineral weathering rates and organic interactions for a Pennsylvania diabase. *Chemical Geology* 290, 89-100.
- Hausrath, E.M., Neaman, A., Brantley, S.L., 2009. Elemental release rates from dissolving basalt and granite with and without organic ligands. *American Journal of Science* 309, 633-660.

- Hausrath, E.M., Olsen, A.A., 2013. Using the chemical composition of carbonate rocks on Mars as a record of secondary interaction with liquid water. *American Mineralogist* 98, 897-906.
- Hay, R.L., Jones, B.F., 1972. Weathering of basaltic tephra on the island of Hawaii. *Geological Society of America Bulletin* 83, 317-332.
- Herbillon, A., 1981. Degree of weathering and surface properties of clays. Characterization of soils in relation to their classification and management for crop production: examples from some areas of the humid tropics/edited by DJ Greenland.
- Hodson, M., 2006a. Searching for the perfect surface area normalizing term—a comparison of BET surface area-, geometric surface area-and mass-normalized dissolution rates of anorthite and biotite. *Journal of Geochemical Exploration* 88, 288-291.
- Hodson, M.E., 2003. The influence of Fe-rich coatings on the dissolution of anorthite at pH 2.6. *Geochimica et Cosmochimica Acta* 67, 3355-3363.
- Hodson, M.E., 2006b. Does reactive surface area depend on grain size? Results from pH 3, 25 C far-from-equilibrium flow-through dissolution experiments on anorthite and biotite. *Geochimica et Cosmochimica Acta* 70, 1655-1667.
- Holdren Jr, G.R., Speyer, P.M., 1987. Reaction rate-surface area relationships during the early stages of weathering. II. Data on eight additional feldspars. *Geochimica et Cosmochimica Acta* 51, 2311-2318.
- Hsu, P.H., 1975. Effect of temperature on the hydrolytic formation of FeOOH and Fe (sub 2) O (sub 3). Univ. Nac. Auton. Mex., Inst. Geol., Mexico (MEX).

- Huertas, F., Caballero, E., de Cisneros, C.J., Huertas, F., Linares, J., 2001. Kinetics of montmorillonite dissolution in granitic solutions. *Applied Geochemistry* 16, 397-407.
- Huertas, F.J., Chou, L., Wollast, R., 1999a. Mechanism of kaolinite dissolution at room temperature and pressure Part II: kinetic study. *Geochimica et Cosmochimica Acta* 63, 3261-3275.
- Huertas, F.J., Chou, L., Wollast, R., 1999b. Mechanism of kaolinite dissolution at room temperature and pressure Part II: Kinetic study. *Geochimica et Cosmochimica Acta* 63, 3261-3275.
- Huertas, F.J., Fiore, S., Huertas, F., Linares, J., 1999c. Experimental study of the hydrothermal formation of kaolinite. *Chemical Geology* 156, 171-190.
- Hurowitz, J., McLennan, S., Tosca, N., Arvidson, R., Michalski, J., Ming, D., Schröder, C., Squyres, S., 2006. In situ and experimental evidence for acidic weathering of rocks and soils on Mars. *J. Geophys. Res* 111, E02S19.
- Hurowitz, J.A., McLennan, S.M., 2007. A ~ 3.5 Ga record of water-limited, acidic weathering conditions on Mars. *Earth and Planetary Science Letters* 260, 432-443.
- Jaisi, D.P., Kukkadapu, R.K., Eberl, D.D., Dong, H., 2005. Control of Fe (III) site occupancy on the rate and extent of microbial reduction of Fe (III) in nontronite. *Geochimica et Cosmochimica Acta* 69, 5429-5440.
- Johnson, J., Anderson, G., Parkhurst, D., 2000. Database 'thermo. com. v8. r6. 230'. Rev. 1.11. Lawrence Livermore Natl. Lab., Livermore, California.

- Karathanasis, A.D., Hajek, B.F., 1982. Transformation of Smectite to Kaolinite in Naturally Acid Soil Systems: Structural and Thermodynamic Considerations. *Soil Sci. Soc. Am. J.* 47, 158-163.
- Karpov, I., Kashik, S., 1968. Computer calculation of standard isobaric-isothermal potentials of silicates by multiple regression from a crystallochemical classification. *Geokhimiya* 7, 806-814.
- Kawano, M., Tomita, K., 1997. Experimental Study on the Formation of Zeolites from Obsidian by Interaction with NaOH and KOH Solutions at 150 and 200 C. *Clays and Clay Minerals* 45, 365-377.
- Keeling, J.L., Raven, M.D., Gates, W.P., 2000. Geology and Characterization of Two Hydrothermal Nontronites from Weathered Metamorphic Rocks at the Uley Graphite Mine, South Australia. *Clays and Clay Minerals* 48, 537-548.
- Kloprogge, J., 1998. Synthesis of smectites and porous pillared clay catalysts: A review. *Journal of Porous Materials* 5, 5-41.
- Kloprogge, J.T., Jansen, J.B.H., Geus, J.W., 1990. Characterization of synthetic Na-beidellite. *Clays and Clay minerals* 38, 409-414.
- Knauss, K.G., Nguyen, S.N., Weed, H.C., 1993. Diopside dissolution kinetics as a function of pH, CO<sub>2</sub>, temperature, and time. *Geochimica et Cosmochimica Acta* 57, 285-294.
- Lamb, A.B., Jacques, A.G., 1938. The slow hydrolysis of ferric chloride in dilute solution. II. The change in hydrogen ion concentration. *Journal of the American Chemical Society* 60, 1215-1225.

- Langevin, Y., Poulet, F., Bibring, J.-P., Gondet, B., 2005. Sulfates in the north polar region of Mars detected by OMEGA/Mars Express. *Science* 307, 1584-1586.
- Langmuir, D., 1997. *Aqueous environmental geochemistry*. Prentice Hall, Upper Saddle River, NJ.
- Lasaga, A.C., 1984. Chemical kinetics of water-rock interactions. *Journal of Geophysical Research: Solid Earth (1978–2012)* 89, 4009-4025.
- Lasaga, A.C., Luttge, A., 2001. Variation of crystal dissolution rate based on a dissolution stepwave model. *Science* 291, 2400-2404.
- Lasaga, A.C., Lüttge, A., 2003. A model for crystal dissolution. *European Journal of Mineralogy* 15, 603-615.
- Le Deit, L., Bourgeois, O., Mège, D., Hauber, E., Le Mouélic, S., Massé, M., Jaumann, R., Bibring, J.-P., 2010. Morphology, stratigraphy, and mineralogical composition of a layered formation covering the plateaus around Valles Marineris, Mars: Implications for its geological history. *Icarus* 208, 684-703.
- Le Deit, L., Flahaut, J., Quantin, C., Hauber, E., Mège, D., Bourgeois, O., Gurgurewicz, J., Massé, M., Jaumann, R., 2012. Extensive surface pedogenic alteration of the Martian Noachian crust suggested by plateau phyllosilicates around Valles Marineris. *Journal of Geophysical Research: Planets (1991–2012)* 117.
- Leshin, L., Mahaffy, P., Webster, C., Cabane, M., Coll, P., Conrad, P., Archer, P., Atreya, S., Brunner, A., Buch, A., 2013. Volatile, isotope, and organic analysis of martian fines with the Mars Curiosity rover. *Science* 341, 1238937.



- Lichtner, P.C., 1988. The quasi-stationary state approximation to coupled mass transport and fluid-rock interaction in a porous medium. *Geochimica et Cosmochimica Acta* 52, 143-165.
- Loizeau, D., Carter, J., Mangold, N., Poulet, F., Rossi, A., Allemand, P., Quantin, C., Bibring, J.-P., 2014. Widespread Surface Weathering on Early Mars, EGU General Assembly Conference Abstracts, p. 4651.
- Loizeau, D., Carter, J., Mangold, N., Poulet, F., Rossi, A., Allemand, P., Quantin, C., Bibring, J., 2013. Widespread Surface Weathering on Early Mars, AGU Fall Meeting Abstracts, p. 1836.
- Loizeau, D., Mangold, N., Poulet, F., Ansan, V., Hauber, E., Bibring, J.-P., Gondet, B., Langevin, Y., Masson, P., Neukum, G., 2010a. Stratigraphy in the Mawrth Vallis region through OMEGA, HRSC color imagery and DTM. *Icarus* 205, 396-418.
- Loizeau, D., Mangold, N., Poulet, F., Ansan, V., Hauber, E., Bibring, J.P., Gondet, B., Langevin, Y., Masson, P., Neukum, G., 2010b. Stratigraphy in the Mawrth Vallis region through OMEGA, HRSC color imagery and DTM. *Icarus* 205, 396-396-418.
- Loizeau, D., Mangold, N., Poulet, F., Bibring, J.P., Gendrin, A., Ansan, V., Gomez, C., Gondet, B., Langevin, Y., Masson, P., 2007a. Phyllosilicates in the Mawrth Vallis region of Mars. *Journal of Geophysical Research: Planets* (1991–2012) 112.
- Loizeau, D., Mangold, N., Poulet, F., Bibring, J.P., Langevin, Y., Ansan, V., Masson, P., Neukum, G., 2007b. Stratigraphic correlation between the clays of the region of Mawrth Vallis as detected by OMEGA and HRSC color images and DTM. *Lunar*

- and Planetary Institute, Houston, TX, United States (USA), United States (USA), pp. @Abstract 3131-@Abstract 3131.
- Loizeau, D., Werner, S., Mangold, N., Bibring, J.-P., Vago, J., 2012. Chronology of deposition and alteration in the Mawrth Vallis region, Mars. *Planetary and Space Science* 72, 31-43.
- Longstaffe, F.J., 1984. The Role of Meteoric Water in Diagenesis of Shallow Sandstones: Stable Isotope Studies of the Milk River Aquifer and Gas Pool, Southeastern Alberta: Part 1. Concepts and Principles.
- Madejová, J., Bujdák, J., Janek, M., Komadel, P., 1998. Comparative FT-IR study of structural modifications during acid treatment of dioctahedral smectites and hectorite. *Spectrochimica Acta Part A: Molecular and Biomolecular Spectroscopy* 54, 1397-1406.
- Madsen, F.T., 1977. Surface area measurements of clay minerals by glycerol sorption on a thermobalance. *Thermochimica acta* 21, 89-93.
- Maher, K., 2010. The dependence of chemical weathering rates on fluid residence time. *Earth and Planetary Science Letters* 294, 101-110.
- Maher, K., Steefel, C.I., DePaolo, D.J., Viani, B.E., 2006. The mineral dissolution rate conundrum: Insights from reactive transport modeling of U isotopes and pore fluid chemistry in marine sediments. *Geochimica et Cosmochimica Acta* 70, 337-363.
- Maher, K., Steefel, C.I., White, A.F., Stonestrom, D.A., 2009. The role of reaction affinity and secondary minerals in regulating chemical weathering rates at the

- Santa Cruz Soil Chronosequence, California. *Geochimica et Cosmochimica Acta* 73, 2804-2831.
- Manceau, A., Drits, V., Lanson, B., Chateigner, D., Wu, J., Huo, D., Gates, W., Stucki, J., 2000a. Oxidation-reduction mechanism of iron in dioctahedral smectites: II. Crystal chemistry of reduced Garfield nontronite. *American Mineralogist* 85, 153-172.
- Manceau, A., Lanson, B., Drits, V., Chateigner, D., Gates, W., Wu, J., Huo, D., Stucki, J., 2000b. Oxidation-reduction mechanism of iron in dioctahedral smectites: I. Crystal chemistry of oxidized reference nontronites. *American Mineralogist* 85, 133-152.
- Marini, L., 2006. Geological sequestration of carbon dioxide: thermodynamics, kinetics, and reaction path modeling. Elsevier.
- Marty, N., Cama, J., Sato, T., Chino, D., Villiéras, F., Razafitianamaharavo, A., Brendlé, J., Giffaut, E., Soler, J.M., Gaucher, E.C., 2011a. Dissolution kinetics of synthetic Na-smectite. An integrated experimental approach. *Geochimica et Cosmochimica Acta* 75, 5849-5864.
- Marty, N.C., Cama, J., Sato, T., Chino, D., Villiéras, F., Razafitianamaharavo, A., Brendlé, J., Giffaut, E., Soler, J.M., Gaucher, E.C., 2011b. Dissolution kinetics of synthetic Na-smectite. An integrated experimental approach. *Geochimica et Cosmochimica Acta* 75, 5849-5864.
- Mattigod, S.V., Sposito, G., 1978. Improved method for estimating the standard free energies of formation ( $\Delta G_f^\circ$ , 298.150) of smectites. *Geochimica et Cosmochimica Acta* 42, 1753-1762.

- May, H., Klennburgh, D., Helmke, P.A., Jackson, M., 1986a. Aqueous dissolution, solubilities and thermodynamic stabilities of common aluminosilicate clay minerals: Kaolinite and smectites. *Geochimica et Cosmochimica Acta* 50, 1667-1677.
- May, H.M., Klennburgh, D.G., Helmke, P.A., Jackson, M.L., 1986b. Aqueous dissolution, solubilities and thermodynamic stabilities of common aluminosilicate clay minerals: Kaolinite and smectites. *Geochimica et Cosmochimica Acta* 50, 1667-1677.
- McKeown, N.K., Bishop, J.L., Dobrea, E.Z.N., Ehlmann, B.L., Parente, M., Mustard, J.F., Murchie, S.L., Swayze, G.A., Bibring, J.-P., Silver, E.A., 2009. Characterization of phyllosilicates observed in the central Mawrth Vallis region, Mars, their potential formational processes, and implications for past climate. *Journal of Geophysical Research* 114, E00D10.
- Metz, V., Amram, K., Ganor, J., 2005a. Stoichiometry of smectite dissolution reaction. *Geochimica et Cosmochimica Acta* 69, 1755-1772.
- Metz, V., Raanan, H., Pieper, H., Bosbach, D., Ganor, J., 2005b. Towards the establishment of a reliable proxy for the reactive surface area of smectite. *Geochimica et Cosmochimica Acta* 69, 2581-2591.
- Michalski, J., Poulet, F., Bibring, J.-P., Mangold, N., 2010a. Analysis of phyllosilicate deposits in the Nili Fossae region of Mars: Comparison of TES and OMEGA data. *Icarus* 206, 269-289.
- Michalski, J.R., Bibring, J.-P., Poulet, F., Loizeau, D., Mangold, N., Dobrea, E.N., Bishop, J.L., Wray, J.J., McKeown, N.K., Parente, M., 2010b. The Mawrth Vallis

- region of Mars: A potential landing site for the Mars Science Laboratory (MSL) mission. *Astrobiology* 10, 687-703.
- Michalski, J.R., Bibring, J.-P., Poulet, F., Loizeau, D., Mangold, N., Dobrea, E.N., Bishop, J.L., Wray, J.J., McKeown, N.K., Parente, M., Hauber, E., Altieri, F., Carozzo, F.G., Niles, P.B., 2010c. The Mawrth Vallis Region of Mars: A Potential Landing Site for the Mars Science Laboratory (MSL) Mission. *Astrobiology* 10, 687-703.
- Michalski, J.R., Dobrea, E.Z.N., 2007. Evidence for a sedimentary origin of clay minerals in the Mawrth Vallis region, Mars. *Geology* 35, 951-954.
- Michalski, J.R., Niles, P.B., Cuadros, J., Baldrige, A.M., 2013. Multiple working hypotheses for the formation of compositional stratigraphy on Mars: Insights from the Mawrth Vallis region. *Icarus* 226, 816-840.
- Michalski, J.R., Noe Dobrea, E.Z., 2007. Evidence for a sedimentary origin of clay minerals in the Mawrth Vallis region, Mars. *Geology* 35, 951-954.
- Millero, F.J., Sotolongo, S., Izaguirre, M., 1987. The oxidation kinetics of Fe (II) in seawater. *Geochimica et Cosmochimica Acta* 51, 793-801.
- Milliken, R., Bish, D., 2014. Distinguishing Hisingerite from Other Clays and its Importance for Mars, Lunar and Planetary Institute Science Conference Abstracts, p. 2251.
- Milliken, R., Fischer, W., Hurowitz, J., 2009. Missing salts on early Mars. *Geophysical Research Letters* 36.

- Milliken, R., Grotzinger, J., Thomson, B., 2010a. Paleoclimate of Mars as captured by the stratigraphic record in Gale Crater. *Geophysical Research Letters* 37, @Citation L04201-@Citation L04201.
- Milliken, R., Grotzinger, J., Thomson, B., 2010b. Paleoclimate of Mars as captured by the stratigraphic record in Gale Crater. *Geophysical Research Letters* 37.
- Milliken, R., Swayze, G., Arvidson, R., Bishop, J., Clark, R., Ehlmann, B., Green, R., Grotzinger, J., Morris, R., Murchie, S., 2008. Opaline silica in young deposits on Mars. *Geology* 36, 847-850.
- Ming, D., Archer, P., Glavin, D., Eigenbrode, J., Franz, H., Sutter, B., Brunner, A., Stern, J., Freissinet, C., McAdam, A., 2014. Volatile and organic compositions of sedimentary rocks in Yellowknife Bay, Gale crater, Mars. *Science* 343, 1245267.
- Mizutani, T., Fukushima, Y., Okada, A., Kamigaito, O., Kobayashi, T., 1991. Synthesis of 1: 1 and 2: 1 iron phyllosilicates and characterization of their iron state by Mössbauer spectroscopy. *Clays and Clay Minerals* 39, 381-386.
- Moore, D.M., Reynolds, R.C., 1989. *X-ray Diffraction and the Identification and Analysis of Clay Minerals*. Oxford university press Oxford.
- Moore, J.M., Clow, G.D., Davis, W.L., Gulick, V.C., Janke, D.R., McKay, C.P., Stoker, C.R., Zent, A.P., 1995. The circum-Chryse region as a possible example of a hydrologic cycle on Mars: Geologic observations and theoretical evaluation. *Journal of Geophysical Research: Planets* (1991–2012) 100, 5433-5447.
- Murchie, S.L., Mustard, J.F., Ehlmann, B.L., Milliken, R.E., Bishop, J.L., McKeown, N.K., Noe Dobrea, E.Z., Seelos, F.P., Buczkowski, D.L., Wiseman, S.M., 2009a. A synthesis of Martian aqueous mineralogy after 1 Mars year of observations

from the Mars Reconnaissance Orbiter. *Journal of Geophysical Research: Planets* (1991–2012) 114.

Murchie, S.L., Mustard, J.F., Ehlmann, B.L., Milliken, R.E., Bishop, J.L., McKeown, N.K., Noe Dobrea, E.Z., Seelos, F.P., Buczkowski, D.L., Wiseman, S.M., Arvidson, R.E., Wray, J.J., Swayze, G., Clark, R.N., Des Marais, D.J., McEwen, A.S., Bibring, J.-P., 2009b. A synthesis of Martian aqueous mineralogy after 1 Mars year of observations from the Mars Reconnaissance Orbiter. *J. Geophys. Res.* 114, E00D06.

Mustard, J.F., Murchie, S., Pelkey, S., Ehlmann, B., Milliken, R., Grant, J., Bibring, J.-P., Poulet, F., Bishop, J., Dobrea, E.N., 2008a. Hydrated silicate minerals on Mars observed by the Mars Reconnaissance Orbiter CRISM instrument. *Nature* 454, 305-309.

Mustard, J.F., Murchie, S.L., Pelkey, S.M., Ehlmann, B.L., Milliken, R.E., Grant, J.A., Bibring, J.P., Poulet, F., Bishop, J., Dobrea, E.N., Roach, L., Seelos, F., Arvidson, R.E., Wiseman, S., Green, R., Hash, C., Humm, D., Malaret, E., McGovern, J.A., Seelos, K., Clancy, T., Clark, R., Marais, D.D., Izenberg, N., Knudson, A., Langevin, Y., Martin, T., McGuire, P., Morris, R., Robinson, M., Roush, T., Smith, M., Swayze, G., Taylor, H., Titus, T., Wolff, M., 2008b. Hydrated silicate minerals on Mars observed by the Mars Reconnaissance Orbiter CRISM instrument. *Nature* 454, 305-309.

Nagy, K., Blum, A., Lasaga, A., 1991. Dissolution and precipitation kinetics of kaolinite at 80 degrees C and pH 3; the dependence on solution saturation state. *American Journal of Science* 291, 649-686.

- Nagy, K.L., Lasaga, A.C., 1993. Simultaneous precipitation kinetics of kaolinite and gibbsite at 80 C and pH 3. *Geochimica et Cosmochimica Acta* 57, 4329-4335.
- Nahon, D., Colin, F., Tardy, Y., 1982. Formation and distribution of Mg, Fe, Mn-smectites in the first stages of the lateritic weathering of forsterite and tephroite. *Clay Minerals* 17, 339-348.
- Nahon, D.B., Colin, F., 1982. Chemical weathering of orthopyroxenes under lateritic conditions. *American Journal of Science* 282, 1232-1243.
- Navarre-Sitchler, A., Brantley, S., 2007. Basalt weathering across scales. *Earth and Planetary Science Letters* 261, 321-334.
- Navarre-Sitchler, A., Steefel, C.I., Sak, P.B., Brantley, S.L., 2011. A reactive-transport model for weathering rind formation on basalt. *Geochimica et Cosmochimica Acta* 75, 7644-7667.
- Navarre-Sitchler, A., Steefel, C.I., Yang, L., Tomutsa, L., Brantley, S.L., 2009. Evolution of porosity and diffusivity associated with chemical weathering of a basalt clast. *Journal of Geophysical Research* 114, F02016.
- Navarre-Sitchler, A., Steefel, C.I., Yang, L., Tomutsa, L., Brantley, S.L., 2009. Evolution of porosity and diffusivity associated with chemical weathering of a basalt clast. *Journal of Geophysical Research: Earth Surface* (2003–2012) 114.
- Navarro-González, R., Navarro, K.F., de la Rosa, J., Iñiguez, E., Molina, P., Miranda, L.D., Morales, P., Cienfuegos, E., Coll, P., Raulin, F., 2006. The limitations on organic detection in Mars-like soils by thermal volatilization–gas chromatography–MS and their implications for the Viking results. *Proceedings of the National Academy of Sciences* 103, 16089-16094.



- Nickel, E.H., 1992. Solid solutions in mineral nomenclature. *Mineralogy and Petrology* 46, 49-53.
- Noe Dobrea, E., Bishop, J., McKeown, N., Fu, R., Rossi, C., Michalski, J., Heinlein, C., Hanus, V., Poulet, F., Mustard, R., 2010a. Mineralogy and stratigraphy of phyllosilicate-bearing and dark mantling units in the greater Mawrth Vallis/west Arabia Terra area: Constraints on geological origin. *Journal of Geophysical Research: Planets* (1991–2012) 115.
- Noe Dobrea, E., Swayze, G., 2010. Acid pedogenesis on Mars? Evidence for top-down alteration on Mars from CRISM and HiRISE data, Lunar and Planetary Science Conference, p. 2620.
- Noe Dobrea, E.Z., Bishop, J.L., McKeown, N.K., Fu, R., Rossi, C.M., Michalski, J.R., Heinlein, C., Hanus, V., Poulet, F., Mustard, R.J.F., Murchie, S., McEwen, A.S., Swayze, G., Bibring, J.P., Malaret, E., Hash, C., 2010b. Mineralogy and stratigraphy of phyllosilicate-bearing and dark mantling units in the greater Mawrth Vallis/west Arabia Terra area: Constraints on geological origin. *J. Geophys. Res.* 115, E00D19.
- Novak, I., Ciel, B., 1978. Dissolution of smectites in hydrochloric acid; II, Dissolution rate as a function of crystallochemical composition. *Clays and Clay minerals* 26, 341-344.
- Nriagu, J.O., 1975. Thermochemical approximations for clay minerals. *Am. Mineral* 60, 834-839.

- Oelkers, E.H., 2001. An experimental study of forsterite dissolution rates as a function of temperature and aqueous Mg and Si concentrations. *Chemical Geology* 175, 485-494.
- Osterloo, M.M., Anderson, F.S., Hamilton, V.E., Hynek, B.M., 2010. Geologic context of proposed chloride-bearing materials on Mars. *Journal of Geophysical Research* 115, E10012.
- Palandri, J.L., Kharaka, Y.K., 2004. A compilation of rate parameters of water-mineral interaction kinetics for application to geochemical modeling. DTIC Document.
- Parkhurst, D.L., 1995. User's guide to PHREEQC: A computer program for speciation, reaction-path, advective-transport, and inverse geochemical calculations.
- Parkhurst, D.L., Appelo, C., 1999. User's guide to PHREEQC (Version 2): A computer program for speciation, batch-reaction, one-dimensional transport, and inverse geochemical calculations.
- Pavlov, A., Blinov, A., Konstantinov, A., 2002. Sterilization of Martian surface by cosmic radiation. *Planetary and Space Science* 50, 669-673.
- Pokrovsky, O.S., Schott, J., 2000. Kinetics and mechanism of forsterite dissolution at 25°C and pH from 1 to 12. *Geochimica et Cosmochimica Acta* 64, 3313-3325.
- Poulet, F., Bibring, J.-P., Mustard, J., Gendrin, A., Mangold, N., Langevin, Y., Arvidson, R., Gondet, B., Gomez, C., Berthé, M., 2005a. Phyllosilicates on Mars and implications for early Martian climate. *Nature* 438, 623-627.
- Poulet, F., Bibring, J.P., Mustard, J.F., Gendrin, A., Mangold, N., Langevin, Y., Arvidson, R.E., Gondet, B., Gomez, C., 2005b. Phyllosilicates on Mars and implications for early martian climate. *Nature* 438, 623-627.

- Poulet, F., Mangold, N., Loizeau, D., Bibring, J.-P., Langevin, Y., Michalski, J., Gondet, B., 2008a. Abundance of minerals in the phyllosilicate-rich units on Mars. *Astronomy and Astrophysics* 487.
- Poulet, F., Mangold, N., Loizeau, D., Bibring, J., Langevin, Y., Michalski, J., Gondet, B., 2008b. Abundance of minerals in the phyllosilicate-rich units on Mars. *Astronomy and Astrophysics* 487, L41.
- Ribeiro, F.R., Fabris, J.D., Kostka, J.E., Komadel, P., Stucki, J.W., 2009. Comparisons of structural iron reduction in smectites by bacteria and dithionite: II. A variable-temperature Mössbauer spectroscopic study of Garfield nontronite. *Pure and Applied Chemistry* 81, 1499-1509.
- Rimstidt, J.D., Newcomb, W.D., 1993. Measurement and analysis of rate data: The rate of reaction of ferric iron with pyrite. *Geochimica et Cosmochimica Acta* 57, 1919-1934.
- Rosso, J.J., Rimstidt, J.D., 2000. A high resolution study of forsterite dissolution rates. *Geochimica et Cosmochimica Acta* 64, 797-811.
- Rozalén, M.L., Huertas, F.J., Brady, P.V., Cama, J., García-Palma, S., Linares, J., 2008a. Experimental study of the effect of pH on the kinetics of montmorillonite dissolution at 25 C. *Geochimica et Cosmochimica Acta* 72, 4224-4253.
- Rozalén, M.L., Huertas, F.J., Brady, P.V., Cama, J., García-Palma, S., Linares, J., 2008b. Experimental study of the effect of pH on the kinetics of montmorillonite dissolution at 25°C. *Geochimica et Cosmochimica Acta* 72, 4224-4253.
- Ruan, H., Gilkes, R., 1996. Kinetics of thermal dehydroxylation of aluminous goethite. *Journal of thermal analysis* 46, 1223-1238.

- Ruff, S.W., 2004. Spectral evidence for zeolite in the dust on Mars. *Icarus* 168, 131-143.
- Ruiz-Agudo, E., Putnis, C.V., Rodriguez-Navarro, C., Putnis, A., 2012. Mechanism of leached layer formation during chemical weathering of silicate minerals. *Geology* 40, 947-950.
- Ryan, P., Huertas, F.J., 2009. The temporal evolution of pedogenic Fe–smectite to Fe–kaolin via interstratified kaolin–smectite in a moist tropical soil chronosequence. *Geoderma* 151, 1-15.
- Sak, P.B., Fisher, D.M., Gardner, T.W., Murphy, K., Brantley, S.L., 2004. Rates of weathering rind formation on Costa Rican basalt. *Geochimica et Cosmochimica Acta* 68, 1453-1472.
- Sato, H., Shibutani, T., Yui, M., 1997. Experimental and modelling studies on diffusion of Cs, Ni and Sm in granodiorite, basalt and mudstone. *Journal of contaminant hydrology* 26, 119-133.
- Schnoor, J.L., 1990. Kinetics of chemical weathering: a comparison of laboratory and field weathering rates. IN: *Aquatic Chemical Kinetics: Reaction Rates of Processes in Natural Waters*. Environmental Science and Technology Series. John Wiley & Sons, New York. 1990. p 475-504. 18 fig, 3 tab, 36 ref.
- Sherman, G.D., 1952. The titanium content of Hawaiian soils and its significance. *Soil Science Society of America Journal* 16, 15-18.
- Smith, M.R., Bandfield, J.L., Cloutis, E.A., Rice, M.S., 2013. Hydrated silica on Mars; combined analysis with near-infrared and thermal-infrared spectroscopy. *Icarus* 223, 633-648.

- Soong, C., 1993. Hydrothermal kinetics of kaolinite-water interaction at pH 4.2 and 7.3, 130 C to 230 C. Pennsylvania State University.
- Sposito, G., 1986. The polymer model of thermochemical clay mineral stability. *Clays and Clay Minerals* 34, 198-203.
- Squyres, S.W., Grotzinger, J., Arvidson, R., Bell III, J., Calvin, W., Christensen, P., Clark, B., Crisp, J., Farrand, W., Herkenhoff, K.E., 2004. In situ evidence for an ancient aqueous environment at Meridiani Planum, Mars. *Science* 306, 1709-1714.
- Srodon, J., 1999. Nature of mixed-layer clays and mechanisms of their formation and alteration. *Annual Review of Earth and Planetary Sciences* 27, 19-53.
- Stadler, M., Schindler, P.W., 1993. Modeling of H (super +) and Cu (super 2+) adsorption on calcium-montmorillonite. *Clays and Clay Minerals* 41, 288-296.
- Steefel, C., 2009a. CrunchFlow software for modeling multicomponent reactive flow and transport. User's manual. Earth Sciences Division. Lawrence Berkeley, National Laboratory, Berkeley, CA. October, 12-91.
- Steefel, C.I., 2009b. CrunchFlow. Software for Modeling Multicomponent Reactive Flow and Transport. User's Manual. Lawrence Berkeley National Laboratory, Berkeley, USA.
- Steefel, C.I., Lasaga, A.C., 1994. A coupled model for transport of multiple chemical species and kinetic precipitation/dissolution reactions with application to reactive flow in single phase hydrothermal systems. *American Journal of Science* 294, 529-592.

- Steeffel, C.I., MacQuarrie, K.T., 1996. Approaches to modeling of reactive transport in porous media. *Reviews in mineralogy and geochemistry* 34, 85-129.
- Steeffel, C.I., Maher, K., 2009. Fluid-rock interaction: A reactive transport approach. *Reviews in mineralogy and geochemistry* 70, 485-532.
- Stumm, W., Lee, G.F., 1961. Oxygenation of ferrous iron. *Industrial & Engineering Chemistry* 53, 143-146.
- Sturhahn, W., 2000. CONUSS and PHOENIX: Evaluation of nuclear resonant scattering data. *Hyperfine Interactions* 125, 149-172.
- Sverdrup, H.U., 1990. The kinetics of base cation release due to chemical weathering. Lund University Press.
- Swoboda-Colberg, N.G., Drever, J.I., 1993. Mineral dissolution rates in plot-scale field and laboratory experiments. *Chemical Geology* 105, 51-69.
- Tardy, Y., Fritz, B., 1981. An ideal solid solution model for calculating solubility of clay minerals. *Clay Minerals* 16, 361-373.
- Tardy, Y., Garrels, K.M., 1974. A method of estimating the Gibbs energies of formation of layer silicates. *Geochimica et Cosmochimica Acta* 38, 1101-1116.
- Taylor, A.S., Blum, J.D., Lasaga, A.C., 2000a. The dependence of labradorite dissolution and Sr isotope release rates on solution saturation state. *Geochimica et Cosmochimica Acta* 64, 2389-2400.
- Taylor, A.S., Blum, J.D., Lasaga, A.C., MacInnis, I.N., 2000b. Kinetics of dissolution and Sr release during biotite and phlogopite weathering. *Geochimica et Cosmochimica Acta* 64, 1191-1208.

- Taylor, G., Eggleton, R., Holzhauser, C., Maconachie, L., Gordon, M., Brown, M., McQueen, K., 1992. Cool climate lateritic and bauxitic weathering. *The Journal of Geology*, 669-677.
- Taylor, G.L., Ruotsala, A., Keeling Jr, R., 1968. Analysis of iron in layer silicates by Mössbauer spectroscopy. *Clays & Clay Minerals* 16, 381-391.
- Thomson, B.J., Bridges, N.T., Milliken, R., Baldridge, A., Hook, S.J., Crowley, J.K., Marion, G.M., de Souza Filho, C.R., Brown, A.J., Weitz, C.M., 2011. Constraints on the origin and evolution of the layered mound in Gale Crater, Mars using Mars Reconnaissance Orbiter data. *Icarus* 214, 413-432.
- Tomita, K., Kawano, M., 2002. Synthesis of smectite from igneous rocks at atmospheric pressure. *Clay Science* 11, 585-599.
- Tomita, K., Yamane, H., Kawano, M., 1993. Synthesis of smectite from volcanic glass at low temperature. *Clays and Clay Minerals* 41, 655-655.
- Tosca, N.J., Knoll, A.H., McLennan, S.M., 2008. Water Activity and the Challenge for Life on Early Mars. *Science* 320, 1204-1207.
- Tosca, N.J., McLennan, S.M., Lindsley, D.H., Schoonen, M.A., 2004a. Acid-sulfate weathering of synthetic Martian basalt: The acid fog model revisited. *Journal of Geophysical Research: Planets* (1991–2012) 109.
- Tosca, N.J., McLennan, S.M., Lindsley, D.H., Schoonen, M.A.A., 2004b. Acid-sulfate weathering of synthetic Martian basalt: The acid fog model revisited. *Journal of Geophysical Research* 109, E05003.
- Treiman, A.H., Morris, R.V., Agresti, D.G., Graff, T.G., Achilles, C.N., Rampe, E.B., Bristow, T.F., Blake, D.F., Vaniman, D.T., Bish, D.L., 2014. Ferrian saponite

- from the Santa Monica Mountains (California, USA, Earth): Characterization as an analog for clay minerals on Mars with application to Yellowknife Bay in Gale Crater. *American Mineralogist* 99, 2234-2250.
- Turpault, M.P., Trotignon, L., 1994. The dissolution of biotite single crystals in dilute HNO<sub>3</sub> at 24°C: Evidence of an anisotropic corrosion process of micas in acidic solutions. *Geochimica et Cosmochimica Acta* 58, 2761-2775.
- Valeton, I., Beißner, H., 1986. Geochemistry and mineralogy of the Lower Tertiary in situ laterites on the Jos Plateau, Nigeria. *Journal of African Earth Sciences* (1983) 5, 535-550.
- Valsami-Jones, E., Ragnarsdottir, K.V., Putnis, A., Bosbach, D., Kemp, A.J., Cressey, G., 1998. The dissolution of apatite in the presence of aqueous metal cations at pH 2–7. *Chemical Geology* 151, 215-233.
- Vandenberghe, R.E., De Grave, E., 2013. Application of Mössbauer spectroscopy in earth sciences, *Mössbauer Spectroscopy*. Springer, pp. 91-185.
- Vaniman, D., Bish, D., Ming, D., Bristow, T., Morris, R., Blake, D., Chipera, S., Morrison, S., Treiman, A., Rampe, E., 2014. Mineralogy of a mudstone at Yellowknife Bay, Gale crater, Mars. *Science* 343, 1243480.
- Vantelon, D., Montarges-Pelletier, E., Michot, L., Pelletier, M., Thomas, F., Briois, V., 2003. Iron distribution in the octahedral sheet of dioctahedral smectites. An Fe K-edge X-ray absorption spectroscopy study. *Physics and Chemistry of Minerals* 30, 44-53.
- Velbel, M., 1993a. Weathering and pedogenesis at the watershed scale: Some recent lessons from studies of acid-deposition effects. *Chemical Geology* 107, 337-339.



- Velbel, M.A., 1993b. Constancy of silicate-mineral weathering-rate ratios between natural and experimental weathering: implications for hydrologic control of differences in absolute rates. *Chemical Geology* 105, 89-99.
- Velde, B., 1995. Composition and Mineralogy of Clay Minerals, in: Velde, B. (Ed.), *Origin and mineralogy of clays; clays and the environment*. Springer-Verlag, Berlin, Berlin, Federal Republic of Germany (DEU), pp. 8-42.
- Vicente, M.A., Suárez, M., López-González, J.d.D., Banares-Munoz, M.A., 1996. Characterization, surface area, and porosity analyses of the solids obtained by acid leaching of a saponite. *Langmuir* 12, 566-572.
- Viviano, C.E., Moersch, J.E., 2013. Using THEMIS data to resolve the discrepancy between CRISM/OMEGA and TES modeled phyllosilicate abundance in Mawrth Vallis. *Icarus* 226, 497-509.
- Weitz, C., Milliken, R., Grant, J., McEwen, A., Williams, R., Bishop, J., 2008. Light-toned strata and inverted channels adjacent to Juventae and Ganges chasmata, Mars. *Geophysical Research Letters* 35, L19202.
- Weitz, C., Milliken, R., Grant, J.A., McEwen, A., Williams, R., Bishop, J., Thomson, B., 2010. Mars Reconnaissance Orbiter observations of light-toned layered deposits and associated fluvial landforms on the plateaus adjacent to Valles Marineris. *Icarus* 205, 73-102.
- Welch, S.A., Taunton, A.E., Banfield, J.F., 2002. Effect of Microorganisms and Microbial Metabolites on Apatite Dissolution. *Geomicrobiology Journal* 19, 343-367.

- White, A.F., 2002. Determining mineral weathering rates based on solid and solute weathering gradients and velocities: application to biotite weathering in saprolites. *Chemical Geology* 190, 69-89.
- White, A.F., Brantley, S.L., 1995. Chemical weathering rates of silicate minerals; an overview. *Reviews in Mineralogy* 31, 1-22.
- White, A.F., Bullen, T.D., Schulz, M.S., Blum, A.E., Huntington, T.G., Peters, N.E., 2001. Differential rates of feldspar weathering in granitic regoliths. *Geochimica et Cosmochimica Acta* 65, 847-869.
- Wieland, E., Stumm, W., 1992. Dissolution kinetics of kaolinite in acidic aqueous solutions at 25 C. *Geochimica et Cosmochimica Acta* 56, 3339-3355.
- Wilson, J., Savage, D., Cuadros, J., Shibata, M., Ragnarsdottir, K.V., 2006. The effect of iron on montmorillonite stability. (I) Background and thermodynamic considerations. *Geochimica et Cosmochimica Acta* 70, 306-322.
- Wilson, S., 1998. Data compilation for USGS reference material GSP-2, Granodiorite, Silver Plume, Colorado. US Geological Survey Open-File Report, 11-12.
- Wogelius, R.A., Walther, J.V., 1992. Olivine dissolution kinetics at near-surface conditions. *Chemical Geology* 97, 101-112.
- Wray, J., Ehlmann, B., Squyres, S., Mustard, J., Kirk, R., 2008. Compositional stratigraphy of clay-bearing layered deposits at Mawrth Vallis, Mars. *Geophysical Research Letters* 35.
- Wray, J.J., Murchie, S.L., Squyres, S.W., Seelos, F.P., Tornabene, L.L., 2009. Diverse aqueous environments on ancient Mars revealed in the southern highlands. *Geology* 37, 1043-1046.

- Yang, L., Steefel, C.I., 2008. Kaolinite dissolution and precipitation kinetics at 22 C and pH 4. *Geochimica et Cosmochimica Acta* 72, 99-116.
- Yongue-Fouateu, R., Yemefack, M., Wouatong, A., Ndjigui, P., Bilong, P., 2009. Contrasted mineralogical composition of the laterite cover on serpentinites of Nkamouna-Kongo, southeast Cameroon. *Clay Minerals* 44, 221-237.
- Zysset, M., Schindler, P.W., 1996. The proton promoted dissolution kinetics of K-montmorillonite. *Geochimica et Cosmochimica Acta* 60, 921-931.

## CURRICULUM VITAE

### **Seth Reilly Gainey**

University of Nevada, Las Vegas  
4505 S. Maryland Pkwy  
Las Vegas, NV 89154-4010  
Email: gaineys@unlv.nevada.edu

## EDUCATION

University of Nevada, Las Vegas, NV Aug. 2011 to May 2015  
PhD Degree in Geoscience, 2015 (expect.)  
Advisor: Dr. Elisabeth Hausrath  
Dissertation title: *An Investigation into Transitions in Clay Mineral Chemistry on Mars*

University of Oklahoma, Norman, OK Aug. 2009 to May 2011  
MS Degree in Geology, 2011  
• Concentration in Geochemistry  
Advisor: Dr. Megan Elwood Madden  
Thesis title: *Kinetics of methane hydrate formation and dissociation under Mars relevant conditions*

Saint Cloud State University, Saint Cloud, MN Aug. 2004 to May 2009  
BS Degree in Geology, 2009  
• Minor in Biology

## PROFESSIONAL EXPERIENCE

University of Nevada, Las Vegas Aug. 2011 to May 2015  
*Teaching Assistant*  
• Lab Instructor for GEOL 101: Introductory Geology: Exploring Planet Earth  
• Supported the overall learning objective of the course, teaching college students about geological systems of the Earth  
• Instructed, prepared coursework, graded papers and answered questions about geology

*Research Assistant*  
• Nontronite dissolution kinetics and implications for Mars  
• Mineral, igneous rock and clay mineral alteration  
• Precipitation of zeolites and phyllosilicates

- Reactive transport modeling of transition in clay mineral chemistry on Mars

Jet Propulsion Laboratory June-Aug, 2011 & June-Aug, 2012  
*Nevada Space Grant Consortium, Summer Internship*

- Nontronite dissolution kinetics, and secondary mineral formation
- Mineral precipitation experiments under oxic and anoxic conditions

University of Oklahoma Aug. 2009 to May 2011  
*Teaching Assistant*

- Lab Instructor for GEOL 1104: The Dynamic Earth
- Supported learning objectives of the course, teaching students about the basics of geological systems of the Earth
- Instructed, prepared coursework, graded papers and answered questions about geology

*Research Assistant*

- Data collection and interpretation of kinetic experiments on hydrate formation and dissociation under Mars relevant conditions

Saint Cloud State University Aug. 2004 to May 2009  
*Teaching Assistant*

- Class-Room Assistant for EAS 109: The Geologic Environment
- Lab Assistant for EAS 220: Earth's Dynamic Systems

#### AWARDS RECEIVED

- NASA Planetary Science Summer School (2014)
- Edwards and Olswang Geology Scholarship (2014, 2015)
- NASA Astrobiology Institute: International Summer School in Astrobiology (2013)
- Graduate and Professional Student Association: Travel Grant (2013, 2014)
- Nevada Space Grant Consortium: Fellow (2013, 2015)
- Bernada French Scholarship (2012, 2013, 2014, 2015)
- Nevada Space Grant Consortium: JPL Summer Intern (2011, 2012)
- Ben Hare Award: For excellence in research (2011)

#### PEER-REVIEWED PUBLICATIONS

- Gainey, S. R., Hausrath E. M., Hurowitz J. A., Milliken R. E., "Nontronite dissolution rates and implications for Mars." *Geochimica et Cosmochimica Acta* 126 (2014): 192-211.

- Gainey, S. R., and M. E. Elwood Madden. "Kinetics of methane clathrate formation and dissociation under Mars relevant conditions." *Icarus* 218.1 (2012): 513-524.
- Elwood Madden, M.E., Leeman, J.R., Root, M.J., Gainey, S. "Reduced sulfur-carbon- water systems on Mars may yield shallow methane hydrate reservoirs." *Planetary and Space Science*, (2011): doi:10.1016/j.pss.2010.05.016.

#### EXTENDED ABSTRACTS, PRESENTATIONS AND OTHER PUBLICATIONS

- Gainey S. R.; Hausrath E. M.; Hurowitz J. A. "Weathering Profiles at Mawrth Vallis Yield Insight into the Aquoues Histroy and Potential Habitability of Mars" *46<sup>th</sup> Lunar and Planetary Science Conference Abstracts*. Vol 46. 2015.
- Schofield R. E.; Hausrath E. M.; Gainey S. R. "Zeolite Weathering in Laboratory and Natural Settings, and Implications for Mars" *46<sup>th</sup> Lunar and Planetary Science Conference Abstracts*. Vol. 46. 2015.
- Lawson, M. J.; Amador E. S.; Carrier, B. L.; Albuja, A.; Bapst, J.; Cahill, K.; Ebersson, F.; Gainey, S.; Gartrelle, G.; Greenberger, R.; Hale, J.; Johnston, S.; Olivares, J.; Parcheta, C.; Sheehan, J.; Thrope, A.; Zareh, S. "Enceladus Environmental Explorer (EVE): A Mission Concept" *In AGU Fall Meeting Abstracts*, 2014.
- Hausrath, E. M.; Adcock C. T.; Gainey, S. R.; Steiner, M. H. "Experimental Evidence Suggests Significant Aqueous Alteration and Abundant Phosphate Release on Mars" *Eighth International Conference on Mars*, 2014.
- Hausrath, E. M.; Adcock, C. T. Elwood Madden, M. E.; Gainey S. R.; Olsen, A. A.; Steiner, M. H. "Using Geochemical Kinetic to Interpret Potential Habitability" *45th Lunar and Planetary Science Conference Abstracts*. Vol. 45. 2014.
- Gainey, S. R., et al. "Formation of Aqueous Minerals: Implications for the Past Habitability of Mars." *Lunar and Planetary Institute Science Conference Abstracts*. Vol. 45. 2014.

- Gainey, S. R., Hausrath E. M., and J. A. Hurowitz. "Clay Mineral Precipitation and Implications for Mars." *Lunar and Planetary Institute Science Conference Abstracts*. Vol. 44. 2013.
- Gainey, S. R., E. M. Hausrath, and J. A. Hurowitz. "Kinetics of Nontronite Dissolution and Implications for Mars." *Lunar and Planetary Institute Science Conference Abstracts*. Vol. 43. 2012.
- Hausrath, E., Adcock, C. T., Gainey, S., Hurowitz, J. A., & Tu, V. "Laboratory experiments on Mars-relevant clay and phosphate minerals yield insights into the aqueous history and potential for habitability on Mars." In *AGU Fall Meeting Abstracts*, vol. 1, p. 03. 2012.
- Elwood Madden, M., Root, M., Gainey, S., Leeman, J., "Gas clathrate hydrate thermodynamics and kinetics: limits on near-surface volatile fluxes for cold terrestrial planetary systems through deep time" *Goldschmidt Conference Abstracts*. 2012.
- Gainey, S. R., et al. "Kinetics of Methane Hydrate Formation and Dissociation Under Mars Relevant Conditions." *Lunar and Planetary Institute Science Conference Abstracts*. Vol. 42. 2011.
- Root, M. J., S. R. Gainey, and M. E. Elwood Madden. "Assessment of Hydrate Reservoirs as Potential Methane Sources on Mars." *Lunar and Planetary Institute Science Conference Abstracts*. Vol. 41. 2010.

#### CONTRIBUTIONS TO UNIVERSITY AND PROFESSIONAL ORGANIZATIONS

- Reviewer for: Chemical Geology, *Geochimica et Cosmochimica Acta*, *Journal of Geophysical Research: Planets, Planetary and Space Science*; Mars Fundamental Research Program, *Earth and Planetary Science Letters*

#### RESEARCH INTERESTS

- Water rock interactions, kinetics, planetary geology, geochemistry, biology, reactive transport modeling and astrobiology

## REFERENCES

Available upon request